Lattice determination of semi-leptonic, heavy-light meson decay form factors

Michael Marshall

Doctor of Philosophy
The University of Edinburgh
22 December 2023

Abstract

The six-quark model and the Cabibbo-Kobayashi-Maskawa (CKM) matrix was first proposed as a "very interesting and elegant" [1–3] mechanism to explain charge-parity (CP) violation. Half a century later, the model still stands and the study of flavour-changing processes has become the field of flavour physics.

Precise experimental measurements from charm factories such as CLEO-c and BESIII and bottom-factories such as Belle, Belle II, BaBar and LHCb continue to test the Standard Model and the unitarity of the CKM matrix to ever greater precision. Hints of potential new physics exist, but to resolve them requires increased precision in theoretical prediction and experimental results.

This work performs a lattice computation of the matrix elements of exclusive semileptonic pseudoscalar meson decays involving charm → down (c → d) flavour transitions (fig 1), for which experimental results became available from BESIII in 2019. From these are extracted the form factors used to parameterise these hadronic matrix elements. The form factors are determined as a function of q^2, over the entire physically allowed kinematic range.

This approach complements the existing literature by performing the computation entirely with domain wall fermions. The charm action utilised in earlier

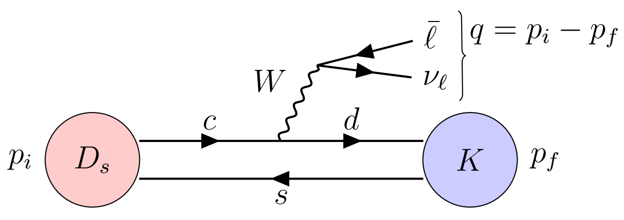

Figure 1 *Tree-level semileptonic decay of an initial pseudoscalar D_s meson (with momentum p_i) to a final pseudoscalar K meson (momentum p_f). Momentum $q = p_i - p_f$ is transferred to the final-state $\ell\nu$ pair.*

RBC/UKQCD studies [4] is employed here, using a stout-smeared [5] Möbius [6] action. The light and strange quarks are simulated with the Shamir [7–11] kernel.

The computation is performed on the RBC/UKQCD $N_f = 2 + 1$ Iwasaki gauge ensembles with heavier than physical pions and limited statistics. Results are broadly in agreement with the one published result in the literature, although there is a mild tension of 3σ at one kinematic point.

The form factors have been determined to an accuracy of 1.2–1.5%, with the result $f_0(0) = f_+(0) = 0.6557(78)$.

Combining this result with the experimental measurement of $|V_{cd}| f_+(0)$ from BESIII, yields a determination of the matrix element $V_{cd} = 0.247(29)_{\mathrm{expt}}(03)_{\mathrm{theory}}$. At 1.2%, the relative theory error in this determination of V_{cd} is around $4\frac{1}{2}\times$ smaller than the 5.7% relative theory error published by the Particle Data Group for the semileptonic determination.

The experimental results from BESIII currently have a relative error of 12%. If the experimental error in the $D_s \to K$ channel were to be reduced, this could become the most precise channel for determining $|V_{cd}|$.

Lay Summary of Thesis

THE UNIVERSITY *of* EDINBURGH

The lay summary is a brief summary intended to facilitate knowledge transfer and enhance accessibility, therefore the language used should be non-technical and suitable for a general audience. Guidance on the lay summary in a thesis. (See the Degree Regulations and Programmes of Study, General Postgraduate Degree Programme Regulations. These regulations are available via: www.drps.ed.ac.uk.)

Name of student:	Michael Marshall	UUN	1786208
University email:	Michael.Marshall@ed.ac.uk		
Degree sought:	PhD	No. of words in the main text of thesis:	21000
Title of thesis:	Lattice determination of semi-leptonic, heavy-light meson decay form factors		

Insert the lay summary text here - the space will expand as you type.

The Standard Model (SM) of particle physics is a very elegant model describing the electromagnetic force, weak nuclear decays and the strong nuclear force. It relies heavily on mathematical formulations of symmetry, which provide a great deal of richness and subtlety but can be difficult to work with.

The SM allows very precise predictions in some spheres, e.g. electromagnetism. Yet performing calculations involving the strong nuclear force using our normal mathematical tools involving equations cannot be done at low energies (typical energies seen outside the heart of a star or a particle accelerator) – because the approximations these equations rely on (perturbation theory) are only valid at higher energies.

We do have one way to perform these types of calculations – Lattice Quantum Chromodynamics (LQCD), the theory used in this thesis. LQCD uses a slightly modified (Euclidean) version of the field theory that applies in the everyday world (Minkowsi space). Rather than solving equations using approximations, this full theory simulates the fields themselves on a supercomputer using a tiny spacetime grid (with only, for example, 32 positions in each spatial direction and 64 steps in time).

The calculation in this thesis (and the preliminary studies leading up to it) took several years to run and analyse. The result is a pair of "form factors" for one specific weak nuclear decay (from D_s mesons to kaons). These are two smooth curves with energy on the *x*-axis and a number on the *y*-axis (between: 0.6557 and 1.000 for the "f_0" form factor; and 0.6557 and 1.592 for the "f_+" form factor). These "non-perturbatively" calculated form factors can be "plugged into" perturbation theory calculations to compute real-world properties mathematically.

In this thesis, the form factors are combined with experimental data to derive a value for a constant of nature called "V_{cd}", which is associated with weak nuclear decays. That is, V_{cd} is one element in a matrix of numbers governing how weak decays "mix up" different generations of matter.

The thesis is highly computational in nature and was performed on supercomputers equipped with GPUs to perform the floating-point calculations. The work might be of interest in more general high-performance computing applications and full code is available at http://lqcd.me/PhD.

Declaration

I declare that this thesis was composed by myself, that the work contained herein is my own except where explicitly stated otherwise in the text, and that this work has not been submitted for any other degree or professional qualification except as specified.

Parts of this work have been published in [12].

(*Michael Marshall, 22 December 2023*)

Acknowledgements

I am very grateful to everyone at the Higgs Centre for Theoretical Physics at the University of Edinburgh for teaching me field theory, then giving me the opportunity to use it. The more I've learned, the greater esteem I have for you.

There is a small army of people, generously funded by the Science and Technology Facilities Council (STFC), who, for their sins, keep the UK supercomputers' lights on. Keeping the wheels spinning at the bleeding edge of technology is no mean feat, and for doing it with such good grace, I thank you.

I have benefitted enormously from the experience of the RBC/UKQCD collaboration, particularly the interest and guidance of everyone in the charm physics Thursday calls. Thanks for all the tricky questions that cut to the heart of everything we discussed.

I very much enjoyed working with Felix Erben on an implementation of distillation, then applying this to semileptonic decays. Thanks for all the discussions, comparing notes validating fit codes and for all the constructive comments on plots.

I owe a special debt of gratitude to J. Tobias Tsang for his patient explanation of so many things I didn't understand. Thanks for always being there and for giving me so much of your time.

To my supervisor, Peter Boyle, thank you for the hand up and for the opportunity. Standing on the shoulders of giants, I've had the great pleasure of seeing the way the universe works and understanding some of it. Thank you for your many kindnesses.

To my wife, Catriona. I cannot thank you enough for your generosity in supporting me to do something I love almost as much as I love you.

Contents

List of Figures

List of Tables

Chapter 1

Introduction

This thesis performs an ab initio computation of the form factors for semileptonic decays of D_s mesons to kaons within the Standard Model. The computation is performed using lattice field theory at several lattice spacings followed by a chiral continuum extrapolation to make contact with current experimental results, which may help to test the unitarity of the Cabbibo-Kobayashi-Maskawa (CKM) [2, 3] matrix.

This chapter introduces the theory necessary to understand this computation of the form factors for the semileptonic meson decay $D_s \to K$ and is structured as follows:

1. Relevant sectors of the standard model in the continuum in Minkowski space.
2. Lattice Quantum Chromodynamics.
3. Lattice techniques used specifically for this computation.

Item 1 is performed in Minkowski space ('in the continuum'), with a mostly '$-$' metric $g_{\mu\nu} = g^{\mu\nu} = \text{diag}(1, -1, -1, -1)$. All other sections, except as noted, are performed in Euclidean space in discrete spacetime ('on the lattice'). The Einstein summation convention is used throughout (except where summations are explicitly shown).

1.1 The Standard Model

This section introduces sectors of the Standard Model of particle physics relevant to the description of semileptonic meson decays [13]. For details, the reader is referred to textbooks such as [14–19].

1.1.1 The Standard Model

The Standard Model (SM) is widely accepted as the best current model for the strong and electroweak interactions observed in the physical universe. It is tractable for computations and precise, with the difference between the SM theoretical prediction of the anomalous magnetic moment of the muon differing from its experimentally measured value by less than 3 parts per million [20].

However, the SM is clearly incomplete as it does not describe phenomena such as gravity, dark matter or neutrino oscillations. The SM is generally understood to be an effective field theory, valid to some upper scale, at least 1 TeV, and possibly much higher, up to the scale of Grand Unified Theories (GUT) [21–24].

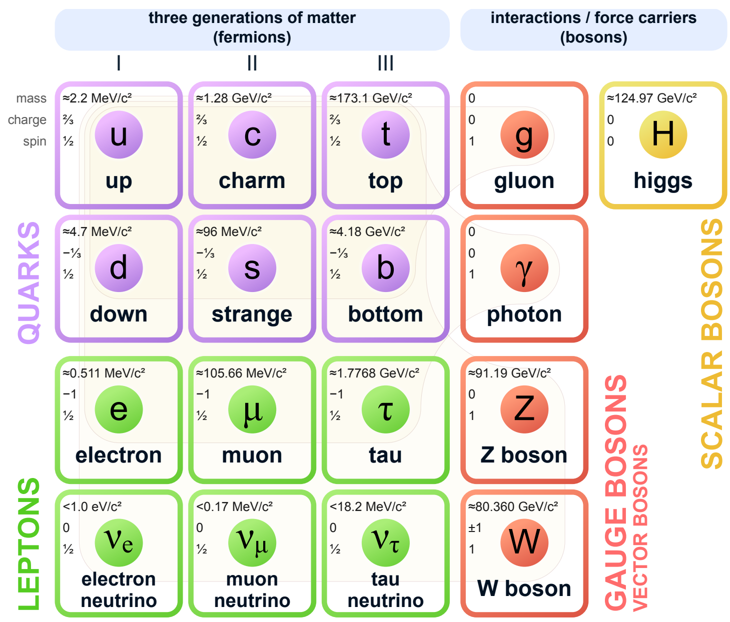

Figure 1.1 *Standard model particle content. Brown loops indicate which bosons (red) couple to which fermions (purple and green). Masses in this graphic were correct as of 2019 – see [25] for current values. Image and description courtesy of [26].*

The SM is a gauge theory with gauge group

$$SU(3)_{\rm C} \otimes SU(2)_{\rm L} \otimes U(1)_{\rm Y}\,, \tag{1.1}$$

where 'U' and 'SU' are the unitary and special unitary groups respectively, 'C' stands for *colour*, 'L' for *left-handed* and 'Y' for *weak hypercharge*. The particle content of the SM is shown in fig 1.1.

$SU(3)_{\rm C}$ is the gauge group of Quantum Chromodynamics (QCD) (see § 1.1.2). $SU(2)_{\rm L} \otimes U(1)_{\rm Y}$ is the gauge group of the electroweak sector (see § 1.1.3).

The Higgs mechanism spontaneously breaks the symmetry group

$$SU(2)_{\rm L} \otimes U(1)_{\rm Y} \longrightarrow U(1)_{\rm EM} \tag{1.2}$$

(where 'EM' denotes electromagnetism). As the Higgs mechanism is not directly relevant to the main work of this thesis, it is not presented in detail. In brief, the main features are:

1. The electroweak gauge bosons corresponding to $SU(2)_{\rm L} \otimes U(1)_{\rm Y}$ have no mass term in the Lagrangian (or they would not obey the gauge rotation symmetries).
2. The Higgs field is a complex scalar field – not shown in equation (1.1) – that interacts with fermions, electroweak gauge bosons and itself.
3. While the Higgs potential is azimuthally symmetric, the degenerate ground state does not respect this overall symmetry – we say the symmetry has been spontaneously broken.
4. When we replace the Higgs field with its vacuum expectation value (VEV), $v = 125.25(17)$ GeV [25], the interaction terms in the Lagrangian, which are otherwise quadratic in the fields, become mass terms.
5. This gives mass to the fermions and, when rotated to the right basis, also gives mass to the $W^{\pm}$ and Z bosons seen in nature, with the Higgs Nambu-Goldstone degrees of freedom appearing as the longitudinal component of the $W^{\pm}$ and Z.
6. The $U(1)_{\rm EM}$ symmetry remaining after spontaneous symmetry breaking (SSB) is associated with the massless photon of electromagnetism.

1.1.2 Quantum Chromodynamics

Ne'eman [27] and Gell-Mann [28] independently proposed a model for pseudo-scalar mesons[1] and spin 1/2 baryons based on $SU(3)$ symmetry – which, in a nod to Buddhism, Gell-Mann termed the Eightfold Way. In 1964, Gell-Mann proposed an $SU(3)$ quark [2] model [29], as did Zweig [30, 31][3]. The theory was extended by others such as Fritzch and Leutwyler [32] and, by 1973, Quantum Chromodynamics existed in the form used today.

QCD is a non-abelian theory of particles charged under the gauge group $SU(3)_{\mathrm{C}}$:

- **Quarks**: massive spin 1/2 fermions in the fundamental representation.
- **Gluons**: massless spin 1 gauge bosons in the adjoint representation. Being a non-abelian theory, the gluons self-interact.

The QCD Lagrangian

$$\mathcal{L}_{\mathrm{QCD}} = \mathcal{L}_{\mathrm{Dirac}} + \mathcal{L}_{\mathrm{Gauge}} \tag{1.3}$$

has a Dirac component for the $N_f = 6$ flavours of quark: u 'up'; d 'down'; c 'charm'; s 'strange'; t 'top'; b 'bottom':

$$\mathcal{L}_{\mathrm{Dirac}} = \sum_{f=1}^{N_f} \sum_{i,j=1}^{3} \bar{\psi}_f^i \left(\mathrm{i}\, \not{D} - m_f\right)_{ij} \psi_f^j \,, \tag{1.4}$$

where $\not{D} = \gamma^\mu D_\mu$ and the covariant derivative D is the colour matrix

$$(D_\mu)_{ij} = \partial_\mu \delta_{ij} + \mathrm{i}\, g A_\mu^a T_{ij}^a \,, \tag{1.5}$$

and

$$0 = D_\mu \gamma 5 + \gamma 5 D_\mu \,. \tag{1.6}$$

The gauge component of the Lagrangian with coupling g is

$$\mathcal{L}_{\mathrm{Gauge}} = -\frac{1}{4} \sum_{a=1}^{8} G_{\mu\nu}^a G^{a\mu\nu} = -\frac{1}{2} \operatorname{tr}\left(G_{\mu\nu} G^{\mu\nu}\right) \,, \tag{1.7}$$

$$G_{\mu\nu}^a = \partial_\mu A_\nu^a - \partial_\nu A_\mu^a - g f_{abc} A_\mu^b A_\nu^c \,, \tag{1.8}$$

$$G_{\mu\nu} = G_{\mu\nu}^a T^a \,, \tag{1.9}$$

[1] Quark bilinears defined by equation (1.92) and table 1.3.
[2] The term *quark* comes from James Joyce's *Finnegan's Wake*.
[3] Zweig called quarks *aces* and predicted exotic states today known as pentaquarks.

using the Generators T_a and structure constants f_{abc} for $SU(3)$

$$[T_a, T_b] = \mathrm{i}\, f_{abc} T_c \,. \tag{1.10}$$

For a local rotation of the gauge symmetry $\Omega\,(x) \in SU(3)$, the quark and gluon fields ψ and A transform as

$$\psi\,(x) \rightarrow \psi'\,(x) = \Omega\,(x)\,\psi\,(x) \tag{1.11}$$

$$A^a_\mu\,(x) \rightarrow A'^a_\mu\,(x) = \Omega\,(x)\left[A^a_\mu\,(x)\,T^a - \frac{\mathrm{i}}{g}\partial_\mu\right]\Omega^\dagger\,(x)\;. \tag{1.12}$$

Chiral symmetry

Massless fermions can be projected to left- and right-handed chiral components ψ_L and ψ_R

$$\psi = \psi_\mathrm{L} + \psi_\mathrm{R} = P_\mathrm{L}\psi + P_\mathrm{R}\psi\,, \qquad \text{with} \qquad P_{\mathrm{L/R}} = \frac{1}{2}\left(\mathbb{1} \mp \gamma_5\right)\,, \tag{1.13}$$

whereby the left and right chiralities decouple in $\mathcal{L}_{\mathrm{Dirac}}$ such that

$$\bar{\psi}\,\mathrm{i}\,\not{D}\psi = \bar{\psi}_\mathrm{L}\,\mathrm{i}\,\not{D}\psi_\mathrm{L} + \bar{\psi}_\mathrm{R}\,\mathrm{i}\,\not{D}\psi_\mathrm{R}\,. \tag{1.14}$$

The massless Lagrangian is invariant under independent flavour rotations of the left and right chiralities, $U\,(N_f)_\mathrm{L} \otimes U\,(N_f)_\mathrm{R}$

$$\psi_\mathrm{L} \rightarrow U\,(N_f)_\mathrm{L}\,\psi_\mathrm{L} \qquad \text{and} \qquad \psi_\mathrm{R} \rightarrow U\,(N_f)_\mathrm{R}\,\psi_\mathrm{R}\,. \tag{1.15}$$

The Lagrangian is invariant under vector transformations involving $U\,(N_f)$ generators λ_i (where $\lambda_i : i \in 1 \ldots N_f^2 - 1$ are the $SU\,(N_f)$ generators and $\lambda_0 \propto \mathbb{1}$)

$$\psi \rightarrow e^{\mathrm{i}\,\alpha\lambda_i}\psi \qquad \text{and} \qquad \bar{\psi} \rightarrow e^{-\,\mathrm{i}\,\alpha\lambda_i}\bar{\psi}\,. \tag{1.16}$$

The Lagrangian is also invariant under the chiral or axial transformations

$$\psi \rightarrow e^{\mathrm{i}\,\alpha\gamma_5\lambda_i}\psi \qquad \text{and} \qquad \bar{\psi} \rightarrow e^{-\,\mathrm{i}\,\alpha\gamma_5\lambda_i}\bar{\psi}\,. \tag{1.17}$$

It can be shown that the measure used in the fermion determinant (§ 1.2.2) is not invariant under chiral transformations involving λ_0. After this chiral anomaly, the residual chiral symmetries of the massless theory are $SU\,(N_f)_\mathrm{L} \otimes SU\,(N_f)_\mathrm{R} \otimes U_\mathrm{V}\,(1)$ (where $U_\mathrm{V}\,(1)$ denotes the vector transformation with generator λ_0).

1.1.3 Electroweak sector

The electroweak sector of the SM, quantum flavour dynamics, or Glashow-Salam-Weinberg (GSW) theory [33, 34], took its modern form in the early 1970s.

Before spontaneous symmetry breaking (SSB), we follow GSW and start by writing a gauge theory of fermions charged under the direct product $SU(2)_{\mathrm{L}} \otimes U(1)_{\mathrm{Y}}$, where the massless gauge bosons of the two groups are as described in table 1.1 and the gauge sector of the electroweak Lagrangian $\mathcal{L}_{\mathrm{EW}}$ is

$$\mathcal{L}_{\text{gauge}} = -\frac{1}{4} W^j_{\mu\nu} W^{j\mu\nu} - \frac{1}{4} B_{\mu\nu} B^{\mu\nu} \,, \tag{1.18}$$

with

$$W^j_{\mu\nu} = \partial_\mu W^j_\nu - \partial_\nu W^j_\mu - g\varepsilon^{jkl} W^k_\mu W^l_\nu \,, \quad j \in \{1,2,3\} \tag{1.19}$$

$$B_{\mu\nu} = \partial_\mu B_\nu - \partial_\nu B_\mu \,. \tag{1.20}$$

Name	Charge	Boson	Generators	Coupling
Weak isospin	$SU(2)_{\mathrm{L}}$	$W^j_{\mu\nu}$	$T \in \{T^1, T^2, T^3\}$	g
Weak hypercharge	$U(1)_{\mathrm{Y}}$	$B_{\mu\nu}$	Y	g'

Table 1.1 *Massless spin 1 bosons of the electroweak sector (before spontaneous symmetry breaking). The $U(1)_Y$ is abelian so the generators commute, i.e. $[T, Y]$.*

All fermions have weak hypercharge, but it is only the left handed fermions which are charged under $SU(2)_{\mathrm{L}}$, existing as left-handed lepton-neutrino pairs in the fundamental representation. There are no right handed neutrinos and right handed leptons are singlets. The particle content, their charges and quantum numbers are summarised in table 1.2 and, for down-type quarks, the electroweak eigenstates (dashed) are not the mass eigenstates (undashed), but rather are related via the CKM matrix V:

$$\begin{pmatrix} d \\ s \\ b \end{pmatrix} = V \begin{pmatrix} d' \\ s' \\ b' \end{pmatrix} \,. \tag{1.21}$$

	Field	T	Y	T^3	$Q = T^3 + Y$
Leptons	$L_i = \begin{pmatrix} \nu_e \\ e \end{pmatrix}_{\mathrm{L}}, \begin{pmatrix} \nu_\mu \\ \mu \end{pmatrix}_{\mathrm{L}}, \begin{pmatrix} \nu_\tau \\ \tau \end{pmatrix}_{\mathrm{L}}$	$\frac{1}{2}$	$-\frac{1}{2}$	$\frac{1}{2}$ $-\frac{1}{2}$	0 -1
	$e_i = e_{\mathrm{R}}, \mu_{\mathrm{R}}, \tau_{\mathrm{R}}$	0	-1	0	-1
Quarks	$Q_i = \begin{pmatrix} u \\ d' \end{pmatrix}_{\mathrm{L}}, \begin{pmatrix} c \\ s' \end{pmatrix}_{\mathrm{L}}, \begin{pmatrix} t \\ b' \end{pmatrix}_{\mathrm{L}}$	$\frac{1}{2}$	$\frac{1}{6}$	$\frac{1}{2}$ $-\frac{1}{2}$	$\frac{2}{3}$ $-\frac{1}{3}$
	$u_i = u_{\mathrm{R}}, c_{\mathrm{R}}, t_{\mathrm{R}}$	0	$\frac{2}{3}$	0	$\frac{2}{3}$
	$d'_i = d'_{\mathrm{R}}, s'_{\mathrm{R}}, b'_{\mathrm{R}}$	0	$-\frac{1}{3}$	0	$-\frac{1}{3}$

Table 1.2 *Fermion quantum numbers under $SU(2)_L \otimes U(1)_Y$. T and Y are the weak isospin and weak hypercharge generators described in table 1.1. T^3 is the third component of weak isospin and Q is electric charge. The index $i \in \{1, 2, 3\}$ runs over the three generations of fermions.*

The fermion sector of the electroweak Lagrangian $\mathcal{L}_{\mathrm{EW}}$ (where $N_{\mathrm{C}} = 3$ is the number of colours and $N_{\mathrm{g}} = 3$ is the number of fermion generations) is

$$\mathcal{L}_{\text{fermion}} = \sum_{i=1}^{N_{\mathrm{g}}} \left(\bar{L}_i \,\mathrm{i}\, \not{D} L_i + e_i \,\mathrm{i}\, \tilde{\not{D}} e_i + \sum_{c=1}^{N_{\mathrm{C}}} \left(\bar{Q}_i^c \,\mathrm{i}\, \not{D} Q_i^c + u_i^c \,\mathrm{i}\, \tilde{\not{D}} u_i^c + d'^c_i \,\mathrm{i}\, \tilde{\not{D}} d'^c_i \right) \right), \tag{1.22}$$

where the left- and right-handed covariant derivatives are

$$\not{D} = \mathbb{1}\partial_\mu + \mathrm{i}\, g \frac{\vec{\sigma}}{2} \vec{W}_\mu + \mathrm{i}\, g' Y B_\mu \mathbb{1} \tag{1.23}$$

$$\tilde{\not{D}} = \partial_\mu + \mathrm{i}\, g' Y B_\mu \,. \tag{1.24}$$

After SSB, the gauge bosons acquire mass via the Higgs mechanism and mix. Rotating to the physical mass eigenstate basis seen in nature, the neutral vector boson Z_μ and the photon A_μ arise as the mixing

$$\begin{pmatrix} Z_\mu \\ A_\mu \end{pmatrix} = \begin{pmatrix} \cos\theta_{\mathrm{W}} & -\sin\theta_{\mathrm{W}} \\ \sin\theta_{\mathrm{W}} & \cos\theta_{\mathrm{W}} \end{pmatrix} \begin{pmatrix} W^3_\mu \\ B_\mu \end{pmatrix}, \tag{1.25}$$

where

$$\sin\theta_{\mathrm{W}} = \frac{g'}{\sqrt{g^2 + g'^2}} \,. \tag{1.26}$$

A_μ is massless and the Z_μ mass $m_Z = v\sqrt{g^2+g'^2}\big/2 \simeq 91.1876(21)$ GeV [25].

The physical W^+_μ and W^-_μ are the linear combinations

$$W^\pm_\mu = W^1_\mu \mp \mathrm{i}\, W^2_\mu\,, \tag{1.27}$$

with mass $m_{W^\pm} = gv/2 \simeq 80.377(12)$ GeV [25].

The Feynman rules needed for this thesis are shown in fig 1.2 (the expression for the full Lagrangian rotated to the physical mass basis can be found in many textbooks).

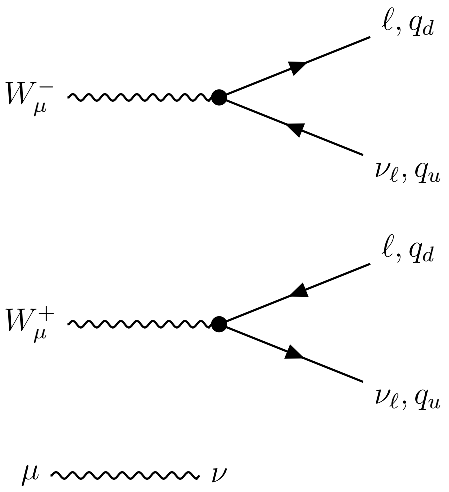

$$\frac{-\mathrm{i}\,g}{2\sqrt{2}}\,\gamma_\mu\,(1-\gamma_5)\times\begin{cases}1 & \text{leptons}\\ V^*_{ud} & \text{quarks}\end{cases}$$

$$\frac{-\mathrm{i}\,g}{2\sqrt{2}}\,\gamma_\mu\,(1-\gamma_5)\times\begin{cases}1 & \text{leptons}\\ V_{ud} & \text{quarks}\end{cases}$$

$$\mathrm{i}\left(\frac{-g^{\mu\nu}+\frac{q^\mu q^\nu}{M^2}}{q^2-M^2+\mathrm{i}\,\delta}\right)$$

Figure 1.2 *Feynman rules required for this thesis: the $W^\pm_\mu$-fermion vertices; and the $W^\pm_\mu$ propagator (given in unitary gauge, with $M = M_W$, the mass of the $W^\pm_\mu$).*

1.1.4 4-fermion interaction and the Fermi constant

This thesis concerns the electroweak, semileptonic decay of a quark to a lepton-neutrino pair via a charged current, mediated by the $W^\pm_\mu$ charged vector boson, such as that shown in fig 1.3.

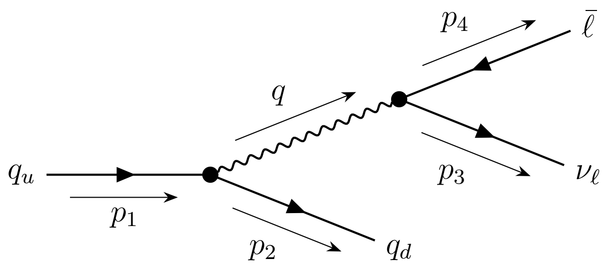

Figure 1.3 *Semileptonic decay of an up quark to a down quark and an antilepton-neutrino pair via a charged current, mediated by the W^+_μ charged vector boson. $q = p_1 - p_2$ is the momentum transferred to the final-state lepton pair.*

Using the Feynman rules (§ 1.1.3) and $P_{\rm L} = (\mathbb{1} - \gamma_5)/2$ from (1.13), the amplitude $\mathrm{i}\,\mathcal{M}$ for this decay is written

$$\mathrm{i}\,\mathcal{M} = \bar{u}_d\,(p_2)\,\frac{-\,\mathrm{i}\,g}{\sqrt{2}}\gamma_\mu P_{\rm L} V_{ud} u_u\,(p_1)\,\mathrm{i}\left(\frac{-g^{\mu\nu} + \frac{q^\mu q^\nu}{M_{\rm W}^2}}{q^2 - M_{\rm W}^2 + \mathrm{i}\,\delta}\right)\bar{u}_{\nu_\ell}\,(p_3)\,\frac{-\,\mathrm{i}\,g}{\sqrt{2}}\gamma_\nu P_{\rm L} v_\ell\,(p_4)\,. \tag{1.28}$$

However, for energies much lower than the mass of the $W^\pm_\mu$,

$$q = p_1 - p_2 \ll M_{\rm W}\,, \tag{1.29}$$

in which case subleading q terms in the propagator can be ignored yielding

$$\mathrm{i}\,\mathcal{M} = -\,\mathrm{i}\,V_{ud}\frac{G_{\rm F}}{\sqrt{2}}\bar{u}_d\,(p_2)\,\gamma_\mu\,(1-\gamma_5)\,u_u\,(p_1)\,\bar{u}_{\nu_\ell}\,(p_3)\,\gamma^\mu\,(1-\gamma_5)\,v_\ell\,(p_4)\;, \tag{1.30}$$

where the Fermi constant $G_{\rm F}$ is defined for this coupling

$$\frac{G_{\rm F}}{\sqrt{2}} = \frac{g^2}{8M_{\rm W}^2} = \frac{1}{2v}\,. \tag{1.31}$$

Thus, for low energies, $p_2 - p_1 \ll M_{\rm W}$, the point-like, 4-fermion interaction shown in fig 1.4 is a useful approximation for the full semileptonic decay mediated by the $W^\pm_\mu$ shown in fig 1.3.

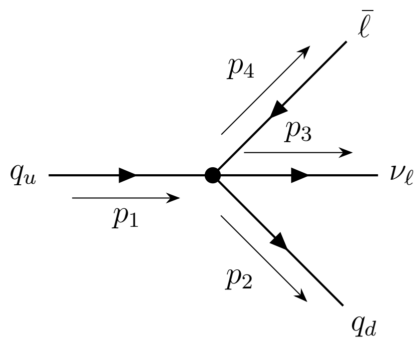

Figure 1.4 *At low energy ($p_1 - p_2 \ll M_W$) the point-like, 4-fermion interaction, with coupling $G_F/\sqrt{2}$ and decay amplitude (1.30), is a valid approximation of the full semileptonic decay shown in fig 1.3.*

1.1.5 Semileptonic decays and their form factors

Figure 1.5 considers semileptonic decays with bound pseudoscalar mesons (see § 1.3.2) in the initial and final states (rather than quarks as shown in fig 1.3).

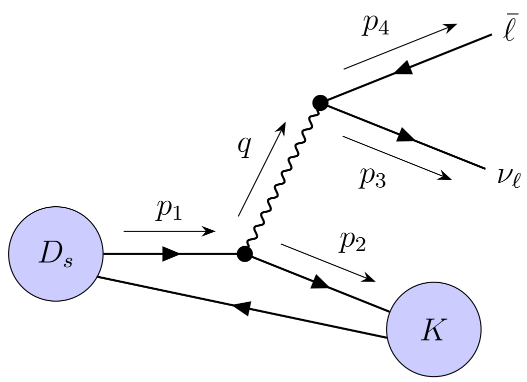

Figure 1.5 *Semileptonic decay of a pseudoscalar D_s meson to a kaon and an antilepton-neutrino pair via a charged current, mediated by the W_μ^+.*

Fig 1.5 factorises into a leptonic current

$$L^\mu = \bar{u}_{\nu_\ell}(p_3)\,\gamma^\mu\,(1-\gamma_5)\,v_\ell\,(p_4) \tag{1.32}$$

and a hadronic matrix element H_μ for the $D_s \to K$ decay

$$H_\mu = \langle K\,(p_2)|J_\mu^{(\mathrm{ps})}|D_s\,(p_1)\rangle\ , \tag{1.33}$$

where $J_\mu^{(\mathrm{ps})}$ is the charged vector current mediating the pseudoscalar decay. We do not write the continuum form of $J_\mu^{(\mathrm{ps})}$ because the methods described later in this thesis are used to perform a nonperturbative lattice computation of H_μ.

The amplitude for fig 1.5 is then

$$\mathrm{i}\,\mathcal{M} = \frac{-\mathrm{i}\,g^2}{8} V_{cd} H_\mu \left(\frac{-g^{\mu\nu} + \frac{q^\mu q^\nu}{M_\mathrm{W}^2}}{q^2 - M_\mathrm{W}^2} \right) L_\nu \tag{1.34}$$

$$\simeq -\mathrm{i}\,\frac{G_F}{\sqrt{2}} V_{cd} H_\mu L^\mu \,. \tag{1.35}$$

Given the pseudoscalar initial and final states described by H_μ, the degrees of freedom of the problem are the meson masses and their momenta. We follow the usual practice [35–37] of parameterising the matrix element H_μ into form factors, i.e. energy-dependent functions which encapsulate all of the complex QCD behaviour associated with the pseudoscalar meson bound states and their decays, as follows

$$H_\mu = f_+\left(q^2\right)\left[\left(p_1 + p_2\right)_\mu - \left(\frac{m_{D_s}^2 - m_K^2}{q^2}\right) q_\mu\right] + f_0\left(q^2\right)\left(\frac{m_{D_s}^2 - m_K^2}{q^2}\right) q_\mu \,, \tag{1.36}$$

where m_{D_s} and m_K are the masses of the D_s meson and kaon respectively.

This parameterisation, in the helicity basis, was first proposed by Martinelli, Sachrajda et al in 1989 [38] who note "that we only need to compute matrix elements of the vector current, since the matrix element of the axial component of the V-A weak current between two pseudoscalar states is zero."

We return to this in more detail in § 1.4.3.

1.2 QCD on the lattice

This section provides an introduction to Lattice QCD in the specific context of the semileptonic meson decay form factors computed in this thesis. For more detail, the reader is referred to texts such as [39–41].

1.2.1 Euclidean space

In lattice QCD, Minkowski space is Wick rotated to Euclidean space (the subscript '4' distinguishes the temporal component of Euclidean spacetime from Minkowskian spacetime)

$$x_0 \to -\mathrm{i}\, x_4 \,. \tag{1.37}$$

The gamma algebra changes from Minkowskian $\left\{\gamma_\mu^{(\mathrm{M})}, \gamma_\nu^{(\mathrm{M})}\right\} = 2g_{\mu\nu}$ to

$$\{\gamma_\mu, \gamma_\nu\} = 2\delta_{\mu\nu}\mathbb{1} \,, \tag{1.38}$$

where

$$\gamma_\mu = \begin{cases} -\mathrm{i}\,\gamma_\mu^{(\mathrm{M})}, & \mu \in \{1,2,3\} \\ \gamma_0^{(\mathrm{M})}, & \mu = 4 \end{cases} . \tag{1.39}$$

Spacetime is discretised, acting as the ultraviolet and infrared regulator in the theory, with Minkowskian spacetime integrals becoming sums over all lattice sites (where $|\Lambda|$ denotes the number of lattice sites)

$$\int \mathrm{d}^4 x \to a^4 \sum_{|\Lambda|} \,, \tag{1.40}$$

where the anisotropic lattices used in this thesis have a spatial length L and temporal extent T, set by the lattice scale a and the integer number of lattice sites in each dimension N_μ

$$N_\mu = \begin{cases} \frac{L}{a}, & \mu = 1,2,3 \\ \frac{T}{a}, & \mu = 4 \end{cases} . \tag{1.41}$$

1.2.2 Lattice path integrals

In Euclidean space, fermion fields $\psi(x)^{a}_{\alpha}$ remain Grassman valued and live on the lattice sites as spin-colour vectors. Gluon fields $U_\mu(x)$, however, now live on the links between lattice sites, taking different values in each direction as $SU(3)$ matrices in the fundamental representation. Detailed descriptions of fermion actions are deferred to § 1.2.4 and gauge actions to § 1.2.3.

The lattice action is real valued and positive definite such that the path integral is now well defined. The action is separated into the gauge action S_{G} and the fermion action S_{F} because the path integrals are performed separately in real simulations.

Vacuum expectation values for observables O are calculated as

$$\langle O\rangle = \frac{1}{Z}\int \mathcal{D}[U]\, e^{-S_{\mathrm{G}}[U]} \int \mathcal{D}\left[\psi,\bar{\psi}\right] e^{-S_{\mathrm{F}}\left[\psi,\bar{\psi},U\right]} O\left[\psi,\bar{\psi},U\right] , \tag{1.42}$$

where Z is the partition function

$$Z = \int \mathcal{D}[U]\, e^{-S_{\mathrm{G}}[U]} \int \mathcal{D}\left[\psi,\bar{\psi}\right] e^{-S_{\mathrm{F}}\left[\psi,\bar{\psi},U\right]} . \tag{1.43}$$

The fermionic and gluonic measures are

$$\mathcal{D}\left[\psi,\bar{\psi}\right] = \prod_{n\in|\Lambda|}\prod_{f,\alpha,c} \mathrm{d}\psi^{(f)}(n)^{\alpha}_{c}\, \mathrm{d}\bar{\psi}^{(f)}(n)^{\alpha}_{c} \tag{1.44}$$

$$\mathcal{D}[U] = \prod_{n\in|\Lambda|}\prod_{\mu=1}^{4} \mathrm{d}U_\mu(n) , \tag{1.45}$$

where $\mathrm{d}U$ is the Haar measure for $SU(3)$.

The Mathews Salam formula [42] gives the fermionic partition function

$$Z_F = \int \mathcal{D}\left[\psi,\bar{\psi}\right] e^{-S_{\mathrm{F}}\left[\psi,\bar{\psi},U\right]} = \det\left[-D\right] , \tag{1.46}$$

where the final result in terms of the Dirac matrix is the fermion determinant.

Wick's theorem allows the computation of fermionic expectation values $\langle\rangle_{\mathrm{F}}$ on each gauge field as the sum of all permutations of orderings of fermionic fields

$$\left\langle \psi_{i_1}\bar{\psi}_{j_1}\ldots\psi_{i_n}\bar{\psi}_{j_n}\right\rangle_{\mathrm{F}} = (-1)^n \sum_{\mathrm{perms}} \mathrm{sgn}\left(\mathrm{perm}\right) D^{-1}_{\mathrm{perm}\,1}\ldots D^{-1}_{\mathrm{perm}\,n}\,. \tag{1.47}$$

The expectation value $\langle O\rangle$ then becomes

$$\langle O\rangle = \frac{1}{Z}\int \mathcal{D}\left[U\right] e^{-S_{\mathrm{G}}[U]} Z_F \left\langle O\right\rangle_{\mathrm{F}}\ . \tag{1.48}$$

It is not possible to sample the full space of gauge configurations. Instead, $e^{-S_{\mathrm{G}}[U]+\ln Z_F}$ is treated as a likelihood and importance is sampled using Monte Carlo techniques [43] to produce an ensemble of N high importance (i.e. very likely) gauge configurations. It is the inclusion of the fermion determinant in the importance sampling that gives rise to nomenclature such as '$2+1$' for the gauge ensembles used in this thesis (which have two degenerate light quarks plus the strange quark included in the ensemble weights).

For this thesis, the ensembles are taken as given. For the observables of interest, fermionic expectation values $\langle\rangle_{\mathrm{F}_n}, n\in\{\,1\ldots N\,\}$ are computed for each configuration n of the gauge fields, which are then averaged to arrive at the gauge-averaged expectation value $\langle O\rangle$

$$\langle O\rangle = \frac{1}{N}\sum_{n=1}^{N}\left\langle O\right\rangle_{\mathrm{F}_n}\ . \tag{1.49}$$

1.2.3 Lattice gauge actions

Gluon fields $U_\mu\left(x\right)$ ('link variables' or 'gauge transporters') live on the links between lattice sites, taking different values in each direction as $SU(3)$ matrices in the fundamental representation. For a local gauge rotation $\Omega\left(x\right)\in SU(3)$, the gauge fields transform as

$$U_\mu\left(x\right)\to U'_\mu\left(x\right) = \Omega\left(x\right)U_\mu\left(x\right)\Omega\left(x+\hat{\mu}\right)^\dagger\ . \tag{1.50}$$

For notational convenience, we define

$$U_{-\mu}\left(x\right) = U_\mu\left(x-\hat{\mu}\right)^\dagger\ . \tag{1.51}$$

Given the gauge transformation properties, the trace of any path-ordered product of link variables around a closed loop is gauge invariant. The shortest possible closed loop is the Plaquette

$$U_{\mu\nu}(x) = U_\mu(x)\, U_\nu(x+\hat{\mu})\, U_{-\mu}(x+\hat{\mu}+\hat{\nu})\, U_{-\nu}(x+\hat{\nu}) \; . \tag{1.52}$$

Wilson [44] used the Plaquette to define the first lattice gauge action

$$S_{\mathrm{G}}[U]_{\mathrm{W}} = \frac{2}{g^2} \sum_{x,\mu<\nu} \mathrm{Re}\,\mathrm{tr}\left[\mathbb{1} - U_{\mu\nu}(x)\right] \; , \tag{1.53}$$

which he showed approached the continuum form up to terms $\mathcal{O}(a^2)$

$$S_{\mathrm{G}}[U]_{\mathrm{W}} = \frac{a^4}{2g^2} \sum_{x,\mu,\nu} \mathrm{tr}\left[F_{\mu\nu}(x)^2\right] + \mathcal{O}\big(a^2\big) \, . \tag{1.54}$$

The gauge ensembles used in this thesis use the Iwasaki gauge action [45, 46] $S_{\mathrm{G}}[U]_{\mathrm{I}}$

$$S_{\mathrm{G}}[U]_{\mathrm{I}} = \frac{\beta}{3}\left((1-8c_1)\sum_{x,\mu<\nu} \mathrm{Re}\left\{\mathrm{tr}\, U_{\mu\nu}(x)\right\} + c_1 \sum_{x,\mu\neq\nu} \mathrm{Re}\left\{\mathrm{tr}\, R_{\mu\nu}(x)\right\}\right) \tag{1.55}$$

with $c = -0.331$ and $\beta \sim 1/g_0^2$, where g_0 is the bare gauge coupling. $R_{\mu\nu}(x)$ is the closed rectangular loop

$$R_{\mu\nu}(x) = U_\mu(x)\, U_\nu(x+\hat{\mu})\, U_\nu(x+\hat{\mu}+\hat{\nu}) \tag{1.56}$$

$$U_{-\mu}(x+\hat{\mu}+2\hat{\nu}) + U_{-\nu}(x+2\hat{\nu})\, U_{-\nu}(x+\hat{\nu}) \; . \tag{1.57}$$

1.2.4 Lattice fermion actions and the Dirac operator

For a local gauge rotation $\Omega(x) \in SU(3)$, fermion fields $\psi(x)$ transform as

$$\psi(x) \to \psi'(x) = \Omega(x)\, \psi(x) \; . \tag{1.58}$$

Combined with (1.50), we see that discrete derivatives, which are built from terms such as $\bar{\psi}(x)\, U_\mu(x)\, \psi(x+\mu)$, are gauge invariant.

The lattice fermion action is generically written

$$S_{\mathrm{F}}\left[\psi,\bar{\psi},U\right]=\sum_{f=1}^{N_f}a^4\sum_{x,y}\bar{\psi}^{(f)}D^{(f)}\left(x,y\right)\psi^{(f)}\left(y\right)\,, \tag{1.59}$$

where $D^{(f)}$ is the Dirac operator for quark flavour f. There are multiple formulations of Dirac operator in current use.

Wilson fermions

Wilson's original formulation of the Dirac operator [44] added an additional $4/a$ to the mass term M to overcome the doubler problem (additional poles associated with momentum components 0 and π/a [47])

$$D_{\mathrm{W}}\left(x,y\right)_{\substack{\alpha\beta\\ab}}=\left(M+\frac{4}{a}\right)\delta_{\alpha\beta}\delta_{ab}\delta_{xy}-\frac{1}{2a}D_{\mathrm{hop}}\left(x,y\right)_{\substack{\alpha\beta\\ab}} \tag{1.60}$$

where the 'hopping' term D_{hop} connects nearest-neighbour sites

$$D_{\mathrm{hop}}\left(x,y\right)_{\substack{\alpha\beta\\ab}}=\sum_{\mu=1}^{4}\left[\left(\mathbb{1}-\gamma_\mu\right)_{\alpha\beta}U_\mu\left(x\right)_{ab}\delta_{x+\hat{\mu},y}+\left(\mathbb{1}+\gamma_\mu\right)_{\alpha\beta}U_\mu\left(x\right)_{ab}\delta_{x-\hat{\mu},y}\right]. \tag{1.61}$$

1.2.5 Ginsparg-Wilson and chiral symmetry

Ginsparg and Wilson [48] showed that on the lattice (1.6) has a remnant symmetry (but with the the appropriate continuum limit)

$$D\gamma_5+\gamma_5D=aD\gamma_5D\,. \tag{1.62}$$

Lattice chiral rotations which match § 1.1.2 in the continuum limit are

$$\psi'=\exp\left\{\mathrm{i}\,\alpha\gamma_5\left(\mathbb{1}-\frac{a}{2}D\right)\right\}\psi \tag{1.63}$$

$$\bar{\psi}'=\bar{\psi}\exp\left\{\mathrm{i}\,\alpha\left(\mathbb{1}-\frac{a}{2}D\right)\gamma_5\right\}. \tag{1.64}$$

Chiral projection operators for ψ_{L} and ψ_{R} on the lattice are

$$\hat{P}_{\mathrm{R}} = \frac{\mathbb{1} + \hat{\gamma}_5}{2} \quad \text{and} \quad \hat{P}_{\mathrm{L}} = \frac{\mathbb{1} - \hat{\gamma}_5}{2}, \quad \text{with} \quad \hat{\gamma}_5 = \gamma_5 \left(\mathbb{1} - aD\right) . \tag{1.65}$$

The lattice equivalent of the continuum chiral symmetry breaking mass term is

$$m \left(\bar{\psi}_{\mathrm{R}}\psi_{\mathrm{L}} + \bar{\psi}_{\mathrm{L}}\psi_{\mathrm{R}}\right) = m\bar{\psi}\left(P_{\mathrm{L}}\hat{P}_{\mathrm{L}} + P_{\mathrm{R}}\hat{P}_{\mathrm{R}}\right)\psi = m\bar{\psi}\left(\mathbb{1} - \frac{a}{2}D\right)\psi . \tag{1.66}$$

Incorporating this term, massive, chiral Ginsparg-Wilson fermions are constructed on the lattice using

$$D_{\mathrm{GW}} = \omega D + m\mathbb{1} , \qquad \text{where} \qquad \omega = 1 - \frac{am}{2} . \tag{1.67}$$

1.2.6 Nielsen-Ninomiya no-go theorem

The Nielson Ninomiya no-go theorem [49–52] tells us that for a generic fermion action in Fourier space of the form

$$\hat{S}_{\mathrm{F}}\left[\psi, \bar{\psi}, U\right] = \int_{-\frac{\pi}{a}}^{\frac{\pi}{a}} \frac{\mathrm{d}^4 k}{(2\pi)^4}\, \hat{\bar{\psi}}\left(-k\right)\left(K\left(k\right) + m\right)\psi\left(k\right) , \tag{1.68}$$

a choice must be made to sacrifice at least one of the following:

1. $K\left(k\right)$ is invertible $\forall k \neq 0$, i.e. no doublers.
2. $\lim_{a\to 0} K\left(k\right) = \mathrm{i}\,\not{k} + \mathcal{O}(ak^2)$, i.e. the correct continuum limit.
3. $\{K\left(k\right), \gamma^5\} = 0$, i.e. chiral symmetry.
4. $K\left(k\right)$ is periodic and analytic, i.e. the action is local.

The Wilson fermion action (1.60), for example, sacrificed chiral symmetry.

1.2.7 Overlap fermions

Overlap fermions D_{OV} were formulated by Neuberger [53], who showed [54] they obey the Ginsbarg-Wilson relation (1.62). In general they have the form

$$D_{\mathrm{OV}} = \frac{1}{a}\left(\mathbb{1} + \gamma_5\,\mathrm{sgn}\left(H\right)\right) , \qquad \text{where} \qquad H = \gamma_5 A , \tag{1.69}$$

and where the kernel A is a γ_5-hermitian Dirac operator specifying the type of overlap operator. Computing the sign function

$$\mathrm{sgn}\,(H) = H|H|^{-1} = H\left(H^2\right)^{-1/2} \tag{1.70}$$

is numerically challenging and various overlap algorithms explore this challenge using a variety of methods.

Using the Wilson fermion action (1.60) for the kernel retains the problem with doublers.

1.2.8 Domain wall fermions

For data production in this thesis, domain wall fermions (DWF) [7] are used. These are a type of overlap fermion and, in the modern formulation, [55] we use the kernel

$$H = \gamma_5 \frac{(b+c)\,D_{\mathrm{W}}}{2+(b-c)\,D_{\mathrm{W}}}\,, \tag{1.71}$$

where $b = c = 1$ selects the Shamir [8–11] kernel and $b = 1.5$, $c = 0.5$ selects the Möbius [6, 56] kernel. Both kernels are used for data production.

DWF circumvent the limits of the Nielsen-Ninomiya no-go theorem by adding a fifth spatial dimension. The generic lattice fermion action (1.59) is extended to a fifth spatial dimension, $s \in \{\,0 \ldots L_s - 1\,\}$ and the 5-dimensional DWF Dirac operator, $D^5_{\mathrm{DW}}\,(x, s; x', s')$, is (setting $a = 1$) [57]

$$D^5_{\mathrm{DW}} = 5 - M_5 - \frac{1}{2}D_{\mathrm{hop}} - \frac{1}{2}D_\perp = D_\parallel \delta_{s,s'} - \frac{1}{2}D_\perp \delta_{x,x'}\,, \tag{1.72}$$

where

$$D_\perp = P_L \delta_{s+1,s'} + P_R \delta_{s-1,s'} \tag{1.73}$$

$$D_\parallel = 5 - M_5 - \frac{1}{2}D_{\mathrm{hop}} = D_{\mathrm{W}}\,(-M_5) + 1\,. \tag{1.74}$$

The fifth dimensional fermion mass M_5 plays a more complicated role than that of a bare mass. Here we use the optimal value for the Iwasaki gauge action, $M_5 = 1.8$ [46], except for the charm action or the F1M ensemble where $M_5 = 1.0$ is used. [58, 59]

Physical fermion fields with opposite chirality live on the first and last slices of the fifth dimension

$$\psi(x) = P_L \psi(x, 0) + P_R \psi(x, L_s - 1) \tag{1.75}$$

$$\bar{\psi}(x) = \psi(x, L_s - 1) P_L + \psi(x, 0) P_R \,. \tag{1.76}$$

Blum et al [60] showed that DWF have small chiral symmetry breaking effects, which can be reduced (by increasing L_s) but not eliminated. These lead to an additive residual mass term m_{res}, such that the effective mass in the Lagrangian m_{eff} for a fermion with bare mass m_f becomes

$$m_{\text{eff}} = m_{\text{res}} + m_f \,. \tag{1.77}$$

1.3 Methods of lattice QCD

This section explains practical implementation considerations and techniques broadly applicable to many Lattice QCD projects.

1.3.1 2-point functions

In a basis of eigenstates of the Hamiltonian $\hat{H}\,|n\rangle = E_n\,|n\rangle$, the Euclidean 2-point correlation function on a lattice of temporal extent T (in integer lattice units) with operator insertions $\hat{O}_i$ and $\hat{O}_f$ at initial time $t_i = 0$ and final time $t_f = t$ is defined as

$$\left\langle \hat{O}_f\,(t)\,\hat{O}_i\,(0)\right\rangle \equiv \frac{1}{Z_T}\,\mathrm{Tr}\left(\mathrm{e}^{-T\hat{H}}\,\hat{O}_f\,(t)\,\hat{O}_i\,(0)\right) \tag{1.78}$$

$$= \frac{1}{Z_T}\,\mathrm{Tr}\left(\mathrm{e}^{-T\hat{H}}\,\mathrm{e}^{t\hat{H}}\,\hat{O}_f\,\mathrm{e}^{-t\hat{H}}\,\hat{O}_i\right) \tag{1.79}$$

$$= \frac{1}{Z_T}\sum_{m,n=0}^{\infty}\,\langle m|\mathrm{e}^{-(T-t)\hat{H}}\,\hat{O}_f\,\mathrm{e}^{-t\hat{H}}|n\rangle\;\langle n|\hat{O}_i|m\rangle \tag{1.80}$$

$$= \frac{1}{Z_T}\sum_{m,n=0}^{\infty}\,\langle m|\hat{O}_f|n\rangle\;\langle n|\hat{O}_i|m\rangle\,\mathrm{e}^{-E_m(T-t)}\,\mathrm{e}^{-E_n t}, \tag{1.81}$$

where $\sum_n |n\rangle\langle n| = 1$ and Z_T is the partition function,

$$Z_T = \mathrm{Tr}\left(e^{-T\hat{H}}\right) = \sum_{n=0}^{\infty}\,\langle n|e^{-T\hat{H}}|n\rangle\,. \tag{1.82}$$

Using $\langle n|n\rangle = 1$ and ordering the spectrum $E_{n+1} \geq E_n$ above the vacuum $E_0 = 0$

$$Z_T = \sum_{n=0}^{\infty} e^{-E_n T} = 1 + \sum_{n=1}^{\infty} e^{-E_n T} \simeq 1 \tag{1.83}$$

for large T.

Considering (1.81), $\mathrm{e}^{-E_m(T-t)}$ is suppressed for small t, except for $m = 0$ (because $E_0 = 0$). Similarly, $\mathrm{e}^{-E_n t}$ is suppressed for large t unless $n = 0$.

Relabelling the vacuum $|\Omega\rangle$ and the ground state $|0\rangle$ (with energy E_0), we continue

$$\left\langle \hat{O}_f\,(t)\,\hat{O}_i\,(0)\right\rangle = \sum_{n=0}^{\infty}\Bigg[\langle\Omega|\hat{O}_f|n\rangle\;\langle n|\hat{O}_i|\Omega\rangle\,\mathrm{e}^{-E_n t} \tag{1.84}$$

$$+\;\langle n|\hat{O}_f|\Omega\rangle\;\langle\Omega|\hat{O}_i|n\rangle\,\mathrm{e}^{-E_n(T-t)}\Bigg], \tag{1.85}$$

where we relabelled $m \to n$ in (1.85). Commonly, (1.84) is referred to as the forward propagating wave, whereas (1.85) is the backward propagating wave.

Using $O^\dagger = \pm O$ for meson bilinears, $\langle n|\hat{O}_f|\Omega\rangle = \pm\langle\Omega|\hat{O}_f|n\rangle^*$. The overlap coefficients $\langle\Omega|\hat{O}_f|n\rangle$ can be shown to be real or purely imaginary [61]. One can, therefore, take the appropriate component and define them to be real – as is done throughout this thesis. Defining

$$A_{f,n} \equiv \begin{cases}\mathrm{Re}\Big\{\langle n|\hat{O}_f^\dagger|\Omega\rangle\Big\}\\ \mathrm{Im}\Big\{\langle n|\hat{O}_f^\dagger|\Omega\rangle\Big\}\end{cases} \in \mathbb{R}\,, \tag{1.86}$$

gives

$$\left\langle \hat{O}_f\,(t)\,\hat{O}_i\,(0)\right\rangle = \sum_{n=0}^{\infty} A_{f,n}A_{i,n}\left(\mathrm{e}^{-E_n t} \pm \mathrm{e}^{-E_n(T-t)}\right). \tag{1.87}$$

For the states of definite momentum used here, the normalisation is

$$1 = |\Omega\rangle\langle\Omega| + \sum_{n=0}^{\infty}\frac{|n\rangle\langle n|}{2E_n}\,, \tag{1.88}$$

which gives the more recognisable result

$$\left\langle \hat{O}_f\,(t)\,\hat{O}_i\,(0)\right\rangle = \sum_{n=0}^{\infty}\frac{A_{f,n}A_{i,n}}{2E_n}\,\mathrm{e}^{-E_n T/2}\begin{cases}\cosh\left(E_n\left(T/2-t\right)\right)\\ \sinh\left(E_n\left(T/2-t\right)\right)\end{cases} \tag{1.89}$$

depending on the sign of the $\pm$ term in (1.87).

1.3.2 Local meson interpolating operators

Local interpolating operators for mesons consist of Dirac bilinears containing a quark field $q(x)_{\underset{c}{\alpha}}$, a gamma structure from table 1.3 and an antiquark field $\bar{q}'(x)_{\underset{c}{\beta}}$

$$\bar{q}'(x)_{\underset{c}{\beta}} = \sum_{\delta} q^*(x)_{\underset{c}{\delta}} [\gamma_4]_{\delta\beta} \,. \tag{1.90}$$

The local meson interpolating operator is

$$O(x) = \sum_{\alpha\beta c} \bar{q}'(x)_{\underset{c}{\alpha}} \Gamma_{\alpha\beta}\, q(x)_{\underset{c}{\beta}} \,, \tag{1.91}$$

with Γ chosen from table 1.3 to have the spin and parity quantum numbers of the state of interest. These determine the Lorentz transformation properties of the meson. Here we restrict our attention to pseudoscalar mesons, which transform as a scalar, though change sign under parity transformations (negation of spatial coordinates).

Corresponding creation operators are constructed either with $\Gamma' = \Gamma$, or another Γ is selected with the same quantum numbers

$$O^{\dagger}(y) = \sum_{\rho\sigma d} \bar{q}(y)_{\underset{d}{\rho}} \Gamma'_{\sigma\rho}\, q'(y)_{\underset{d}{\sigma}} \,. \tag{1.92}$$

Γ	State	Spin	Parity	Mesons in this thesis
$\gamma_5, \gamma_4\gamma_5$	Pseudoscalar	0	$-$	D_s, K
$\mathbb{1}, \gamma_4$	Scalar	0	$+$	
$\gamma_i, \gamma_4\gamma_i$	Vector	1	$-$	
$\gamma_i\gamma_5$	Axial vector	1	$+$	
$\gamma_i\gamma_j$	Tensor	1	$+$	

Table 1.3 *Gamma structures used in fermion bilinears. The listed Γ structures create mesons with the spin and parity quantum numbers and Lorentz transformation properties shown for each state.*

Unless otherwise specified, data presented in this thesis are constructed with $\Gamma = \gamma_5$. Data constructed using $\Gamma = \gamma_4\gamma_5$, will be denoted 'axial'.

1.3.3 Wick's theorem

In order to evaluate the two point correlator (1.122), one must evaluate the Grassman integrals comprising the fermionic expectation value

$$\left\langle O(x)\, O^{\dagger}(y)\right\rangle = \left\langle \sum_{\alpha\beta c} \bar{q}'(x)_{\substack{\alpha\\c}}\, \Gamma_{\alpha\beta}\, q(x)_{\substack{\beta\\c}} \sum_{\rho\sigma d} \bar{q}(y)_{\substack{\rho\\d}}\, \Gamma'_{\sigma\rho}\, q'(y)_{\substack{\sigma\\d}} \right\rangle \tag{1.93}$$

$$= -\sum_{\substack{\alpha\beta c\\ \rho\sigma d}} \left\langle \Gamma'_{\sigma\rho}\, q'(y)_{\substack{\sigma\\d}}\, \bar{q}'(x)_{\substack{\alpha\\c}}\, \Gamma_{\alpha\beta}\, q(x)_{\substack{\beta\\c}}\, \bar{q}(y)_{\substack{\rho\\d}} \right\rangle \tag{1.94}$$

Wick's theorem tells us that we can compute the expectation value by contracting all permutations of quark fields of the same flavour. Each contraction is a linear operator, the inverse Dirac matrix, for a quark field of flavour q propagating to row x from column y,

$$D_q^{-1}(x,y)_{\substack{\beta\rho\\cd}} = \left\langle \overbrace{q(x)_{\substack{\beta\\c}}\, \bar{q}(y)_{\substack{\rho\\d}}} \right\rangle . \tag{1.95}$$

For the flavour nonsymmetric mesons studied here, Wick's theorem gives

$$\left\langle O(x)\, O^{\dagger}(y)\right\rangle = -\operatorname{Tr}\left[\Gamma'^{\dagger} D_{q'}^{-1}(y,x)\, \Gamma D_q^{-1}(x,y)\right] . \tag{1.96}$$

The overall negative sign is dropped as it has no physical significance.

In general, additional permutations of quark contractions lead to disconnected diagrams. However, this does not apply to the mesons discussed here.

1.3.4 Smeared meson interpolating operators

Smeared quark fields $\tilde{q}(x)$ are defined as

$$\tilde{q}(x)_{\substack{\alpha\\a}} = \sum_{z\beta b} S_s^{(x,\alpha,a)*}(z)_{\substack{\beta\\b}}\, q(z)_{\substack{\beta\\b}} , \tag{1.97}$$

which are then used to construct Smeared interpolators O_s

$$O_s(x) = \bar{\tilde{q}}'(x)\, \Gamma\, \tilde{q}(x) \tag{1.98}$$

$$= \sum_{v,w} q'^{*}(v)\, S_s^{(x)}(v)\, \gamma_4 \Gamma\, S_s^{(x)*}(w)\, q(w) \tag{1.99}$$

for various smearing functions S_s taken from the literature, where s labels the smearing.

The smearing function as written in (1.97) can be thought of as a matrix, where each index is a composite spacetime-spin-colour index. However, in this thesis, only one smearing function depends on the spatial component x, the 'true' point (§ 1.3.4), which is only ever used at the sink – never as a smearing source.

When the 2-point function is evaluated for the mesons in this thesis, the creation operator is placed on a specific timeslice. Correspondingly, the smearing sources depend on spin, colour and timeslice, but do not depend on spatial position, so these are defined to include a spatial sum. It is best to consider them as a collection of 12 (one for each of the 4 spin $\times$ 3 colour combinations) vectors associated with a source located on a specific timeslice. This plays a role in why propagator solves require 12 inversions of the Dirac matrix, as seen in § 1.3.6.

Replacing local with smeared interpolators, (1.96) becomes

$$\left\langle O_{\text{snk}}\left(x\right) O_{\text{src}}^{\dagger}\left(y\right)\right\rangle = \sum_{ruvw} \text{Tr}\Big[\Gamma'^{\dagger} S_{\text{src}}^{(y)*}\left(w\right) D_{q'}^{-1}\left(w,r\right) S_{\text{snk}}^{(x)}\left(r\right) \\ \Gamma S_{\text{snk}}^{(x)*}\left(u\right) D_{q}^{-1}\left(u,v\right) S_{\text{src}}^{(y)}\left(v\right)\Big]. \tag{1.100}$$

For most types of smearing functions, the dependence on x in a smearing function $S_{\text{snk}}^{(x)}\left(r\right)$ is only to the timeslice x_4. These are usually referred to as sources or sinks on a timeslice.

The three smearing functions used in this thesis (see table 1.4) are introduced in the following sections.

Smearing	Sink	Source	Label
'True' point	yes	–	P
Gauge-fixed wall	yes	yes	W
$\mathbb{Z}\left(2\right)$wall	–	yes	P

Table 1.4 *Smearings used in this thesis and whether they have been used at the sink or source (see § 1.3.7). Throughout, sinks or sources are referred to generally as 'P' = Point or 'W' = Wall. In case of 'P', this denotes* $\mathbb{Z}\left(2\right)$ *for point sources and the 'true' point for point sinks.*

'True' point

The 'true' point smearing locates a smeared quark field at a single specified location via the Kronecker delta function

$$S_{\text{point}}^{(y,\beta,b)}\,(x)_{\substack{\alpha\\a}} = \delta_{x,y}\,\delta_{\alpha,\beta}\,\delta_{a,b}\,, \tag{1.101}$$

where the Kronecker delta function is defined such that

$$\delta_{i,j} = \begin{cases} 1, & i = j \\ 0, & i \neq j \end{cases}\,. \tag{1.102}$$

Inserting S_{point} into (1.97), this is defined so that the smeared quark field remains local, i.e.

$$\tilde{q}_{\text{point}}\,(x)_{\substack{\alpha\\a}} = q\,(x)_{\substack{\alpha\\a}}\,. \tag{1.103}$$

Gauge-fixed wall

Gauge-fixed wall smearings, S_W, have a wall of constant charge at each spatial position on a specified timeslice $t = x_4$

$$S_W^{(y,\alpha,a)}\,(x)_{\substack{\beta\\b}} = \delta_{x_4,y_4}\,\delta_{\alpha,\beta}\,\delta_{a,b}. \tag{1.104}$$

Note that there is no delta function over the spatial component of y, leaving a spatial sum over timeslice y_4 after insertion in 1.97, consuming the sum over $\mathbf{y}$ in the correlation function (1.122).

The wall-smeared quark field is

$$\tilde{q}_W\,(x)_{\substack{\alpha\\a}} = \sum_{\mathbf{y}} q\,(\mathbf{y}, x_4)_{\substack{\alpha\\a}}\,. \tag{1.105}$$

Used as a source, this introduces a volume factor as the quark field at each point already contains the sum over the timeslice.

The gauge-fixed wall is not gauge-covariant, so the gauge must be fixed (see § 1.3.11) when using this smearing.

$\mathbb{Z}(2)$ wall

For $\mathbb{Z}(2)$ wall sources [62, 63], the distribution $\mathcal{D}$ is defined as the random choice of separate real and imaginary components ± 1, normalised to fit on the unit circle

$$\mathcal{D} = \mathbb{Z}(2) \otimes \mathbb{Z}(2) = \left\{ \frac{\pm 1 \pm \mathrm{i}}{\sqrt{2}} \right\}. \tag{1.106}$$

At each lattice site, a complex number is drawn from this distribution so that

$$S_P^{(y,\alpha,a)}(x)_{\substack{\beta \\ b}} = \mathcal{D}\, \delta_{x_4,y_4}\, \delta_{\alpha,\beta}\, \delta_{a,b}\,, \tag{1.107}$$

where $(\delta_{\alpha\beta})$ ensures the smearing commutes with any choice of Γ' in (1.100). This is motivated by the observation that, for each random vector of $\mathbb{Z}(2)$ noises, $S_P^{(r)}$ (where each $r = \{x, \alpha, a\}$ labels a separate 'hit' of noise)

$$\left\langle S_P^{(r)}(x)_{\substack{\alpha \\ a}} \right\rangle = 0 \tag{1.108}$$

and

$$\left\langle S_P^{(r)}(x)_{\substack{\alpha \\ a}}\, S_P^{(s)*}(y)_{\substack{\beta \\ b}} \right\rangle = \delta_{x,y}\, \delta_{\alpha,\beta}\, \delta_{a,b}\, \delta_{r,s}\,, \tag{1.109}$$

where this expectation value is normally defined as a hit average over multiple random vectors, $S^{(r)}$. However, in this thesis, a single hit of noise is used – relying on the fact that the hit and gauge averages may be performed simultaneously, so that under the gauge average (1.108) and (1.109) are true.

Thus, under the gauge average, the $\mathbb{Z}(2)$ smearing acts like the 'true' point, such that a $\mathbb{Z}(2)$ source with a 'true' point sink acts like a sum over point sources at each site on the source (up to a volume factor). Being point sources, the gauge does not need to be fixed.

Prior to commencing the main work in this thesis, exploratory studies [12, 64, 65] examined the possibility of rotations between point and wall smearings. It was found that, while source rotations were able to reduce the time for plateau onset, it was not possible to find an equivalent sink rotation using the wall sink operator (which induced large statistical error).

1.3.5 γ_5 hermiticity and momentum projection

The Dirac operator is γ_5 hermitian ($\gamma_5 D = (\gamma_5 D)^\dagger$), which is exploited in order to reduce the number of propagator solves in the full simulation. The smeared 2-point correlation function (1.100) becomes

$$\left\langle O_{\text{snk}}(x)\, O_{\text{src}}^\dagger(y)\right\rangle = \sum_{ruvw} \text{Tr}\left[\Gamma'^\dagger S_{\text{src}}^{(y)*}(w)\, \gamma_5 \left[D_{q'}^{-1}(w,r)\right]^\dagger \gamma_5\, S_{\text{snk}}^{(x)}(r) \right.$$
$$\left. \Gamma S_{\text{snk}}^{(x)*}(u)\, D_q^{-1}(u,v)\, S_{\text{src}}^{(y)}(v)\right], \quad (1.110)$$

and, because the smearings are diagonal in Dirac indices (and hence commute with γ_5),

$$\left\langle O_{\text{snk}}(x)\, O_{\text{src}}^\dagger(y)\right\rangle = \sum_{ruvw} \text{Tr}\left[\Gamma'^\dagger \gamma_5 \left[S_{\text{snk}}^{(x)*}(r)\, D_{q'}^{-1}(r,w)\, S_{\text{src}}^{(y)}(w)\right]^* \right.$$
$$\left. \gamma_5\, \Gamma S_{\text{snk}}^{(x)*}(u)\, D_q^{-1}(u,v)\, S_{\text{src}}^{(y)}(v)\right]. \quad (1.111)$$

The correlation function is evaluated at definite momenta, but only the smearing functions depend on x and y. The momentum projected smearing functions are

$$S_s^{(x,\alpha,a,\mathbf{p})}(y)_{\substack{\beta \\ b}} = S_s^{(x,\alpha,a)}(y)_{\substack{\beta \\ b}}\, \mathrm{e}^{\mathrm{i}\,\mathbf{p}\cdot\mathbf{x}} \quad (1.112)$$

so that the momentum projected 2-point correlation function becomes

$$\mathrm{e}^{-\mathrm{i}\,\mathbf{p}\cdot(\mathbf{x}-\mathbf{y})} \left\langle O_{\text{snk}}(x)\, O_{\text{src}}^\dagger(y)\right\rangle = -\sum_{ruvw} \text{Tr}\left[\Gamma'^\dagger \gamma_5 \left[S_{\text{snk}}^{(x,\mathbf{0})*}(r)\, D_{q'}^{-1}(r,w)\, S_{\text{src}}^{(y,\mathbf{0})}(w)\right]^* \right.$$
$$\left. \gamma_5\, \Gamma S_{\text{snk}}^{(x,\mathbf{p})*}(u)\, D_q^{-1}(u,v)\, S_{\text{src}}^{(y,\mathbf{p})}(v)\right]. \quad (1.113)$$

1.3.6 Propagators and sliced propagators

The Dirac matrix is a matrix in spacetime, spin and colour. On the smallest gauge ensemble used in this thesis, this would require

$$\left(\left(\frac{L}{a}\right)^3 \times \frac{T}{a} \times N_s \times N_c\right)^2 \times 16 = \left(24^3 \times 64 \times 4 \times 3\right)^2 \times 16 \tag{1.114}$$

$$\simeq 1.8 \text{ PB} \tag{1.115}$$

to instantiate the matrix in double precision (16 bytes per complex number). Numerically inverting it would be computationally impractical and its sparse nature would demand further study.

Fortunately, as seen in (1.113), the full Dirac matrix – let alone its inverse – is not required to numerically evaluate the momentum projected 2-point correlation function. Rather, the action of the inverse of the Dirac matrix on each smearing source is used.

The lattice propagator G, for a quark field with Dirac operator D_q, from a smeared source S to every site, x, on the lattice is defined as

$$G^{(y,\mathbf{p})}_{q,\mathrm{src}}\left(x\right)_{\substack{\alpha\beta\\ab}} = \sum_{v\delta c} D_q^{-1}\left(x,v\right)_{\substack{\alpha\delta\\ac}} S^{(y,\beta,b,\mathbf{p})}_{\mathrm{src}}\left(v\right)_{\substack{\delta\\c}}, \tag{1.116}$$

which is a vector over each lattice site x, where each site is a spin-colour matrix.

There is no sum over β or b in (1.116) – instead, they select one of the 12 source vectors. Subsequently, for each spin-colour combination, vector solutions, G, are found to

$$DG = S \tag{1.117}$$

using the numerical techniques outlined in § 1.3.12. Rewriting (1.113) in terms of the lattice propagator vector G,

$$\begin{aligned} e^{-\,i\,\mathbf{p}\cdot(\mathbf{x}-\mathbf{y})}\left\langle O_{\mathrm{snk}}\left(x\right) O^{\dagger}_{\mathrm{src}}\left(y\right)\right\rangle = \sum_{ru} \mathrm{Tr}\Bigg[\Gamma'^{\dagger}\gamma_5 \left[S^{(x,\mathbf{0})*}_{\mathrm{snk}}\left(r\right) G^{(y,\mathbf{0})}_{q',\mathrm{src}}\left(r\right)\right]^* \\ \gamma_5\,\Gamma S^{(x,\mathbf{p})*}_{\mathrm{snk}}\left(u\right) G^{(y,\mathbf{p})}_{q,\mathrm{src}}\left(u\right)\Bigg]. \end{aligned} \tag{1.118}$$

Point sink

In the case of the 'true' point sink, (1.101) is inserted into (1.118) which becomes

$$\mathrm{e}^{-\,\mathrm{i}\,\mathbf{p}\cdot(\mathbf{x}-\mathbf{y})}\left\langle O_P\left(x\right)O^{\dagger}_{\mathrm{src}}\left(y\right)\right\rangle = \mathrm{Tr}\left[\Gamma'^{\dagger}\gamma_5\,G^{(y,\mathbf{0})}_{q',\mathrm{src}}\left(x\right)^*\gamma_5\,\Gamma\,\mathrm{e}^{-\,\mathrm{i}\,\mathbf{p}\cdot\mathbf{x}}\,G^{(y,\mathbf{p})}_{q,\mathrm{src}}\left(x\right)\right]\,, \tag{1.119}$$

which is a spin-colour trace at each lattice site x (after projecting each site at the sink to definite momentum $\mathbf{p}$).

Wall sinks and sliced propagators

When the wall smearing (1.104) is used for the sink, it is useful to define a sliced propagator

$$G^{(\mathbf{q},y,\mathbf{p})}_{W,q,\mathrm{src}}\left(t\right)_{\substack{\alpha\beta\\ab}} = \sum_{\mathbf{x}}\mathrm{e}^{\mathrm{i}\,\mathbf{q}\cdot\mathbf{x}}\,G^{(y,\mathbf{p})}_{q,\mathrm{src}}\left(\mathbf{x},t\right)_{\substack{\alpha\beta\\ab}}\,, \tag{1.120}$$

which is a single spin-colour trace on each sink timeslice, $t = x_4$. Each lattice site is multiplied by the momentum phase $\mathrm{e}^{-\,\mathrm{i}\,\mathbf{p}\cdot\mathbf{x}}$ before the spatial sums implementing the momentum projection are taken.

We rewrite (1.118) using a wall sink

$$\mathrm{e}^{-\,\mathrm{i}\,\mathbf{p}\cdot(\mathbf{x}-\mathbf{y})}\left\langle O_W\left(x\right)O^{\dagger}_{\mathrm{src}}\left(y\right)\right\rangle = \mathrm{Tr}\left[\Gamma'^{\dagger}\gamma_5\,G^{(\mathbf{0},y,\mathbf{0})}_{W,q',\mathrm{src}}\left(x_4\right)^*\gamma_5\,\Gamma G^{(-\mathbf{p},y,\mathbf{p})}_{W,q,\mathrm{src}}\left(x_4\right)\right]\,. \tag{1.121}$$

Matching the trace to the code

The trace in expressions (1.119) and (1.121) are both performed by the same code in `Meson.hpp` from Hadrons [66]:

```
#define mesonConnected(q1, q2, gSnk, gSrc) \
(g5*(gSnk))*(q1)*(adj(gSrc)*g5)*adj(q2)
```

Using propagators or sliced propagators (depending on the sink smearing), `q1` is set to the forward propagator and `q2` the backward propagator (i.e. propagator being computed with γ_5 hermeticity). Using the cyclicality of the trace, the code begins with the γ_5 before `gSnk` $= \Gamma$. The code explicitly takes the adjoint of the gamma at the source, `adj(gSrc)`$= \Gamma'^\dagger$.

1.3.7 2-point correlation function

Two-point correlation functions $C^{(2)}_{if}$ are constructed placing the creation interpolating operator on timeslice t_i and projecting the 2-point function using smeared interpolators (see § 1.3.4) to definite momentum, $\mathbf{p}$

$$C^{(2)}_{if}\left(t;\mathbf{p}\right) = \sum_{\mathbf{xy}} \mathrm{e}^{-\,\mathrm{i}\,\mathbf{p}\cdot(\mathbf{x}-\mathbf{y})} \left\langle O_f\left(\mathbf{x}, t+t_i\right) O^\dagger_i\left(\mathbf{y}, t_i\right)\right\rangle \,, \tag{1.122}$$

where the subscripts i=initial and f=final on $C^{(2)}$ label the source and sink as either P=Point or W=Wall. The usual factor of $1/|\Lambda_3|$ (the number of spatial lattice sites) is omitted from this definition, both for clarity and because these factors are not applied within Grid [67] or Hadrons [66].

Once the propagators are constructed, the contractions (i.e. the trace and final sum) require minimal computing time to perform, although the method depends on the choice of sink smearing.

The source smearing functions, by definition (§ 1.3.4), have no dependence on the spatial component of y. Thus, the final sum over $\mathbf{y}$ is not taken, as this would merely introduce a volume factor.

Point sink contraction

Using (1.119), the 2-point correlator becomes

$$C^{(2)}_{iP}\left(t\right) = \sum_{\mathbf{x}} \mathrm{Tr}\left[\Gamma'^\dagger \gamma_5\, G^{(y,\mathbf{0})}_{q',\mathrm{src}}\left(x\right)^* \gamma_5\, \Gamma\, \mathrm{e}^{-\,\mathrm{i}\,\mathbf{p}\cdot\mathbf{x}}\, G^{(y,\mathbf{p})}_{q,\mathrm{src}}\left(x\right)\right] \,. \tag{1.123}$$

The trace is performed at each sink lattice site x using the propagator vectors, then summed separately over each timeslice.

This matches the (abridged) `Meson.hpp` code in Hadrons to perform the contraction (making use of `mesonConnected`)

```
auto &q1 = envGet(PropagatorField1, par().q1);
auto &q2 = envGet(PropagatorField2, par().q2);
envGetTmp(LatticeComplex, c);
PropagatorField1 &sink = envGet(PropagatorField1, par().sink);
c = trace(mesonConnected(q1, q2, gSnk, gSrc)*sink);
sliceSum(c, buf, Tp);
```

where `sink` is the momentum phase applied at each site and `sliceSum` performs the sum on each timeslice.

Wall sink contraction

Using (1.121), the 2-point correlator becomes

$$C^{(2)}_{iW}(t) = \sum_{\mathbf{x}} \mathrm{Tr}\left[\Gamma'^{\dagger}\gamma_5\, G^{(\mathbf{0},y,\mathbf{0})}_{W,q',\mathrm{src}}(x_4)^{*}\,\gamma_5\,\Gamma G^{(-\mathbf{p},y,\mathbf{p})}_{W,q,\mathrm{src}}(x_4)\right]. \tag{1.124}$$

The trace is performed once on each timeslice using the sliced propagators.

The (abridged) `Meson.hpp` code performing the spatial sum on each timeslice in (1.124) is

```
auto &q1 = envGet(SlicedPropagator1, par().q1);
auto &q2 = envGet(SlicedPropagator2, par().q2);
for (unsigned int t = 0; t < nt; ++t)
  result[i].corr[t] = TensorRemove(trace(mesonConnected(q1[t], q2[t],
                                                        gSnk, gSrc)));
```

The spatial sum in (1.124) introduces a volume factor for each wall sink, which arises because the spatial sum has already been taken and $\sum_{\mathbf{x}} f(\mathbf{x}) = A \implies \sum_{\mathbf{x}}\left(\sum_{\mathbf{x}} f(\mathbf{x})\right) = |\Lambda_3| A$.

1.3.8 3-point function

The 3-point function shown in fig 1.6 is

$$C \equiv \left\langle \hat{O}_f(t_f)\,\hat{V}_{\mu}(t)\,\hat{O}^{\dagger}_i(t_i)\right\rangle. \tag{1.125}$$

This is a semileptonic decay of an initial pseudoscalar meson P_i (created by $\hat{O}_i^\dagger$) to a final pseudoscalar meson P_f (annihilated by $\hat{O}_f$). This is a decay from a heavy quark h to a light quark ℓ via the vector current

$$V_\mu = \bar{\ell}\gamma_\mu h \tag{1.126}$$

with a light spectator ℓ'.

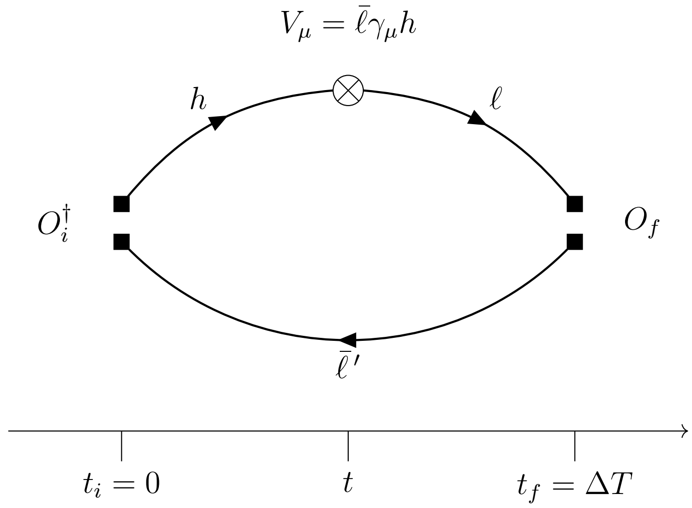

Figure 1.6 *3-point correlation function for a heavy pseudoscalar meson with creation operator $O_i^\dagger$ decaying to a light pseudoscalar meson with annihilation operator O_f via a vector current $V_\mu = \bar{h}\,\gamma_\mu\,\ell$. That is, a h=heavy quark decaying to ℓ=light quark with another light spectator $\bar{\ell}'$. The labels 'if' label the initial- and final-state meson smearings S_i and S_f in the operators $O_i^\dagger$ and O_f, respectively (P=Point or W=Wall, see § 1.3.4). The vector current, V_μ, is local.*

For $t_i < t < t_f$

When the current is time ordered before the annihilation operator, the 3-point correlation function becomes

$$C = \sum_p \langle p|\mathrm{e}^{-\hat{H}\left(T-t_f\right)}\,\hat{O}_f\,\mathrm{e}^{-\hat{H}\left(t_f-t\right)}\,\hat{V}_\mu\,\mathrm{e}^{-\hat{H}(t-t_i)}\,\hat{O}_i^\dagger\,\mathrm{e}^{-\hat{H}t_i}|p\rangle \tag{1.127}$$

$$= \sum_{mnp} \mathrm{e}^{-E_p\left(T+t_i-t_f\right)}\,\langle p|\hat{O}_f|m\rangle\,\mathrm{e}^{-E_m\left(t_f-t\right)}\,\langle m|\hat{V}_\mu|n\rangle\,\mathrm{e}^{-E_n(t-t_i)}\,\langle n|\hat{O}_i^\dagger|p\rangle\ . \tag{1.128}$$

For large T, only $|p\rangle = |\Omega\rangle \implies E_p = 0$ survives

$$C = \sum_{mn} \langle\Omega|\hat{O}_f|m\rangle\, \mathrm{e}^{-E_m\left(t_f - t\right)}\, \langle m|\hat{V}_\mu|n\rangle\, \mathrm{e}^{-E_n(t-t_i)}\, \langle n|\hat{O}_i^\dagger|\Omega\rangle\,. \tag{1.129}$$

The states $|m\rangle$ ($|n\rangle$) overlap the final (initial) states. Relabelling the energies and reintroducing continuum normalisation

$$C = \sum_{mn} \frac{A_{f,m}A_{i,n}}{4E_{f,m}E_{i,n}} \langle m|\hat{V}_\mu|n\rangle\, \mathrm{e}^{-E_{f,m}\left(t_f - t\right)}\, \mathrm{e}^{-E_{i,n}(t-t_i)}\,. \tag{1.130}$$

For $t_i < t_f < t$

When the current is time ordered after the annihilation operator

$$\begin{aligned} C &= \sum_{n} \langle n|\mathrm{e}^{-\hat{H}(T-t)}\, \hat{V}_\mu\, \mathrm{e}^{-\hat{H}\left(t-t_f\right)}\, \hat{O}_f\, \mathrm{e}^{-\hat{H}\left(t_f-t_i\right)}\, \hat{O}_i^\dagger\, \mathrm{e}^{-\hat{H}t_i}|n\rangle && (1.131)\\ &= \sum_{mnp} \mathrm{e}^{-E_n(T+t_i-t)}\, \langle n|\hat{V}_\mu|m\rangle\, \mathrm{e}^{-E_m\left(t-t_f\right)}\, \langle m|\hat{O}_f|p\rangle\, \mathrm{e}^{-E_p\left(t_f-t_i\right)}\, \langle p|\hat{O}_i^\dagger|n\rangle\,. && (1.132)\end{aligned}$$

We are interested in large enough wall separations $\Delta T = t_f - t_i$ such that only $|p\rangle = |\Omega\rangle \implies E_p = 0$ survives

$$C = \sum_{mn} \mathrm{e}^{-E_n(T+t_i-t)}\, \langle n|\hat{V}_\mu|m\rangle\, \mathrm{e}^{-E_m\left(t-t_f\right)}\, \langle m|\hat{O}_f|\Omega\rangle\, \langle\Omega|\hat{O}_i^\dagger|n\rangle\,. \tag{1.133}$$

Again the states $|m\rangle$ ($|n\rangle$) overlap the final (initial) states. After relabelling the energies and reintroducing continuum normalisation

$$\begin{aligned} C &= \sum_{mn} \frac{A_{f,m}A_{i,n}}{4E_{f,m}E_{i,n}} \langle m|\hat{V}_\mu^\dagger|n\rangle^*\, \mathrm{e}^{-E_{f,m}\left(t-t_f\right)}\, \mathrm{e}^{-E_{i,n}(T+t_i-t)} && (1.134)\\ &= c_\mu \sum_{mn} \frac{A_{f,m}A_{i,n}}{4E_{f,m}E_{i,n}} \langle m|\hat{V}_\mu|n\rangle\, \mathrm{e}^{-E_{f,m}\left(t-t_f\right)}\, \mathrm{e}^{-E_{i,n}(T+t_i-t)}\,, && (1.135)\end{aligned}$$

taking $\langle m|\hat{V}_\mu|n\rangle \in \mathbb{R}$ and using $V_\mu^\dagger = c_\mu V_\mu$ where

$$c_\mu = \begin{cases} -1, & \gamma_4 \\ 1, & \gamma_i \end{cases}\,. \tag{1.136}$$

When both time orderings are included [68, 69]

$$\left\langle \hat{O}_f\left(t_f\right) \hat{V}_\mu\left(t\right) \hat{O}_i^\dagger\left(t_i\right)\right\rangle = \sum_{mn} \frac{A_{f,m} A_{i,n}}{4 E_{f,m} E_{i,n}} \langle m|\hat{V}_\mu|n\rangle \Bigg[\tag{1.137}$$

$$\theta\left(t_f - t\right) \mathrm{e}^{-E_{f,m}\left(t_f - t\right)} \mathrm{e}^{-E_{i,n}\left(t - t_i\right)} \tag{1.138}$$

$$+ c_\mu \theta\left(t - t_f\right) \mathrm{e}^{-E_{f,m}\left(t - t_f\right)} \mathrm{e}^{-E_{i,n}\left(T + t_i - t\right)} \Bigg] . \tag{1.139}$$

1.3.9 3-point correlation function

The 3-point correlation function projects the 3-point function shown in fig 1.6 to definite incoming momentum $\mathbf{p}$ at the source (t_i) and outgoing momenta $\mathbf{p}'$ at the sink (t_f) and $\mathbf{q} = \mathbf{p} - \mathbf{p}'$ at the local current

$$C_{if}^{(3)\mu}\left(t; \mathbf{p}, \mathbf{p}'\right) = \sum_{\mathbf{xyz}} \mathrm{e}^{-\,\mathrm{i}\,\mathbf{p}\cdot(\mathbf{x}-\mathbf{z})} \mathrm{e}^{-\,\mathrm{i}\,\mathbf{p}'\cdot(\mathbf{z}-\mathbf{y})} \left\langle O_f\left(\mathbf{x}, t_f\right) V^\mu\left(\mathbf{z}, t\right) O_i^\dagger\left(\mathbf{y}, t_i\right)\right\rangle . \tag{1.140}$$

For the decay $D_s \to K$, the three quarks involved (c, s and ℓ) are non flavour symmetric, which simplifies the Wick contractions. We can immediately write (again dropping the physically insignificant overall $-$ sign)

$$C^\mu = \mathrm{e}^{-\,\mathrm{i}\,\mathbf{p}\cdot(\mathbf{x}-\mathbf{z})} \mathrm{e}^{-\,\mathrm{i}\,\mathbf{p}'\cdot(\mathbf{z}-\mathbf{y})} \left\langle O_{\mathrm{snk}}\left(x\right) V^\mu\left(z\right) O_{\mathrm{src}}^\dagger\left(y\right)\right\rangle \tag{1.141}$$

$$= \sum_{ruvw} \mathrm{Tr}\Bigg[\Gamma'^\dagger S_{\mathrm{src}}^{(y,\mathbf{0})*}\left(w\right) D_{\ell'}^{-1}\left(w, r\right) S_{\mathrm{snk}}^{(x,\mathbf{0})}\left(r\right) \tag{1.142}$$

$$\Gamma S_{\mathrm{snk}}^{(x,\mathbf{p})*}\left(u\right) D_\ell^{-1}\left(u, z\right) \tag{1.143}$$

$$\gamma^\mu\ \mathrm{e}^{-\,\mathrm{i}\,\mathbf{z}\cdot(\mathbf{p}'-\mathbf{p})} D_h^{-1}\left(z, v\right) S_{\mathrm{src}}^{(y,\mathbf{p}')}\left(v\right) \Bigg] . \tag{1.144}$$

Using γ_5 hermeticity (and the fact that smearing sources are diagonal in spin),

$$C^\mu = \sum_{ruvw} \mathrm{Tr}\Bigg[\Gamma'^\dagger \gamma_5 \Big(D_\ell^{-1}\left(z, u\right) S_{\mathrm{snk}}^{(x,\mathbf{p})}\left(u\right) \gamma_5 \tag{1.145}$$

$$\Gamma \gamma_5 S_{\mathrm{snk}}^{(x,\mathbf{0})^*}\left(r\right) D_{\ell'}^{-1}\left(r, w\right) S_{\mathrm{src}}^{(y,\mathbf{0})}\left(w\right) \Big)^* \gamma_5 \tag{1.146}$$

$$\gamma^\mu\ \mathrm{e}^{-\,\mathrm{i}\,\mathbf{z}\cdot(\mathbf{p}'-\mathbf{p})} D_h^{-1}\left(z, v\right) S_{\mathrm{src}}^{(y,\mathbf{p}')}\left(v\right) \Bigg] , \tag{1.147}$$

which in terms of propagator vectors G is

$$C^{\mu} = \sum_{ru} \mathrm{Tr}\left[\Gamma'^{\dagger}\gamma_5 \left(D_{\ell}^{-1}(z,u)\, S_{\mathrm{snk}}^{(x,\mathbf{p})}(u)\,\gamma_5\right.\right. \tag{1.148}$$

$$\left.\Gamma\,\gamma_5\, S_{\mathrm{snk}}^{(x,\mathbf{0})^*}(r)\, G_{\ell',\mathrm{src}}^{(y,\mathbf{0})}(r)\right)^*\gamma_5 \tag{1.149}$$

$$\left.\gamma^{\mu}\ \mathrm{e}^{-\,\mathrm{i}\,\mathbf{z}\cdot(\mathbf{p}'-\mathbf{p})}\, G_{h,\mathrm{src}}^{(y,\mathbf{p}')}(z)\right]. \tag{1.150}$$

The bracketed term in (1.148) is a sequential propagator, defined in § 1.3.10 [70].

Once the sequential propagator is constructed, the 3-point correlator (1.140) is evaluated using the point-sink 2-point correlation function (1.123), setting $\Gamma_{\mathrm{snk}} = \gamma_{\mu}$ and the sink momentum to $\mathbf{p}' - \mathbf{p}$.

1.3.10 Sequential source method

The bracketed term in (1.148) is a sequential propagator. Two variants are used:

1. **point sink** – the sequential source described in the literature [70]; and
2. **wall sink** – the smeared sequential source defined below.

'True' point sink = sequential source

When the smearing at the sink is a 'true' point, (1.148) becomes

$$C^{\mu} = \mathrm{Tr}\left[\Gamma'^{\dagger}\gamma_5 \left(D_{\ell}^{-1}(z,x)\,\mathrm{e}^{\mathrm{i}\,\mathbf{p}\cdot\mathbf{x}}\,\gamma_5\,\Gamma\,\gamma_5\, G_{\ell',\mathrm{src}}^{(y,\mathbf{0})}(x)\right)^*\gamma_5\right. \tag{1.151}$$

$$\left.\gamma^{\mu}\ \mathrm{e}^{-\,\mathrm{i}\,\mathbf{z}\cdot(\mathbf{p}'-\mathbf{p})}\, G_{h,\mathrm{src}}^{(y,\mathbf{p}')}(z)\right]. \tag{1.152}$$

and the bracketed term is computed using the sequential source method [70]. This is straightforward. A sequential source vector S_{seq} (which is a spin-colour vector at each lattice site) is defined as

$$S_{\mathrm{seq},\,q',\mathrm{src}}^{(\mathbf{p},\Gamma,y,\mathbf{p}')}(x) = \mathrm{e}^{\mathrm{i}\,\mathbf{p}\cdot\mathbf{x}}\,\Gamma\, G_{q',\mathrm{src}}^{(y,\mathbf{p}')}(x)\ , \tag{1.153}$$

and a sequential propagator is defined as a solve to the sequential source

$$G^{(\mathbf{p},\Gamma,y,\mathbf{p}')}_{q,\,\mathrm{seq},\,q',\,\mathrm{src}}\left(x\right) = \sum_{y} D_q^{-1}\left(x,y\right)\; S^{(\mathbf{p},\Gamma,y,\mathbf{p}')}_{\mathrm{seq},\,q',\,\mathrm{src}}\left(y\right)\;. \tag{1.154}$$

For clarity, this requires the Dirac matrix to be inverted 12 times for each combination of Γ and momentum on the sequential timeslice and for each source smearing.

The point-sink 3-point correlator becomes

$$C^{(3)\mu}_{iP}\left(t;\mathbf{p},\mathbf{p}'\right) = \sum_{\mathbf{z}} \mathrm{Tr}\left[\Gamma'^{\dagger}\gamma_5\,\left[G^{(\mathbf{p},\gamma_5\Gamma\gamma_5,y,\mathbf{0})}_{\ell,\,\mathrm{seq},\,\ell',\,\mathrm{src}}\left(z\right)\right]^{*}\gamma_5 \right. \tag{1.155}$$

$$\left. \gamma_\mu\;\mathrm{e}^{-\,\mathrm{i}\,\mathbf{z}\cdot(\mathbf{p}'-\mathbf{p})}\,G^{(y,\mathbf{p}')}_{h,\mathrm{src}}\left(z\right)\right]\,, \tag{1.156}$$

which is computed using the point-sink 2-point correlation function (1.123), setting $\Gamma_{\mathrm{snk}} = \gamma_\mu$ and the sink momentum to $\mathbf{p}' - \mathbf{p}$.

The (abridged) `SeqGamma.hpp` code in Hadrons used to create the source matches (1.153)

```
auto  &ph  = envGet(LatticeComplex, momphName_);
envGetTmp(PropagatorField, wallTmp);
SlicedPropagator qSliced;
sliceSum(q, qSliced, Tp);
src = Zero();
for(unsigned int loop_t = par().tA; loop_t <= par().tB; ++loop_t)
{
    wallTmp = g * qSliced[loop_t];
    src = src + where((t == loop_t), ph*wallTmp, 0.*wallTmp);
}
```

Wall-smeared sequential source

When the sink smearing is a wall, (1.148) becomes

$$C^{\mu} = \sum_{u} \mathrm{Tr}\left[\Gamma'^{\dagger}\gamma_5 \left(D_{\ell}^{-1}(z,u)\, \mathrm{e}^{\mathrm{i}\,\mathbf{p}\cdot\mathbf{x}}\, \delta_{u_4,x_4}\gamma_5\,\Gamma\,\gamma_5\, G_{W,\ell',\mathrm{src}}^{(\mathbf{0},y,\mathbf{0})}(x_4)\right)^{*}\gamma_5 \right. \tag{1.157}$$

$$\left. \gamma^{\mu}\ \mathrm{e}^{-\mathrm{i}\,\mathbf{z}\cdot(\mathbf{p}'-\mathbf{p})}\, G_{h,\mathrm{src}}^{(y,\mathbf{p}')}(z)\right]. \tag{1.158}$$

Again, this is straightforward. A wall-smeared sequential source vector $S_{W,\mathrm{seq}}$ (which is a spin-colour vector at each lattice site) is defined as

$$S_{W\mathrm{seq},\,q',\mathrm{src}}^{(\mathbf{p},\Gamma,y,\mathbf{p}')}(x) = \mathrm{e}^{\mathrm{i}\,\mathbf{p}\cdot\mathbf{x}}\, \delta_{u_4,x_4}\Gamma\, G_{W,q',\mathrm{src}}^{(\mathbf{0},y,\mathbf{0})}(x_4)\ , \tag{1.159}$$

then a smeared sequential propagator as a solve to the smeared sequential source is defined as

$$G_{q,\,W\mathrm{seq},\,q',\,\mathrm{src}}^{(\mathbf{p},\Gamma,y,\mathbf{p}')}(x) = \sum_{y} D_q^{-1}(x,y)\ S_{W\mathrm{seq},\,q',\,\mathrm{src}}^{(\mathbf{p},\Gamma,y,\mathbf{p}')}(y)\ . \tag{1.160}$$

The wall-sink 3-point correlation function becomes

$$C_{iW}^{(3)}(t;\mathbf{p},\mathbf{p}') = \sum_{\mathbf{z}} \mathrm{Tr}\left[\Gamma'^{\dagger}\gamma_5 \left[G_{\ell,\,W\mathrm{seq},\,\ell',\,\mathrm{src}}^{(\mathbf{p},\gamma_5\Gamma\gamma_5,y,\mathbf{0})}(z)\right]^{*}\gamma_5 \right. \tag{1.161}$$

$$\left. \gamma_{\mu}\ \mathrm{e}^{-\mathrm{i}\,\mathbf{z}\cdot(\mathbf{p}'-\mathbf{p})}\, G_{h,\mathrm{src}}^{(y,\mathbf{p}')}(z)\right]. \tag{1.162}$$

which is again computed using the point sink 2-point correlation function (1.123), setting $\Gamma_{\mathrm{snk}} = \gamma_{\mu}$ and the sink momentum to $\mathbf{p}' - \mathbf{p}$.

Hadrons code for the wall-smeared sequential source, `SeqGammaWall.hpp`, was created by the author and added to Hadrons for this thesis. This matches (1.159) by inspection

```
auto  &ph  = envGet(LatticeComplex, momphName_);
envGetTmp(PropagatorField, wallTmp);
SlicedPropagator qSliced;
sliceSum(q, qSliced, Tp);
src = Zero();
for(unsigned int loop_t = par().tA; loop_t <= par().tB; ++loop_t)
{
```

```
    wallTmp = g * qSliced[loop_t];
    src = src + where((t == loop_t), ph*wallTmp, 0.*wallTmp);
}
```

1.3.11 Gauge-fixing

Wall-sources are the extreme of a noncovariant spatial distribution, hence the gauge must be fixed before measuring observables using wall-sources. For point sources, this is not required; however, for data production in this thesis we choose to use the same gauge-fixed configurations for point- and wall-sources.

We fix to Coulomb gauge which is defined by the condition

$$\Delta_i A_i = 0\,, \tag{1.163}$$

where Δ_i is a spatial lattice derivative, and we do not write its form because these are normally specified by the gauge fixing procedure being used. Here we use the gauge fixing procedure outlined in [71]. This gauge-fixing algorithm is iterative, making small local gauge rotations (controlled by a step-size $\alpha \in \mathbb{R}$) towards a field configuration obeying the gauge fixing condition. In practical terms, larger step sizes α lead to faster convergence on a solution. However, the algorithm fails to converge for large step sizes. For this thesis, small pilot runs were performed to tune the parameter α for the ensembles of interest.

1.3.12 Inverting the Dirac Matrix – solvers

Computer code to numerically determine solutions G to equation (1.116) is normally separated into two separate code implementations:

1. Linear operator(s) for the quark action(s) of interest, capable of performing the matrix multiply DG (see S 1.2.4); and
2. Linear solver algorithms capable of solving for G in $DG = S$.

Solvers start from an initial guess for G, then work iteratively to refine G by minimising the solver residual $|r|^2$ where

$$r = DG - S\,. \tag{1.164}$$

The basis for the methods used in this thesis is the conjugate gradient (CG) algorithm [72]. This is an iterative method where at each step i, a search direction vector $\mathbf{p}^{(i)}$ is chosen, orthogonal to all previous search directions. Then a scalar α is found that minimises the residual (1.164) for the i-th guess $G^{(i)} = G^{(i-1)} + \alpha\mathbf{p}^{(i)}$. The set of orthogonal vectors $\mathbf{p}^{(i)}$ form a Kryolov space $\mathcal{K}$.

If the low-lying eigenvectors and eigenvalues $Dv^{(i)} = \lambda^{(i)} v^{(i)}$ are known, then deflation is used [73], whereby the Kryolov space is initialised with the known low-lying eigenvectors which dominate the solution, and the guess is initialised

$$G^{(i)} = \sum_{j=1}^{N_{\text{low}}} \frac{1}{\lambda^{(j)}} v^{(j)} v^{(j)\dagger} , \tag{1.165}$$

where N_{low} is the number of known lowest modes.

Various forms of preconditioning are used to speed up solutions based on the properties of the matrix being inverted. Data production for this thesis used the inexact preconditioned conjugate gradient method with inner-outer iteration [74, 75].

1.4 Lattice QCD for heavy-light semileptonic decays

This section explains further lattice techniques that might not be employed in all lattice projects, but were required for this thesis. Further background on quark flavour physics is provided in [76].

1.4.1 Stout smearing

Peardon [5] noted that interpolating operators constructed from gauge link smeared operators had better overlap with low-lying states because they decouple from the high frequency modes of the theory. He proposed an iterative method ("stout" smearing) which is analytical everywhere in the complex plane, respects hypercubic lattice symmetry (if the parameters do), does not require nondifferentiable projection back to $SU(3)$ and is numerically stable and fast.

Here, we choose a 4-dimensional, isotropic setup (one of two Peardon recommended)

$$\rho_{\mu\nu} = \rho. \tag{1.166}$$

The method works by defining at each lattice site x the weighted sum, $C_\mu(x)$, of all staples starting at x and terminating at $x + \hat{\mu}$

$$C_\mu(x) = \sum_{\mu\neq\nu} \rho_{\mu\nu} \Big[U_\nu(x)\, U_\mu(x+\hat{\nu})\, U_\nu^\dagger(x+\hat{\mu}) \tag{1.167}$$

$$U_\nu^\dagger(x-\hat{\nu})\, U_\mu(x-\hat{\nu})\, U_\nu(x-\hat{\nu}+\hat{\mu}) \Big]. \tag{1.168}$$

The matrix $\Omega_\mu(x)$ is defined at each site in each direction (no sum over μ)

$$\Omega_\mu(x) = C_\mu(x)\, U_\mu^\dagger(x), \tag{1.169}$$

which is combined into the Hermitian, traceless matrix $Q_\mu(x)$ (by subtracting the trace divided by the dimensionality)

$$Q_\mu(x) = \frac{\mathrm{i}}{2}\left(\Omega_\mu^\dagger(x) - \Omega_\mu(x)\right) - \frac{\mathrm{i}}{2N}\,\mathrm{Tr}\left(\Omega_\mu^\dagger(x) - \Omega_\mu(x)\right). \tag{1.170}$$

Being Hermitian and traceless, exponentiating $Q_\mu(x)$ returns an element in $SU(3)$.

We then smear iteratively for n steps, with the smeared gauge fields for the next step, $U_\mu^{(n+1)}$, resulting from the product of this smearing operator to the current gauge fields, $U_\mu^{(n)}$

$$U_\mu^{(n+1)} = \exp\left(\mathrm{i}\, Q_\mu(x)\right) U_\mu^{(n)}. \tag{1.171}$$

As the product of two members of $SU(3)$, the smeared fields are also members of $SU(3)$.

1.4.2 Renormalisation

Single action

Though interested in the renormalised matrix element of semileptonic pseudoscalar meson decay $P_i \to P_f$ via the vector current $\mathcal{V}_\mu$, we must compute this on the lattice using the local vector current $V_\mu = \bar{q}'\gamma_\mu q$, which is renormalised multiplicatively with Z_V

$$\langle P_f(\mathbf{p}_f)|\mathcal{V}_\mu\left(\mathbf{q}^2\right)|P_i(\mathbf{p}_i)\rangle = Z_V \langle P_f(\mathbf{p}_f)|V_\mu\left(\mathbf{q}^2\right)|P_i(\mathbf{p}_i)\rangle\ . \tag{1.172}$$

This can be parameterised by two form factors, f_+ multiplying the sum and f_- multiplying the difference of the quark field 4-momenta respectively

$$Z_V \langle P_f(\mathbf{p}_f)|V_\mu\left(\mathbf{q}^2\right)|P_i(\mathbf{p}_i)\rangle = f_+^{P_iP_f}\left(q^2\right)(p_i + p_f)_\mu + f_-^{P_iP_f}\left(q^2\right)(p_i - p_f)_\mu\ . \tag{1.173}$$

For $P_i = P_f$ at zero momentum transfer and considering the rest frame, where $p_i = p_f \implies p_i + p_f = (2E_i, \mathbf{0})$ and $p_i - p_f = 0$, charge conservation tells us to normalise $f_+^{P_iP_i} = 1$ giving

$$Z_V = \frac{2E_i}{\langle P_i(\mathbf{0})|V_0(\mathbf{0})|P_i(\mathbf{0})\rangle}\,. \tag{1.174}$$

Noting the form of (1.87), the backward propagating wave can either be subtracted using overlap coefficients extracted from a fit, or half the midpoint can be used to construct the forward propagating 2-point function $\tilde{C}_i(t, \mathbf{p})$

$$\tilde{C}_i(t, \mathbf{p}) \equiv C_i(t, \mathbf{p}_i) - \frac{1}{2} C_i\left(\frac{T}{2}, \mathbf{p}\right) \mathrm{e}^{-E_i(T/2-t)}, \tag{1.175}$$

which is then used to extract Z_V by taking a ratio of (1.175) over (1.140)

$$\frac{\tilde{C}_{P_i}(t_f - t_i, \mathbf{0})}{C^{(0)}_{P_i P_i \text{bare}}(t_i, t, t_f, \mathbf{0}, \mathbf{0})} \approx \frac{\frac{|Z_i|^2}{2E_i} \mathrm{e}^{-E_i(t_f - t_i)}}{\frac{|Z_i|^2}{4E_i^2} \langle P_i(\mathbf{0}) | V_0(\mathbf{0}) | P_i(\mathbf{0}) \rangle \mathrm{e}^{-E_i(t - t_i + t_f - t)}} \tag{1.176}$$

$$= \frac{2E_i}{\langle P_i(\mathbf{0}) | V_0(\mathbf{0}) | P_i(\mathbf{0}) \rangle}. \tag{1.177}$$

This ratio is used to extract Z_V for the heavy and light actions ($Z_{V,\mathrm{h}}$ and $Z_{V,\ell}$) directly from the data. The mixed action $Z_{V,\mathrm{m}}$ cannot be extracted in this way because the condition $P_i = P_f$ demands the same action, because here the charm action is stout smeared (§ 1.4.1), while the light and strange action is not.

Introducing Z_q as multiplicative quark field renormalisation factors, once the following ratios are determined fully nonperturbatively (see next section)

$$R_m = \frac{Z_{V,\mathrm{m}}}{\sqrt{Z_{q,\mathrm{h}} Z_{q,\ell}}} \tag{1.178}$$

$$R_h = \frac{Z_{V,\mathrm{h}}}{Z_{q,\mathrm{h}}} \tag{1.179}$$

$$R_\ell = \frac{Z_{V,\ell}}{Z_{q,\ell}}, \tag{1.180}$$

they may be combined into the ratio

$$\rho = R_m \Big/ \sqrt{R_h R_\ell} \tag{1.181}$$

allowing the mixed action $Z_{V,\mathrm{mixed}}$ to be determined

$$Z_{V,\mathrm{mixed}} = \rho \sqrt{Z_{V,\mathrm{h}} Z_{V,\ell}}. \tag{1.182}$$

The ratio ρ is close to 1, and the practice of setting $\rho = 1$ is termed mostly nonperturbative renormalisation. For this thesis, mostly nonperturbative renormalisation was used until the final stages (i.e. the chiral continuum fit in chapter 4), when the ρ factors became available.

The Rome-Southampton method

In order to make contact with physical results, lattice operators must be matched to perturbative renormalisation schemes in the continuum such as $\overline{\text{MS}}$. [77] This can be done fully nonperturbatively on the lattice using a number of regularisation invariant (RI), intermediate momentum subtraction schemes such as the Rome-Southampton method, RI-MOM. [78]

RI schemes all follow the same general method. In each scheme we impose the condition that the renormalised projected, amputated vertex function matches the tree-level value at a specific kinematic point. By doing so, we make no reference to the regulator used in any given scheme. Instead, all that is needed is a self-consistent calculation of the scattering amplitude for each scheme. Thus, RI serves as a convenient interchange scheme between the different regularisations.

The renormalisation scale is imposed through the momenta of the quark fields entering in the operators. Each scheme has differing kinematic requirements imposed, leading to small variations across schemes.

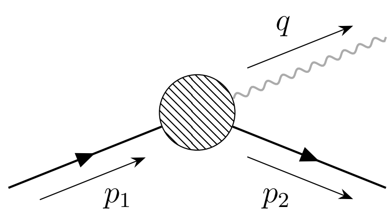

Figure 1.7 *Momentum diagram for renormalisation of a quark bilinear operator $O_\Gamma = \overline{\psi}'\,\Gamma\,\psi$. The departing momentum carried by the current (in this thesis $\Gamma = \gamma_\mu$) is $q = p_1 - p_2$.*

RI-MOM required asymmetric (exceptional) momentum configurations (fig 1.7)

$$p_1^2 = p_2^2 = -\mu^2, \qquad \mu > 0 \tag{1.183}$$

$$p_1 = p_2, \qquad q = 0\,, \tag{1.184}$$

but this was associated with "chiral symmetry breaking and other unwanted infrared effects" [79]. RI-SMOM schemes such as RI-SMOM$^{\gamma_\mu}$ [79], RI/mS-MOM [80] or RI-SMOM$^{\not q}$ [81] suppress these effects by requiring symmetric (nonexceptional) momentum configurations

$$p_1^2 = p_2^2 = q^2 = -\mu^2, \qquad \mu > 0\,, \tag{1.185}$$

$$p_1 \neq p_2, \qquad q \neq 0\,. \tag{1.186}$$

Regardless of scheme, one proceeds as follows[4].

In a fixed gauge (Landau gauge is used here – Coulomb gauge cannot be used as it has a remaining degree of freedom), the momentum space vertex (Green's) function V_Γ for quark bilinear $O_\Gamma = \bar{q}\,'\,\Gamma_\mu q$ is computed

$$V_\Gamma\left(p_1, p_2\right) = \sum_{xyz} \mathrm{e}^{-\,\mathrm{i}\,p_1\cdot(x-z)}\,\mathrm{e}^{-\,\mathrm{i}\,p_2\cdot(z-y)}\,\langle q'\left(x\right)\,O_\Gamma\left(z\right)\,\bar{q}\left(y\right)\rangle\ . \tag{1.187}$$

Using the methods described above, this becomes

$$V_\Gamma\left(p_1, p_2\right) = \sum_{z} \gamma_5\, G^{(p_1)}_{q\,',\mathrm{vol}}\left(z\right)^\dagger\,\gamma_5\,\Gamma\, G^{(p_2)}_{q,\mathrm{vol}}\left(z\right)\ , \tag{1.188}$$

which is a single spin-colour matrix. The propagator from a volume source G_{vol} is obtained from a solve to a volume source S_{vol} (first used by QCDSF [82]) in order to extract the most information from each gauge configuration

$$S^{(\alpha,a,p)}_{\mathrm{vol}}\left(x\right)_{\substack{\beta\\ b}} = \delta_{ab}\delta_{\alpha\beta}\,\mathrm{e}^{\mathrm{i}\,p\cdot x}\ . \tag{1.189}$$

The amputated vertex function is then obtained as the individually gauge-averaged product of the momentum-space inverse quark propagators with the vertex function

$$\Lambda_\Gamma\left(p_1, p_2\right) = \left\langle \left[G^{(p_1)}_{q\,',\mathrm{vol}}\left(p_1\right)\right]^{-1}\right\rangle \left\langle V_\Gamma\left(p_1, p_2\right)\right\rangle \left\langle \left[G^{(p_2)}_{q,\mathrm{vol}}\left(p_2\right)\right]^{-1}\right\rangle\ , \tag{1.190}$$

where G is the spin-colour matrix

$$G^{(p_2)}_{q,\mathrm{vol}}\left(p\right) = \sum_{x} \mathrm{e}^{-\,\mathrm{i}\,p\cdot x}\, G^{(p)}_{q,\mathrm{vol}}\left(x\right)\ . \tag{1.191}$$

[4]The fully nonperturbative RI/SMOM determination of the ratios (1.178)–(1.180) outlined in the remainder of this section was not performed by the author.

The vertex Λ_Γ is bare, so the renormalisation condition appropriate for the scheme is imposed to obtain $Z_V / \sqrt{Z_q Z_{q'}}$. For this study, RI-SMOM$^{\gamma_\mu}$ is used

$$\frac{Z_V}{\sqrt{Z_q Z_{q'}}} = \left(\frac{1}{48} \mathrm{Tr} \left[\gamma_\nu V_\Gamma^\nu (\mu, \mu)_{\mathrm{sym}} \right] \right)^{-1} , \tag{1.192}$$

where $V_\Gamma^\nu (\mu, \mu)_{\mathrm{sym}}$ is the vector vertex renormalised at the scale μ. The subscript 'sym' indicates that there is a prescription for symmetric momentum required by RI-SMOM$^{\gamma_\mu}$.

1.4.3 Form factor parameterisations

This section is in the continuum, with a mostly '−' (West Coast) metric

$$g_{\mu\nu} = g^{\mu\nu} = \begin{pmatrix} 1 & 0 & 0 & 0 \\ 0 & -1 & 0 & 0 \\ 0 & 0 & -1 & 0 \\ 0 & 0 & 0 & -1 \end{pmatrix} . \tag{1.193}$$

As set out in § 1.1.5 the transition matrix element $\mathrm{i}\,\mathcal{M}$ for a semileptonic decay of pseudoscalar D or D_s mesons (for clarity we write D) to light pseudoscalar mesons P (pion or kaon), involving the decay from charm c to light quark q, is written in terms of the product of the Fermi constant G_F, CKM matrix element V_{cq}, a leptonic current L_μ and a Hadronic current H^μ

$$\mathrm{i}\,\mathcal{M} = -\,\mathrm{i}\,\frac{G_F}{\sqrt{2}} V_{cq} L_\mu H^\mu . \tag{1.194}$$

The hadronic current H^μ, i.e. the matrix element of the renormalised vector current $\mathcal{V}^\mu \equiv Z_V i\bar{q}\gamma^\mu c$, is parameterised by form factors

$$H^\mu \equiv \langle P(p) | \mathcal{V}^\mu | D(p') \rangle \tag{1.195}$$

$$= f_+ \left(q^2\right) \left[(p' + p)^\mu - \left(\frac{m_D^2 - m_P^2}{q^2} \right) q^\mu \right] + f_0 \left(q^2\right) \left(\frac{m_D^2 - m_P^2}{q^2} \right) q^\mu , \tag{1.196}$$

where

$$p' = (E_D, \mathbf{p}_D) \equiv \text{4-momentum of the initial } D \text{ (or } D_s) \text{ meson} \tag{1.197}$$
$$p = (E_P, \mathbf{p}_P) \equiv \text{4-momentum of the final pseudoscalar meson } P\,. \tag{1.198}$$

As noted in § 1.1.5, only the vector current is used because the axial current does not contribute [38, 83].

Conservation of 4-momentum gives

$$q^\mu = p'^\mu - p^\mu = (E_D - E_P, \mathbf{p}_D - \mathbf{p}_P)\ . \tag{1.199}$$

Here, we hold the initial D at rest (i.e. $\mathbf{p}_D = 0$) such that

$$p' \to (m_D, \mathbf{0}) \tag{1.200}$$
$$p \to (E_P, \mathbf{p}) \tag{1.201}$$
$$q^\mu = (m_D - E_P, -\mathbf{p}) = \left(m_D - \sqrt{m_P^2 + \mathbf{p}^2}, -\mathbf{p}\right)\ . \tag{1.202}$$

The square of the momentum q^2 transferred from the D to the lepton pair is

$$q^2 = m_D^2 + m_P^2 - 2m_D E_P\,. \tag{1.203}$$

There are two kinematic points of interest. Firstly, $q_0 \equiv q^2 = 0$, where there is maximum recoil of the final-state meson

$$E_{P,\max} \equiv E_P\Big|_{q_0} = \frac{m_D^2 + m_P^2}{2m_D}\,. \tag{1.204}$$

Secondly, the maximum 4-momentum transferred to the current $q^2_{\max}$ occurs when the final-state meson remains at rest

$$q^2_{\max} = (m_D - m_P)^2\ . \tag{1.205}$$

The temporal component of (1.196) with our kinematics is

$$
\begin{aligned}
H^0 &= \langle P(\mathbf{p})|\mathcal{V}^0|D\left(\mathbf{0}\right)\rangle && (1.206)\\
&= f_+\left(q^2\right)\left[\left(m_D+E_P\right)-\left(\frac{m_D^2-m_P^2}{q^2}\right)\left(m_D-E_P\right)\right] && (1.207)\\
&\qquad + f_0\left(q^2\right)\left(\frac{m_D^2-m_P^2}{q^2}\right)\left(m_D-E_P\right) && (1.208)\\
&= \frac{1}{q^2}\Bigg[f_+\left(q^2\right)\Big[\left(m_D+E_P\right)\left(m_D^2+m_P^2-2m_DE_P\right) && (1.209)\\
&\qquad\qquad -\left(m_D^3-m_D^2E_P-m_P^2m_D+m_P^2E_P\right)\Big] && (1.210)\\
&\qquad + f_0\left(q^2\right)\left(m_D^2-m_P^2\right)\left(m_D-E_P\right)\Bigg] && (1.211)\\
&= \frac{1}{q^2}\Bigg[f_+\left(q^2\right)\Big[\Big(\cancel{m_D^3}+\cancel{m_D^2E_P}+m_Dm_P^2+\cancel{E_Pm_P^2}-\cancel{2m_D^2E_P} && (1.212)\\
&\qquad\qquad -2m_DE_P^2\Big)-\cancel{m_D^3}+\cancel{m_D^2E_P}+m_P^2m_D-\cancel{m_P^2E_P}\Big] && (1.213)\\
&\qquad + f_0\left(q^2\right)\left(m_D^2-m_P^2\right)\left(m_D-E_P\right)\Bigg] && (1.214)\\
&= \frac{1}{q^2}\left[-2m_D\left(E_P^2-m_P^2\right)f_+\left(q^2\right)+\left(m_D^2-m_P^2\right)\left(m_D-E_P\right)f_0\left(q^2\right)\right]\,. && (1.215)
\end{aligned}
$$

The spatial component of (1.196) with our kinematics is

$$
\begin{aligned}
H^i &= \langle P(\mathbf{p})|\mathcal{V}^i|D\left(\mathbf{0}\right)\rangle && (1.216)\\
&= \frac{p^i}{q^2}\Bigg[f_+\left(q^2\right)\Big[\left(m_D^2+m_P^2-2m_DE_P\right)+\left(m_D^2-m_P^2\right)\Big] && (1.217)\\
&\qquad - f_0\left(q^2\right)\left(m_D^2-m_P^2\right)\Bigg] && (1.218)\\
&= \frac{p^i}{q^2}\Big[2m_D\left(m_D-E_P\right)f_+\left(q^2\right)-\left(m_D^2-m_P^2\right)f_0\left(q^2\right)\Big]\,. && (1.219)
\end{aligned}
$$

Parallel and perpendicular form factors are defined in terms of the matrix elements computed on the lattice

$$f_{\parallel}\left(E_P\right) = \frac{\langle P(\mathbf{p})|\mathcal{V}^0|D\left(\mathbf{0}\right)\rangle}{\sqrt{2m_D}} \qquad \text{and} \tag{1.220}$$

$$f_{\perp}\left(E_P\right) = \frac{\langle P(\mathbf{p})|\mathcal{V}^i|D\left(\mathbf{0}\right)\rangle}{p^i\sqrt{2m_D}} \ . \tag{1.221}$$

We do not have access to $\langle P(\mathbf{p})|\mathcal{V}^i|D\left(\mathbf{0}\right)\rangle$ at zero spatial momentum, so $f_{\perp}\left(m_P\right)$ remains unknown. Thus, we need not define how to take the limit as $p^i \to 0$.

The dimensionless quantities f_+ and f_0 can be written

$$f_+\left(q^2\right) = \frac{1}{\sqrt{2m_D}}\left(f_{\parallel}\left(E_P\right) + \left(m_D - E_P\right) f_{\perp}\left(E_P\right)\right) \tag{1.222}$$

$$f_0\left(q^2\right) = \frac{\sqrt{2m_D}}{m_D^2 - m_P^2}\left(\left(m_D - E_P\right) f_{\parallel}\left(E_P\right) + \left(E_P^2 - m_P^2\right) f_{\perp}\left(E_P\right)\right) \ . \tag{1.223}$$

Lack of knowledge of $f_{\perp}\left(m_P\right)$ prevents $f_+\left(q^2_{\text{max}}\right)$ from being constructed. However, at q^2_{max}, $E_P^2 - m_P^2 = 0$; thus $f_0\left(q^2_{\text{max}}\right)$ can be constructed.

Validating (1.222) by inserting (1.215) into the right hand side (RHS) of (1.222)

$$\text{RHS} = \frac{1}{2q^2 m_D}\Bigg[- 2m_D\left(E_P^2 - m_P^2\right) f_+\left(q^2\right) + \left(m_D^2 - m_P^2\right)\left(m_D - E_P\right) f_0\left(q^2\right) \tag{1.224}$$

$$+ \left(m_D - E_P\right)\left[2m_D\left(m_D - E_P\right) f_+\left(q^2\right) - \left(m_D^2 - m_P^2\right) f_0\left(q^2\right)\right]\Bigg] \tag{1.225}$$

$$= \frac{f_+\left(q^2\right)}{q^2}\left[- E_P^2 + m_P^2 + m_D^2 - 2m_D E_P + E_P^2\right] \tag{1.226}$$

$$= f_+\left(q^2\right) \ . \tag{1.227}$$

Similarly, we validate (1.223) by inserting (1.219) into RHS (1.223)

$$\text{RHS} = \frac{1}{q^2\left(m_D^2 - m_P^2\right)}\Bigg((m_D - E_P)\Big[-2m_D\left(E_P^2 - m_P^2\right) f_+\left(q^2\right) \tag{1.228}$$

$$+ \left(m_D^2 - m_P^2\right)(m_D - E_P) f_0\left(q^2\right)\Big] + \left(E_P^2 - m_P^2\right) \tag{1.229}$$

$$\Big[2m_D(m_D - E_P) f_+\left(q^2\right) - \left(m_D^2 - m_P^2\right) f_0\left(q^2\right)\Big]\Bigg) \tag{1.230}$$

$$= \frac{f_0\left(q^2\right)}{q^2\left(m_D^2 - m_P^2\right)}\Bigg((m_D - E_P)\left(m_D^2 - m_P^2\right)(m_D - E_P) \tag{1.231}$$

$$- \left(E_P^2 - m_P^2\right)\left(m_D^2 - m_P^2\right)\Bigg) \tag{1.232}$$

$$= \frac{f_0\left(q^2\right)}{q^2}\left(m_D^2 + E_P^2 - 2m_D E_P - E_P^2 + m_P^2 \right) \tag{1.233}$$

$$= f_0\left(q^2\right) . \tag{1.234}$$

Defining $\mathbf{p}_{\text{max}} \equiv \mathbf{p}\big|_{q_0}$, we evaluate $f_0(0)$ (1.223) substituting (1.204)

$$f_0(0) = \frac{\sqrt{2m_D}}{m_D^2 - m_P^2}\Bigg[\left(m_D - \left(\frac{m_D^2 + m_P^2}{2m_D}\right)\right) \frac{\langle P(\mathbf{p}_{\text{max}})|\mathcal{V}^0|D(\mathbf{0})\rangle}{\sqrt{2m_D}} \tag{1.235}$$

$$+ \left(\left(\frac{m_D^2 + m_P^2}{2m_D}\right)^2 - m_P^2 \right) \frac{\langle P(\mathbf{p}_{\text{max}})|\mathcal{V}^i|D(\mathbf{0})\rangle}{\mathbf{p}^i_{\text{max}}\sqrt{2m_D}} \Bigg] \tag{1.236}$$

$$= \frac{1}{4m_D^2\left(m_D^2 - m_P^2\right)}\Bigg[2m_D\left(m_D^2 - m_P^2\right) \langle P(\mathbf{p}_{\text{max}})|\mathcal{V}^0|D(\mathbf{0})\rangle \tag{1.237}$$

$$+ \left(m_D^2 - m_P^2\right)^2 \frac{\langle P(\mathbf{p}_{\text{max}})|\mathcal{V}^i|D(\mathbf{0})\rangle}{\mathbf{p}^i_{\text{max}}} \Bigg] \tag{1.238}$$

$$= \frac{1}{\sqrt{2m_D}}\Bigg[\frac{\langle P(\mathbf{p}_{\text{max}})|\mathcal{V}^0|D(\mathbf{0})\rangle}{\sqrt{2m_D}} \tag{1.239}$$

$$+ \left(\frac{m_D^2 - m_P^2}{2m_D}\right) \frac{\langle P(\mathbf{p}_{\text{max}})|\mathcal{V}^i|D(\mathbf{0})\rangle}{\mathbf{p}^i_{\text{max}}\sqrt{2m_D}} \Bigg] \tag{1.240}$$

$$= \frac{1}{\sqrt{2m_D}}\Big[f_\parallel\left(E_{P,\text{max}}\right) + \left(m_D - E_{P,\text{max}}\right) f_\perp\left(E_{P,\text{max}}\right) \Big] = f_+(0) . \tag{1.241}$$

That is this construction satisfies the constraint

$$f_0(0) = f_+(0) . \tag{1.242}$$

1.4.4 Chiral continuum fit form

For this thesis, it is possible to generate form factor data spanning the entire physically allowable kinematic range. Consequently, the data are fitted directly to a form factor ansatz, which is a function of the energy of the light product meson E_L, the simulated pion mass M_π^{s} and the lattice spacing a. The ansatz is derived from next-to-leading order (NLO) $SU(2)$ chiral perturbation theory for heavy-light mesons (HMχPT) in the hard-kaon limit [84–86]

$$f_X\left(E_L, M_\pi^{\mathrm{s}}, a^2\right) = f_X^{(\mathrm{cont})}\left(E_L\right) + f_X^{(\mathrm{lat})}\left(E_L, M_\pi^{\mathrm{s}}, a^2\right) . \tag{1.243}$$

$f_X^{(\mathrm{cont})}$ is a continuum prediction, which is an expansion of $n_{E,X}$ terms of E_L/Λ

$$f_X^{(\mathrm{cont})}\left(E_L\right) = \frac{\Lambda}{E_L + \Delta_{xy,X}}\left[c_{X,0} + \sum_{n=1}^{n_{E,X}} e_{X,n-1}\left(\frac{E_L}{\Lambda}\right)^n\right] . \tag{1.244}$$

$f_X^{(\mathrm{lat})}$ is a lattice correction containing the additional pion mass dependence M_π^{s} and discretisation effects (which is modelled as a function of a^2 because we use an all DWF action)

$$f_X^{(\mathrm{lat})}\left(E_L, M_\pi^{\mathrm{s}}, a^2\right) = \frac{\Lambda}{E_L + \Delta_{xy,X}}\left[c_{X,0}\left(\frac{\delta f\left(M_\pi^s\right) - \delta f\left(M_\pi^p\right)}{\left(4\pi f_\pi\right)^2}\right)\right. \tag{1.245}$$

$$\left. + c_{X,1}\frac{\Delta M_\pi^2}{\Lambda^2} + d_X\left(a\Lambda\right)^2\right] . \tag{1.246}$$

The parameters of the ansatz are

$$f_X \equiv \text{Form factor } X \in \{\,+,0\,\}\text{, i.e. vector and scalar} \tag{1.247}$$

$$\delta f \equiv \text{chiral log and finite volume corrections} \tag{1.248}$$

$$E_L \equiv \text{final-state hadron energy} \tag{1.249}$$

$$c_{X,n}, d_X, e_{X,n} \equiv \text{dimensionless fit constants for form factor X} \tag{1.250}$$

$$M_\pi^s \equiv \text{simulated pion mass (differs by ensemble)} \tag{1.251}$$

$$M_\pi^p \equiv \text{physical pion mass (isospin averaged)} \tag{1.252}$$

$$\Delta M_\pi^2 = \left(M_\pi^s\right)^2 - \left(M_\pi^p\right)^2 \tag{1.253}$$

$$f_\pi \equiv \text{pion decay constant}\,, \tag{1.254}$$

and $\Lambda = 1$ GeV is introduced as:

- a dimensionful scale to make the fit parameters dimensionless; and
- the renormalisation scale in the one loop chiral logs in δf.

In the chiral limit, simulated pions take their physical masses

$$M_\pi^s = M_\pi^p\,, \tag{1.255}$$

and in the continuum limit

$$a \to 0\,, \tag{1.256}$$

so that, in the chiral continuum limit, by design we have

$$f_X^{(\mathrm{lat})}\left(E_L, M_\pi^{\mathrm{s}}, a^2\right) = 0\,, \tag{1.257}$$

and hence

$$f_X\left(E_L, M_\pi^{\mathrm{p}}, 0\right) = f_X^{(\mathrm{cont})}\left(E_L\right)\,. \tag{1.258}$$

We use the same pole structure as [87] $\Delta_{xy,X}$

$$\Delta_{xy,X} = \frac{M^2_{D_x^*(J^P)} - M^2_{D_y} - M_L^2}{2M_{Dy}}\,, \tag{1.259}$$

with the squared masses in the numerator $M^2_{D_x^*(J^P)}$, $M^2_{D_y}$ and M_L^2 defined per the below and table 1.5

$$\begin{aligned}
x &\equiv \text{quark the charm decays to} && (1.260)\\
y &\equiv \text{spectator quark} \in \{\, s, \ell \,\} && (1.261)\\
D_x^*\left(J^P\right) &\equiv \text{excited } c\text{-}x \text{ meson the } w \text{ couples to in HM}\chi\text{PT} && (1.262)\\
J^P &\equiv \text{spin } J \text{ and parity } P \text{ quantum numbers} && (1.263)\\
&= 1^- \text{ for vector or } 0^+ \text{ for scalar form factors respectively} && (1.264)\\
M_L &\equiv \text{light hadron mass} && (1.265)\\
D_y &\equiv \text{initial heavy, pseudoscalar meson}\,. && (1.266)
\end{aligned}$$

J^P	$D_x^*\left(J^P\right)$	$\Delta_{xy,X}$	$\left(\Delta_{xy,X}\right)^{\text{PDG}}$
1^-	D^*	$\Delta_{ls,+/\perp}$	-22 MeV
0^+	$D_0^*\,(2300)$	$\Delta_{ls,0/\parallel}$	348 MeV

Table 1.5 *Parameters entering the chiral continuum fit for $D_s \to K$ decays. Columns describe: the spin J and parity P of the excited pole meson; the pole meson D_x^* (lightest meson) for each J^P (quantum numbers); the name of the pole term, and which form factors each applies to; and the value of the pole term* (1.259) *using PDG [25] values. Table adapted from [87].*

The hard $SU(2)$ χPT chiral log and finite volume corrections have this form

$$\delta f\,(M) = -\frac{3}{4}\Big[\delta f^{\log}\,(M) + \delta f^{\text{FV}}\,(M)\Big] \times \begin{cases} (1+3g^2) & D \to \pi \\ 3g^2 & D \to K \\ 1 & D_s \to K \end{cases}, \tag{1.267}$$

where g is the coupling and the chiral logs $\delta f^{\log}$ and finite volume corrections δf^{FV} are

$$\delta f^{\log}\,(M) = M^2 \ln\left(\frac{M^2}{\Lambda^2}\right) \tag{1.268}$$

$$\delta f^{\text{FV}}\,(M) = \frac{4M}{L}\sum_{|\mathbf{n}|\neq 0}\frac{K_1\left(|\mathbf{n}|ML\right)}{|\mathbf{n}|}\,. \tag{1.269}$$

The sum in δf^{FV} runs over all non-zero lattice vectors $\mathbf{n}$ (with integer components) in the finite volume of the spatial lattice and where K_1 is a modified Bessel function of the second kind.

Arfken, Weber and Harris [88] say of K_1 "The confusion of choice and notation for this solution is perhaps greater than anywhere else in this field." Rather than add to this confusion, the reader is referred to a mathematical textbook such as [88] or online reference such as [89] for the definition of K_1, and the interested programmer to the GNU Scientific Library [90] functions `gsl_sf_bessel_K1` and `gsl_sf_bessel_K1_e` (which were used for data production).

Chapter 2

Data generation

All of the data production and analysis for this project was performed using a C++ 14 code, Meson Lattice Utilities (MLU) [91], developed by the author for this thesis.

Data were produced on Science and Technology Facilities Council (STFC) supercomputers using the MLU module `xml3pt` using the Grid [67] library for QCD and the Hadrons [66] library for computation workflow management. Preliminary studies and data production for the first ensemble ($C1$) were performed on Tesseract (table 2.1), with all subsequent data production on Tursa (table 2.2). Data validation was performed on $C1$ during commissioning of Tursa to ensure continuity with data produced on Tesseract.

Data analysis was performed using MLU, which used the GNU Scientific Library (GSL) [90] for nonlinear least squares fitting on an Apple Mac Studio 2022 (Apple M1 Ultra, 20 CPU cores, 48 GPU cores, 64GB RAM).

2.1 Supercomputing resources

Supercomputing resources were generously provided through the DiRAC University Consortium [92] by the Science and Technology Facilities Council (STFC) [93] as part of the UK Research Initiative.

Tesseract is a Hewlett Packard Enterprise (HPE) SGI 8600 CPU based supercomputer as described in table 2.1.

Manufacturer	Hewlett Packard Enterprise (HPE)
Model	SGI 8600
Nodes	1468 CPU, 8 GPU
CPUs	2× Intel Xeon Skylake Silver 4116, 2.1 GHz, 12-core/node
Total CPU cores	35424
RAM	141 TB
Disk	3PB DDN Lustre
Network	Intel Omnipath 100Gbit/s, 16 nodes / leaf switch

Table 2.1 *Tesseract [94] hardware overview.*

Tursa (Scots Gaelic for "standing stone") is an Atos Sequana XH2000 GPU based supercomputer as described in table 2.2.

Manufacturer	Atos
Model	Sequana XH2000
Nodes	114 GPU, 6 CPU
CPU	GPU Nodes 2× AMD EPYC Rome 7272, 2.9GHz, 12-core/node CPU Nodes 2× AMD EPYC Rome 7H12, 2.66GHz, 64-core/node
Total CPU cores	3504
GPU	4× Nvidia RedStone A100-40 (640 Tensor/6,912 CUDA cores)/node
Total GPU cores	291,840 Tensor cores, 3,151,872 CUDA cores
RAM	1 TB/GPU node, 256 GB/CPU node, 117 TB total
Disk	4PB DDN Lustre
Network	Mellanox 200 Gbit/s HDR Infiniband Interconnect (fat tree topology)

Table 2.2 *Tursa [95] supercomputer hardware overview.*

2.2 Overall strategy of the calculation

On each of a number of different ensembles (with varying lattice spacings and simulated pion masses):

- Raw data are produced covering the physically allowed kinematic range (§ 2.3)

1. 3-point functions for the decays of interest
2. 2-point functions for mesons involved in the decays of interest.

- Per-ensemble data analysis is performed at each available momentum (§ 3.1)

1. 2-point functions are fitted
2. Determination of Z_V is made for a mostly nonperturbative renormalisation scheme
3. Ratios of the raw data are formed and renormalised using the mostly nonperturbative renormalisation scheme
4. Ratios are fitted to extract matrix elements
5. Matrix elements are adjusted to a fully nonperturbative renormalisation scheme
6. Form factors are constructed from the renormalised matrix elements.

The per-ensemble results are a collection of data points, f_0 and f_+, at each Fourier momentum, covering the physically allowed kinematic range. for each ensemble.

These are then combined into the chiral continuum analysis described in chapter 4.

2.3 Data production

2.3.1 Ensemble parameters

This isospin symmetric lattice QCD simulation is performed using RBC/UKQCD's 2 + 1 flavour Iwasaki gauge action [45] and DWF action [7, 10, 11] ensembles. There are three inverse lattice spacings, coarse (C) [96] $\sim$ 1.7848(50) GeV, medium (M) [97, 98] $\sim$ 2.3833(86) GeV and fine (F) [81] $\sim$ 2.708(10) GeV.

Heavier than physical pions are simulated on all ensembles, with multiple pion masses simulated on the coarse and medium ensembles in order to disentangle chiral and lattice spacing effects. The most recent determinations of parameters for these ensembles [4] are summarised in table 2.3.

Name	L/a	T/a	a^{-1} / GeV	m_π / MeV	$m_\pi L$
$C1$	24	64	1.7848(50)	339.76(1.22)	4.57
$C2$	24	64	1.7848(50)	430.63(1.38)	5.79
$M1$	32	64	2.3833(86)	303.56(1.38)	4.08
$M2$	32	64	2.3833(86)	360.71(1.58)	4.84
$M3$	32	64	2.3833(86)	410.76(1.74)	5.51
$F1M$	48	96	2.708(10)	232.01(1.01)	4.11

Table 2.3 *Ensembles used for data production. Ensemble names begin with (C)oarse, (M)edium or (F)ine indicating lattice spacing a. L/a and T/a are the spatial and temporal lattice extents in integer units. The last two columns show the pion mass m_π and product $m_\pi L$.*

Name	Start	Stop	Step	N_{conf}	N_{meas}
$C1$	3000	6180	20	160	1
$C2$	1540	4080	20	128	1
$M1$	880	3420	20	128	1
$M2$	820	2090	10	128	1
$M3$	580	2960	20	120	1
$F1M$	200	1620	20	72	2

Table 2.4 *Trajectories used on each ensemble. Start and Stop are the first and last trajectory numbers, while Step is the separation between trajectories. N_{conf} is the number of configurations and N_{meas} is the number of measurements (binned together) on each ensemble.*

To minimise autocorrelations, the configurations used on each ensemble are as widely separated as possible and begin once the trajectory is thermalised, as determined in prior studies (see table 2.4). [81, 96–98]

2.3.2 Quark field parameters – light and strange

All ensembles used have heavier than physical pions in the sea; thus, the light valence bare quark masses, am_ℓ, are all set to their unitary value, i.e. the same light bare sea-quark mass used in ensemble generation.

Bare strange quark masses are all set to the physical value determined in [81, 99] for the coarse and medium ensembles and [4] for F1M.

Name	DWF	b_5	c_5	M_5	L_s	$am_\ell^{\text{sea,val}}$	am_s^{sea}	$am_s^{\text{val, phys}}$
$C1$	S	1	0	1.8	16	0.005	0.04	0.03224(18)
$C2$	S	1	0	1.8	16	0.01	0.04	0.03224(18)
$M1$	S	1	0	1.8	16	0.004	0.03	0.02477(18)
$M2$	S	1	0	1.8	16	0.006	0.03	0.02477(18)
$M3$	S	1	0	1.8	16	0.008	0.03	0.02477(18)
$F1M$	M	1.5	0.5	1.0	12	0.002144	0.02144	0.02217(16)

Table 2.5 *Simulation parameters for light and strange quark fields. DWF indicates whether the DWF action is (S)hamir or (M)öbius and parameters b, c and M_5 (§ 1.2.8). Light and strange bare quark masses in lattice units am_ℓ and am_s are shown. The light action is unitary (i.e. light valence quarks are simulated at the same unphysical mass as sea quarks), whereas the strange action is partially quenched (i.e. strange valence quarks are simulated at physical masses with sea quarks slightly heavier).*

Strange and light quark fields were simulated using the same DWF action [7, 10, 11] as previous work [4], i.e. the Shamir SGN function approximation ($\text{SGN}^{\text{Shamir}}(x) \simeq |x|/x$) [8, 9] for all ensembles – except F1M which used the Möbius [6] SGN function approximation. Grid [67] uses the generalised Möbius DWF action described in equation (2.15) of [6], with parameters $b_5 = 1$ and $c_5 = 0$ for Shamir, whereas $b_5 = 1.5$ and $c_5 = 0.5$ recover Möbius (in both cases, we have $a_5 = b_5 - c_5$). In all cases, we set the Wilson mass term $M_5 = 1.8$ and $L_s = 16$ as determined by [46, 60], except on the fine ensemble, where we set $M_5 = 1.0$ and $L_s = 12$ [58, 59].

The eigenvectors of the two different approximations to the sign function used for these two actions have been found to be preserved, and hence "the Möbius rescaling can be understood as an improved algorithm for essentially the same lattice Dirac action" [6]. This is important as it allows us to include data from all 6 ensembles in the same continuum extrapolation.

Strange and light quark parameters are summarised in table 2.5.

2.3.3 Quark field parameters – charm

Our intention was to simulate the charm as close as possible to the physical point. No previous determination had been made of the bare charm quark mass needed to simulate the physical charm. For this setup there were data with a range of bare charm quark masses and the corresponding D_s and η_c pseudoscalar meson masses induced (am_h am_{hs} and am_{hh} respectively in table 6 from [4]) straddling the physical point.

Using these data, the lattice spacings and the physical D_s mass from the Particle Data Group (PDG) [25], multiple linear and quadratic fits to the data were performed, and then interpolated to the physical point using an average from those models. Bare quark masses were then checked against those obtained from similar fits using data for am_{hh} and the physical η_c from the PDG, which were in agreement.

The parameters for the charm are described in table 2.6, again with earlier studies [58, 59] determining that stout smearing [5] (see § 1.4.1) the gauge links before computing the propagators was necessary to bring residual mass effects, am_{res}, under control [58].

Name	DWF	b_5	c_5	M_5	L_s	am_h^{val}	ρ	N_{steps}
$C1, C2$	M	1.5	0.5	1.0	12	0.6413	0.1	3
$M1, M2, M3$	M	1.5	0.5	1.0	12	0.447	0.1	3
$F1M$	M	1.5	0.5	1.0	12	0.385	0.1	3

Table 2.6 *Simulation parameters for charm quark fields. The first six columns are as described in table 2.5. The charm action is quenched (no charm quarks in the sea), with bare charm valence quark masses indicated by* am_h^{val}*. The bare mass selected was an interpolation to the physical* D_s *based on data from prior studies [58, 59]. The interpolation was performed on ensembles* $C1$*,* $M1$ *and* $F1M$*, then used on all ensembles with the same lattice spacing. The Möbius DWF action (*$b_5 = 1.5, c_5 = 0.5$*) with* $M_5 = 1.0$ *amd* $L_s = 12$*) is used on all ensembles, with 3 steps of stout smearing [5] using* $\rho = 0.1$*.*

2.3.4 Kinematic range – choice of Fourier momenta

The energy difference between the initial D_s and final-state kaon sets an upper limit on the physically allowable momentum of the final-state kaon. Using the PDG masses for the D_s and K and the lattice dispersion relation, the maximum Fourier momentum of the kaon is shown in table 2.7 in integer lattice units $n^2 = \sum_\mu (n_\mu)^2$.

Name	n^2
$C1, C2$	4
$M1, M2, M3$	4
$F1M$	6

Table 2.7 *Maximum Fourier momentum of the kaon on each ensemble in integer lattice units* n^2.

Given the substantial production cost for each momentum, a single Fourier component was chosen for each integer n^2 as shown in table 2.8.

n^2	0	1	2	3	4	5	6
x	0	1	1	1	2	2	2
y	0	0	1	1	0	1	1
z	0	0	0	1	0	0	1

Table 2.8 *Components of Fourier momenta for integer lattice momenta* n^2.

The integer lattice momenta n_μ are related to momentum components ap_μ by

$$ap_\mu = \frac{2\pi n_\mu}{N_\mu} \,, \tag{2.1}$$

and the Lattice dispersion relation is

$$E\left(m, \mathbf{p}, a\right) = 2a^{-1} \sinh^{-1} \sqrt{\sinh^2\left(\frac{am}{2}\right) + \sum_{i=1}^{3} \sin^2\left(\frac{ap_i}{2}\right)} \,. \tag{2.2}$$

2.3.5 2-point correlation function data

2-point correlation function data are generated

$$C_{if}^{(2)}\left(t; \mathbf{p}\right) = \sum_{\mathbf{xy}} \mathrm{e}^{-\,\mathrm{i}\,\mathbf{p}\cdot(\mathbf{x}-\mathbf{y})} \left\langle O_f\left(\mathbf{x}, t+t_i\right) O_i^\dagger\left(\mathbf{y}, t_i\right)\right\rangle \,, \tag{2.3}$$

as per fig 2.1 using the methods outlined in § 1.3.7, for all:

- Combinations of quarks $q, q' \in \{ c, s, \ell \}$ (tables 2.5 and 2.6);
- Integer lattice momenta (table 2.7); and
- Point and wall source and sink smearings (§ 1.3.4),

where the propagator vectors are computed using (1.116) and the propagator vector for the anti-quark q' is computed using γ_5 hermeticity.

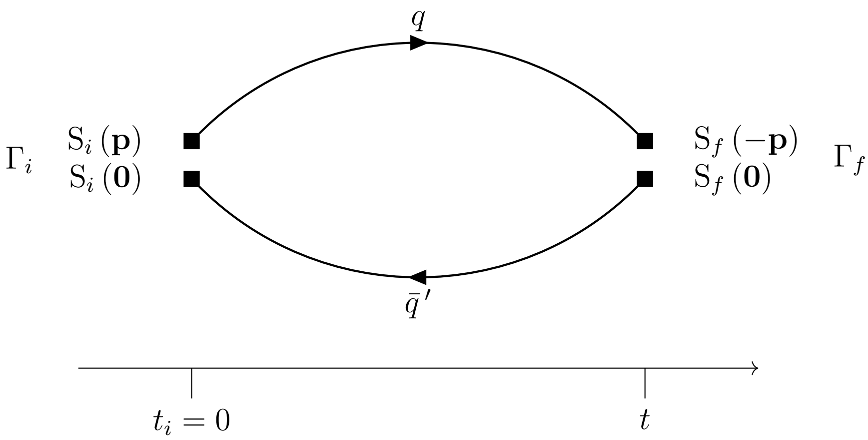

Figure 2.1 *2-point correlator, $C^{(2)}_{if}(t;\mathbf{p})$ for meson consisting of quark q and antiquark $\bar{q}$ with momentum $\mathbf{p}$. The labels 'if' label the initial and final smearings S, P=Point or W=Wall (see § 1.3.4). We can also independently choose gamma structures $\Gamma_i, \Gamma_f \in \{ \gamma_5, \gamma_4\gamma_5 \}$ for a pseudoscalar meson. The anti-quark propagator is computed using γ_5 hermeticity.*

2.3.6 3-point correlation function data

3-point correlation function data for the $D_s \to K$ decay are generated

$$C^{(3)\mu}_{if}(t) = \sum_{\mathbf{xyz}} \mathrm{e}^{-\mathrm{i}\,\mathbf{p}\cdot(\mathbf{x}-\mathbf{z})}\,\mathrm{e}^{-\mathrm{i}\,\mathbf{p}'\cdot(\mathbf{z}-\mathbf{y})} \left\langle O_f(\mathbf{x}, t_f)\, V_\mu(\mathbf{z}, t)\, O^\dagger_i(\mathbf{y}, t_i) \right\rangle , \tag{2.4}$$

using the methods outlined in § 1.3.9, for all:

- Integer lattice momenta (table 2.7),
- Point and wall source and sink smearings (§ 1.3.4),

and for the integer temporal (wall) separations, $\Delta\, T/a$ listed in table 2.9.

Ensemble	Wall separations ($\Delta T/a$)
$C1$, $C2$	12, 16, 20, 24, 28, 32
$M1$, $M2$, $M3$	16, 20, 24, 28, 32
$F1M$	16, 20, 24, 28, 32

Table 2.9 *Wall separations $\Delta T/a$ in integer lattice units.*

Because the light propagators are the most expensive to compute, in order to generate as much data as possible for the least computational cost, three optimisations are made:

- The charm is used for the sequential solve as this is faster than using light.
- The D_s is kept at rest – avoiding sequential solves for each non-zero sequential momentum.
- Two 3-point correlation functions are computed: one with the D_s on timeslice $\Delta T/a$ (fig 2.2) and another with the D_s on timeslice $(T - \Delta T)/a$ (fig 2.3) – reusing the light propagator on timeslice 0.

Additional Γ structures on timeslice t_i and at the current are essentially free, so all combinations are taken. Because each Γ on timeslice $\Delta T/a$ requires an additional sequential solve, only data with γ_5 at the sink are computed (i.e. the axial sink is not computed).

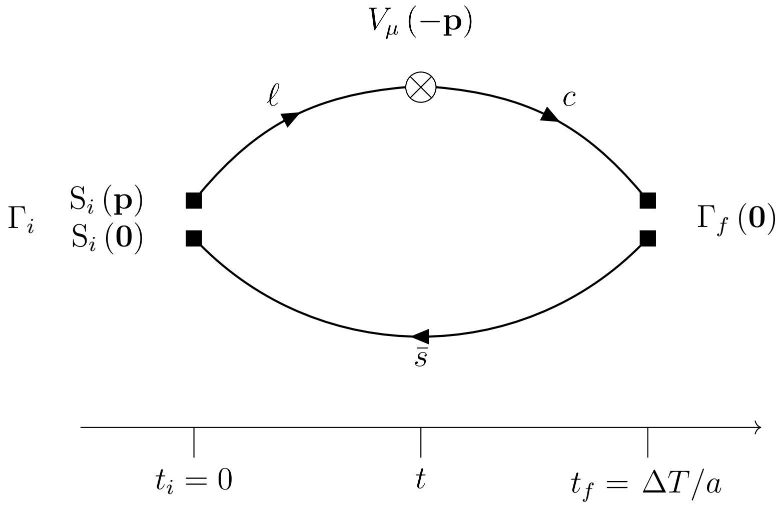

Figure 2.2 *3-point correlation function $C_{if}^{(3)\mu,fwd}(t)$ of semileptonic $D_s \to K$ decay via local vector current V_μ. The light propagator is formed from a source S_i at $t_i = 0$ with momentum $\mathbf{p}$. A strange propagator is formed from a zero momentum source at $t_i = 0$, from which a sequential charm propagator is formed via $t_f = \Delta T/a$. The contraction is performed using γ_5 hermeticity on the sequential propagator.*

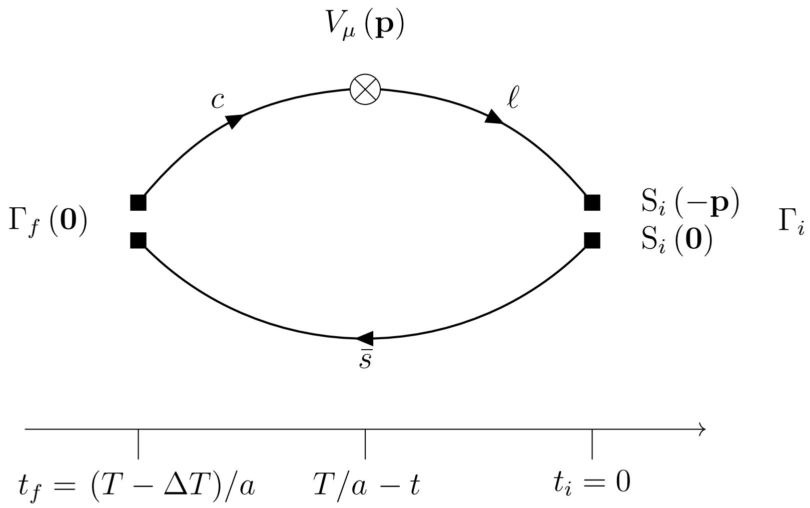

Figure 2.3 *3-point correlation function $C_{if}^{(3)\mu,back}(t)$ of semileptonic $D_s \to K$ decay via local vector current V_μ. The light propagator is formed from a source S_i at $t_i = 0$ with momentum $-\mathbf{p}$. A strange propagator is formed from a zero momentum source at $t_i = 0$, from which a sequential charm propagator is formed via $t_f = (T - \Delta T)/a$. The contraction is performed using γ_5 hermeticity on the light propagator.*

Forward and backward correlator measurements are binned together

$$C_{if}^{(3)\mu}(t) = \frac{1}{2}\left(C_{fi}^{(3)\mu,\mathrm{fwd}}\left(\frac{\Delta T}{a} - t\right) + C_{if}^{(3)\mu,\mathrm{back}}\left(\frac{T-\Delta T}{a} + t\right)\right) . \tag{2.5}$$

We define the spatial correlator $C_{if}^{(3)i}$ as the average over non-zero spatial Fourier momentum components scaled by the integer lattice momentum component in each direction

$$C_{if}^{(3)i}(t) = \frac{1}{N}\sum_{\mu=1,2,3}\frac{C_{if}^{(3)\mu}(t)}{n_\mu} \quad , \tag{2.6}$$

where N counts the number of non-zero momentum components with the Heaviside θ function

$$N = \sum_{\mu=1,2,3}\theta\left(n_\mu\right) . \tag{2.7}$$

2.4 Measurement processing & hypothesis testing

2.4.1 Measurement processing and error propagation

For this project, equivalent raw data measurements on the same configuration are not treated as statistically independent, but instead are averaged together ("binned", see Binned data below) before statistical analysis. The binned data are then bootstrapped using 10,000 replicas (see Bootstrapped data below).

Raw data

Raw data are the individual results of measurements, e.g. 2-point functions with a source on different timeslices, or the forward and backward 3-point functions described in § 2.3.6. Autocorrelation is present, so these measurements are not treated as statistically independent.

We take N_{raw} measurements, each of which is a vector of N_t data points

$$N_{\text{config}} \equiv \text{number of configurations we take measurements on} \tag{2.8}$$
$$N_{\text{meas}} \equiv \text{number of measurements per configuration} \tag{2.9}$$
$$N_{\text{raw}} \equiv \text{total number of raw measurements} = N_{\text{config}} \times N_{\text{meas}} \tag{2.10}$$
$$\mathbf{x}_i \equiv \text{vector of } N_t \text{ data points for measurement } i \tag{2.11}$$
$$N_t \equiv \text{number of timeslices on the ensemble, i.e. } T/a \tag{2.12}$$
$$i = 1 \ldots N_{\text{raw}}\,. \tag{2.13}$$

Binned data

Binned data are averages over one or more raw measurements (a 'bin'). Raw data measurements are adjusted for symmetries such as time translation invariance while binning. Bin sizes must be larger than the correlation length of the data, in order that the binned measurements may be taken to be statistically independent – even if the raw data are not.

$$\text{Bin size} \equiv \text{number of raw data measurements in each bin} \tag{2.14}$$
$$N_{\text{samples}} \equiv \text{number of measurements after binning} \tag{2.15}$$
$$= \frac{N_{\text{raw}}}{\text{bin size}} \text{ (rounded up)} \tag{2.16}$$
$$\mathbf{x}_j^{\text{bin}} \equiv \text{vector of } N_t \text{ data points for binned measurement } j \tag{2.17}$$
$$j = 1 \ldots N_{\text{samples}}\,. \tag{2.18}$$

The mean ('central') value for a measurement is the bin average

$$\overline{\mathbf{x}} \equiv \frac{1}{N_{\text{samples}}} \sum_{j=1}^{N_{\text{samples}}} \mathbf{x}_j^{\text{bin}}\,. \tag{2.19}$$

Bootstrapped data

Bootstrapping allows an arbitrary number N_{boot} of estimates of the mean to created. Each bootstrap replica is an estimate of $\overline{\mathbf{x}}$, consisting of averages over

N_{samples} random samples (with replacement) from the binned data.

$$N_{\text{boot}} \equiv \text{number of bootstrap replicas – 10000 in this thesis} \tag{2.20}$$
$$\overline{\mathbf{x}}_k^{\text{boot}} \equiv \text{vector of } N_t \text{ data points, } k\text{-th estimate of mean} \tag{2.21}$$
$$k = 1 \ldots N_{\text{boot}} \,. \tag{2.22}$$

For each replica k, $s \in \{\, 1 \ldots N_{\text{samples}} \,\}$ random numbers $r_s \in \{\, 1 \ldots N_{\text{samples}} \,\}$ are drawn in order that

$$\overline{\mathbf{x}}_k^{\text{boot}} = \frac{1}{N_{\text{samples}}} \sum_{s=1}^{N_{\text{samples}}} \mathbf{x}_{r_s}^{\text{bin}} \,. \tag{2.23}$$

The central replica is the average over all samples without replacement

$$\overline{\mathbf{x}}_{\text{central}} \equiv \overline{\mathbf{x}} \,. \tag{2.24}$$

The bootstrap average is not an unbiassed estimator of the data

$$\overline{\mathbf{x}}_{\text{avg}}^{\text{boot}} \equiv \frac{1}{N_{\text{boot}}} \sum_{s=1}^{N_{\text{boot}}} \overline{\mathbf{x}}_s^{\text{boot}} \neq \overline{\mathbf{x}} \,, \tag{2.25}$$

(because the replacement is random), however this bias is small (see § 2.4.4).

For functions of observables, estimates of the function are the function of the central value $\hat{f}\left(\overline{\mathbf{x}}\right)$. For error propagation:

- The function is performed over every bootstrap replica.
- Results are sorted into monotonic sequences of estimates $\hat{f}_n$.
- Statistical errors are quoted as $+\left[\hat{f}_{(N_{\text{boot}}-N_{1\sigma})} - \hat{f}\left(\overline{\mathbf{x}}\right)\right] - \left[\hat{f}\left(\overline{\mathbf{x}}\right) - \hat{f}_{N_{1\sigma}}\right]$.

The Gaussian distribution allows us to compute the width $K_{1\sigma}$, hence $N_{1\sigma}$

$$K_{1\sigma} = \frac{1}{\sqrt{2\pi}} \int_{-1}^{1} \mathrm{d}u \, \mathrm{e}^{-\frac{u^2}{2}} \simeq 0.682689492137086 \tag{2.26}$$
$$N_{1\sigma} = \frac{1 - K_{1\sigma}}{2} N_{\text{boot}} \simeq .158655253931457 \, N_{\text{boot}} \tag{2.27}$$

Jackknife data

Jackknife creates exactly N_{samples} estimates of the mean

$$\overline{\mathbf{x}}_k^{\text{jackknife}} \equiv \text{vector of } N_t \text{ data points, } k\text{-th estimate of mean} \tag{2.28}$$

$$k = 1 \ldots N_{\text{samples}} \,. \tag{2.29}$$

Each jackknife replica is an estimate of $\overline{\mathbf{x}}$, consisting of averages over all samples from the binned data excluding a different binned sample per jackknife replica

$$\overline{\mathbf{x}}_k^{\text{jackknife}} = \left(\frac{1}{N_{\text{samples}} - 1}\right) \sum_{s=1, s\neq k}^{N_{\text{samples}}} \mathbf{x}_s^{\text{bin}} \,. \tag{2.30}$$

For functions of observables, estimates of the function are the function of the central value $\hat{f}\left(\overline{\mathbf{x}}\right)$. For error propagation

- The function is performed over every jackknife replica.
- The variance σ^2 is computed and statistical errors quoted as $\pm\sigma$, where

$$\sigma^2 = \left(\frac{N_{\text{samples}} - 1}{N_{\text{samples}}}\right) \sum_{k=1}^{N_{\text{samples}}} \left(\hat{f}\left(\mathbf{x}_k^{\text{jackknife}}\right) - \hat{f}\left(\overline{\mathbf{x}}\right)\right)^2 \,. \tag{2.31}$$

Owing to the low statistics, Jackknife proved unhelpful in the construction of covariance matrices for fits in this thesis.

2.4.2 Multivariate random data

Following the National Institute of Standards and Technology (NIST) [89], if n iid (independent and identically distributed), p-dimensional samples $\mathbf{x}_i$ are drawn from a p-variate normal distribution

$$n \equiv \text{number of samples (measurements)} \tag{2.32}$$

$$p \equiv \text{number of dimensions (data points) in each sample} \tag{2.33}$$

$$\mathbf{x}_i = \begin{pmatrix} x_{i,1} & x_{i,2} & \dots & x_{i,p} \end{pmatrix}^T \tag{2.34}$$

$$\overline{\mathbf{x}} \equiv \text{sample mean} = \frac{1}{n}\sum_{i=1}^{n} \mathbf{x}_i \tag{2.35}$$

$$\mathbf{x}_1, \dots \mathbf{x}_n \sim \mathcal{N}_p\left(\boldsymbol{\mu}, \boldsymbol{\Sigma}\right) \tag{2.36}$$

$$\mathcal{N}_p\left(\boldsymbol{\mu}, \boldsymbol{\Sigma}\right) \equiv p\text{-variate normal distribution, mean } \boldsymbol{\mu}\text{, covariance } \boldsymbol{\Sigma} \tag{2.37}$$

$$\boldsymbol{\Sigma} \equiv \text{population (true) covariance matrix} \tag{2.38}$$

$$\boldsymbol{\Sigma}_{\boldsymbol{\mu}} \equiv \text{covariance matrix of mean} = \frac{\boldsymbol{\Sigma}}{n}\,, \tag{2.39}$$

then we can compute a 'test statistic' (or cost function) χ^2

$$\chi^2 = \left(\overline{\mathbf{x}} - \boldsymbol{\mu}\right)^T \boldsymbol{\Sigma}_{\boldsymbol{\mu}}^{-1}\left(\overline{\mathbf{x}} - \boldsymbol{\mu}\right)\,, \tag{2.40}$$

which is $\propto$ the distance of the sample mean from the true mean – i.e. χ^2 is small when $\overline{\mathbf{x}} \approx \boldsymbol{\mu}$. χ^2 can be shown to be [100] distributed as

$$\chi^2 \sim \chi^2_p \tag{2.41}$$

where χ^2_p is the χ^2 distribution with p degrees of freedom.

2.4.3 Multivariate goodness of fit

When fitting data to a model, $\mathbf{x}_i$ from the previous section is redefined to the difference between model predictions, $\mathbf{Th}$ (Theory), and the data

$$\mathbf{x}_i \longrightarrow \mathbf{x}'_i = \mathbf{Th} - \mathbf{x}_i = \begin{pmatrix} \mathrm{Th}_1 - x_{i,1} \\ \mathrm{Th}_2 - x_{i,2} \\ \vdots \\ \mathrm{Th}_p - x_{i,p} \end{pmatrix}\,. \tag{2.42}$$

For a good model, $\mathbf{Th} \approx \mathbf{x}_i$, i.e. $\mathbf{x}'_i \approx 0$ and we test the null hypothesis H_0

$$H_0 : \boldsymbol{\mu}' = \mathbf{0}\,, \tag{2.43}$$

with the alternate hypothesis H_1 that the model does not explain the data

$$H_1 : \boldsymbol{\mu}' \neq \mathbf{0} \,. \tag{2.44}$$

Since the model prediction is fixed, $\boldsymbol{\Sigma}_{\overline{\mathbf{x}}'} = \boldsymbol{\Sigma}_{\overline{\mathbf{x}}}$. However, in this thesis (and when fitting lattice data generally), the population covariance is unknown. Instead, an estimate for the covariance of the mean $\hat{\boldsymbol{\Sigma}}_{\overline{\mathbf{x}}}$ must be made from the sample data (for details see § 2.4.4). Setting $H_0 : \boldsymbol{\mu}' = \mathbf{0}$ in (2.40) we define the test statistic t^2

$$t^2 = \left(\mathbf{Th} - \overline{\mathbf{x}}\right)^T \hat{\boldsymbol{\Sigma}}_{\overline{\mathbf{x}}}^{-1} \left(\mathbf{Th} - \overline{\mathbf{x}}\right) \,. \tag{2.45}$$

The estimates of $\overline{\mathbf{x}}$ often come from bootstrap or jackknife replicas (§ 2.4.1).

Hotelling [101] showed that when $\hat{\boldsymbol{\Sigma}}_{\overline{\mathbf{x}}}$ is estimated from the data in this way, t^2 is distributed as the T^2 distribution (the multivariate equivalent of Student's t-distribution) with p' and $n'-1$ degrees of freedom, where

$$t^2 \sim T^2_{p',n'-1} \,, \tag{2.46}$$

and Hotelling's T^2 distribution [100, 102] is closely related to the Fisher–Snedecor F-distribution

$$T^2_{p,n-1} = \frac{p\,(n-1)}{n-p} F_{p,n-p} \,, \tag{2.47}$$

with

$$p' \equiv \text{fit degrees of freedom} = p - r \tag{2.48}$$

$$r \equiv \text{number of parameters in the model} \tag{2.49}$$

$$n' \equiv \text{number samples in the estimate of } \hat{\boldsymbol{\Sigma}}_{\overline{\mathbf{x}}} \quad . \tag{2.50}$$

The rationale for p' is that each parameter in our model can explain 1 of our p data points, such that the degrees of freedom of our problem are reduced.

To compute a p-value, we transform the t^2 statistic into f

$$f = \frac{n'-p'}{p'\,(n'-1)} t^2 \tag{2.51}$$

and since $f \sim F_{p',n-p'}$, we form the p value

$$p\text{-value} = \int_f^\infty \mathrm{d}x \, F_{p',n'-p'}\,(x) \; . \tag{2.52}$$

For some confidence level α (in this thesis 0.05), if we find

$$p\text{-value} < \alpha \, , \tag{2.53}$$

then we reject our null hypothesis that our model explains the data. Otherwise, we cannot reject the null hypothesis, so we accept the alternate hypothesis that our model explains the data at the confidence level used.

Comparison of Hotelling's T^2 and χ^2 distributions

Hotelling [103] showed that, in the large n limit, Hotelling's T^2 distribution approaches the χ^2 distribution [essentially because for large n, $\hat{\mathbf{\Sigma}}_{\overline{\mathbf{x}}} \to \mathbf{\Sigma}_{\boldsymbol{\mu}} \implies$ (2.45) $\to$ (2.40)].

A thorough comparison of the effectiveness of these two distributions when computing p-values – for lattice data using estimates of the covariance matrix constructed from the data being fitted – was performed by RBC/UKQCD collaborator Chris Kelly [104]. For small numbers of samples, particularly with large numbers of degrees of freedom, both distributions underestimated the true p-value, with Hotelling's T^2 more closely matching the true p-value.

```
#include <gsl/gsl_cdf.h>
template <typename T> T qValueHotelling( T TestStatistic, unsigned int dof, unsigned int SampleSize )
{
  if( SampleSize <= dof )
    throw std::runtime_error( "Number of data points " + std::to_string( SampleSize - 1 )
                         + " < degrees of freedom " + std::to_string( dof ) );
  const unsigned int Nu{ SampleSize - dof }; \
  const T tFactor{ static_cast<T>( Nu ) / ( dof * ( SampleSize - 1 ) ) }
  return FDistQ{ gsl_cdf_fdist_Q( TestStatistic * tFactor, dof, Nu ) };
}
```

The implementation of p-value computation using the Hotelling distribution as implemented in GSL [90, 91] (above) was regression tested against the prior study. A small sample of output is reproduced below for $p' = 28, n' = 100$, where lower case is the original output from the prior study [104] (lower case) and upper case is the reproduction for this thesis.

```
TEST FOR k=28, N=100 lower/UPPER = original/REPRODUCTION
chisq=39.2 chisq/dof=1.4 p(T2)=0.458856 p(chi2)=0.0777593
CHISQ=39.2 CHISQ/dof=1.4 P(T2)=0.458856 P(CHI2)=0.0777593
chisq=41.0667 chisq/dof=1.46667 p(T2)=0.400877 p(chi2)=0.0529546
CHISQ=41.0667 CHISQ/dof=1.46667 P(T2)=0.400876 P(CHI2)=0.0529542
chisq=42.9333 chisq/dof=1.53333 p(T2)=0.347096 p(chi2)=0.0353251
CHISQ=42.9333 CHISQ/dof=1.53333 P(T2)=0.347097 P(CHI2)=0.0353253
```

We see comparison evaluations for $\chi^2 \in \{\, 39.2, 41.0667, 42.9333 \,\}$. p(T2)/p(chi2) is the p-value computed using the χ^2/Hotelling distribution. Both codes produce the same output to 5 significant digits.

2.4.4 Estimating sample covariance matrix of mean $\hat{\mathbf{\Sigma}}_{\overline{\mathbf{x}}}$

For all fits in this thesis:

- The covariance matrix is constructed from the binned data (where available) and unfrozen (constructed independently on each bootstrap replica).
- Where binned data are not available, such as for ratios defined as an ensemble average, the covariance matrix is constructed from the bootstrapped data and frozen to the central replica.

Binned data

The sample covariance is constructed directly from the data

$$n = N_{\text{samples}} \tag{2.54}$$

$$\hat{\mathbf{\Sigma}}^{\text{bin}} = \frac{1}{n-1} \sum_{i=1}^{n} \left(\mathbf{x}_i^{\text{bin}} - \overline{\mathbf{x}}\right) \left(\mathbf{x}_i^{\text{bin}} - \overline{\mathbf{x}}\right)^T , \tag{2.55}$$

then the sample covariance of the mean is estimated

$$\hat{\mathbf{\Sigma}}_{\overline{\mathbf{x}}}^{\text{bin}} = \frac{\hat{\mathbf{\Sigma}}^{\text{bin}}}{n} . \tag{2.56}$$

This procedure gives the estimate of $\hat{\mathbf{\Sigma}}_{\overline{\mathbf{x}}}^{\text{boot}}$ for the central replica.

When fits are performed on other replicas, the sample covariance of the mean for bootstrap replica k, i.e. the unfrozen $\hat{\mathbf{\Sigma}}_{\overline{\mathbf{x}}}^{\text{boot},k}$, can be estimated by selecting the $\mathbf{x}_i^{\text{bin}}$ with replacements appropriate for replica k in (2.55).

Bootstrapped data

When constructing the estimate of the covariance matrix of the mean $\hat{\mathbf{\Sigma}}_{\overline{\mathbf{x}}}$ directly from the bootstrap replicas, the bootstrap average is used as the mean

$$\hat{\mathbf{\Sigma}}_{\overline{\mathbf{x}}}^{\text{boot}} = \frac{1}{N_{\text{boot}}} \sum_{i=1}^{N_{\text{boot}}} \left(\overline{\mathbf{x}}_i^{\text{boot}} - \overline{\mathbf{x}}_{\text{avg}}^{\text{boot}}\right) \left(\overline{\mathbf{x}}_i^{\text{boot}} - \overline{\mathbf{x}}_{\text{avg}}^{\text{boot}}\right)^T . \tag{2.57}$$

As mentioned near (2.25), the average of the bootstrap replicas has a slight bias away from $\overline{\mathbf{x}}$. Instead, the covariance matrix can be estimated using $\overline{\mathbf{x}}_{\text{avg}}^{\text{boot}} \to \overline{\mathbf{x}}$, but this has a negligible effect.

This procedure gives a single estimate of $\hat{\mathbf{\Sigma}}_{\overline{\mathbf{x}}}^{\text{boot}}$ for the central replica. When fits are performed on other replicas, the same, "frozen" $\hat{\mathbf{\Sigma}}_{\overline{\mathbf{x}}}^{\text{boot}}$ must be used.

When computing p-values, $n = N_{\text{samples}}$ are used, i.e. the number of samples from which the bootstrap replicas were constructed (not N_{boot}).

Jackknife data

For completeness, $\hat{\mathbf{\Sigma}}_{\overline{\mathbf{x}}}$ can be estimated from a jackknife resample

$$\hat{\mathbf{\Sigma}}_{\overline{\mathbf{x}}}^{\text{jackknife}} = \left(\frac{N_{\text{samples}} - 1}{N_{\text{samples}}}\right) \sum_{i=1}^{N_{\text{samples}}} \left(\overline{\mathbf{x}}_i^{\text{jackknife}} - \overline{\mathbf{x}}\right) \left(\overline{\mathbf{x}}_i^{\text{jackknife}} - \overline{\mathbf{x}}\right)^T . \tag{2.58}$$

Owing to the lack of statistics (small N_{samples}), jackknife estimates of the covariance of the mean were not useful for this thesis.

2.5 Fitting

All of the fits in this thesis were performed using `MLU` [91]. Becasue this was written by the author for this thesis, this section briefly outlines the fitting process and regression tests undertaken to ensure correctness.

2.5.1 Overview of fit code

Fit code within `MLU`:

- Allows 1 or more data files to be fitted simultaneously.
- Allows models to be specified independently per data file (§ 2.5.4).
- Maintains a global parameter list, shared by all models.
- Parameter names include the 'object' (e.g. meson) they apply to for disambiguation
  - E.g. in most 3-point fits, there will be two distinct sets of energies
  - ...one for the initial- and one for the final-state meson.
- Fits can be composed, with parameters retrieved from a previous fit.
- Each model has a guess algorithm appropriate for the model.
- Guess arbitration occurs at the start of a fit, i.e. models iteratively take guesses until all free-parameters have a starting-point.
- An uncorrelated fit is performed on the central replica using the initial guess, the result of which becomes the guess for a correlated fit on each replica.
- Fit statistics are computed from the fit replicas (bootstrap or jackknife).
- Parameters may be specified as belonging to a monotonic series such that for a sequence of n states

$$p_n^{\text{effective}} = p_{n-1}^{\text{effective}} + p_n^2 \,. \tag{2.59}$$

These are used to fit excited-state energies (which are expected to be monotonically increasing). This simplifies the models and obviates the requirement to impose constraints in the fit, while allowing the fitted model to remain analytic.

`MultiFit` uses GSL [90] nonlinear least squares optimiser for the implementation of the Levenberg-Marquardt algorithm described in the next section. Minuit [105] is also supported and was used for regression testing.

2.5.2 Levenberg-Marquardt

Marquardt noted that contemporary minimisation algorithms "not infrequently [ran] aground:

1. The Taylor series method because of divergence of the successive iterates,
2. The steepest-descent (or gradient) methods because of agonizingly slow convergence after the first few iterations."[106]

The Levenberg-Marquardt algorithm [106, 107] avoids the pitfalls of both methods by interpolating between them. For simplicity, this section describes uncorrelated fits. This is extended to correlated fits in § 2.5.3 below.

Consider a fit to n data points $(y_i, \mathbf{x}_i)$ where

$$
\begin{aligned}
y_i &\equiv \text{the data points being fitted} && (2.60)\\
\mathbf{x}_i &\equiv \text{a vector of } m \text{ independent variables per } y_i && (2.61)\\
i &= 1 \dots n\,. && (2.62)
\end{aligned}
$$

Each component of the consolidated fit function f_i makes a prediction for y_i from the independent variables $\mathbf{x}_i$ and the k-dimensional vector of parameters $\mathbf{p}$

$$f_i\left(\mathbf{x}_i, \mathbf{p}\right) : \mathbb{R}^{m+k} \rightarrow \mathbb{R}^n\,, \tag{2.63}$$

(for simplicity, f_i is treated as a function of $\mathbf{p}$ only in the below). In order to minimise (2.45), it is enough (for an uncorrelated fit) to minimise the cost function Φ

$$\Phi = \sum_{i=1}^{n} \left(y_i - f_i\right)^2 \equiv \left\|y_i - f_i\right\|^2\,. \tag{2.64}$$

f_i is approximated using a first-order Taylor series expanded about the current guess $\mathbf{p}$ (adopting Einstein summation convention)

$$
\begin{aligned}
f_i &\approx f_i\left(\mathbf{p}\right) + J_{ij}\delta_j && (2.65)\\
J_{ij} &\equiv \left.\frac{\partial f_i}{\partial p_j}\right|_{\mathbf{p}}\,. && (2.66)
\end{aligned}
$$

Inserting the Taylor series and differentiating (2.64)

$$\frac{\partial \Phi}{\partial p_i} = 2\sum_{j=1}^{n} \left(y_j - f_j\left(\mathbf{p}\right) - J_{jk}\delta_k\right) J_{ji} \tag{2.67}$$

and look for an improved guess $\mathbf{p} + \boldsymbol{\delta}$ by setting $\partial\Phi/\partial p_i = 0$

$$\mathbf{J}^T\mathbf{J}\boldsymbol{\delta} = \mathbf{J}^t\left(\mathbf{y} - \mathbf{f}\left(\mathbf{p}\right)\right) . \tag{2.68}$$

Defining

$$\mathbf{A} \equiv \mathbf{J}^T\mathbf{J} \tag{2.69}$$
$$\mathbf{g} \equiv \mathbf{J}^t\left(\mathbf{y} - \mathbf{f}\left(\mathbf{p}\right)\right) . \tag{2.70}$$

Taylor series methods optimise $\boldsymbol{\delta}_T$ by solving

$$\mathbf{A}\boldsymbol{\delta}_T = \mathbf{g}\,, \tag{2.71}$$

whereas steepest descent methods choose a direction for $\boldsymbol{\delta}_g$ then pick a step size

$$\boldsymbol{\delta}_g = -\boldsymbol{\nabla}\Phi\,. \tag{2.72}$$

In both cases, algorithms generally adjust the step size $|\boldsymbol{\delta}|$.

Rather, the innovation in the Levenberg-Marquardt algorithm is to solve for arbitrary $\lambda \geq 0$

$$\left(\mathbf{A} + \lambda\mathbb{1}\right)\boldsymbol{\delta}_0 = \mathbf{g}\,. \tag{2.73}$$

Marquardt then offers proofs for three theorems (for details see [106]):

1. $\boldsymbol{\delta}_0$ minimises Φ on an n-sphere of radius $\|\boldsymbol{\delta}\|^2 = \|\boldsymbol{\delta}_0\|^2$.
2. Calling the solution for λ of (2.73) $\boldsymbol{\delta}\left(\lambda\right)$, $\|\boldsymbol{\delta}\left(\lambda\right)\|^2$ is a monotonically decreasing function of lambda such that as $\lambda \to \infty$, $\|\boldsymbol{\delta}\left(\lambda\right)\|^2 \to 0$.
3. Let γ be the angle between $\boldsymbol{\delta}_0$ and $\boldsymbol{\delta}_g$. Then, as $\lambda \to \infty$, $\gamma \to 0$; i.e. $\boldsymbol{\delta}_0$ rotates towards the angle of steepest descent as λ grows large.

Theorem 2 shows that λ is a mechanism whereby the algorithm's search radius can be restricted, thereby avoiding the problems of Taylor series methods. λ should be kept as small as possible, so long as we stay within a region where the Taylor series is known to be a good approximation. Unless already at the minimum, there is always the option of increasing λ to find a search direction that reduces cost. By theorem 3, increasing λ moves us closer to the direction of steepest descent.

Marquardt then cites Curry's finding [108] that steepest descent methods are not scale invariant, i.e. that while the direction of steepest descent on n-spherical surfaces always points to the minimum, on a hyper-ellipsoid they do not. Countering this is straightforward – the dimensions of the p_i are transformed to an n-sphere by rescaling the diagonals of $\mathbf{A}$ to one

$$\mathbf{A} \rightarrow \mathbf{A}^{(*)} = \left(\frac{A_{ij}}{\sqrt{A_{ii}}\sqrt{A_{jj}}} \right) \tag{2.74}$$

$$\mathbf{g} \rightarrow \mathbf{g}^{(*)} = \left(\frac{g_i}{\sqrt{A_{ii}}} \right) . \tag{2.75}$$

Solving the rescaled (2.73) for $\boldsymbol{\delta}_0^{(*)}$ allows us to recover

$$\delta_{0i} = \frac{\delta_{0i}^{(*)}}{\sqrt{A_{ii}}} . \tag{2.76}$$

The search algorithm is then:

1. Start with a user-provided guess for $\mathbf{p}$, e.g. $\lambda = 10^{-2}$, $\nu = 10$.
2. Compute $\boldsymbol{\delta}_0$.
3. Compute the ratio ρ, where the numerator is the actual cost reduction from (2.64) and the denominator computes the cost difference $\Phi^{(T)}$ using the Taylor series approximation of f_i (2.65)

$$\rho = \frac{\Phi\left(\mathbf{p} + \boldsymbol{\delta}_0\right) - \Phi\left(\mathbf{p}\right)}{\Phi^{(T)}\left(\mathbf{p} + \boldsymbol{\delta}_0\right) - \Phi^{(T)}\left(\mathbf{p}\right)} . \tag{2.77}$$

4. Either
   (a) If $\rho \leq 0$, **reject step**.
      i. Decrease radius, $\lambda \rightarrow \nu\lambda$.
   (b) Otherwise, **accept step**.
      i. Increase radius, $\lambda \rightarrow \lambda/\nu$.
      ii. Stop if converged, i.e. the components of $\boldsymbol{\delta}_0$ are below a minimum (relative) tolerance.

iii. Goto step 2.

5. Goto step 2.

In practice, there are many minor refinements.

2.5.3 Correlated fits

The estimate of the covariance matrix of the mean $\hat{\boldsymbol{\Sigma}}_{\overline{\mathbf{x}}}$ can be expressed in terms of the correlation matrix ρ by extracting the diagonal scaling matrix S with diagonal elements S_{ii}

$$\hat{\boldsymbol{\Sigma}}_{\overline{\mathbf{x}}} = S\rho S\,, \qquad \text{with} \qquad S_{ii} = \sqrt{\left(\hat{\boldsymbol{\Sigma}}_{\overline{\mathbf{x}}}\right)_{ii}}\,. \tag{2.78}$$

This reduces the condition number of ρ, helping with the inversion. ρ is symmetric, positive definite and square, therefore its inverse $\rho^{-1} = LL^T$ can be Cholesky decomposed into the product of a lower triangular matrix L and its transpose. The estimate of the inverse covariance matrix of the mean is thus

$$\hat{\boldsymbol{\Sigma}}_{\overline{\mathbf{x}}}^{-1} = S^{-1}LL^TS^{-1}\,. \tag{2.79}$$

For a correlated fit, Hotelling's t^2 statistic (2.45) is used as the cost function

$$\Phi = (\mathbf{y}-\mathbf{f})^T\,S^{-1}LL^TS^{-1}\,(\mathbf{y}-\mathbf{f}) \tag{2.80}$$

$$= \left\|L^TS^{-1}\,(\mathbf{y}-\mathbf{f})\right\|^2\,. \tag{2.81}$$

This can be implemented by making the transformation

$$\mathbf{y} \to L^TS^{-1}\mathbf{y} \tag{2.82}$$

$$\mathbf{f} \to L^TS^{-1}\mathbf{f}\,, \tag{2.83}$$

then proceeding as for uncorrelated fits (§ 2.5.2). For reference, in this thesis, the reciprocal condition number $\kappa_{\text{cond}}^{-1}$ of matrix A is computed using the GSL library's [90] `gsl_linalg_cholesky_rcond` function acting on the Cholesky decomposition of A

$$\kappa_{\text{cond}}^{-1} \equiv \frac{1}{||A||_1 \cdot ||A{-}1||_1}\,, \tag{2.84}$$

where the one-norm of a matrix A is defined

$$||A||_1 \equiv \max_{1 \leq j \leq n} \sum_{i=1}^{n} |a_{ij}| \,. \tag{2.85}$$

With the exception of the fits used to extract Z_V (§ 2.6), all of the fits used in this thesis are fully correlated.

2.5.4 Fit models

A number of standard models $M_{\text{name}}(t)$ have been implemented, each of which returns the model prediction for timeslice t based on the specified values of parameters (the set of which varies by model).

In all models:

- Series of excited-state energies are modelled as monotonic sequences per (2.59).
- Parameter disambiguation (§ 2.5) can slightly modify the models
  - e.g. $A_f \equiv A_i \implies$ the product $A_{f,n} A_{i,n} \to A_{f,n}^2$.

2-point models

These three models have been designed to fit 2-point correlation function data per (1.89), with: positive parity; negative parity; or ignoring around-the-world effects, respectively

$$M_{\cosh}(t) = \sum_{n=0}^{n_{\exp}-1} \frac{A_{f,n} A_{i,n}}{2E_n} \, \mathrm{e}^{-E_n T/2} \cosh\left(E_n \left(T/2 - t\right)\right) \tag{2.86}$$

$$M_{\sinh}(t) = \sum_{n=0}^{n_{\exp}-1} \frac{A_{f,n} A_{i,n}}{2E_n} \, \mathrm{e}^{-E_n T/2} \sinh\left(E_n \left(T/2 - t\right)\right) \tag{2.87}$$

$$M_{\exp}(t) = \sum_{n=0}^{n_{\exp}-1} \frac{A_{f,n} A_{i,n}}{2E_n} \, \mathrm{e}^{-E_n t} \,. \tag{2.88}$$

Model parameters are as described near (1.89), with the addition that

$$n_{\text{exp}} \equiv \text{the number of terms appearing in the tower of states}\,. \tag{2.89}$$

3-point model

This model has been designed to fit 3-point correlation function data per (1.130), ignoring around-the-world effects and for the case $t_i < t < t_f$

$$M_{3\text{pt}}\left(t\right) = \frac{A_{f,0}A_{i,0}}{4E_{f,0}E_{i,0}} \left\langle 0|\hat{V}_\mu|0\right\rangle \mathrm{e}^{-E_{f,0}\left(t_f - t\right)}\, \mathrm{e}^{-E_{i,0}\left(t-t_i\right)} \tag{2.90}$$

$$+\,\theta\left(n_{\text{exp}}-2\right) \frac{A_{f,0}A_{i,1}}{4E_{f,0}E_{i,1}} \left\langle 0|\hat{V}_\mu|1\right\rangle \mathrm{e}^{-E_{f,0}\left(t_f - t\right)}\, \mathrm{e}^{-E_{i,1}\left(t-t_i\right)} \tag{2.91}$$

$$+\,\theta\left(n_{\text{exp}}-2\right) \frac{A_{f,1}A_{i,0}}{4E_{f,1}E_{i,0}} \left\langle 1|\hat{V}_\mu|0\right\rangle \mathrm{e}^{-E_{f,1}\left(t_f - t\right)}\, \mathrm{e}^{-E_{i,0}\left(t-t_i\right)} \tag{2.92}$$

$$+\,\theta\left(n_{\text{exp}}-3\right) \frac{A_{f,1}A_{i,1}}{4E_{f,1}E_{i,1}} \left\langle 1|\hat{V}_\mu|1\right\rangle \mathrm{e}^{-E_{f,1}\left(t_f - t\right)}\, \mathrm{e}^{-E_{i,1}\left(t-t_i\right)}\,, \tag{2.93}$$

where

$$\theta\left(t\right) \equiv \text{Heaviside step function} = \begin{cases} 1 & t \geq 0 \\ 0 & t < 0 \end{cases} \tag{2.94}$$

and n_{exp} allows inclusion of singly- and doubly-excited (in addition to ground-ground) matrix elements.

2.5.5 Correctness tests

Comparison with other fit codes

A comparison of results when fitting the same data between `MLU` code and a collaborator's code was also performed:

- Six 2-point correlation functions of the same pseudoscalar meson: ALL – ALS; ALS – ALS; PLL – PLS; PLS – ALL; PLS – ALS; and PLS – PLS.
- 'P' = pseudoscalar (γ_5); 'A' = axial ($\gamma_4\gamma_5$); 'L' = local; and 'S' = smeared.
- These are simultaneously fitted to a 2-state model for each meson.

- 22 timeslices are used from each correlation function.
- For this fit, the same covariance matrix was used.
- Solver precision set to $1e{-7}$.
- Test performed 3-Jul-2022.

Regression test of **MLU** fit code against collaborator's fit code using same data and covariance matrix. Fit results agree on each bootstrap sample (see tables 2.10 and 2.11).

Replica	E_0	E_0^{MLU}	E_1	E_1^{MLU}
0	0.968121128	0.968121117	1.410854418	1.410851762
1	0.967999101	0.967999098	1.412129688	1.412128599
2	0.967926192	0.967926192	1.386049653	1.386049496
3	0.968034948	0.968034948	1.397297793	1.397298099
4	0.968037807	0.96803782	1.408385175	1.408385891

Table 2.10 *Comparison of ground and first excited-state energies E_0 and E_1 with MLU fit results E_0^{MLU} and E_1^{MLU}.*

Replica	ALL_0	$\text{ALL}_0^{\text{MLU}}$	ALL_1	$\text{ALL}_1^{\text{MLU}}$
0	53.13848567	53.13847947	55.99497714	55.99441649
1	53.10157214	53.10157024	56.07354905	56.0733176
2	53.04026734	53.04026681	51.41680222	51.41677699
3	53.09851766	53.098518	52.06335909	52.06341802
4	53.10120683	53.10121274	55.41869795	55.41879188

Table 2.11 *Comparison of ground and first excited-state overlap coefficients ALL_0 and ALL_1 with MLU fit results ALL_0^{MLU} and ALL_1^{MLU}.*

Comparison between GSL and Minuit2

This test uses the `MLU` fit code, comparing results when calling GSL [90] (see fig 2.4) vs Minuit2 [105] (see fig 2.5) libraries. Test performed 10-Aug-2020.

In both cases a simultaneous two state (ground- and first excited-state) fit is performed to two correlation functions for the same pseudoscalar meson using two different smearings.

```
Loading folded correlators
  GFWPZ2/fold35/h1_l_p_0_0_0_PP_PP.fold.4147798751.h5 (fold)
  GFWPZ2/fold35/h1_l_p_0_0_0_PP_PW.fold.4147798751.h5 (fold)
  File Operators: PP PW
   Fit Operators: PP PW
=================================================================
Correlated GSL fit on timeslices 11 to 17 using 2 Open MP threads
trust-region/levenberg-marquardt with numeric derivatives
Tolerance 1e-07. Using uncorrelated fit as guess for each replica.
 Correlated fit 1 on central replica, calls 9, chi^2 13.27484686092
dof 8, chi^2/dof 1.659355857616, Stop: step size, f()=80, df()=0
   E0 0.9971303491739        +/- 0.0009133870886602
   E1 1.41003775569        +/- 0.09523896790729
  PP0 30.70610395934        +/- 0.2351339598434
  PW0 12491.95697198        +/- 102.9579358186
  PP1 44.49192135972        +/- 18.53882408405
  PW1 -6235.662718102        +/- 4410.502568491
Mon Aug 10 11:46:57 2020. Total duration 0.0 seconds.
```

Figure 2.4 *Correlated fit results using GSL cf fig 2.5*

```
Correlated Minuit2 fit on timeslices 11 to 17 using 2 Open MP threads
Tolerance 1e-07. Using uncorrelated fit as guess for each replica.
Correlated fit 4 on central replica, calls 30, chi^2 13.27484686063
edm 5.572096917176e-17, dof 8, chi^2/dof 1.659355857578
   E0 0.9971303477        +/- 0.000911081920224
   E1 1.410036751443        +/- 0.08607724933247
  PP0 30.70610303273        +/- 0.2274727258344
  PW0 12491.95770106        +/- 101.780637291
  PP1 44.49171672909        +/- 17.13430893717
  PW1 -6235.65232636        +/- 4133.152257712
Mon Aug 10 11:49:42 2020. Total duration 1.0 seconds.
```

Figure 2.5 *Correlated fit results using Minuit2 cf fig 2.4*

Each fit uses a tolerance of 10^{-7}, and the GSL and Minuit2 fits agree to 7 significant figures (except first excited-state overlap coefficients, which agree to 6 significant figures).

2.6 Renormalisation

This section presents renormalisation results prepared per § 1.4.2 and fitted per § 2.5. Results are tabulated in table 2.12.

Name	heavy aE_0 $[D_s]$	heavy p-value	heavy Z_V	light aE_0 $[K]$	light p-value	light Z_V	mixed Z_V
C1	1.10403(61)	0.623	1.037(13)	0.30620(47)	0.411	0.7113(58)	0.8590(74)
C2	1.10465(74)	0.429	1.036(14)	0.32522(57)	0.062	0.7319(59)	0.8709(82)
M1	0.82568(57)	0.71	0.9964(80)	0.22449(85)	0.63	0.7412(51)	0.8594(51)
M2	0.82567(68)	0.078	1.0211(82)	0.23064(55)	0.82	0.7549(60)	0.8780(58)
M3	0.82554(62)	1.00	1.0022(96)	0.23852(68)	0.348	0.7414(57)	0.8620(62)
F1M	0.72911(21)	0.59	0.9932(42)	0.19084(22)	0.78	0.7639(42)	0.8711(34)

Table 2.12 *Mostly nonperturbative renormalisation results for each ensemble (first column). For each of the heavy and light actions, we see: 1) the ground state energy in lattice units aE_0 entering the Z_V extraction; 2) the meson name in square brackets; 3) the Hotelling p-value of the aE_0 fit; and 4) Z_V. The final column shows the mixed action Z_V, computed per (1.182) taking $\rho = 1$, i.e. $Z_{V,m} = \sqrt{Z_{V,h} Z_{V,\ell}}$. Error propagation for $Z_{V,m}$ comes from the bootstrap.*

Examining the fitted energies in table 2.12, the D_s meson masses are stable across the coarse ensembles and again across the medium ensembles. This stability results from:

1. The charm quark mass having been tuned to its physical value (as described in § 2.3.3).
2. Using fixed bare strange quark masses at each lattice spacing, separately for sea and valence quarks (see table 2.5).

The kaon masses differ on each ensemble, reflecting the increasing bare light quark masses used across members of the coarse and medium collections of ensembles.

Scanning the Z_V columns, for both the heavy and light actions, Z_V for ensembles C1 and C2 are compatible, as are ensembles M1 and M3. However, for both the heavy and light actions, Z_V for M2 is $\sim 2\sigma$ higher than the other medium ensembles. This was examined in detail (see appendix A.9 for a summary of that analysis) and it was concluded that this was a statistical fluctuation in the data. Systematic effects associated with Z_V were examined as global fit alternative (m) in § 4.3.

2.6.1 Z_V results – all ensembles

In this section (figures 2.6 – 2.29) two diagrams are shown for each combination of ensemble and action (heavy and light):

1. The fit to the ratio (1.176) used to extract Z_V

$$Z_V = \frac{\tilde{C}^{(2)}(\Delta T)}{C^{(3)}(t)} . \tag{2.95}$$

   - Each data point estimates Z_V and data points are highly correlated.
   - Thinning (removing data points) brought the correlation matrix under control, but at the expense of rejecting data points.
   - An uncorrelated fit to a constant is performed in the plateau region.
   - The plot shows the ratio Z_V vs time t.

2. The 2-point correlation function fit extracting the mass am_{eff} of the D_s entering (1.175)

   - Simultaneous fit to 2, point-sink 2-point correlation functions
     - 2-exponential fit to the point-source data – left panel ‘p-p’
     - 1-exponential[1] fit to wall-source data – right panel ‘p-w’
   - The plot shows the effective mass am_{eff} vs time t

$$am_{\text{eff}}(t) = \ln\left[\frac{C^{(2)}\left(t-\frac{1}{2}\right)}{C^{(2)}\left(t+\frac{1}{2}\right)}\right] . \tag{2.96}$$

In these fits and all subsequent fits shown in this thesis:

- Red data points are included in the fit; black data points are excluded from the fit; and error bars show 1 standard deviation.
- Dark blue box symbols with light blue shaded error bars are the fit results.

[1] Except on F1M and C2, where a 2-state fit was performed.

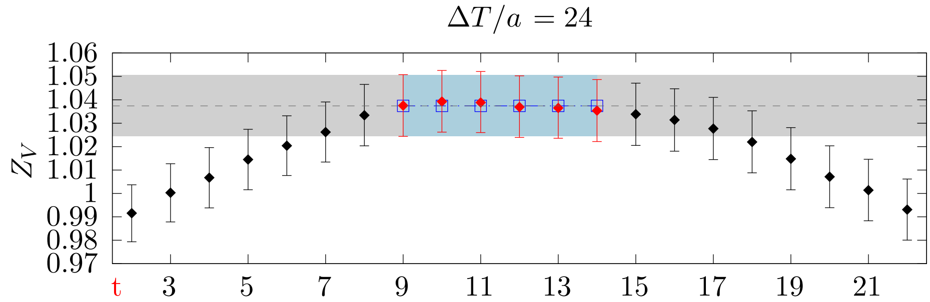

Figure 2.6 *Ensemble C1, heavy action,* (2.95) $Z_{V,hh} = 1.037(13)$ *from decay of heavy quark with strange spectator, wall separation* $\Delta T/a = 24$.

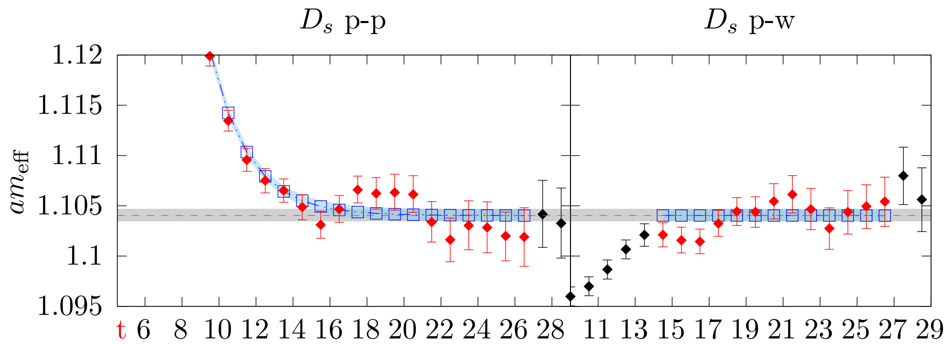

Figure 2.7 *Ensemble C1, heavy action, effective mass entering fit,* (2.96) $am_{eff} = 1.10403(61)$*, Hotelling p-value 0.623.*

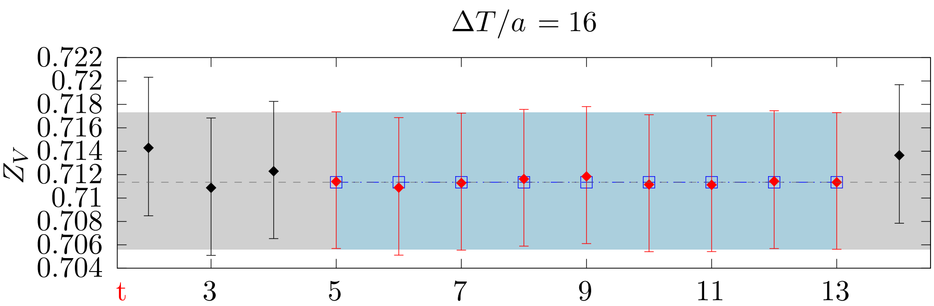

Figure 2.8 *Ensemble C1, light action,* (2.95) $Z_{V,l} = 0.7113(58)$ *from decay of light quark with strange spectator, wall separation* $\Delta T/a = 16$.

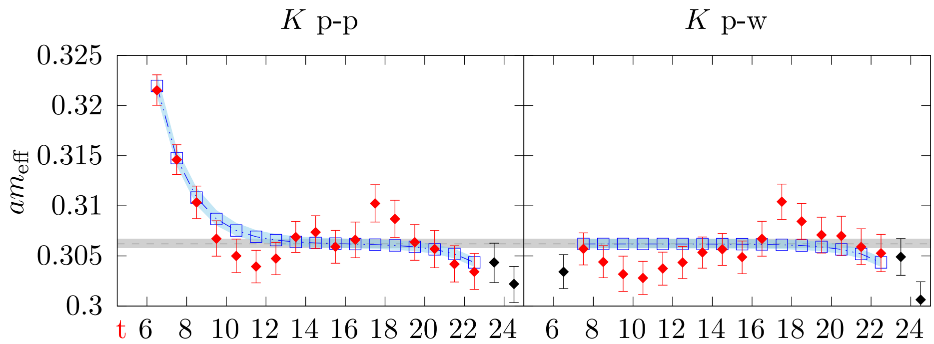

Figure 2.9 *Ensemble C1, light action, effective mass entering fit,* (2.96) $am_{eff} = 0.30620(47)$*, Hotelling p-value 0.411.*

Mostly nonperturbative renormalisation – C2

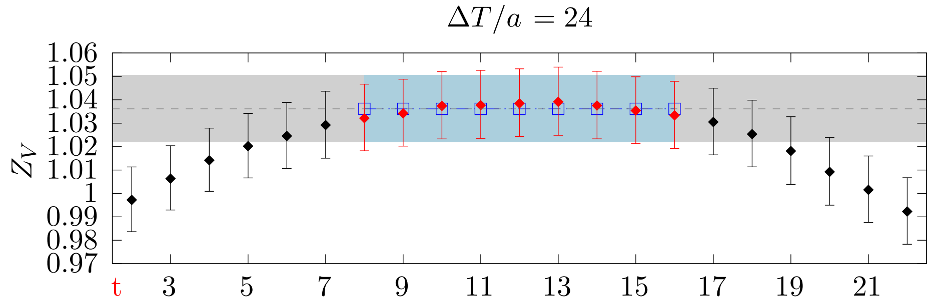

Figure 2.10 *Ensemble C2, heavy action,* (2.95) $Z_{V,hh} = 1.036(14)$ *from decay of heavy quark with strange spectator, wall separation* $\Delta T/a = 24$*.*

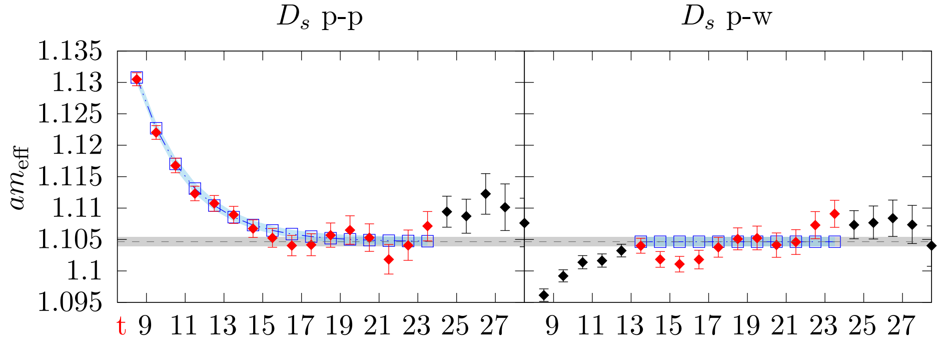

Figure 2.11 *Ensemble C2, heavy action, effective mass entering fit,* (2.96) $am_{\mathit{eff}} = 1.10465(74)$*, Hotelling p-value 0.429.*

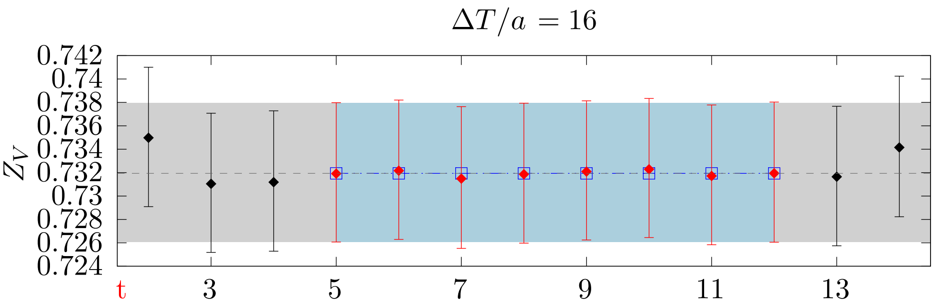

Figure 2.12 *Ensemble C2, light action,* (2.95) $Z_{V,l} = 0.7319(59)$ *from decay of light quark with strange spectator, wall separation* $\Delta T/a = 16$*.*

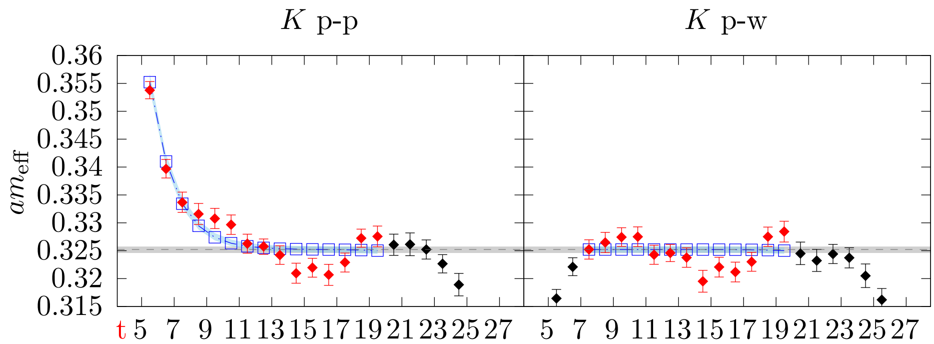

Figure 2.13 *Ensemble C2, light action, effective mass entering fit,* (2.96) $am_{\mathit{eff}} = 0.32522(57)$*, Hotelling p-value 0.062.*

Mostly nonperturbative renormalisation – M1

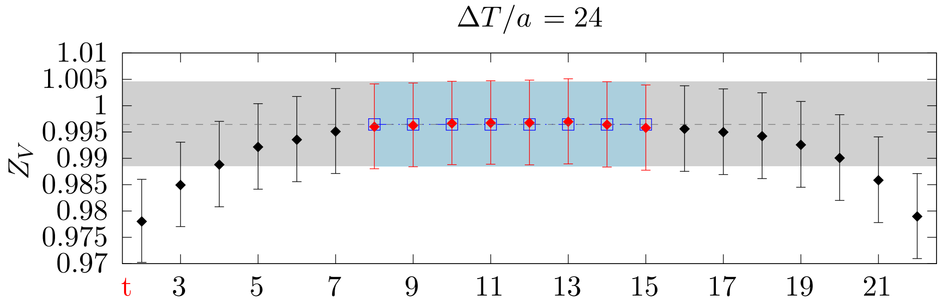

Figure 2.14 *Ensemble M1, heavy action,* (2.95) $Z_{V,hh} = 0.9964(80)$ *from decay of heavy quark with strange spectator, wall separation* $\Delta T/a = 24$.

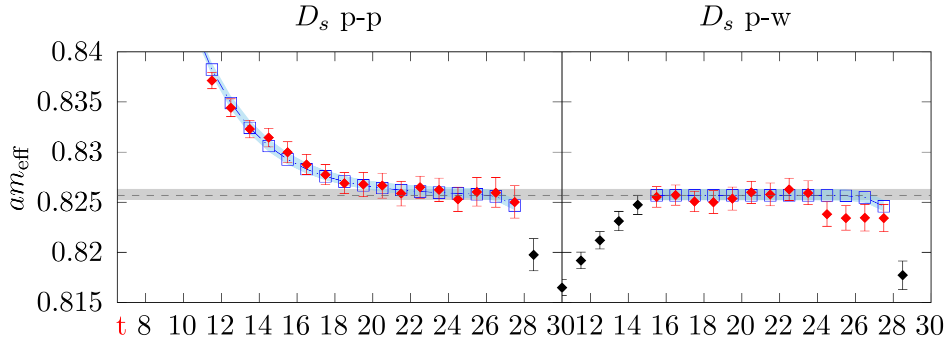

Figure 2.15 *Ensemble M1, heavy action, effective mass entering fit,* (2.96) $am_{eff} = 0.82568(57)$*, Hotelling p-value 0.71.*

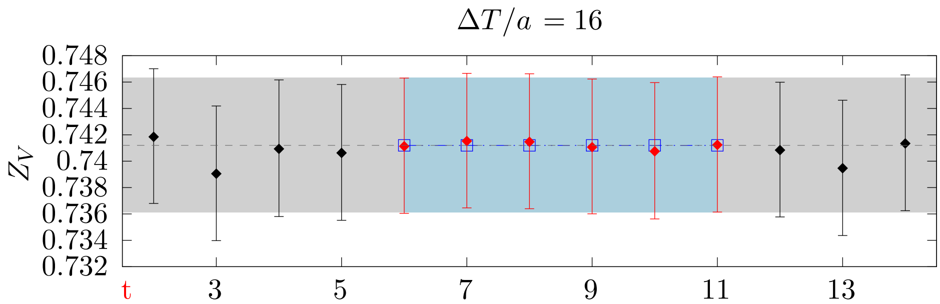

Figure 2.16 *Ensemble M1, light action,* (2.95) $Z_{V,l} = 0.7412(51)$ *from decay of light quark with strange spectator, wall separation* $\Delta T/a = 16$.

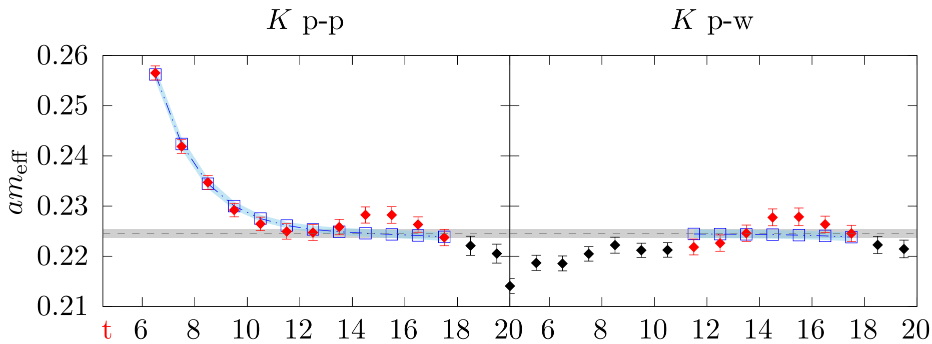

Figure 2.17 *Ensemble M1, light action, effective mass entering fit,* (2.96) $am_{eff} = 0.22449(85)$*, Hotelling p-value 0.63.*

Mostly nonperturbative renormalisation – M2

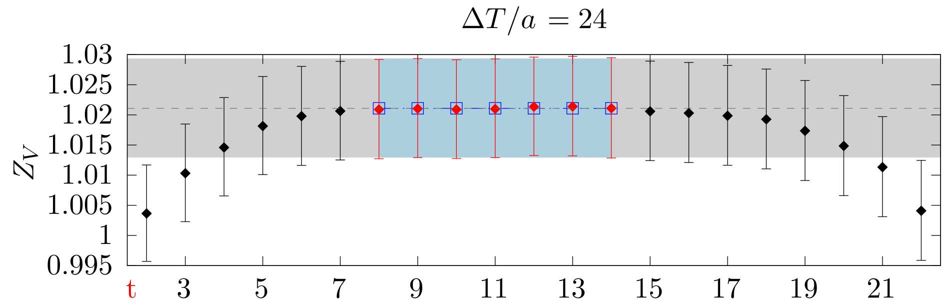

Figure 2.18 *Ensemble M2, heavy action, (2.95) $Z_{V,hh} = 1.0211(82)$ from decay of heavy quark with strange spectator, wall separation $\Delta T/a = 24$.*

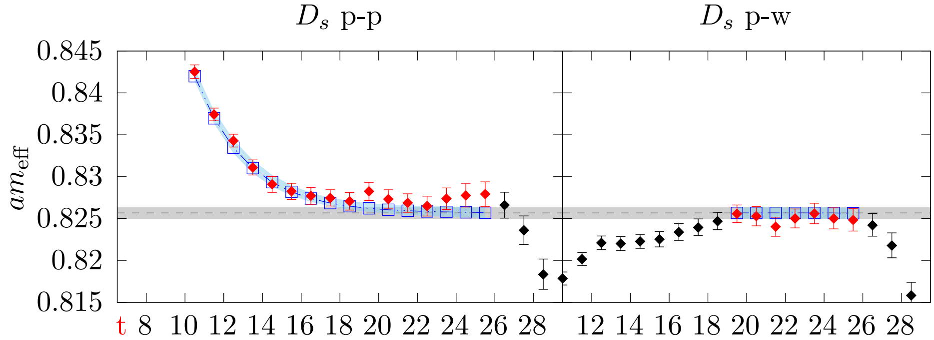

Figure 2.19 *Ensemble M2, heavy action, effective mass entering fit, (2.96) $am_{eff} = 0.82567(68)$, Hotelling p-value 0.078.*

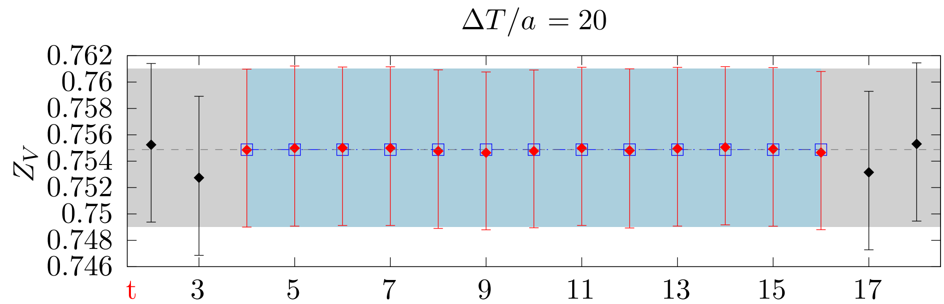

Figure 2.20 *Ensemble M2, light action, (2.95) $Z_{V,l} = 0.7549(60)$ from decay of light quark with strange spectator, wall separation $\Delta T/a = 20$.*

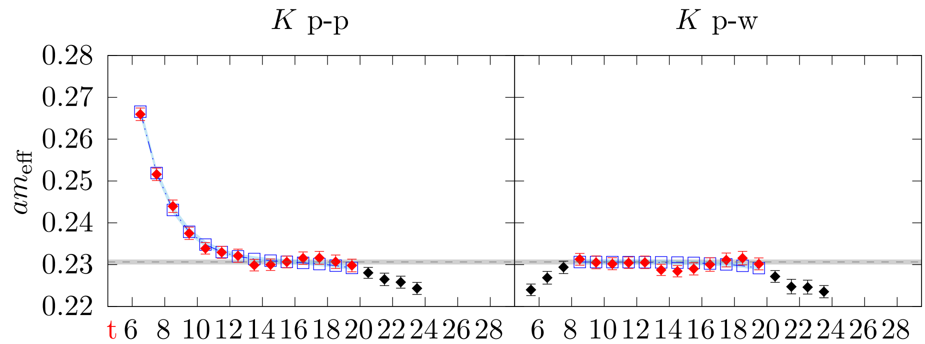

Figure 2.21 *Ensemble M2, light action, effective mass entering fit, (2.96) $am_{eff} = 0.23064(55)$, Hotelling p-value 0.82.*

Mostly nonperturbative renormalisation – M3

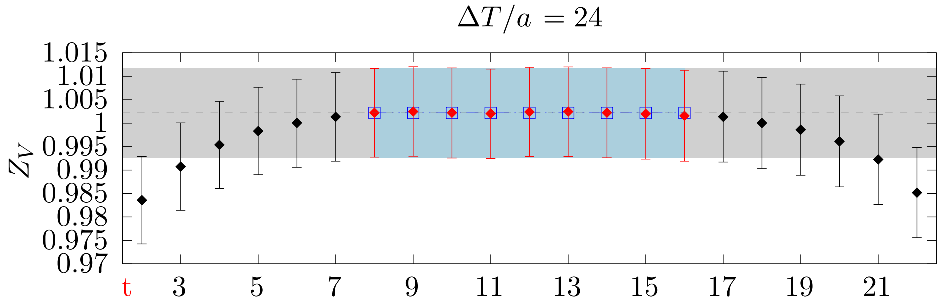

Figure 2.22 *Ensemble M3, heavy action, (2.95) $Z_{V,hh} = 1.0022(96)$ from decay of heavy quark with strange spectator, wall separation $\Delta T/a = 24$.*

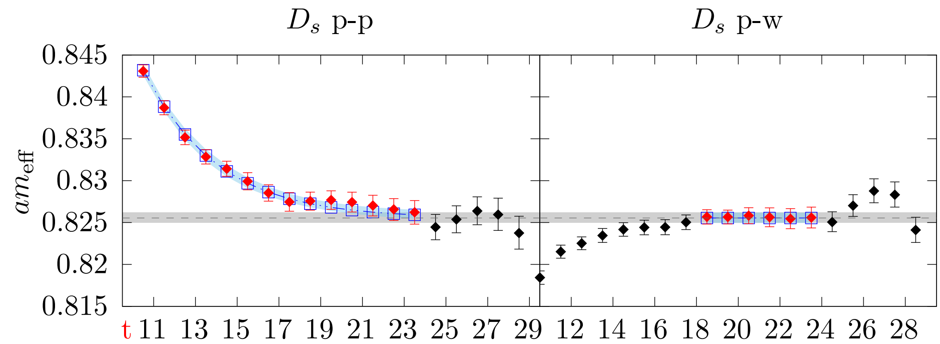

Figure 2.23 *Ensemble M3, heavy action, effective mass entering fit, (2.96) $am_{eff} = 0.82554(62)$, Hotelling p-value 1.00.*

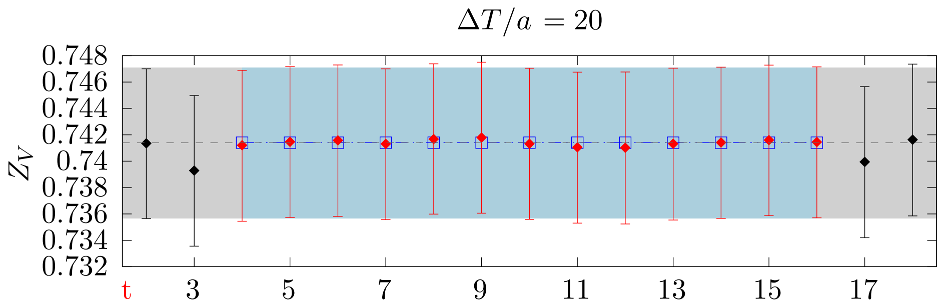

Figure 2.24 *Ensemble M3, light action, (2.95) $Z_{V,l} = 0.7414(57)$ from decay of light quark with strange spectator, wall separation $\Delta T/a = 20$.*

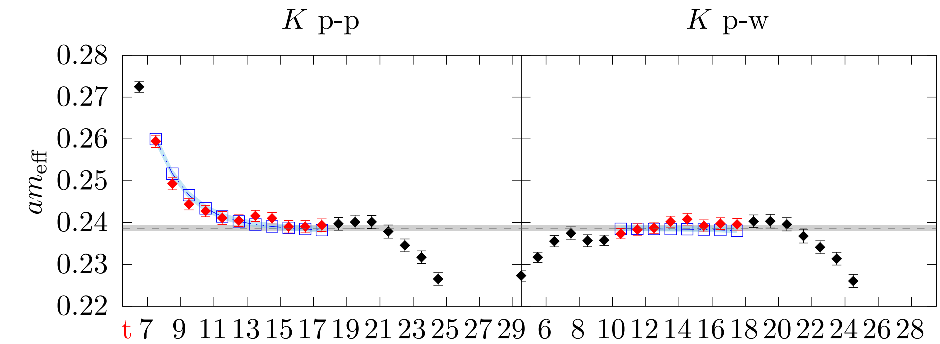

Figure 2.25 *Ensemble M3, light action, effective mass entering fit, (2.96) $am_{eff} = 0.23852(68)$, Hotelling p-value 0.348.*

Mostly nonperturbative renormalisation – F1M

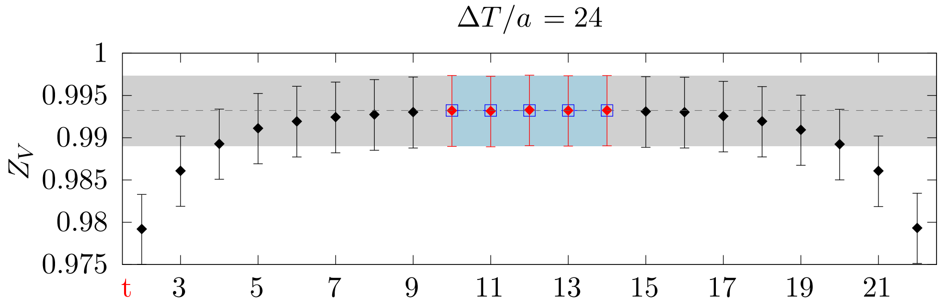

Figure 2.26 *Ensemble F1M, heavy action,* (2.95) $Z_{V,hh} = 0.9932(42)$ *from decay of heavy quark with strange spectator, wall separation* $\Delta T/a = 24$*.*

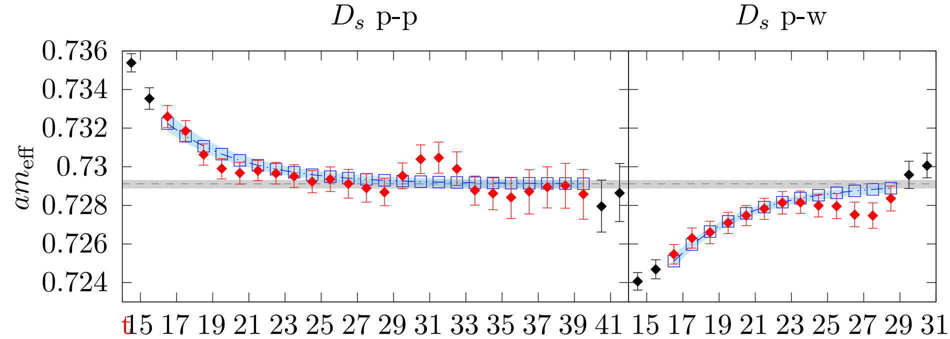

Figure 2.27 *Ensemble F1M, heavy action, effective mass entering fit,* (2.96) $am_{\mathit{eff}} = 0.72911(21)$*, Hotelling p-value 0.59.*

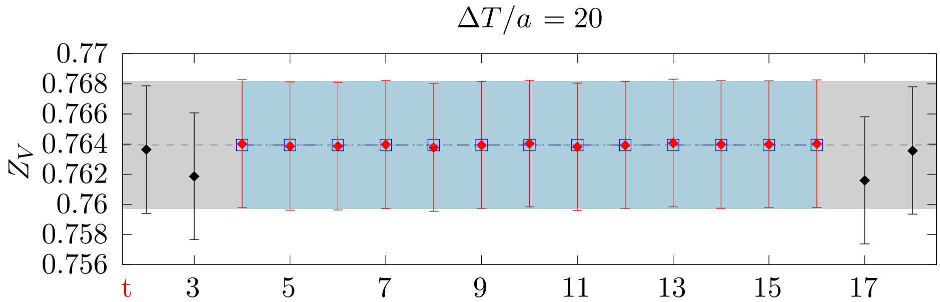

Figure 2.28 *Ensemble F1M, light action,* (2.95) $Z_{V,l} = 0.7639(42)$ *from decay of light quark with strange spectator, wall separation* $\Delta T/a = 20$*.*

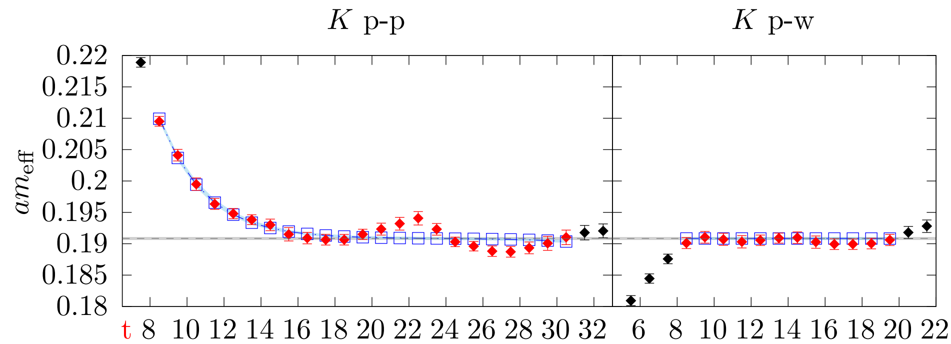

Figure 2.29 *Ensemble F1M, light action, effective mass entering fit,* (2.96) $am_{\mathit{eff}} = 0.19084(22)$*, Hotelling p-value 0.78.*

Chapter 3

Per ensemble form factor results

This chapter presents results for the extraction of form factors on each ensemble and is structured as follows:

- The ratios of 2- and 3-point correlation functions from which the vector current matrix elements of interest will be extracted are presented in § 3.1, before outlining the general fit procedure applied to every ensemble.
- Matrix element results are presented for one ensemble in detail in § 3.2.
  - Starting with the 2-point functions in § 3.2.1.
  - The matrix element extraction at $n^2 = 0$ is presented in § 3.2.2.
  - Matrix element extraction for non-zero momenta on the same ensemble follow a similar procedure and are presented together in § 3.2.3.
- For all other ensembles the 2-point function and $n^2 = 0$ matrix element fit results are presented in § 3.3, where, for brevity, the non-zero momentum matrix element fit results have been moved to appendices A.1 to A.5.
- A summary of the mostly nonperturbatively renormalised matrix elements at each momenta on each ensemble are presented in table form in § 3.4.
- Results for the fully nonperturbative renormalisation correction factors ρ are presented in § 3.5 for each ensemble.
- The fully nonperturbatively renormalised form factor results for each ensemble are presented in § 3.6.

The results from this chapter are then fed into a global fit as outlined in chapter 4.

In terms of the order of presentation of the data for each of the six ensembles, first the data for the finest ensemble are presented. Then, for each of the other ensembles, the zero-momentum data are presented, relegating non-zero momentum matrix element fit figures to the appendix for reference. The advantage of presenting the most precise data with the finest increments of momenta in detail is that the exposition is clearer.

One disadvantage to this approach is that, on all other ensembles, the matrix elements extracted at each momenta asymptotically approach the same value for large wall separations. No order of presentation would be perfect and the reader is invited to compare results for multiple ensembles at the appropriate point in § 3.2.2.

3.1 Vector current matrix element extraction

Analogously to the ratio (1.176) used to get access to the matrix element to extract Z_V, ratios of 2 and 3-point correlation functions are formed to extract the matrix elements of the mostly nonperturbatively renormalised vector current.

Using definitions $C_{if}^{(3)\mu}$ (1.137), $\tilde{C}_i$ (1.175) and A_i (1.86), we define the ratio R_3^μ

$$R_3^\mu \left(t_i, t, t_f, \mathbf{p}_i, \mathbf{p}_f\right) = Z_V A_i A_f \frac{C_{P_i P_f}^{(3)\mu} \left(t_i, t, t_f, \mathbf{p}_i, \mathbf{p}_f\right)}{\tilde{C}_{P_i} \left(t - t_i, \mathbf{p}_i\right) \tilde{C}_{P_f} \left(t_f - t, \mathbf{p}_f\right)} \tag{3.1}$$

in order that for large enough wall separations $\Delta T/a = t_f - t_i$, i.e. where the ground states dominate, the ratio R_3^μ gives the renormalised vector matrix elements

$$R_3^\mu \simeq \langle P_f \left(\mathbf{p}_f\right) | \mathcal{V}^\mu \left(\mathbf{q}^2\right) | P_i \left(\mathbf{p}_i\right) \rangle \ . \tag{3.2}$$

R_3^μ are produced for all Fourier momenta $\mathbf{p}_f$ covering the physically allowable kinematic range (holding $\mathbf{p}_i = 0$) for a range of wall separations $\Delta T/a$.

The R_3^μ data are then fitted simultaneously for multiple wall separations using n-state models for the 2 and 3-point functions. For the 3-point function we ignore around-the-world effects and consider only the case where $t_t < t < t_f$

$$C^{(3)\mu,\text{model}}_{P_i P_f} = \sum_{m,n} \frac{A_{f,m} A_{i,n}}{4 E_{f,m} E_{i,n}} \langle P_{f,m} | \mathcal{V}_\mu | P_{i,n} \rangle \, \mathrm{e}^{-E_{f,m}\left(t_f - t\right)} \, \mathrm{e}^{-E_{i,n}(t-t_i)} \,, \quad (3.3)$$

where we truncate the sum over states m, n by specifying N_{exp}

$$N_{\text{exp}} = \begin{cases} 1, & \text{ground state only} \\ 2, & \text{ground + singly-exited states} \\ 3, & \text{ground + singly- + doubly-exited states} \end{cases} \,, \quad (3.4)$$

where

$$\text{ground state} \equiv m = 0, n = 0 \quad (3.5)$$

$$\text{singly-excited states} \equiv \begin{cases} m = 0, n = 1 \\ m = 1, n = 0 \end{cases} \quad (3.6)$$

$$\text{doubly-excited states} \equiv m = 1, n = 1 \,, \quad (3.7)$$

and we use $n = 2$-state fits for the $\tilde{C}$

$$\tilde{C}_i^{\text{model}} = \sum_n A_{f,n} A_{i,n} \, \mathrm{e}^{-E_n t} \;. \quad (3.8)$$

3.1.1 Ratio fit procedure

This section outlines the fitting procedure and the rationale for choices made, before the ratio fit results themselves are presented § 3.2.

The fit procedure presented here was developed iteratively. As the data on each ensemble were fitted, we found principles that applied generally across all of the data in this thesis. As this procedure was expanded, fit range selections were refined across all ensembles and momenta.

This fitting procedure applies to all data points on all ensembles, with some variations as noted. These guidelines serve as a starting point for fit selections, which are then tailored in each fit to obtain best results.

(a) **Two-step fits.** It was not possible to simultaneously fit the 2- and 3-point data while maintaining p-values above the rejection threshold. Remembering the discussion near (2.48), if

$$p \equiv \text{number of data points in the fit} \tag{3.9}$$

$$r \equiv \text{number of parameters in the model} \tag{3.10}$$

$$p' \equiv \text{fit degrees of freedom} = p - r \tag{3.11}$$

$$n' \equiv \text{number samples in the estimate of } \hat{\boldsymbol{\Sigma}}_{\overline{\mathbf{x}}}\,, \tag{3.12}$$

then there must be more data points than parameters to fit, i.e.

$$p > r\,, \tag{3.13}$$

and the estimate of the covariance matrix must also have been constructed using more data samples than there are degrees of freedom in the fit, i.e.

$$p' < n' < 72 \text{ (on the F1M ensemble).} \tag{3.14}$$

The 2-point data were fitted first, with those results fed into the 3-point data fits as an input. This had the advantage that 3-point fits could all share the same D_s fit results (overlap coefficients and energies) replica by replica.

(b) **Permutation-invariant cost function.** The definition of the cost function 2.45 is invariant under a permutation of the data points entering the fit. The cost, for example, of three data points each contributing a 2-σ component to the cost is the same whether those data points are consecutive or equally spaced throughout the fit. However, under some circumstances, our knowledge of physics gives reason to reject a specific ordering – such as the case of a fit to a 2-point correlation function where significant contributions to the fit cost Φ_i from early timeslices indicate excited-state contamination which is poorly modelled by the fit form. In such cases, we use our knowledge of physics to reject such fits.

(c) D_s **2-point fit.** The same D_s 2-point, zero-momentum, point-source, point-sink, 2-state fit enters all of the ratio fits on each ensemble. The wall-source, point sink data are simultaneously fitted to a single exponential model in the region of the plateau. On the finest ensemble (F1M) the wall-source data are fitted to a two-state model.

(d) **Kaon 2-point fit.** Kaon energies and overlap coefficients are needed at each of the Fourier momenta for which there are 3-point data. Best results were obtained by fitting the point-source, point-sink kaon data simultaneously for all momenta and enforcing the lattice dispersion relation. For higher momentum kaon data, this results in small error bars. However, low statistics meant that it was otherwise very difficult for the fitter to consistently identify the ground state energies. In some cases, it was necessary to thin (i.e. drop data points) from the fit to keep the correlation matrix under control. Where this was necessary, only the non-zero-momentum correlation functions were thinned (except on F1M).

(e) **Prefer singly-excited 3-point fits.** For all ratio fits, singly-excited states are included in the three-point models, $N_{\rm exp} = 2$ (3.4). Doubly-excited states are also included where this improves the quality of the fits, i.e. where at least some of the doubly-excited matrix elements are sufficiently resolved from zero. The choice of $N_{\rm exp}$ is made per ensemble.

(f) **Simultaneous, multiple wall-separations.** At least two (and preferably three) wall separations $\Delta T/a$ are fitted simultaneously. We prefer to include larger wall separations (near plateau), but will discard noisy wall separations with large statistical errors.

(g) **Data points straddle curvature.** Where possible, data points are preferred from each ratio covering both the rising and falling trend, as are more rather than fewer data points. We prefer not to use data points closer to the source or sink than the relevant 2-point fit.

(h) **Thinning used minimally.** Preference is given to smaller fit ranges, from which all data points are used. Thinning is used as a second choice in the small number of cases where reducing fit ranges fails, e.g. kaon 2-point fits and a small number of ratio fits on the $M3$ ensemble.

(i) **Multiple fit choices possible.** It must be possible to select multiple fit ranges, using data from different combinations of wall-separations, which result in compatible fits – i.e. fit results within 1-σ of the chosen fit.

Results for each ensemble are reported in the following sections, starting with the finest ensemble (F1M), which is presented in detail.

3.2 Ensemble F1M fit results

First, results for the 2-point function fits entering the ratio fit in § 3.2.1 are presented, followed by detailed matrix element fit results at $n^2 = 0$ in § 3.2.2, and matrix element fit results at $n^2 \neq 0$ in § 3.2.3.

A summary of the results for the F1M matrix elements is presented in table 3.1, which is deferred to § 3.4 where results for all ensembles are collated.

3.2.1 F1M 2-point functions

Following the ratio fit procedure in § 3.1.1, the masses, energies and overlap coefficients for the D_s and kaon are extracted from separate, multicorrelator fits. In all cases, data from point-sink correlation functions are fitted.

There is a degree of freedom in the fit form in the choice of sign of the point overlap coefficient, $A_{\mathrm{P},n}$, which is constrained in the fit to be positive. This applies to all ensembles.

F1M D_s 2-point fit

Fig 3.1 shows results of the preferred fit for the D_s on ensemble F1M. The point- and wall-source correlation functions (both with a point sink) are fitted simultaneously to a 2-state (ground and first excited-state) cosh model (2.86). Both correlation functions are well described by the 2-state model from timeslice 13 to timeslices 28 and 29 respectively, after which there is a statistical ripple in the data.

Using both the point- and wall-source data simultaneously gave the best results for quality and stability of the fit. Axial data are included in the plot for reference, but are not included in the final fit selection.

We ensure that the fit results are insensitive to variations in the fit start and stop times for both correlation functions. A scan over multiple fit ranges is included at appendix A.7.

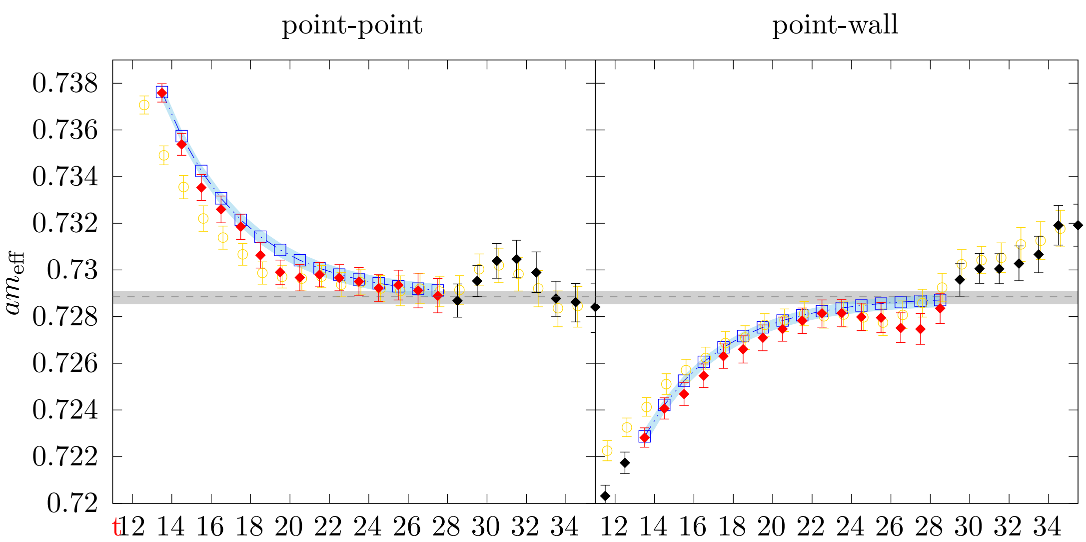

p-val	am_0	am_1	$t_{\rm P}$-fit	$A_{\rm P,0}$	$A_{\rm P,1}$	$t_{\rm W}$-fit	$A_{\rm W,0}$	$A_{\rm W,1}$
0.97	0.72885(29)	0.979(14)	13-28	46.07(17)	55.1(4.4)	13-29	54244(350)	-41651(4500)

Figure 3.1 *Effective mass* $am_{\it eff}\left(t+\frac{1}{2}\right) = \ln C^{(2)}(t)/C^{(2)}(t+1)$ *vs* t*, for 2-point* D_s *correlation function fit on ensemble F1M. Simultaneous 2-exponential fit to point source on timeslices* t_P*-fit 13-28 and 2-exponential fit to wall source on timeslices* t_W*-fit 13-29. Hotelling p-value for the fit is 0.97, with extracted masses* am_n *and overlap coefficients* $A_{op,n}$ *shown in the table above. Grey band is the fitted ground-state mass (*am_0*). Yellow points are the axial data for reference only (i.e. not included in fit).*

The error on the fitted result is slightly smaller than the error on the data points entering the fit at early timeslices. The fit error grows towards larger timeslices but is less than half the error on the data points at greatest times. This is as expected, i.e. fit error is constrained more by the error on the most accurate data points entering the fit. Furthermore, the fit is to a fully correlated exponential decay over many timeslices, whereas the plot is an estimate of the effective mass $am_{\rm eff}$ timeslice by timeslice

$$am_{\rm eff}\left(t+\frac{1}{2}\right) = \ln C^{(2)}(t)/C^{(2)}(t+1)\,. \tag{3.15}$$

F1M kaon 2-point fit

In the case of the kaon, the effective energies and overlap coefficients are required at each Fourier momentum. As per the D_s, the point- and wall-source data are fitted separately at each momentum. However, for larger integer lattice momenta

n^2, the correlation function data have large statistical ripples and obtaining fit results which are insensitive to large fit range changes proves challenging. See fig 3.2 for a simultaneous fit to the kaon point- and wall-source data at $n^2 = 6$ – the largest integer Fourier momentum on this ensemble.

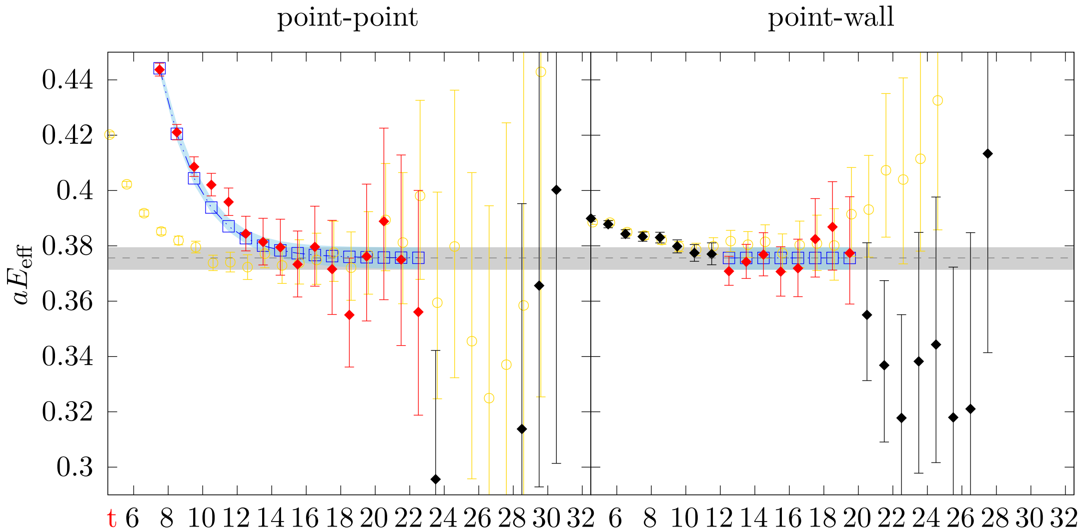

Figure 3.2 *Effective energy $aE_{\mathit{eff}} = \ln C^{(2)}(t+1)/C^{(2)}(t)$ vs t, for simultaneous fit to point- and wall-source kaon 2-point correlation function at a single integer lattice momentum $n^2 = 6$. The point-source data are fitted on timeslices $[7, 23]$ to a 2-state model, while the wall-source data are fitted on timeslices $[12, 20]$ to a 1-state model. The grey band shows the fitted ground state energy $aE_0 = 0.3756(40)$ with Hotelling p-value 0.57. Yellow points are the axial data for reference only (not included in fit). This F1M fit was not used in the final result.*

While there is no reason to expect that data on all ensembles should be described by the same dispersion relation, in practice it can. We performed a separate study which found that both the ground and first excited-state energies extracted from separate fits at each Fourier momenta are consistent with the lattice dispersion relation (2.2) on all ensembles. Results for this preliminary study are included at appendix A.8. We concluded that, while enforcing the use of the lattice dispersion relation in the kaon fits does introduce lattice artefacts into the analysis, the global fit includes terms which quantify discretisation effects, hence taking the chiral continuum limit nevertheless gives the correct result.

Thus, our global fit strategy is to perform separate simultaneous fits to the point- and wall-source data at each momentum in order to determine appropriate fit ranges. However, for the final kaon fit, the point-source data are simultaneously fitted at every momentum while imposing the lattice dispersion relation to constrain the energy levels at each non-zero momentum.

In order to bring the correlation matrix under control for this ensemble, it was necessary to thin the data, including every second timeslice from the zero-momentum correlation function in the fit and every third timeslice thereafter. Fit results are shown in fig 3.3.

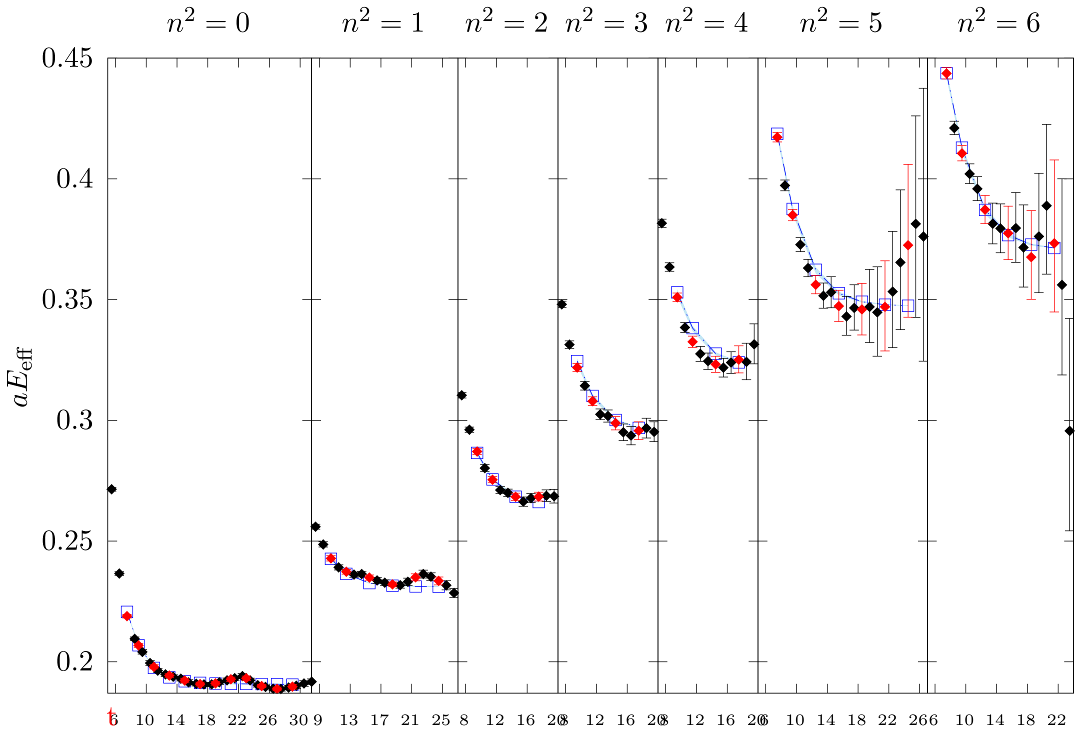

n^2	aE_0	aE_1	$A_{\mathrm{P},0}$	$A_{\mathrm{P},1}$	t-fit
0	0.19084(28)	0.643(20)	29.12(11)	77.2(5.3)	7;8-30:2
1	0.23109(23)	0.656(20)	29.20(11)	76.2(5.9)	10;11-26:3
2	0.26521(20)	0.668(19)	29.24(13)	73.9(5.1)	9;10-19:3
3	0.29534(18)	0.679(19)	28.90(16)	77.7(5.6)	9;10-19:3
4	0.32215(17)	0.691(18)	29.06(16)	73.9(5.1)	9;10-19:3
5	0.34724(15)	0.702(18)	28.65(22)	77.3(4.3)	7;8-26:3
6	0.37057(14)	0.713(18)	28.83(22)	75.2(4.3)	7;8-23:3

Figure 3.3 *Effective energy $aE_{\mathit{eff}} = \ln C^{(2)}(t+1)/C^{(2)}(t)$ vs t, for 2-point kaon correlation function fit on ensemble F1M. Simultaneous 2-exponential fit to point source correlation functions for all Fourier momenta on timeslices t-fit 7;8-30:2 ($n^2 = 0$), 10;11-26:3 ($n^2 = 1$), 9;10-19:3 ($n^2 = 2$), 9;10-19:3 ($n^2 = 3$), 9;10-19:3 ($n^2 = 4$), 7;8-26:3 ($n^2 = 5$) and 7;8-23:3 ($n^2 = 6$). Hotelling p-value for the fit is 0.128, with fitted energies aE_n and overlap coefficients $A_{op,n}$ shown in the table above.*

The following syntax was adopted to describe fit ranges. A fit range is a sequence of 1 or more, semicolon-separated sub-ranges of the form "t_{start}[-t_{end}[:n_{thin}]]". t_{start} is the starting timeslice and t_{end} is the optional ending timeslice in a range of timeslices. For a range, n_{thin} optionally indicates that every n_{thin}-th timeslice will be kept. For example, the fit ranges "7-9;11-17:3" and "7;8;9;11;14;17" are equivalent.

By including data points from each integer lattice momentum n^2, data points with widely varying relative error are included. The variance on the fitted result is most constrained by the most precise data points entering the fit. While at $n^2 = 0$ the variance of the fitted result is commensurate with that of the data, for $n^2 = 6$ the fit variance is much smaller than that of the data.

3.2.2 F1M matrix element $n^2 = 0$

The masses, energies and overlap coefficients for the D_s and kaon from the 2-state fits are then used in a simultaneous fit to R_3 (3.1) for multiple wall separations $\Delta T/a$. On this ensemble, doubly-excited states are included in the 3-point models, i.e. $N_{\text{exp}} = 3$ (3.4).

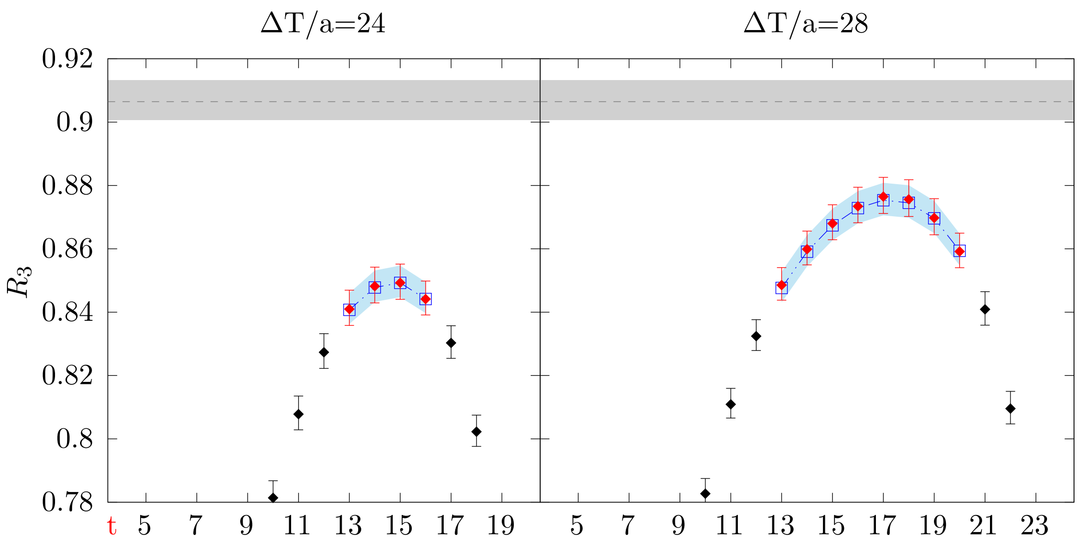

Figure 3.4 *Temporal component of mostly nonperturbatively renormalised ratio R_3 vs t, for $D_s \to K$ at $n^2 = 0$ on ensemble F1M. Simultaneous fit to wall separations $\Delta T/a$ 24 and 28 on timeslices 13-16 and 13-20, respectively. The grey band is the matrix element $\langle K|\gamma_4\left(n^2=0\right)|D_s\rangle = 0.9065(62)$. Hotelling p-value for the fit is 0.62, with excited-state matrix elements shown in table 3.1.*

The preferred fit is shown in fig 3.4, which is a simultaneous fit to the R_3 ratio (3.1) for wall separations $\Delta T/a \in \{24, 28\}$. Comparing the data points entering the fit (red) with the fit results (blue) we observe several indicators of high quality:

1. The central values of the fitted function coincide with the central values of the data within 1σ.
2. The excited-state model of R_3 matches the curvature of the data points within each wall separation. That is, a) there are fitted data points either side of the maximum within each wall separation; and b) there is no evidence of any significant bias away from the midpoints at either end of the two blue fit curves.
3. The excited-state model of R_3 models the effects of wall separation very well. That is, the multiple σ shift in the R_3 maximum between wall separations $\Delta T/a = 24$ and $\Delta T/a = 28$ (i.e. from $\sim$0.85 to $\sim$0.88, respectively, showing excited-state contamination at these wall separations) is tracked.

The dashed line with the grey error band at the top of fig 3.4 is the fit result for the ground-state matrix element. For large enough wall separations, we expect the peak in R_3 to asymptotically approach the ground-state matrix element. It is a feature of this finest ensemble that the R_3 ratio peak does not actually reach the ground-state matrix element determined by the fit, even for the largest wall separations $\Delta T/a = 32$.

For comparison with fig 3.4, a fit to wall separations $\Delta T/a \in \{28, 32\}$ is shown in fig 3.5. The value for the ground state matrix element from this fit is 0.9055(57), which is compatible with the preferred fit. In addition, the R_3 peak is closer to the ground state matrix element for $\Delta T/a = 32$ than $\Delta T/a = 28$ – i.e. excited-state contamination reduces asymptotically for larger wall separations, but excited-state contamination is still present.

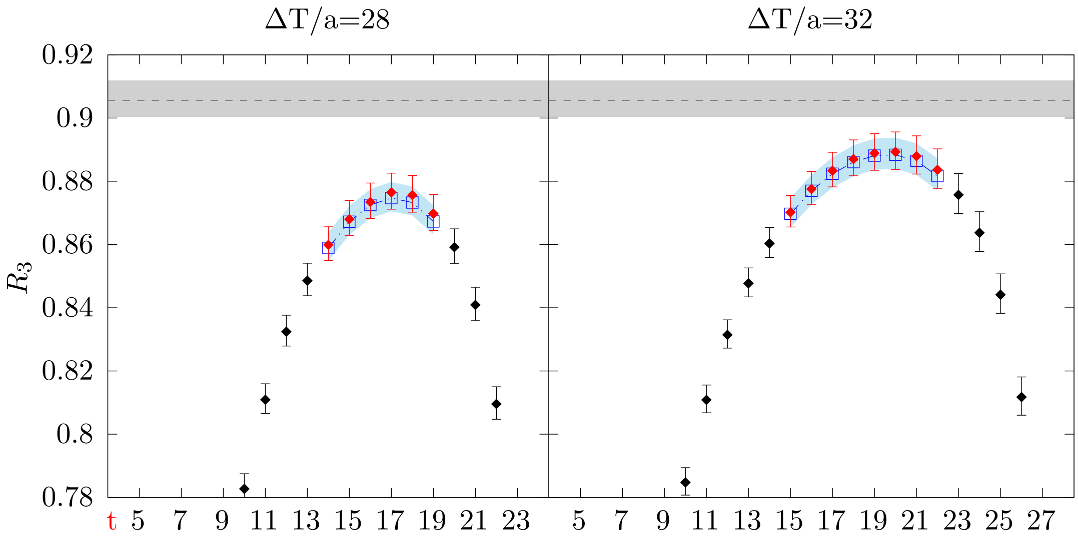

Figure 3.5 *Fit to wall separations $\Delta T/a \in \{28, 32\}$ on timeslices $[14, 19]$ and $[15, 22]$ respectively and otherwise as described in fig 3.4. The grey band shows the fitted result for $\langle K|\gamma_4\left(n^2=0\right)|D_s\rangle = 0.9055(57)$ (Hotelling p-value 0.96), compatible with the preferred fit, fig 3.4.*

From these two fit results, the value extracted for the ground state matrix element is certainly plausible, but it would be more convincing if we saw R_3 approach the ground state matrix element. For all other ensembles, R_3 approaches the matrix element for larger wall separations. The reader is invited to compare this fit with the equivalent for ensemble M1 in § 3.3.1 or indeed for any of the other ensembles in § 3.3.2, 3.3.3, 3.3.4 or 3.3.5.

The reason R_3 does not approach the matrix element on the fine ensemble is the lattice spacing. The maximum wall separation of $\Delta T/a = 32$, is 2.33 fm in physical units. Other ensembles show that R_3 does approach the ground state matrix element at around 2.65 fm, i.e. $\Delta T/a = 32$ on the medium ensembles and $\Delta T/a = 28$ on the coarse ensembles.

It is a strength of the work in this thesis that matrix elements are extracted from fits at narrower wall separations, thus ensuring the statistical variance of the fitted matrix elements is minimised. Nevertheless, by producing data for wider wall separations, fitted results can be directly compared with uncontaminated R_3 results to ensure the excited state modelling in the fits is correct.

3.2.3 F1M matrix elements $n^2 \neq 0$

For $n^2 \neq 0$, we have access to both the temporal and spatial matrix elements. Preferred fits for the temporal matrix elements for $n^2 \in \{1, 2, 3, 4, 5, 6\}$ are plotted in figures 3.6, 3.8, 3.10, 3.12, 3.14 and 3.16 respectively. Preferred fits for the spatial matrix elements for $n^2 \in \{1, 2, 3, 4, 5, 6\}$ are plotted in figures 3.7, 3.9, 3.11, 3.13, 3.15 and 3.17 respectively.

F1M matrix elements $n^2 = 1$

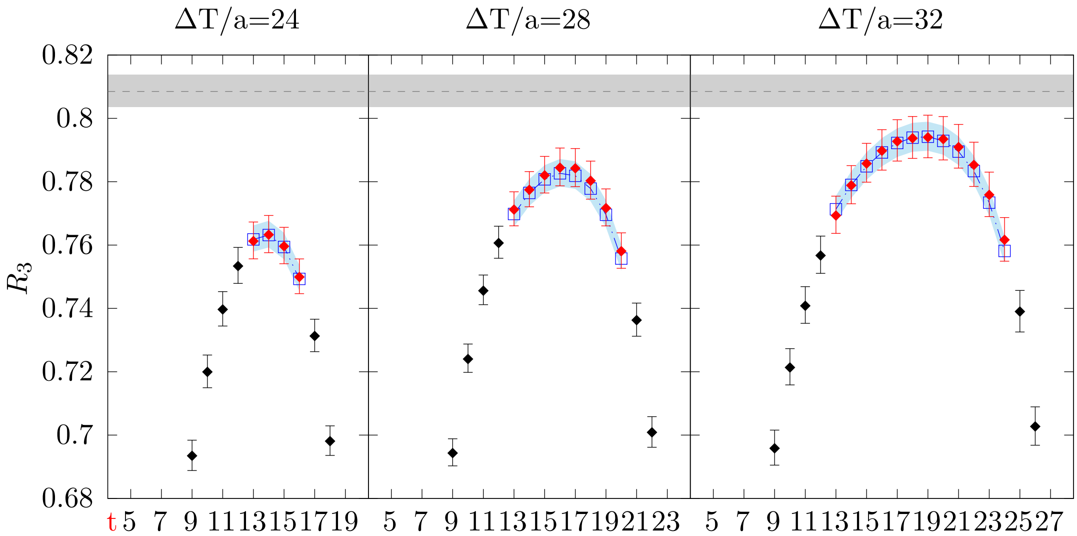

Figure 3.6 *Temporal component of mostly nonperturbatively renormalised ratio R_3 vs t, for $D_s \to K$ at $n^2 = 1$ on ensemble F1M. Simultaneous fit to wall separations $\Delta T/a$ 24, 28 and 32 on timeslices 13-16, 13-20 and 13-24, respectively. The grey band is the matrix element $\langle K|\gamma_4\left(n^2 = 1\right)|D_s\rangle = 0.8085(51)$. Hotelling p-value for the fit is 0.47, with excited-state matrix elements shown in table 3.1.*

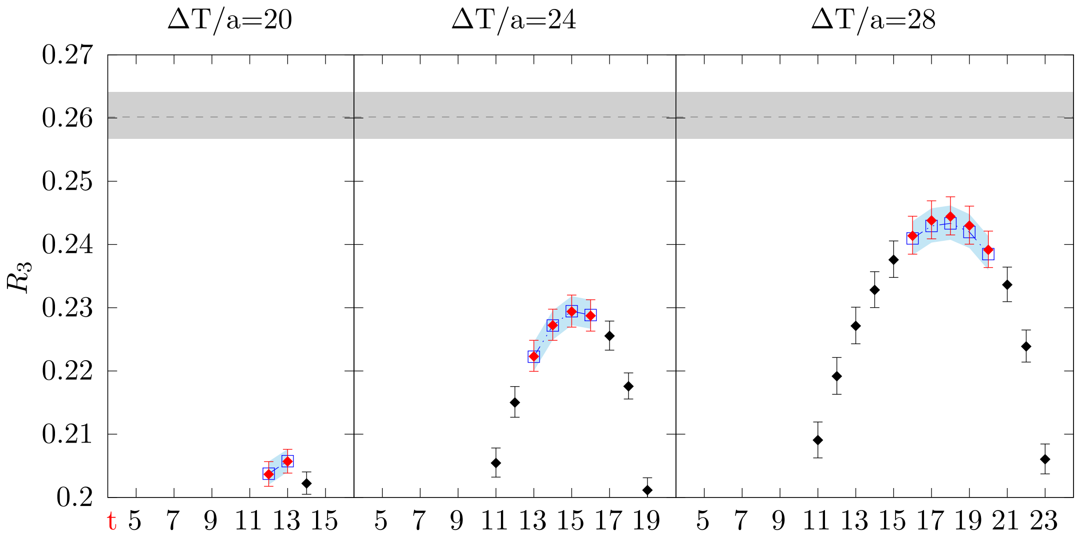

Figure 3.7 *Spatial component of mostly nonperturbatively renormalised ratio R_3 vs t, for $D_s \to K$ at $n^2 = 1$ on ensemble F1M. Simultaneous fit to wall separations $\Delta T/a$ 20, 24 and 28 on timeslices 12;13, 13-16 and 16-20, respectively. The grey band is the matrix element $\langle K|\gamma_i\left(n^2=1\right)|D_s\rangle = 0.2602(37)$. Hotelling p-value for the fit is 0.98, with excited-state matrix elements shown in table 3.1.*

F1M matrix elements $n^2 = 2$

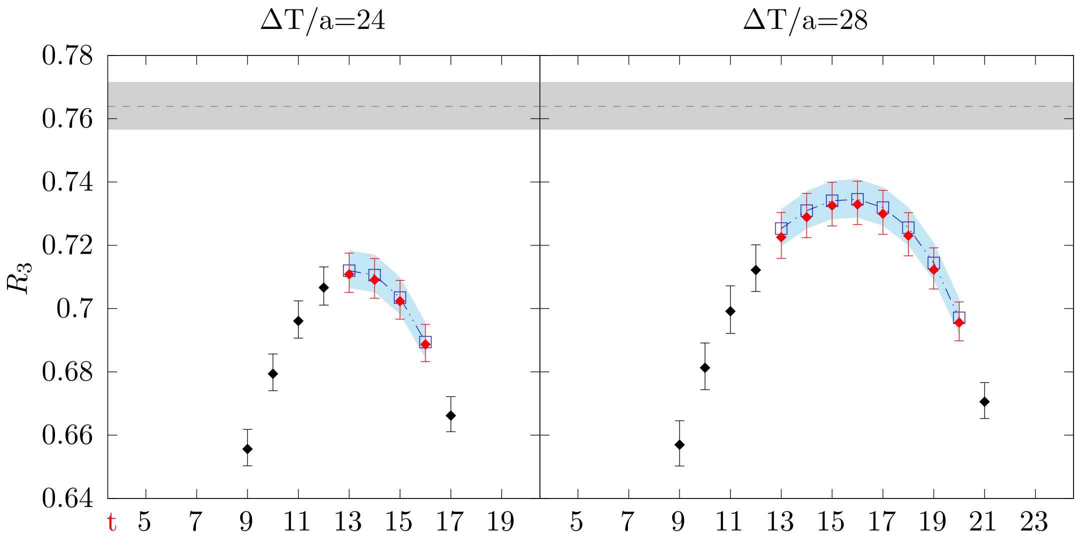

Figure 3.8 *Temporal component of mostly nonperturbatively renormalised ratio R_3 vs t, for $D_s \to K$ at $n^2 = 2$ on ensemble F1M. Simultaneous fit to wall separations $\Delta T/a$ 24 and 28 on timeslices 13-16 and 13-20, respectively. The grey band is the matrix element $\langle K|\gamma_4\left(n^2=2\right)|D_s\rangle = 0.7639(74)$. Hotelling p-value for the fit is 0.89, with excited-state matrix elements shown in table 3.1.*

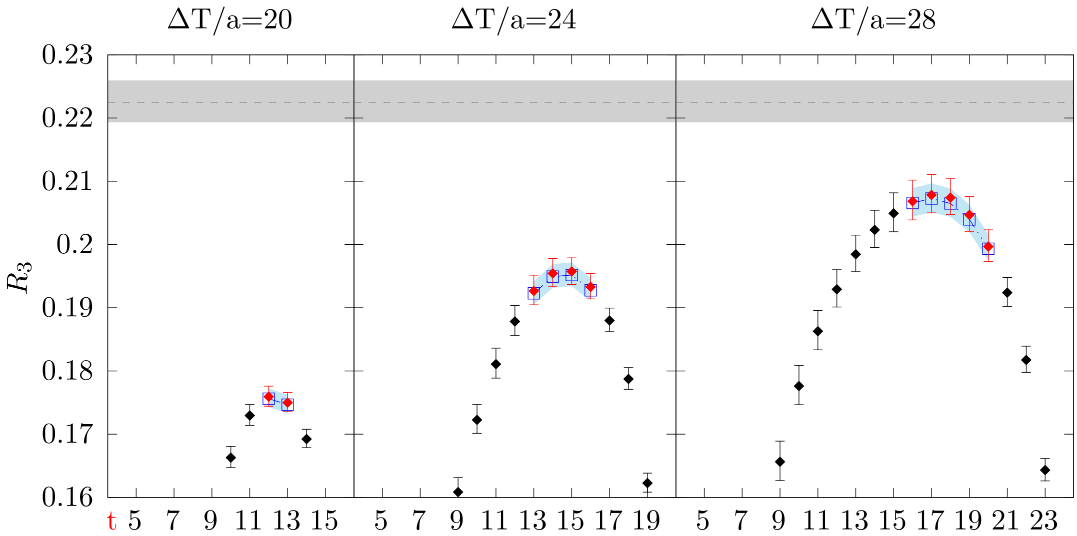

Figure 3.9 *Spatial component of mostly nonperturbatively renormalised ratio R_3 vs t, for $D_s \to K$ at $n^2 = 2$ on ensemble F1M. Simultaneous fit to wall separations $\Delta T/a$ 20, 24 and 28 on timeslices 12;13, 13-16 and 16-20, respectively. The grey band is the matrix element $\langle K|\gamma_i\left(n^2=2\right)|D_s\rangle = 0.2225(33)$. Hotelling p-value for the fit is 0.93, with excited-state matrix elements shown in table 3.1.*

F1M matrix elements $n^2 = 3$

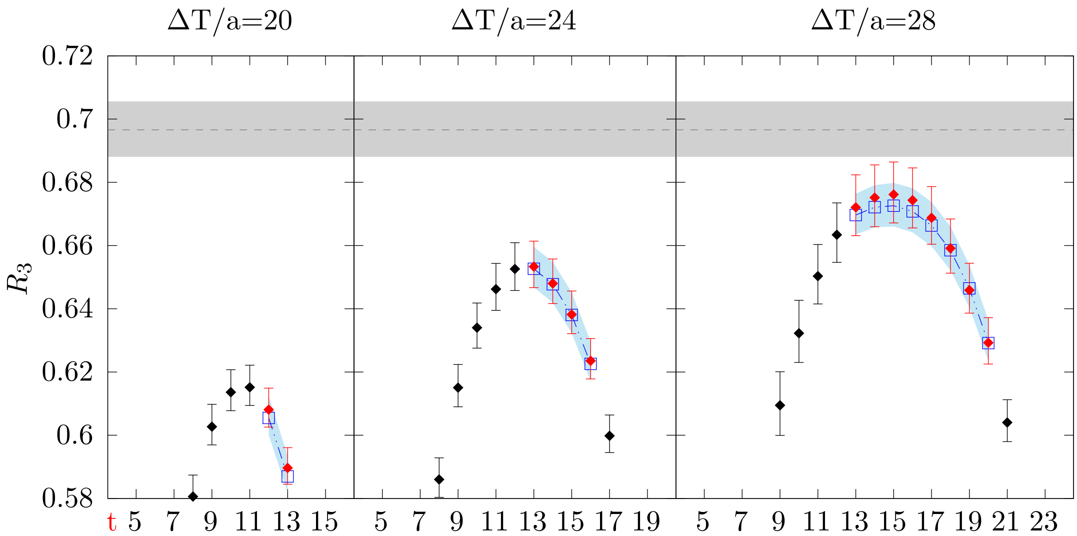

Figure 3.10 *Temporal component of mostly nonperturbatively renormalised ratio R_3 vs t, for $D_s \to K$ at $n^2 = 3$ on ensemble F1M. Simultaneous fit to wall separations $\Delta T/a$ 20, 24 and 28 on timeslices 12;13, 13-16 and 13-20, respectively. The grey band is the matrix element $\langle K|\gamma_4\left(n^2=3\right)|D_s\rangle = 0.6966(87)$. Hotelling p-value for the fit is 0.64, with excited-state matrix elements shown in table 3.1.*

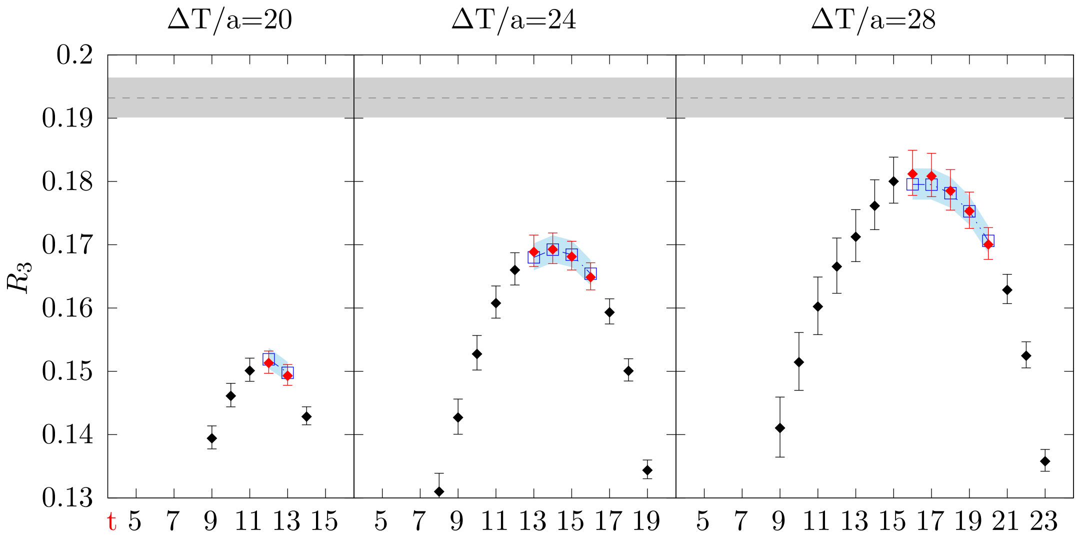

Figure 3.11 *Spatial component of mostly nonperturbatively renormalised ratio R_3 vs t, for $D_s \to K$ at $n^2 = 3$ on ensemble F1M. Simultaneous fit to wall separations $\Delta T/a$ 20, 24 and 28 on timeslices 12;13, 13-16 and 16-20, respectively. The grey band is the matrix element $\langle K|\gamma_i\left(n^2=3\right)|D_s\rangle = 0.1932(31)$. Hotelling p-value for the fit is 0.69, with excited-state matrix elements shown in table 3.1.*

F1M matrix elements $n^2 = 4$

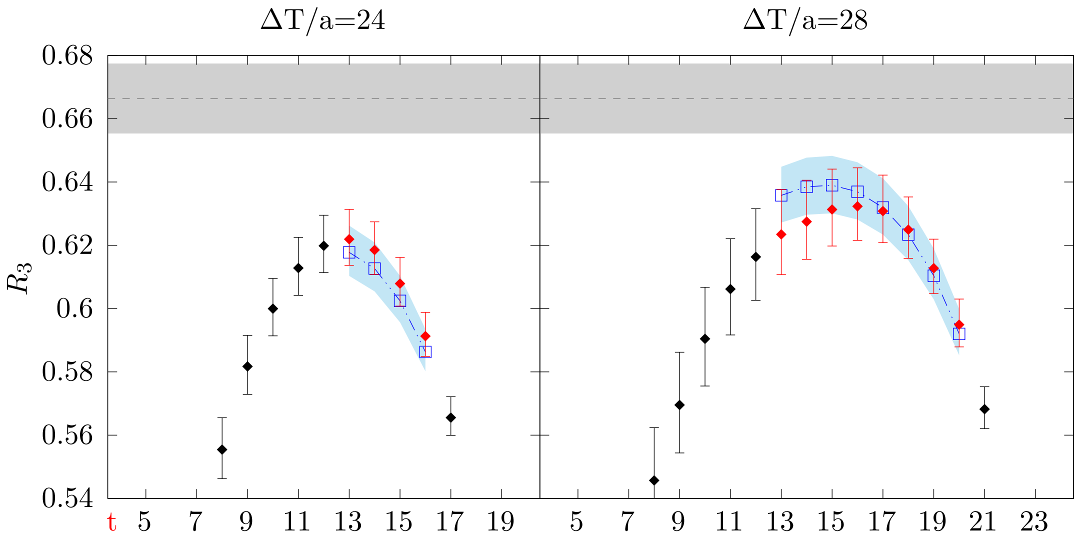

Figure 3.12 *Temporal component of mostly nonperturbatively renormalised ratio R_3 vs t, for $D_s \to K$ at $n^2 = 4$ on ensemble F1M. Simultaneous fit to wall separations $\Delta T/a$ 24 and 28 on timeslices 13-16 and 13-20, respectively. The grey band is the matrix element $\langle K|\gamma_4\left(n^2=4\right)|D_s\rangle = 0.666(11)$. Hotelling p-value for the fit is 0.30, with excited-state matrix elements shown in table 3.1.*

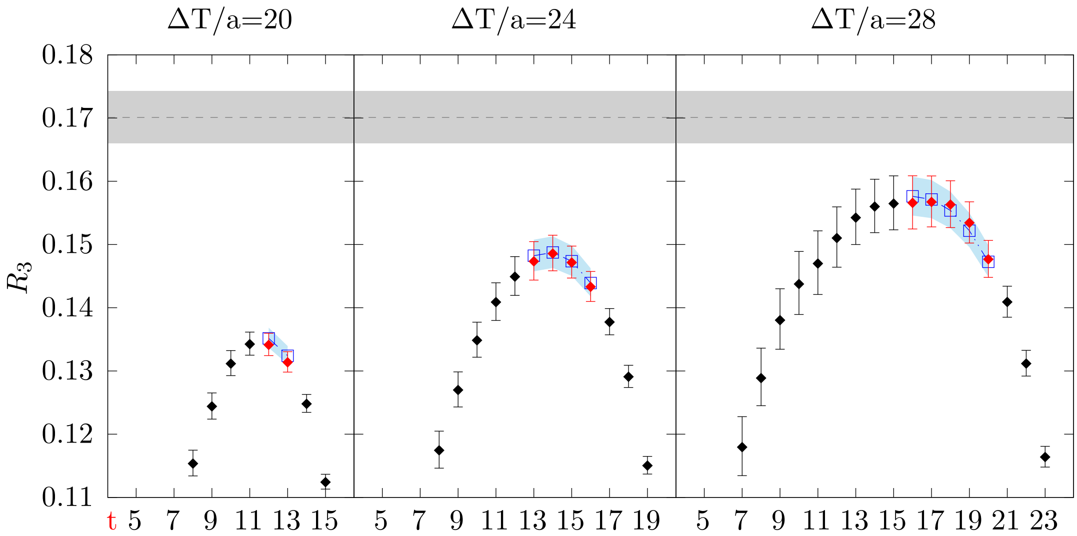

Figure 3.13 *Spatial component of mostly nonperturbatively renormalised ratio R_3 vs t, for $D_s \to K$ at $n^2 = 4$ on ensemble F1M. Simultaneous fit to wall separations $\Delta T/a$ 20, 24 and 28 on timeslices 12;13, 13-16 and 16-20, respectively. The grey band is the matrix element $\langle K|\gamma_i \left(n^2 = 4\right)|D_s\rangle = 0.1701(41)$. Hotelling p-value for the fit is 0.57, with excited-state matrix elements shown in table 3.1.*

F1M matrix elements $n^2 = 5$

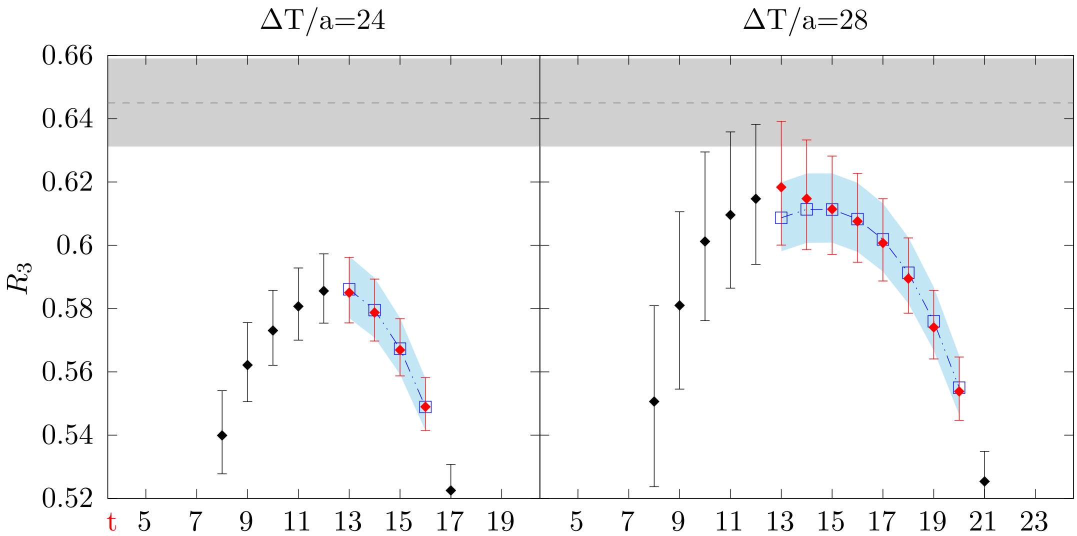

Figure 3.14 *Temporal component of mostly nonperturbatively renormalised ratio R_3 vs t, for $D_s \to K$ at $n^2 = 5$ on ensemble F1M. Simultaneous fit to wall separations $\Delta T/a$ 24 and 28 on timeslices 13-16 and 13-20, respectively. The grey band is the matrix element $\langle K|\gamma_4 \left(n^2 = 5\right)|D_s\rangle = 0.645(14)$. Hotelling p-value for the fit is 0.98, with excited-state matrix elements shown in table 3.1.*

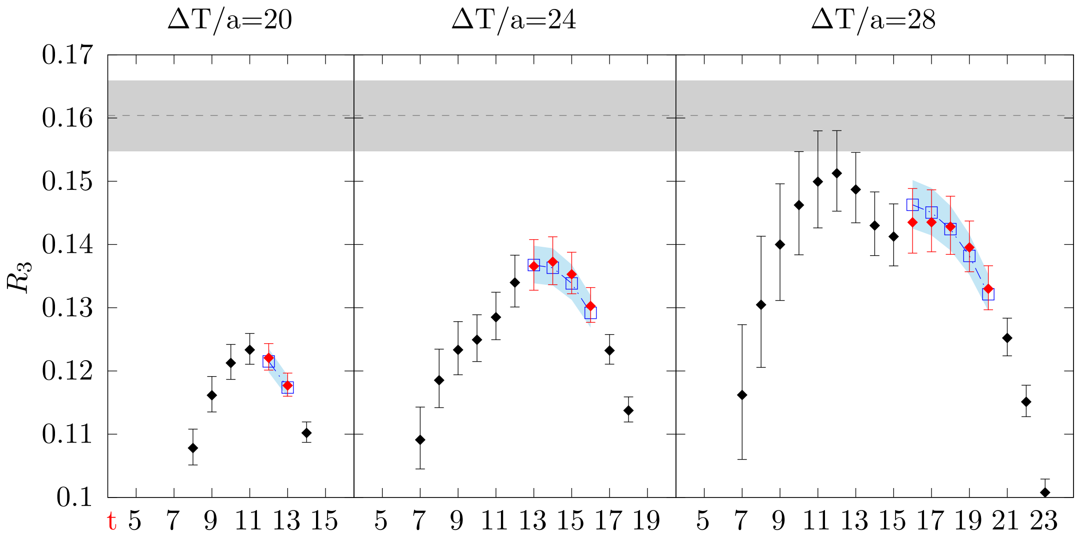

Figure 3.15 *Spatial component of mostly nonperturbatively renormalised ratio R_3 vs t, for $D_s \to K$ at $n^2 = 5$ on ensemble F1M. Simultaneous fit to wall separations $\Delta T/a$ 20, 24 and 28 on timeslices 12;13, 13-16 and 16-20, respectively. The grey band is the matrix element $\langle K|\gamma_i\left(n^2=5\right)|D_s\rangle = 0.1604(56)$. Hotelling p-value for the fit is 0.89, with excited-state matrix elements shown in table 3.1.*

F1M matrix elements $n^2 = 6$

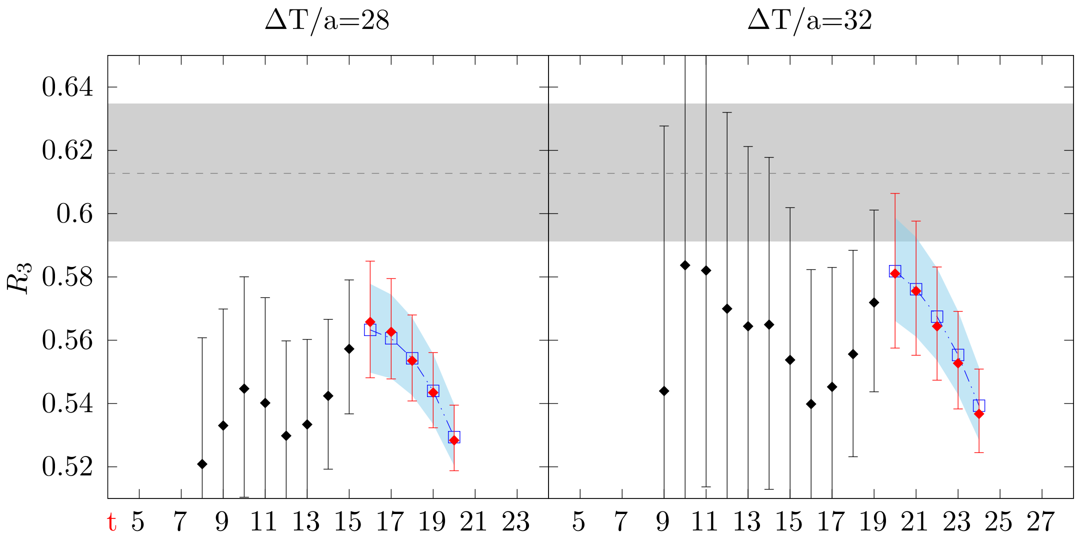

Figure 3.16 *Temporal component of mostly nonperturbatively renormalised ratio R_3 vs t, for $D_s \to K$ at $n^2 = 6$ on ensemble F1M. Simultaneous fit to wall separations $\Delta T/a$ 28 and 32 on timeslices 16-20 and 20-24, respectively. The grey band is the matrix element $\langle K|\gamma_4\left(n^2=6\right)|D_s\rangle = 0.613(22)$. Hotelling p-value for the fit is 0.43, with excited-state matrix elements shown in table 3.1.*

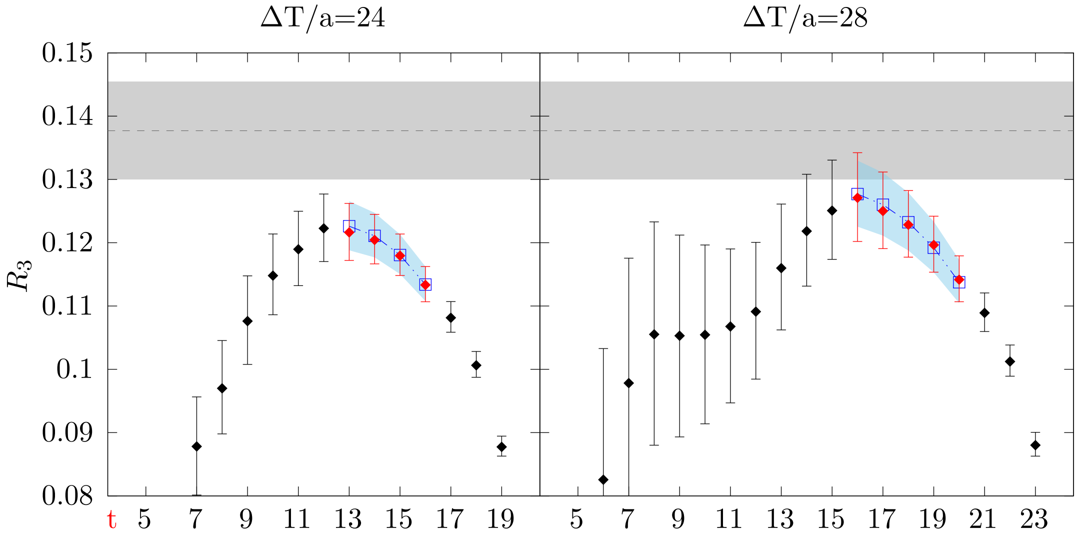

Figure 3.17 *Spatial component of mostly nonperturbatively renormalised ratio* R_3 *vs* t*, for* $D_s \to K$ *at* $n^2 = 6$ *on ensemble F1M. Simultaneous fit to wall separations* $\Delta T/a$ *24 and 28 on timeslices 13-16 and 16-20, respectively. The grey band is the matrix element* $\langle K|\gamma_i\left(n^2=6\right)|D_s\rangle = 0.1377(77)$*. Hotelling p-value for the fit is 0.99, with excited-state matrix elements shown in table 3.1.*

3.3 Matrix element results other ensembles

Results for the 2-point correlation function fits and matrix element fits at zero momentum are presented in the following subsections. Figures showing the matrix element fits at non-zero momenta for ensembles M1, M2, M3, C1 and C2 are deferred to appendices A.1 to A.5, respectively. A summary of results for matrix elements at all momenta on all ensembles is presented in § 3.4.

3.3.1 Ensemble M1 fit results

Results for 2-point function and matrix element fits are presented below.

M1 two point functions

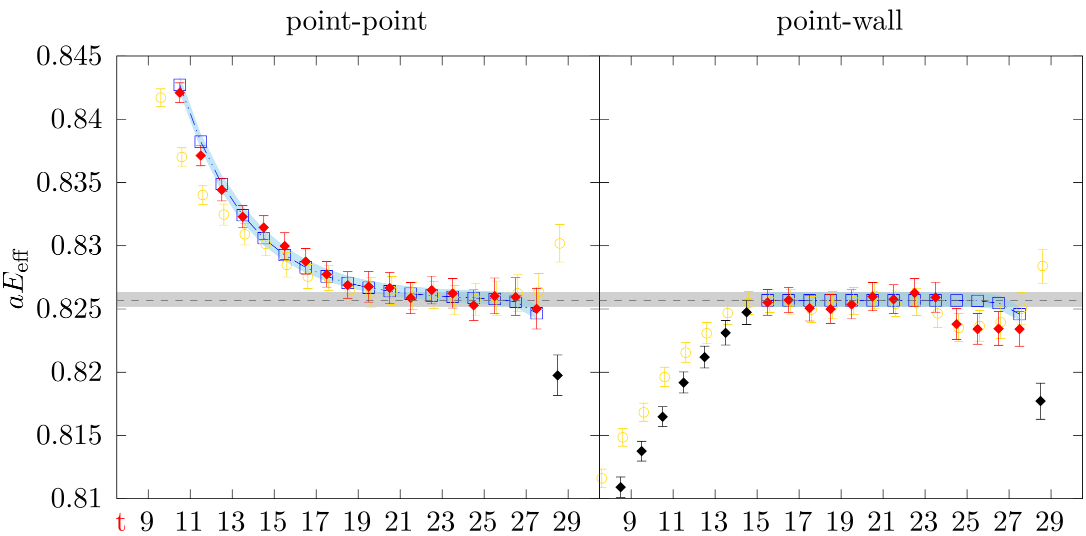

p-val	am_0	am_1	t_{P}-fit	$A_{\text{P},0}$	$A_{\text{P},1}$	t_{W}-fit	$A_{\text{W},0}$
0.71	0.82568(57)	1.146(37)	10-28	31.96(24)	48.0(7.2)	15-28	25243(190)

Figure 3.18 *Effective mass* $am_{\textit{eff}}\left(t+\frac{1}{2}\right) = \ln C^{(2)}(t)/C^{(2)}(t+1)$ *vs* t*, for 2-point* D_s *correlation function fit on ensemble M1. Simultaneous 2-exponential fit to point source on timeslices* t_P*-fit 10-28 and 1-exponential fit to wall source on timeslices* t_W*-fit 15-28. Hotelling p-value for the fit is 0.71, with extracted masses* am_n *and overlap coefficients* $A_{op,n}$ *shown in the table above. Grey band is the fitted ground-state mass (*am_0*). Yellow points are the axial data for reference only (i.e. not included in fit).*

The same procedure is followed for the D_s on this and subsequent ensembles as for the F1M ensemble, except that for the wall-source, we fit to a single-exponential model. The largest region possible is fitted while still maintaining fit stability for small variations of fit ranges. The results of the preferred fit for the D_s on ensemble M1 is shown in fig 3.18.

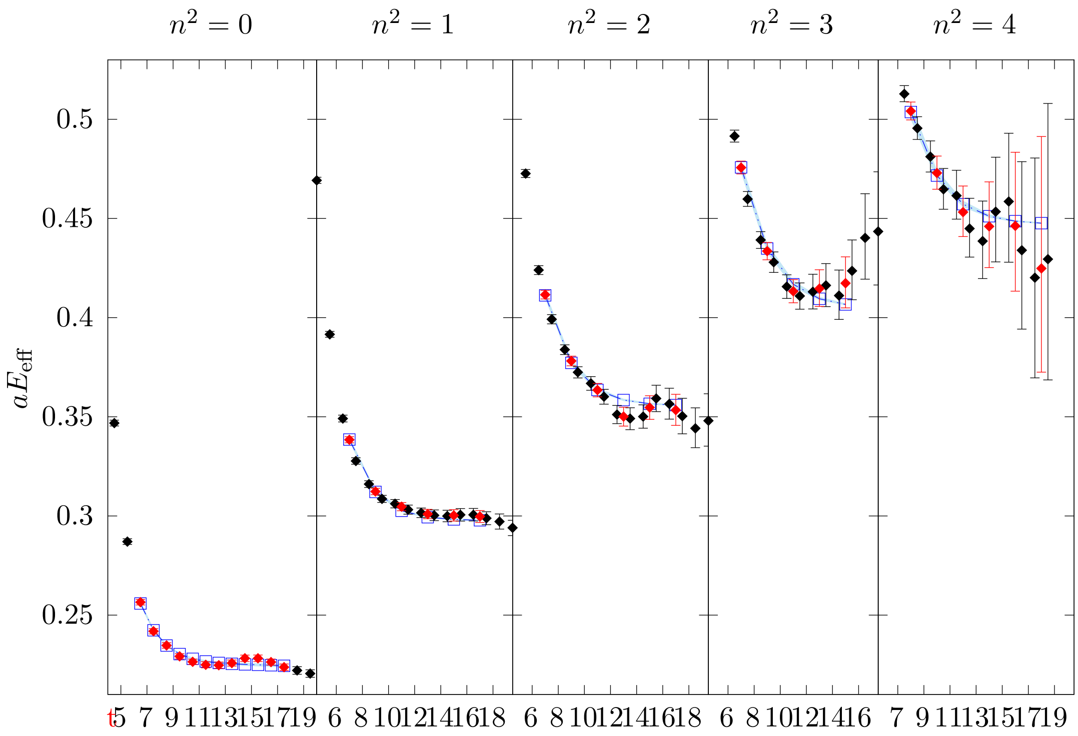

n^2	aE_0	aE_1	$A_{\text{P},0}$	$A_{\text{P},1}$	t-fit
0	0.22506(78)	0.826(34)	21.47(18)	66.9(6.7)	6-18
1	0.29772(59)	0.846(33)	21.22(16)	67.8(6.6)	6-18:2
2	0.35551(49)	0.866(32)	21.22(19)	68.1(6.4)	6-18:2
3	0.40485(43)	0.886(32)	21.01(23)	68.6(6.2)	6-16:2
4	0.44695(38)	0.904(31)	21.00(24)	69.0(7.0)	7-19:2

Figure 3.19 *Effective energy* $aE_{\mathit{eff}} = \ln C^{(2)}(t+1)/C^{(2)}(t)$ *vs* t*, for 2-point kaon correlation function fit on ensemble M1. Simultaneous 2-exponential fit to point source correlation functions for all Fourier momenta on timeslices t-fit 6-18 (*$n^2 = 0$*), 6-18:2 (*$n^2 = 1$*), 6-18:2 (*$n^2 = 2$*), 6-16:2 (*$n^2 = 3$*) and 7-19:2 (*$n^2 = 4$*). Hotelling p-value for the fit is 0.454, with fitted energies* aE_n *and overlap coefficients* $A_{op,n}$ *shown in the table above.*

The same procedure is followed for the kaon fit as for the F1M ensemble. However, with fewer data points in the fit, we do not need to thin the data for $n^2 = 0$. Results of the preferred fit for the kaon on ensemble M1 are shown in fig 3.19.

M1 matrix elements

Whereas on the fine ensemble the maximum wall separation $T/a = 32$ was 2.33 fm, on the medium ensembles, the same integer wall separation in lattice units is a physical length of 2.65 fm. The same procedure is followed on the medium and coarse ensembles as for F1M, but there is unambiguous access to a plateau in R_3 and/or smaller wall separations (in integer lattice units).

The preferred fit for the temporal vector current at $n^2 = 0$ is shown in fig 3.20. For larger wall separations, R_3 approaches the ground state matrix element.

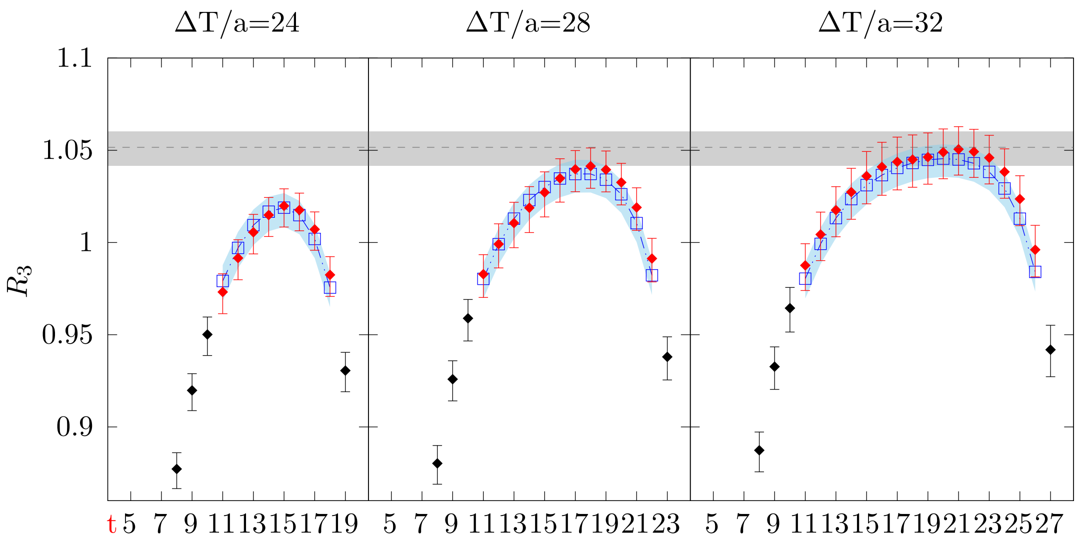

Figure 3.20 *Temporal component of mostly nonperturbatively renormalised ratio R_3 vs t, for $D_s \to K$ at $n^2 = 0$ on ensemble M1. Simultaneous fit to wall separations $\Delta T/a$ 24, 28 and 32 on timeslices 11-18, 11-22 and 11-26, respectively. The grey band is the matrix element $\langle K|\gamma_4\left(n^2 = 0\right)|D_s\rangle = 1.0516(93)$. Hotelling p-value for the fit is 0.555, with excited-state matrix elements shown in table 3.2.*

Matrix element fits for non-zero momenta are included in appendix A.1.

3.3.2 Ensemble M2 fit results

Following the same procedure as for previous ensembles, the results for ensemble M2 of the preferred fit for the kaon are shown in fig 3.21, for the D_s in fig 3.22 and for the matrix element of the temporal component of the vector current at $n^2 = 0$ in fig 3.23. Matrix element fits for non-zero momenta are included in appendix A.2.

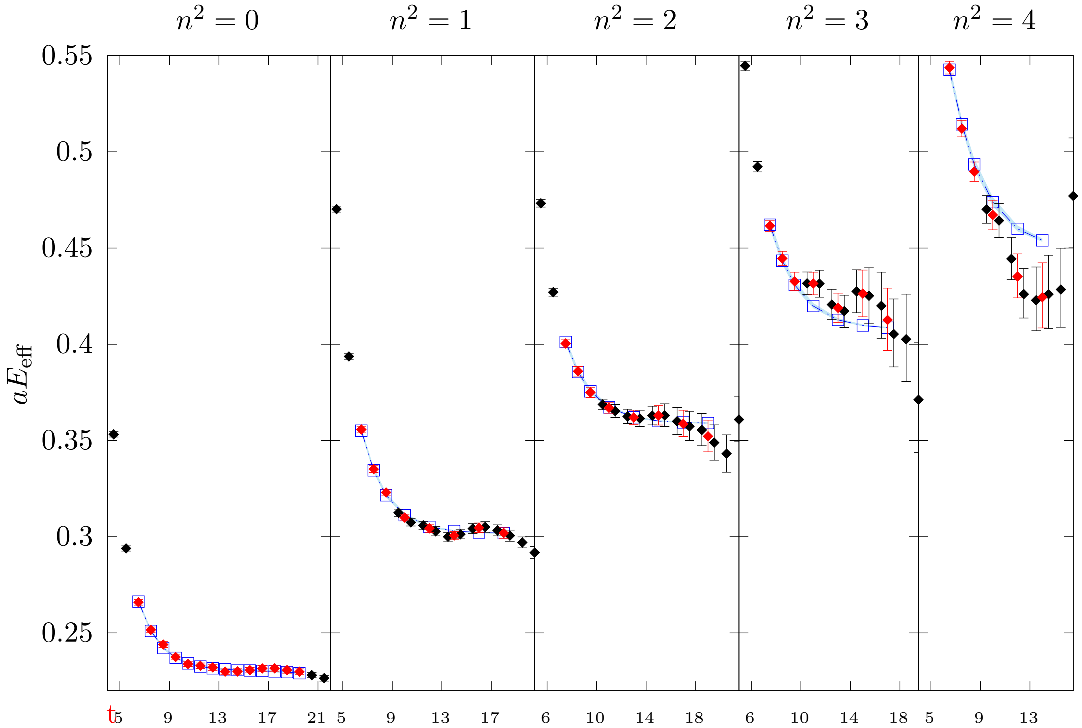

n^2	aE_0	aE_1	$A_{\text{P},0}$	$A_{\text{P},1}$	t-fit
0	0.23052(59)	0.814(29)	21.30(12)	67.6(5.7)	6-20
1	0.30184(45)	0.834(28)	21.33(13)	66.4(5.3)	6-9;11-19:2
2	0.35895(37)	0.855(27)	21.37(13)	64.3(5.3)	7-10;12-20:2
3	0.40785(33)	0.874(26)	21.21(17)	64.6(5.2)	7-10;12-18:2
4	0.44965(29)	0.893(26)	21.30(22)	65.1(4.5)	6-9;11-15:2

Figure 3.21 *Effective energy $aE_{eff} = \ln C^{(2)}(t+1)/C^{(2)}(t)$ vs t, for 2-point kaon correlation function fit on ensemble M2. Simultaneous 2-exponential fit to point source correlation functions for all Fourier momenta on timeslices t-fit 6-20 ($n^2 = 0$), 6-9;11-19:2 ($n^2 = 1$), 7-10;12-20:2 ($n^2 = 2$), 7-10;12-18:2 ($n^2 = 3$) and 6-9;11-15:2 ($n^2 = 4$). Hotelling p-value for the fit is 0.643, with fitted energies aE_n and overlap coefficients $A_{op,n}$ shown in the table above.*

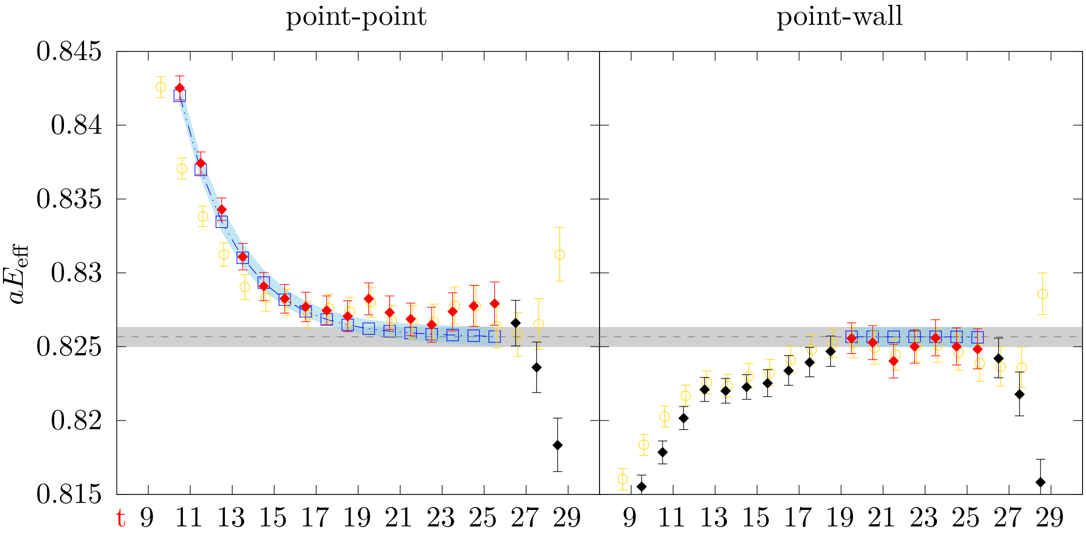

p-val	am_0	am_1	$t_{\rm P}$-fit	$A_{\rm P,0}$	$A_{\rm P,1}$	$t_{\rm W}$-fit	$A_{\rm W,0}$
0.078	0.82567(68)	1.207(59)	10-26	32.06(28)	61(15)	19-26	25206(250)

Figure 3.22 *Effective mass* $am_{\mathit{eff}}\left(t+\frac{1}{2}\right) = \ln C^{(2)}\left(t\right)/C^{(2)}\left(t+1\right)$ *vs* t*, for 2-point* D_s *correlation function fit on ensemble M2. Simultaneous 2-exponential fit to point source on timeslices* t_P*-fit 10-26 and 1-exponential fit to wall source on timeslices* t_W*-fit 19-26. Hotelling p-value for the fit is 0.078, with extracted masses* am_n *and overlap coefficients* $A_{op,n}$ *shown in the table above. Grey band is the fitted ground-state mass (*am_0*). Yellow points are the axial data for reference only (i.e. not included in fit).*

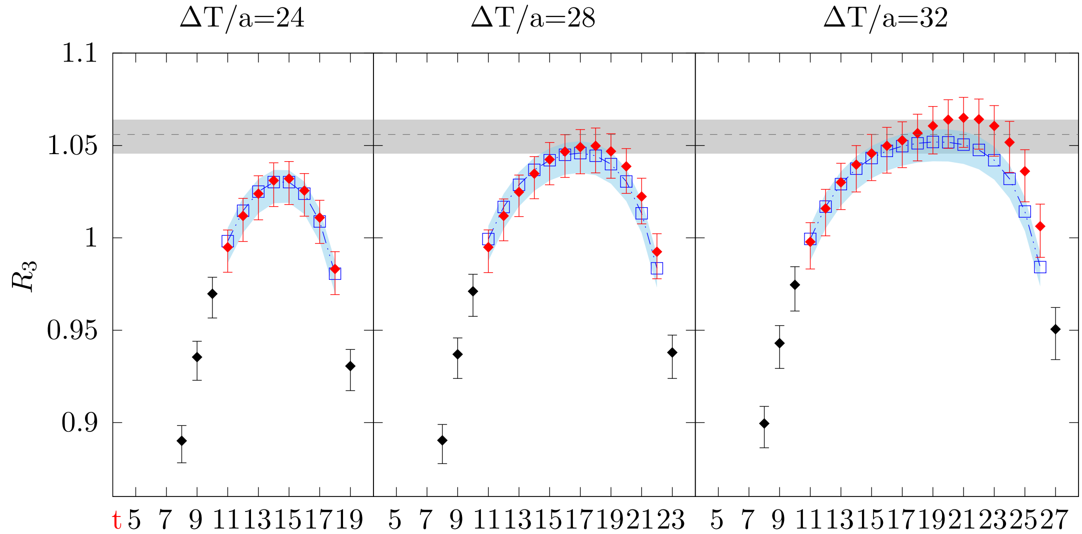

Figure 3.23 *Temporal component of mostly nonperturbatively renormalised ratio* R_3 *vs* t*, for* $D_s \to K$ *at* $n^2 = 0$ *on ensemble M2. Simultaneous fit to wall separations* $\Delta T/a$ *24, 28 and 32 on timeslices 11-18, 11-22 and 11-26, respectively. The grey band is the matrix element* $\langle K|\gamma_4\left(n^2=0\right)|D_s\rangle = 1.0559(92)$*. Hotelling p-value for the fit is 0.488, with excited-state matrix elements shown in table 3.3.*

3.3.3 Ensemble M3 fit results

Following the same procedure as for previous ensembles, the results for ensemble M3 of the preferred fit for the kaon are shown in fig 3.24, for the D_s in fig 3.25 and for the matrix element of the temporal component of the vector current at $n^2 = 0$ in fig 3.26. Matrix element fits for non-zero momenta are included in appendix A.3.

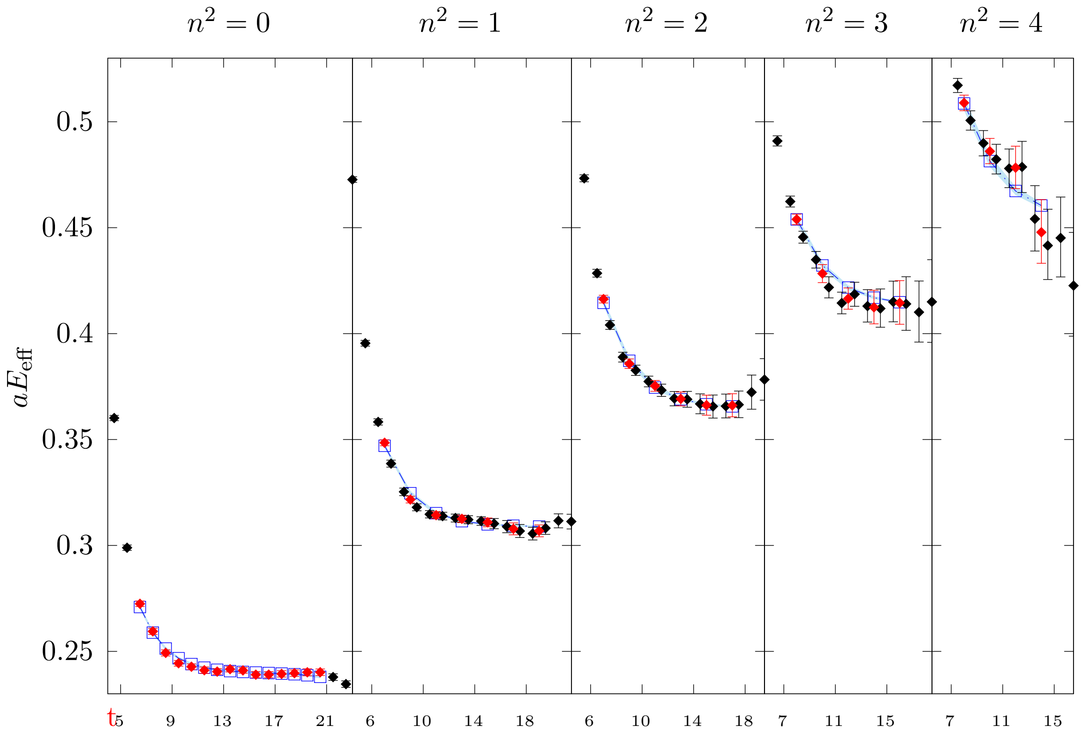

n^2	aE_0	aE_1	$A_{P,0}$	$A_{P,1}$	t-fit
0	0.23988(64)	0.758(32)	22.34(16)	53.7(5.0)	6-21
1	0.30901(49)	0.780(31)	22.29(15)	53.8(4.8)	6-20:2
2	0.36496(42)	0.802(30)	22.25(18)	53.9(4.5)	6-18:2
3	0.41312(36)	0.824(29)	22.11(19)	53.0(4.9)	7-17:2
4	0.45440(33)	0.843(28)	21.78(28)	56.1(4.6)	7-15:2

Figure 3.24 *Effective energy* $aE_{\text{eff}} = \ln C^{(2)}(t+1)/C^{(2)}(t)$ *vs t, for 2-point kaon correlation function fit on ensemble M3. Simultaneous 2-exponential fit to point source correlation functions for all Fourier momenta on timeslices t-fit 6-21 ($n^2 = 0$), 6-20:2 ($n^2 = 1$), 6-18:2 ($n^2 = 2$), 7-17:2 ($n^2 = 3$) and 7-15:2 ($n^2 = 4$). Hotelling p-value for the fit is 0.68, with fitted energies* aE_n *and overlap coefficients* $A_{op,n}$ *shown in the table above.*

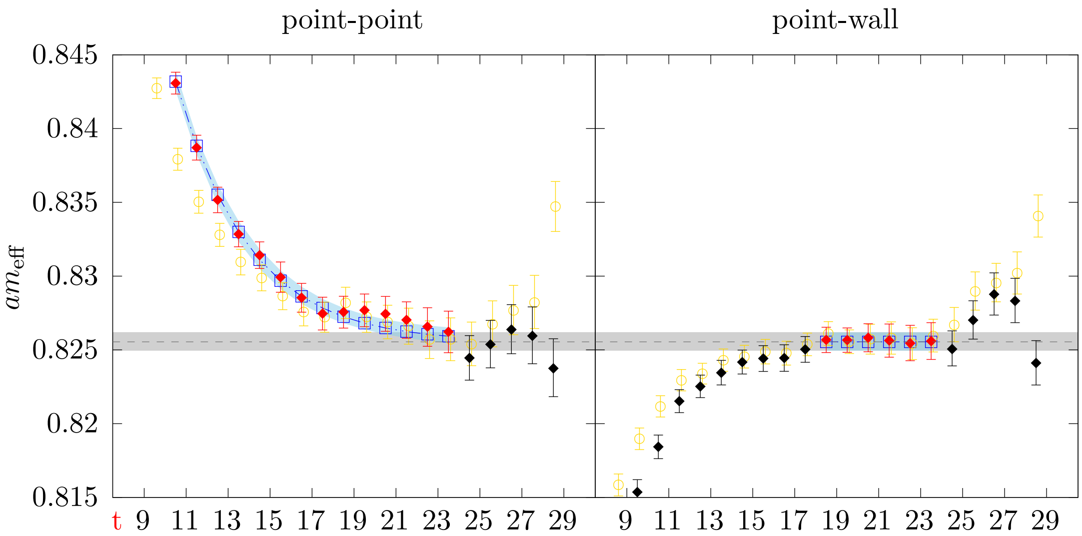

p-val	am_0	am_1	t_{P}-fit	$A_{\text{P},0}$	$A_{\text{P},1}$	t_{W}-fit	$A_{\text{W},0}$
1.00	0.82554(62)	1.125(35)	10-24	31.95(26)	44.8(6.1)	18-24	24945(220)

Figure 3.25 *Effective mass* $am_{\mathit{eff}}\left(t+\frac{1}{2}\right) = \ln C^{(2)}(t)/C^{(2)}(t+1)$ *vs* t*, for 2-point* D_s *correlation function fit on ensemble M3. Simultaneous 2-exponential fit to point source on timeslices* t_P*-fit 10-24 and 1-exponential fit to wall source on timeslices* t_W*-fit 18-24. Hotelling p-value for the fit is 1.00, with extracted masses* am_n *and overlap coefficients* $A_{op,n}$ *shown in the table above. Grey band is the fitted ground-state mass (*am_0*). Yellow points are the axial data for reference only (i.e. not included in fit).*

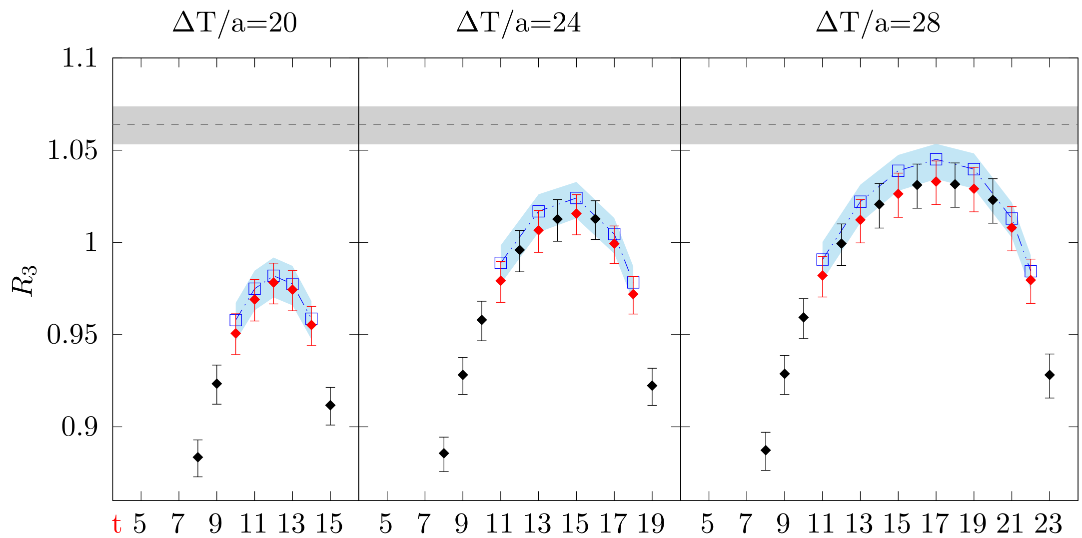

Figure 3.26 *Temporal component of mostly nonperturbatively renormalised ratio* R_3 *vs* t*, for* $D_s \to K$ *at* $n^2 = 0$ *on ensemble M3. Simultaneous fit to wall separations* $\Delta T/a$ *20, 24 and 28 on timeslices 10-14, 11-17:2;18 and 11-21:2;22, respectively. The grey band is the matrix element* $\langle K|\gamma_4\left(n^2=0\right)|D_s\rangle = 1.064(10)$*. Hotelling p-value for the fit is 0.64, with excited-state matrix elements shown in table 3.4.*

3.3.4 Ensemble C1 fit results

Following the same procedure as for previous ensembles, the results of the preferred fit for the D_s on ensemble C1 are shown in fig 3.27.

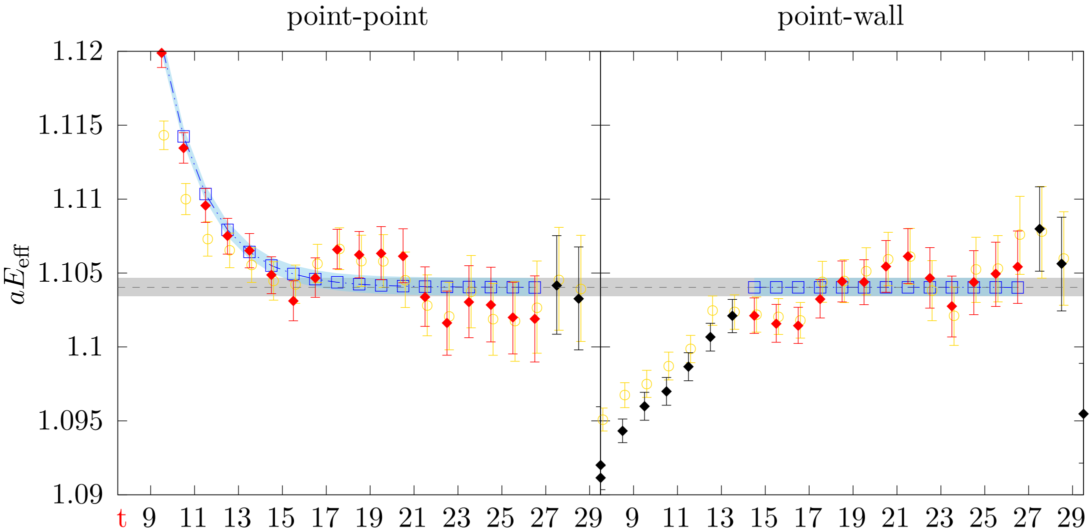

p-val	am_0	am_1	t_{P}-fit	$A_{\text{P},0}$	$A_{\text{P},1}$	t_{W}-fit	$A_{\text{W},0}$
0.623	1.10403(61)	1.593(14)	6-27	35.45(22)	80.6(2.6)	14-27	12980(100)

Figure 3.27 *Effective mass* $am_{\text{eff}}\left(t+\frac{1}{2}\right) = \ln C^{(2)}(t)/C^{(2)}(t+1)$ *vs* t*, for 2-point* D_s *correlation function fit on ensemble C1. Simultaneous 2-exponential fit to point source on timeslices* t_{P}*-fit 6-27 and 1-exponential fit to wall source on timeslices* t_{W}*-fit 14-27. Hotelling p-value for the fit is 0.623, with extracted masses* am_n *and overlap coefficients* $A_{op,n}$ *shown in the table above. Grey band is the fitted ground-state mass (*am_0*). Yellow points are the axial data for reference only (i.e. not included in fit).*

The same procedure is followed for the kaon fit as for previous ensembles, however, statistics are such ($n' = 160$ independent samples, the largest across all our ensembles) that there is no need to thin the data.

The results of the preferred fit for the kaon on ensemble C1 is shown in fig 3.28.

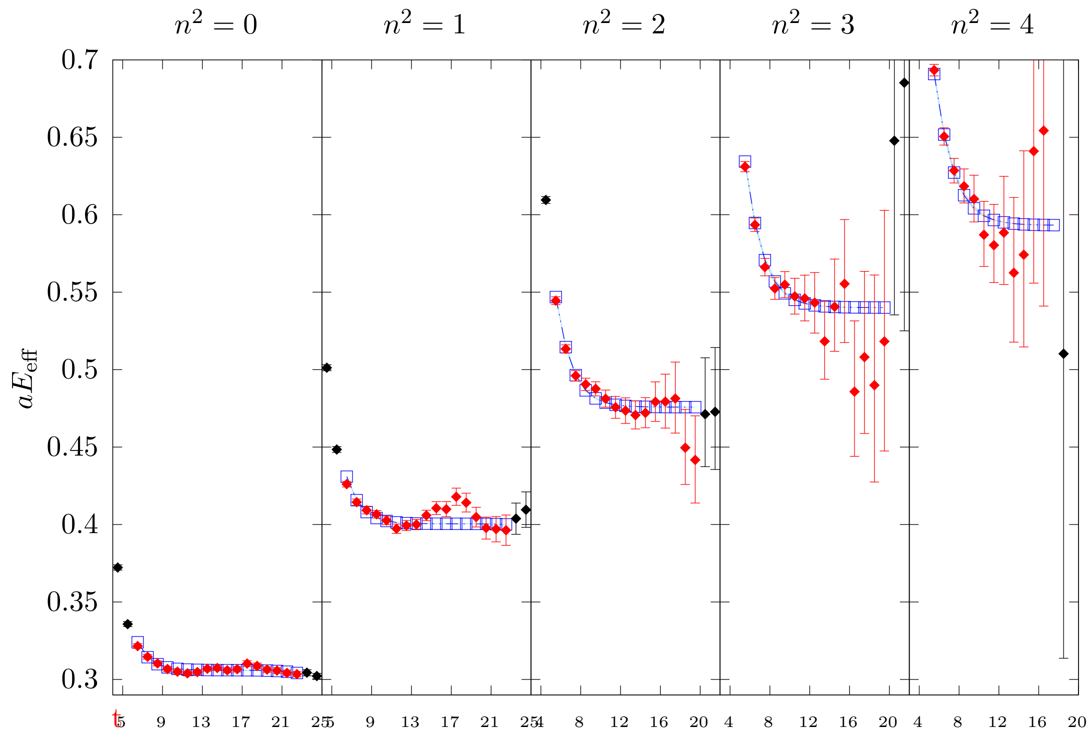

n^2	aE_0	aE_1	$A_{\text{P},0}$	$A_{\text{P},1}$	t-fit
0	0.30601(47)	1.087(32)	24.15(11)	87.3(7.9)	6-23
1	0.40046(35)	1.112(31)	24.05(14)	84.7(6.9)	6-23
2	0.47578(29)	1.137(30)	24.01(14)	78.8(5.6)	5-20
3	0.54006(26)	1.161(29)	23.66(18)	80.5(5.3)	5-20
4	0.59320(23)	1.183(28)	24.16(22)	76.5(4.8)	5-18

Figure 3.28 *Effective energy* $aE_{\mathit{eff}} = \ln C^{(2)}(t+1)/C^{(2)}(t)$ *vs* t*, for 2-point kaon correlation function fit on ensemble C1. Simultaneous 2-exponential fit to point source correlation functions for all Fourier momenta on timeslices t-fit 6-23 (*$n^2 = 0$*), 6-23 (*$n^2 = 1$*), 5-20 (*$n^2 = 2$*), 5-20 (*$n^2 = 3$*) and 5-18 (*$n^2 = 4$*). Hotelling p-value for the fit is 0.1197, with fitted energies* aE_n *and overlap coefficients* $A_{op,n}$ *shown in the table above.*

On the coarse ensembles, wall separation $T/a = 24 \simeq 2.65$ fm – similar to the wall separation $T/a = 32$ on the medium ensembles. The same procedure is followed as for previous ensembles, but using smaller wall separations.

The preferred fit for the temporal vector current at $n^2 = 0$ is shown in fig 3.29.

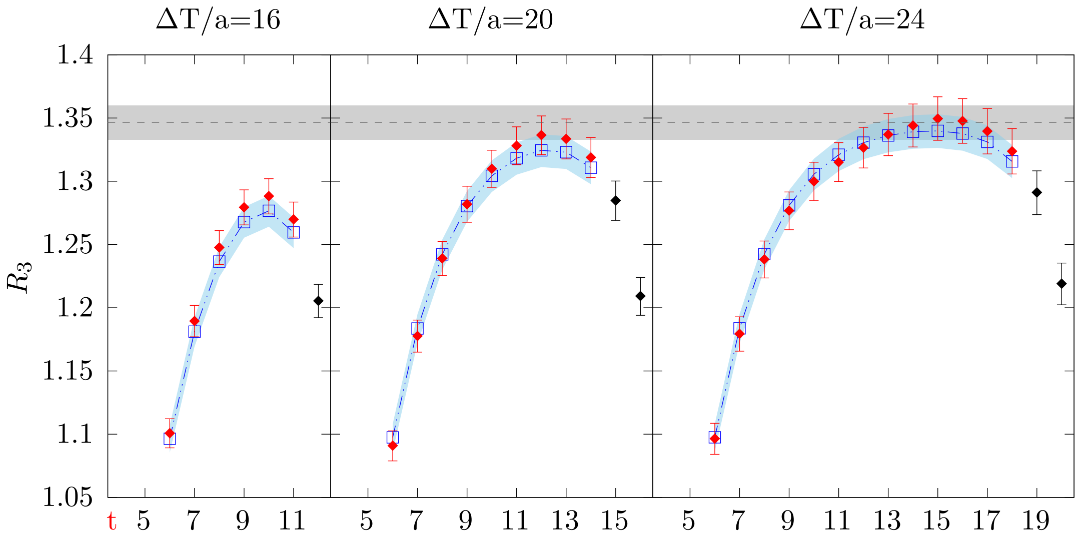

Figure 3.29 *Temporal component of mostly nonperturbatively renormalised ratio R_3 vs t, for $D_s \to K$ at $n^2 = 0$ on ensemble C1. Simultaneous fit to wall separations $\Delta T/a$ 16, 20 and 24 on timeslices 6-11, 6-14 and 6-18, respectively. The grey band is the matrix element $\langle K|\gamma_4\,(n^2 = 0)|D_s\rangle = 1.346(14)$. Hotelling p-value for the fit is 0.256, with excited-state matrix elements shown in table 3.5.*

Matrix element fits for non-zero momenta are included in appendix A.4.

3.3.5 Ensemble C2 fit results

Following the same procedure as for previous ensembles, the results for ensemble C2 of the preferred fit for the kaon are shown in fig 3.30, for the D_s in fig 3.31 and for the matrix element of the temporal component of the vector current at $n^2 = 0$ in fig 3.32. Matrix element fits for non-zero momenta are included in appendix A.5.

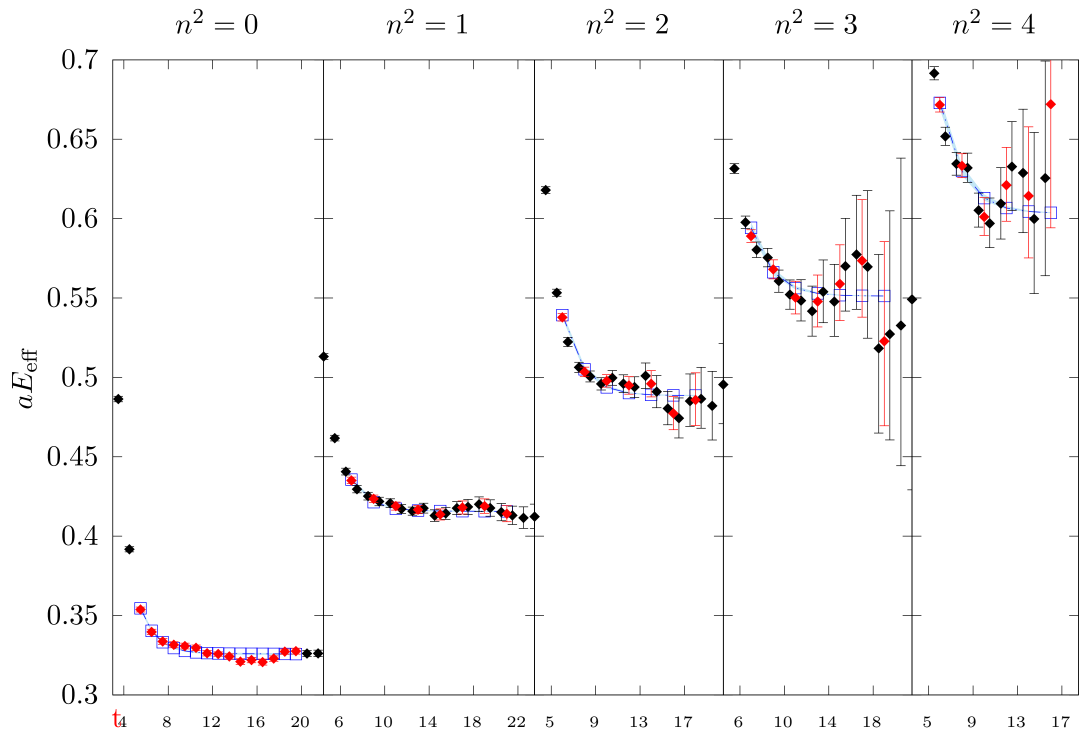

n^2	aE_0	aE_1	$A_{\text{P},0}$	$A_{\text{P},1}$	t-fit
0	0.32589(61)	1.028(52)	25.43(14)	63.6(8.0)	5-20
1	0.41569(47)	1.055(50)	25.25(16)	65.6(9.0)	6-22:2
2	0.48853(40)	1.082(49)	24.97(18)	65.7(7.8)	5-19:2
3	0.55120(35)	1.108(47)	24.68(22)	69.5(9.3)	6-20:2
4	0.60326(32)	1.131(46)	25.17(30)	64.3(7.0)	5-17:2

Figure 3.30 *Effective energy* $aE_{\text{eff}} = \ln C^{(2)}(t+1)/C^{(2)}(t)$ *vs* t*, for 2-point kaon correlation function fit on ensemble C2. Simultaneous 2-exponential fit to point source correlation functions for all Fourier momenta on timeslices t-fit 5-20 (*$n^2 = 0$*), 6-22:2 (*$n^2 = 1$*), 5-19:2 (*$n^2 = 2$*), 6-20:2 (*$n^2 = 3$*) and 5-17:2 (*$n^2 = 4$*). Hotelling p-value for the fit is 0.474, with fitted energies* aE_n *and overlap coefficients* $A_{op,n}$ *shown in the table above.*

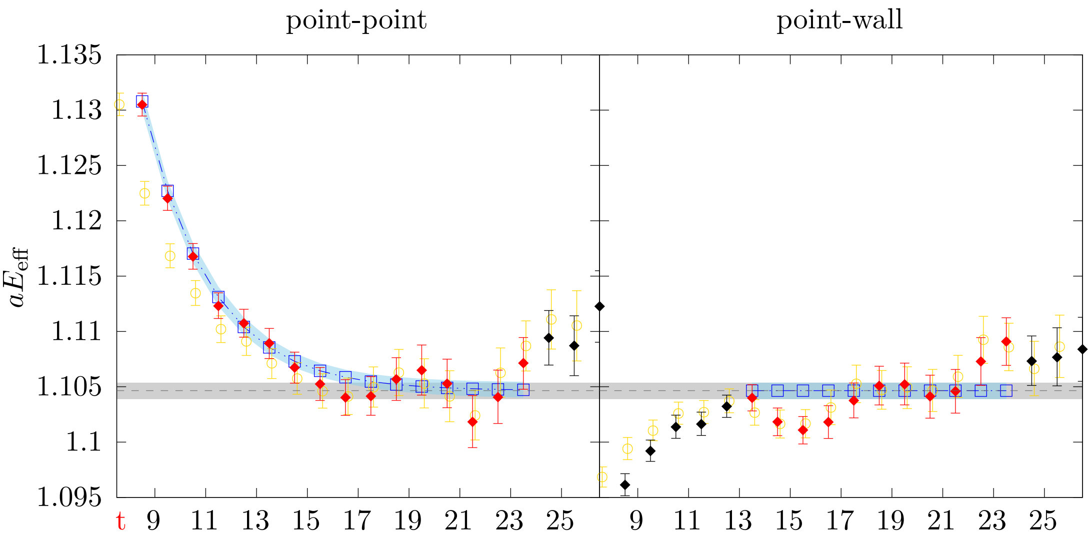

p-val	am_0	am_1	t_{P}-fit	$A_{\text{P},0}$	$A_{\text{P},1}$	t_{W}-fit	$A_{\text{W},0}$
0.429	1.10465(74)	1.497(36)	8-24	35.49(29)	58.3(6.9)	13-24	12694(100)

Figure 3.31 *Effective mass $am_{eff}\left(t+\frac{1}{2}\right) = \ln C^{(2)}(t)/C^{(2)}(t+1)$ vs t, for 2-point D_s correlation function fit on ensemble C2. Simultaneous 2-exponential fit to point source on timeslices t_P-fit 8-24 and 1-exponential fit to wall source on timeslices t_W-fit 13-24. Hotelling p-value for the fit is 0.429, with extracted masses am_n and overlap coefficients $A_{op,n}$ shown in the table above. Grey band is the fitted ground-state mass (am_0). Yellow points are the axial data for reference only (i.e. not included in fit).*

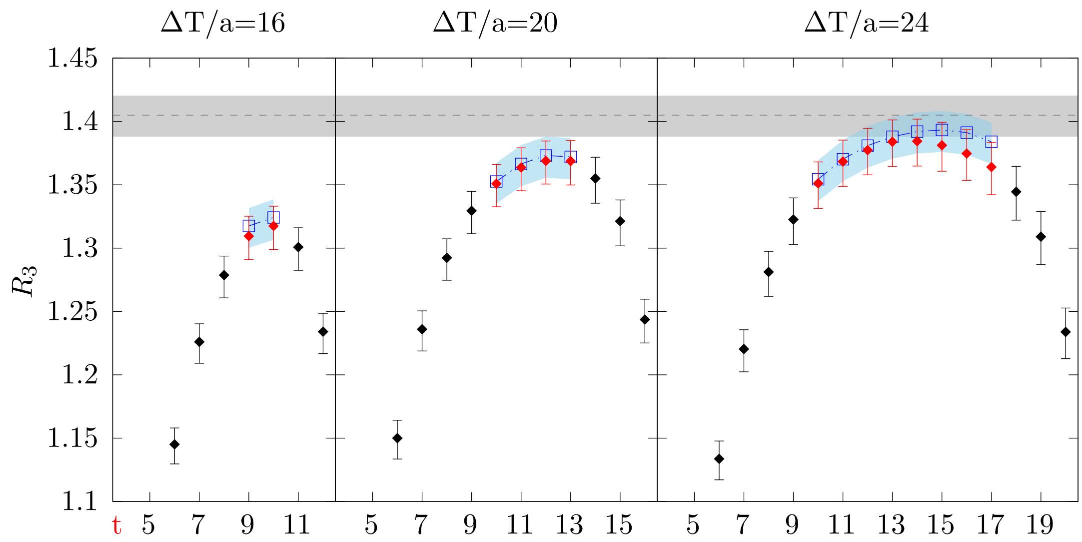

Figure 3.32 *Temporal component of mostly nonperturbatively renormalised ratio R_3 vs t, for $D_s \to K$ at $n^2 = 0$ on ensemble C2. Simultaneous fit to wall separations $\Delta T/a$ 16, 20 and 24 on timeslices 9;10, 10-13 and 10-17, respectively. The grey band is the matrix element $\langle K|\gamma_4\left(n^2=0\right)|D_s\rangle = 1.405(16)$. Hotelling p-value for the fit is 0.37, with excited-state matrix elements shown in table 3.6.*

3.4 Matrix element summary - all ensembles

The ground and excited-state matrix elements extracted via the R_3 ratio fits at each integer lattice momentum n^2 for each of the ensembles are shown in tables 3.1 to 3.6 below.

	$\langle K\|\gamma_4\|D_s\rangle$					$\langle K\|\gamma_i\|D_s\rangle$				
n^2	p	gnd-gnd	gnd-ex	ex-gnd	ex-ex	p	gnd-gnd	gnd-ex	ex-gnd	ex-ex
0	0.62	0.9065(62)	-0.657(79)	0.50(11)	6.8(8.0)					
1	0.47	0.8085(51)	-0.150(62)	0.39(12)	14.1(4.2)	0.98	0.2602(37)	-0.712(62)	0.119(70)	-0.5(1.4)
2	0.89	0.7639(74)	-0.153(87)	0.223(99)	5.8(5.4)	0.93	0.2225(33)	-0.496(51)	0.034(45)	0.9(1.1)
3	0.64	0.6966(87)	0.16(10)	0.53(12)	-0.9(1.9)	0.69	0.1932(31)	-0.348(52)	0.107(39)	-0.18(93)
4	0.30	0.666(11)	0.040(94)	0.37(11)	2.0(5.3)	0.57	0.1701(41)	-0.284(59)	0.044(38)	1.63(94)
5	0.98	0.645(14)	-0.09(14)	0.400(81)	2.1(4.9)	0.89	0.1604(56)	-0.281(88)	0.021(50)	1.5(1.2)
6	0.43	0.613(22)	-0.79(70)	0.65(13)	-19(15)	0.99	0.1377(77)	-0.09(12)	0.026(57)	2.4(1.9)

Table 3.1 *Ground (gnd) and excited-state (ex) matrix elements for all integer lattice momenta n^2 on ensemble F1M. The individual fits are shown in § 3.2.2 and 3.2.3.*

	$\langle K\|\gamma_4\|D_s\rangle$					$\langle K\|\gamma_i\|D_s\rangle$				
n^2	p	gnd-gnd	gnd-ex	ex-gnd	ex-ex	p	gnd-gnd	gnd-ex	ex-gnd	ex-ex
0	0.555	1.0516(93)	-0.77(23)	0.18(18)	-26(38)					
1	0.230	0.902(12)	-0.365(74)	0.17(13)	17(41)	0.334	0.3363(66)	-0.64(11)	0.42(14)	-10(10)
2	0.296	0.801(14)	-0.00(17)	0.73(19)	-35(51)	0.58	0.2701(59)	-0.401(93)	0.23(11)	-10.9(8.6)
3	0.169	0.765(25)	-0.12(37)	0.65(21)	-80(64)	0.27	0.2238(89)	-0.26(12)	0.13(11)	-1.6(4.6)
4	1.00	0.691(28)	0.06(31)	0.63(22)	-3.2(9.9)	0.35	0.187(10)	-0.15(15)	0.22(12)	-3.1(4.1)

Table 3.2 *Ground (gnd) and excited-state (ex) matrix elements for all integer lattice momenta n^2 on ensemble M1. The individual fits are shown in § 3.3.1 and appendix A.1.*

	$\langle K\|\gamma_4\|D_s\rangle$				$\langle K\|\gamma_i\|D_s\rangle$			
n^2	p	gnd-gnd	gnd-ex	ex-gnd	p	gnd-gnd	gnd-ex	ex-gnd
0	0.488	1.0559(92)	-1.02(49)	0.49(11)				
1	0.725	0.920(11)	-0.35(13)	0.33(10)	0.145	0.3298(54)	-0.89(26)	0.255(67)
2	0.49	0.830(14)	-0.03(15)	0.38(15)	0.85	0.2527(55)	-0.31(12)	0.367(83)
3	0.37	0.762(17)	0.05(24)	0.60(15)	0.60	0.2250(75)	-0.27(14)	0.126(95)
4	0.22	0.767(21)	-0.03(21)	0.31(10)	0.27	0.1974(91)	-0.48(21)	0.150(88)

Table 3.3 *Ground (gnd) and excited-state (ex) matrix elements for all integer lattice momenta n^2 on ensemble M2. The individual fits are shown in § 3.3.2 and appendix A.2.*

n^2	p	$\langle K\|\gamma_4\|D_s\rangle$ gnd-gnd	gnd-ex	ex-gnd	p	$\langle K\|\gamma_i\|D_s\rangle$ gnd-gnd	gnd-ex	ex-gnd
0	0.64	1.064(10)	-0.51(14)	0.12(11)				
1	0.41	0.915(12)	-0.023(97)	0.29(12)	0.53	0.3353(54)	-0.533(78)	0.051(50)
2	0.525	0.834(12)	0.118(73)	0.431(95)	0.55	0.2752(47)	-0.326(60)	0.024(36)
3	0.98	0.782(19)	0.15(10)	0.19(12)	0.70	0.2357(64)	-0.257(63)	0.051(45)
4	0.66	0.752(21)	0.11(22)	0.46(14)	0.65	0.2082(75)	-0.089(51)	0.057(38)

Table 3.4 *Ground (gnd) and excited-state (ex) matrix elements for all integer lattice momenta n^2 on ensemble M3. The individual fits are shown in § 3.3.3 and appendix A.3.*

n^2	p	$\langle K\|\gamma_4\|D_s\rangle$ gnd-gnd	gnd-ex	ex-gnd	p	$\langle K\|\gamma_i\|D_s\rangle$ gnd-gnd	gnd-ex	ex-gnd
0	0.256	1.346(14)	-0.473(40)	1.58(30)				
1	0.246	1.169(14)	0.25(11)	1.28(25)	0.213	0.4290(68)	-1.09(17)	0.43(12)
2	0.42	1.090(16)	0.141(74)	0.46(13)	0.38	0.3475(74)	-0.49(13)	0.248(89)
3	0.62	0.982(22)	0.39(14)	0.80(15)	0.521	0.2976(71)	-0.37(11)	0.199(73)
4	0.49	0.964(35)	0.90(27)	0.13(40)	0.91	0.272(10)	-0.48(17)	0.105(84)

Table 3.5 *Ground (gnd) and excited-state (ex) matrix elements for all integer lattice momenta n^2 on ensemble C1. The individual fits are shown in § 3.3.4 and appendix A.4.*

n^2	p	$\langle K\|\gamma_4\|D_s\rangle$ gnd-gnd	gnd-ex	ex-gnd	ex-ex	p	$\langle K\|\gamma_i\|D_s\rangle$ gnd-gnd	gnd-ex	ex-gnd	ex-ex
0	0.37	1.405(16)	0.12(20)	0.42(68)	14(28)					
1	0.46	1.214(20)	0.36(28)	-0.29(72)	176(130)	0.189	0.4344(80)	-0.59(15)	0.28(14)	-0.2(6.7)
2	0.32	1.069(21)	0.39(16)	0.08(34)	50(21)	0.84	0.3599(84)	-0.40(10)	-0.17(19)	7.2(6.0)
3	0.098	1.031(31)	0.44(25)	0.97(37)	-9(12)	0.78	0.294(12)	-0.18(12)	0.27(18)	3.3(4.9)
4	0.66	0.955(50)	0.37(63)	0.65(47)	13(16)	0.145	0.257(13)	0.01(12)	0.107(89)	1.8(4.7)

Table 3.6 *Ground (gnd) and excited-state (ex) matrix elements for all integer lattice momenta n^2 on ensemble C2. The individual fits are shown in § 3.3.5 and appendix A.5.*

3.5 Fully nonperturbative RI-SMOM$^{\gamma_\mu}$ renormalisation

The fully nonperturbative RI/SMOM determination of the ratios (1.178)–(1.180), as per § 1.4.2, presented in this section was not performed by the author of this thesis. Results from the study described in [109] are reproduced in table 3.7 by kind permission of Rajnandini Mukherjee.

Ensemble	$\frac{Z_{V,\ell}}{Z_{q,\ell}}$	$\frac{Z_{V,\mathrm{h}}}{Z_{q,\mathrm{h}}}$	$\frac{Z_{V,\mathrm{m}}}{Z_{q,\mathrm{m}}}$	μ/GeV	$\rho = \frac{Z_{V,\mathrm{m}}}{\sqrt{Z_{V,\ell}Z_{V,\mathrm{h}}}}$
C1	0.95510(12)	0.96007(20)	0.96256(28)	1.982	1.00520(32)
C2	0.95454(19)	0.95986(16)	0.96218(37)	1.982	1.00520(41)
M1	0.96399(21)	0.96606(27)	0.96904(45)	1.985	1.00416(50)
M2	0.96398(17)	0.96617(21)	0.96915(39)	1.985	1.00423(43)
M3	0.96361(24)	0.96602(32)	0.96886(55)	1.985	1.00420(61)
F1M	0.96566(11)	0.96815(15)	0.97063(26)	2.005	1.00385(28)

Table 3.7 *RI/SMOM determination of the ratios* (1.178)–(1.180)*, per § 1.4.2. Data provided by Rajnandini Mukherjee [109]. μ is the renormalisation scale for ρ on each ensemble. ρ is a multiplicative factor which can be applied to the mostly nonperturbatively renormalised matrix elements extracted in the previous sections to make them fully nonperturbatively renormalised. Error quoted for ρ assumes uncorrelated errors in component ratios.*

The renormalisation ratios ρ in table 3.7 are available at a range of renormalisation scales μ. Over the range 2–3 GeV, the ρ vary by around 1 per mille. Error associated with the choice of renormalisation scale is subleading, and for the purpose of this analysis the lowest renormalisation scale μ available on each ensemble (see table 3.7) has been used.

3.6 Fully nonperturbatively renormalised form factors

Now that the temporal and spatial matrix elements have been extracted at each Fourier momenta, the form factors are assembled. First the fully nonperturbatively renormalised correction factor ρ from table 3.7 is applied

$$\langle K(\mathbf{p})|\mathcal{V}_4|D_s(\mathbf{0})\rangle = \rho\,\langle K(\mathbf{p})|\gamma_4|D_s(\mathbf{0})\rangle \tag{3.16}$$

$$\langle K(\mathbf{p})|\mathcal{V}_i|D_s(\mathbf{0})\rangle = \rho\,\langle L(\mathbf{p})|\gamma_i|D_s(\mathbf{0})\rangle\;. \tag{3.17}$$

Following § 1.4.3 we compute $f_\parallel$ (1.220) and $f_\perp$ (1.221):

$$f_\parallel (E_P) = \frac{\langle K(\mathbf{p})|\mathcal{V}_4|D_s(\mathbf{0})\rangle}{\sqrt{2m_{D_s}}} \tag{3.18}$$

$$f_\perp (E_P) = \frac{\langle K(\mathbf{p})|\mathcal{V}_i|D_s(\mathbf{0})\rangle}{\sqrt{2m_{D_s}}} \frac{aN_\mu}{2\pi n_\mu}, \tag{3.19}$$

being careful to remember that the integer Fourier momentum component n_μ in the denominator of (3.19) has already been applied in the definition of the spatially averaged 3-point correlation function $C_{if}^{(3)i} = \langle K(\mathbf{p})|\gamma_i|D_s(\mathbf{0})\rangle$ (2.6)

$$f_\perp (E_P) = \frac{\rho\, C_{if}^{(3)i}}{\sqrt{2m_{D_s}}} \frac{aN_\mu}{2\pi}. \tag{3.20}$$

We then compute f_+ and f_0 using (1.222) and (1.223)

$$f_+ \left(q^2\right) = \frac{1}{\sqrt{2m_D}} \left(f_\parallel (E_P) + (m_D - E_P) f_\perp (E_P)\right) \tag{3.21}$$

$$f_0 \left(q^2\right) = \frac{\sqrt{2m_D}}{m_D^2 - m_P^2} \left((m_D - E_P) f_\parallel (E_P) + \left(E_P^2 - m_P^2\right) f_\perp (E_P)\right). \tag{3.22}$$

Table 3.8 collects the fitted D_s masses am_{D_s} from previous sections and shows the fully nonperturbatively computed $Z_{V,\mathrm{m}}$ (i.e. after applying the correction ρ from table 3.7 to the $Z_{V,\mathrm{m}}\big|_{\rho=1}$ from table 2.12).

Name	am_{D_s}	$Z_{V,\mathrm{m}}$
C1	1.10403(61)	0.8635(75)
C2	1.10465(74)	0.8754(83)
M1	0.82568(57)	0.8630(52)
M2	0.82567(68)	0.8817(58)
M3	0.82554(62)	0.8656(62)
F1M	0.72885(29)	0.8744(34)

Table 3.8 *Values entering the form factors on each ensemble D_s meson masses am_{D_s} and fully nonperturbative renormalisation factors $Z_{V,m}$ for the mixed action.*

Tables 3.9–3.14 show form factor results at each momentum on each ensemble.

n^2	aE_K	$(aq)^2$	$\langle K\vert\mathcal{V}_4\vert D_s\rangle$	$\langle K\vert\mathcal{V}_i\vert D_s\rangle$	$f_\parallel\sqrt{a}$	$f_\perp/\sqrt{a}$	f_0	f_+
0	0.19084(28)	0.28946(40)	0.9099(62)		0.7537(52)		0.9894(67)	0.6242(43)
1	0.23109(23)	0.23078(34)	0.8116(51)	0.2612(37)	0.6722(42)	1.652(23)	0.8849(55)	1.238(11)
2	0.26521(20)	0.18104(30)	0.7668(74)	0.2233(33)	0.6351(61)	1.413(21)	0.8355(76)	1.069(10)
3	0.29534(18)	0.13713(28)	0.6993(87)	0.1939(32)	0.5792(72)	1.227(20)	0.7648(88)	0.920(11)
4	0.32215(17)	0.09805(25)	0.669(11)	0.1707(41)	0.5540(92)	1.080(26)	0.727(11)	0.823(13)
5	0.34724(15)	0.06148(23)	0.647(14)	0.1610(56)	0.536(12)	1.019(35)	0.709(14)	0.766(16)
6	0.37057(14)	0.02747(22)	0.615(22)	0.1382(78)	0.509(18)	0.875(49)	0.661(21)	0.681(22)

Table 3.9 *Fully nonperturbatively renormalised form factor results for ensemble F1M. At each integer lattice momentum n^2, the kaon energy aE_K and the D_s mass am_{D_s} from table 3.8 are used to compute the current momentum $(aq)^2$ per (1.203). The fully nonperturbatively renormalised temporal and spatial matrix elements $\langle K|\mathcal{V}_4|D_s\rangle$ and $\langle K|\mathcal{V}_i|D_s\rangle$ are then used to compute $f_\parallel$, $f_\perp$, f_0 and f_+ per (3.18), (3.19), (3.21) and (3.22).*

n^2	aE_K	$(aq)^2$	$\langle K\vert\mathcal{V}_4\vert D_s\rangle$	$\langle K\vert\mathcal{V}_i\vert D_s\rangle$	$f_\parallel\sqrt{a}$	$f_\perp/\sqrt{a}$	f_0	f_+
0	0.22506(78)	0.3607(11)	1.0560(93)		0.8217(72)		1.0050(88)	0.6395(57)
1	0.29772(59)	0.24075(80)	0.905(12)	0.3377(66)	0.7046(91)	1.339(26)	0.861(11)	1.098(16)
2	0.35551(49)	0.14532(65)	0.804(14)	0.2712(59)	0.626(11)	1.075(24)	0.765(12)	0.880(13)
3	0.40485(43)	0.06385(56)	0.768(25)	0.2248(89)	0.597(20)	0.891(36)	0.717(20)	0.757(21)
4	0.44695(38)	-0.00567(48)	0.694(28)	0.188(10)	0.540(22)	0.744(41)	0.642(21)	0.639(21)

Table 3.10 *Form factor results for ensemble M1 (same format as table 3.9).*

n^2	aE_K	$(aq)^2$	$\langle K\vert\mathcal{V}_4\vert D_s\rangle$	$\langle K\vert\mathcal{V}_i\vert D_s\rangle$	$f_\parallel\sqrt{a}$	$f_\perp/\sqrt{a}$	f_0	f_+
0	0.23052(59)	0.35421(97)	1.0604(92)		0.8252(72)		1.0040(87)	0.6421(57)
1	0.30184(45)	0.23643(78)	0.924(11)	0.3312(54)	0.7189(89)	1.313(22)	0.872(10)	1.095(13)
2	0.35895(37)	0.14213(67)	0.834(14)	0.2538(55)	0.649(11)	1.006(22)	0.775(11)	0.870(13)
3	0.40785(33)	0.06137(59)	0.766(17)	0.2259(76)	0.596(13)	0.895(30)	0.716(15)	0.755(16)
4	0.44965(29)	-0.00765(52)	0.770(21)	0.1982(92)	0.599(17)	0.786(36)	0.700(20)	0.696(20)

Table 3.11 *Form factor results for ensemble M2 (same format as table 3.9).*

n^2	aE_K	$(aq)^2$	$\langle K\vert\mathcal{V}_4\vert D_s\rangle$	$\langle K\vert\mathcal{V}_i\vert D_s\rangle$	$f_\parallel\sqrt{a}$	$f_\perp/\sqrt{a}$	f_0	f_+
0	0.23988(64)	0.34300(96)	1.068(10)		0.8314(81)		1.0027(97)	0.6470(63)
1	0.30901(49)	0.22886(75)	0.919(12)	0.3367(54)	0.7154(92)	1.335(21)	0.865(11)	1.093(13)
2	0.36496(42)	0.13649(63)	0.837(12)	0.2764(47)	0.6516(96)	1.096(19)	0.789(10)	0.900(11)
3	0.41312(36)	0.05697(55)	0.785(19)	0.2367(64)	0.611(15)	0.938(25)	0.737(16)	0.776(17)
4	0.45440(33)	-0.01120(48)	0.755(22)	0.2090(75)	0.588(17)	0.828(30)	0.703(16)	0.697(16)

Table 3.12 *Form factor results for ensemble M3 (same format as table 3.9).*

n^2	aE_K	$(aq)^2$	$\langle K\|\mathcal{V}_4\|D_s\rangle$	$\langle K\|\mathcal{V}_i\|D_s\rangle$	$f_\parallel\sqrt{a}$	$f_\perp/\sqrt{a}$	f_0	f_+
0	0.30601(47)	0.6368(11)	1.353(14)		0.9108(92)		0.9599(98)	0.6129(62)
1	0.40046(35)	0.42829(90)	1.175(14)	0.4312(68)	0.7909(94)	1.109(18)	0.8325(96)	1.057(13)
2	0.47578(29)	0.26197(78)	1.095(16)	0.3493(74)	0.737(11)	0.898(19)	0.769(10)	0.876(13)
3	0.54006(26)	0.12005(69)	0.987(22)	0.2991(71)	0.664(15)	0.769(18)	0.696(13)	0.739(13)
4	0.59320(23)	0.00271(62)	0.969(35)	0.273(11)	0.652(24)	0.703(27)	0.680(19)	0.681(19)

Table 3.13 *Form factor results for ensemble C1 (same format as table 3.9).*

n^2	aE_K	$(aq)^2$	$\langle K\|\mathcal{V}_4\|D_s\rangle$	$\langle K\|\mathcal{V}_i\|D_s\rangle$	$f_\parallel\sqrt{a}$	$f_\perp/\sqrt{a}$	f_0	f_+
0	0.32589(61)	0.6065(13)	1.412(16)		0.950(11)		0.987(11)	0.6392(73)
1	0.41569(47)	0.4081(11)	1.220(20)	0.4366(80)	0.821(13)	1.122(21)	0.854(13)	1.072(15)
2	0.48853(40)	0.24715(93)	1.074(22)	0.3618(85)	0.723(14)	0.930(22)	0.758(13)	0.872(14)
3	0.55120(35)	0.10869(82)	1.036(31)	0.296(12)	0.697(21)	0.760(30)	0.715(19)	0.752(20)
4	0.60326(32)	-0.00633(73)	0.960(50)	0.259(13)	0.646(34)	0.664(33)	0.661(27)	0.659(27)

Table 3.14 *Form factor results for ensemble C2 (same format as table 3.9).*

Chapter 4

Momentum and lattice spacing dependence of semileptonic decay form-factors via global fit

This section sets out how the final result is constructed from per-ensemble results.

4.1 Chiral continuum fit inputs

The $D_s \to K$ form factor results from § 3.6 are now fitted to the chiral continuum fit form (1.243), (1.244) and (1.245) presented in § 1.4.4:

$$f_X\left(E_L, M_\pi^{\mathrm{s}}, a^2\right) = f_X^{(\mathrm{cont})}\left(E_L\right) + f_X^{(\mathrm{lat})}\left(E_L, M_\pi^{\mathrm{s}}, a^2\right)\ , \tag{4.1}$$

with

$$f_X^{(\mathrm{cont})}\left(E_L\right) = \frac{\Lambda}{E_L + \Delta_{xy,X}}\left[c_{X,0} + \sum_{n=1}^{n_{E,X}} e_{X,n-1}\left(\frac{E_L}{\Lambda}\right)^n\right] \tag{4.2}$$

and

$$f_X^{(\mathrm{lat})}\left(E_L, M_\pi^{\mathrm{s}}, a^2\right) = \frac{\Lambda}{E_L + \Delta_{xy,X}}\left[c_{X,0}\left(\frac{\delta f\left(M_\pi^s\right) - \delta f\left(M_\pi^p\right)}{\left(4\pi f_\pi\right)^2}\right)\right. \tag{4.3}$$

$$\left. + c_{X,1}\frac{\Delta M_\pi^2}{\Lambda^2} + d_X\left(a\Lambda\right)^2\right]. \tag{4.4}$$

In addition to the per ensemble form factor results from chapter 3, there are a number of physical inputs to the fit taken from the PDG [25], starting with physical meson masses $M^{\mathrm{p}}_{\mathrm{meson}}$ for

$$M^{\mathrm{p}}_{\pi^\pm} = 139.57039(18)\,\mathrm{MeV} \tag{4.5}$$
$$M^{\mathrm{p}}_{\pi^0} = 134.9768(5)\,\mathrm{MeV} \tag{4.6}$$
$$M^{\mathrm{p}}_{\pi} \equiv \text{isospin average of } \pi^\pm \text{ and } \pi_0 \tag{4.7}$$
$$= \left(2M^{\mathrm{p}}_{\pi^\pm} + M^{\mathrm{p}}_{\pi^0}\right)/3 = 138.03919(33)\,\mathrm{MeV} \tag{4.8}$$
$$M^{\mathrm{p}}_{K^\pm} = 493.677(16)\,\mathrm{MeV} \tag{4.9}$$
$$M^{\mathrm{p}}_{K^0} = 497.611(13)\,\mathrm{MeV} \tag{4.10}$$
$$M^{\mathrm{p}}_{K} \equiv \text{average of } K^\pm \text{ and } K_0 \tag{4.11}$$
$$= 495.644(21)\,\mathrm{MeV} \tag{4.12}$$
$$M^{\mathrm{p}}_{D_s} \equiv M^{\mathrm{p}}_{D_s^\pm} = 1.96835(7)\,\mathrm{GeV} \tag{4.13}$$
$$M^{\mathrm{p}}_{D_0^\star} = 2.343(10)\,\mathrm{GeV} \tag{4.14}$$
$$M^{\mathrm{p}}_{D^*(2010)^\pm} = 2.01026(5)\,\mathrm{GeV} \tag{4.15}$$
$$M^{\mathrm{p}}_{D^*(2007)^0} = 2.00685(5)\,\mathrm{GeV} \tag{4.16}$$
$$M^{\mathrm{p}}_{D^\star} \equiv \text{average of } D^*\left(2010\right)^\pm \text{ and } D^*\left(2007\right)^0 \tag{4.17}$$
$$= 2.008555(50)\,\mathrm{GeV} \tag{4.18}$$
$$M^{\mathrm{p}}_{D^\star_{s0}(2317)^\pm} = 2.3178(5)\,\mathrm{GeV} \tag{4.19}$$
$$M^{\mathrm{p}}_{D_s^{\star\pm}} = 2.1122(4)\,\mathrm{GeV} \tag{4.20}$$

and the pion decay constant

$$f_\pi = 130.19(89)\,\mathrm{MeV}\,. \tag{4.21}$$

Data for inverse lattice spacing for each ensemble from table 2.3 [4]

$$a^{-1} = \begin{cases} 1.7848(50)\,\mathrm{GeV} & \mathrm{C1,\ C2} \\ 2.708(10)\,\mathrm{GeV} & \mathrm{F1M} \\ 2.3833(86)\,\mathrm{GeV} & \mathrm{M1,\ M2,\ M3} \end{cases} . \tag{4.22}$$

For each of the above, a random bootstrap sample is created using the normal distribution and the mean and standard distribution listed. Unique numbers are used for the seed for each distribution to avoid cross-correlations.

As set out in § 3.6, the scale Λ is set at

$$\Lambda = 1\,\text{GeV}\,. \tag{4.23}$$

4.1.1 Pion mass fits

The pion masses entering the global fit are taken from separate simultaneous fits on each ensemble to both the point- and wall-source zero momentum pion 2-point correlation functions.

				m_π/MeV	
Name	n_{state}	am_π	p-value	fit	ref [4]
C1	1	0.19005(57)	0.68	339.3(1.4)	339.76(1.22)
C2	1	0.24161(59)	0.067	431.2(1.6)	430.63(1.38)
M1	1	0.12640(58)	0.305	301.2(1.8)	303.56(1.38)
M2	2	0.14991(53)	0.87	357.3(1.7)	360.71(1.58)
M3	2	0.17056(59)	0.522	406.5(2.0)	410.76(1.74)
F1M	2	0.08536(33)	0.376	231.2(1.3)	232.01(1.01)

Table 4.1 *Pion mass fits on each ensemble. The number of states in each fit is indicated in n_{state} (it was not possible to fit an excited-state on each ensemble). The effective pion mass in lattice units am_π (2.96) and p-value for the fit are shown for each ensemble. This is converted to physical units m_π in the 'fit' column and this can be compared with prior results [4] in the 'ref' column.*

Fitted pion masses are shown in table 4.1 together with reference values for the pion masses on these ensembles from other studies with greater statistics. The fits themselves are shown in figures 4.1 to 4.6. The fits describe this data set well, and agree with results from prior determinations with higher statistics [4] within 1σ in most cases, extending to 2σ on ensembles M2 and M3.

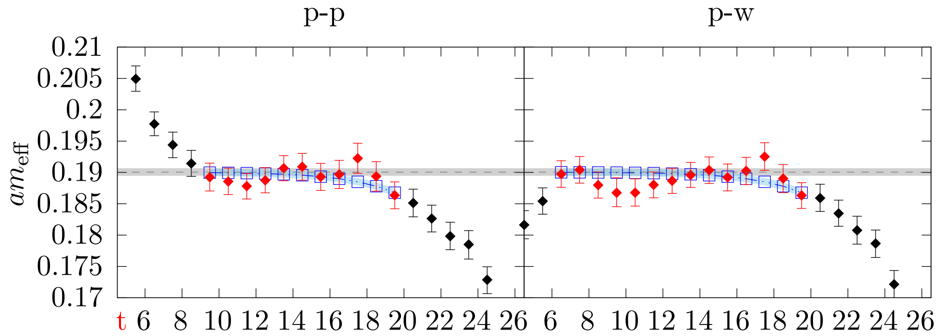

Figure 4.1 *Ensemble C1 pion mass* $am_\pi\left(t+\frac{1}{2}\right) = \ln C^{(2)}(t)/C^{(2)}(t+1)$ *vs* t*, from 1-state fit to point- (left panel) and wall-source (right panel) pion 2-point correlation functions with point sinks. The grey band is the fitted effective mass in lattice units* am_π*. The fit includes around-the-world effects, hence the curvature in both the data and the fit.* $am_\pi = 0.19005(57)$ $m_\pi = 339.3(1.4)$ *MeV, Hotelling p-value = 0.68*

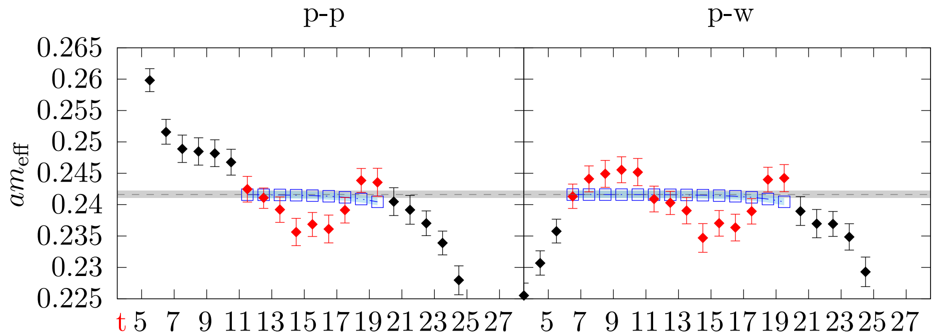

Figure 4.2 *Ensemble C2 pion mass:* $am_\pi = 0.24161(59)$*;* $m_\pi = 431.2(1.6)$ *MeV; 1-state fit; Hotelling p-value = 0.067; as described in fig 4.1.*

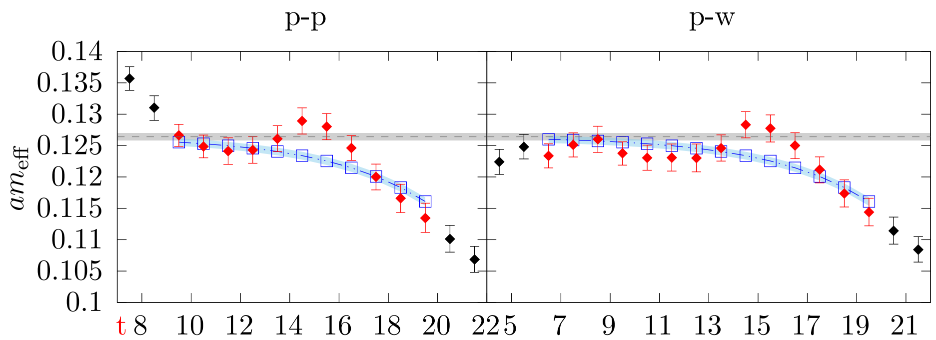

Figure 4.3 *Ensemble M1 pion mass:* $am_\pi = 0.12640(58)$*;* $m_\pi = 301.2(1.8)$ *MeV; 1-state fit; Hotelling p-value = 0.305; as described in fig 4.1.*

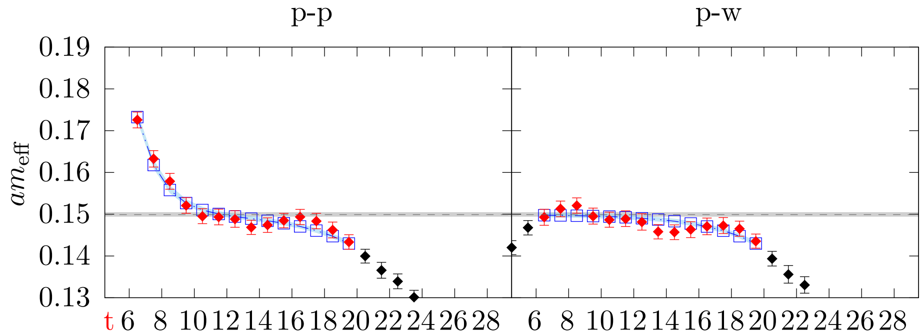

Figure 4.4 *Ensemble M2 pion mass:* $am_\pi = 0.14991(53)$; $m_\pi = 357.3(1.7)$ *MeV; 2-state fit; Hotelling p-value = 0.87; as described in fig 4.1.*

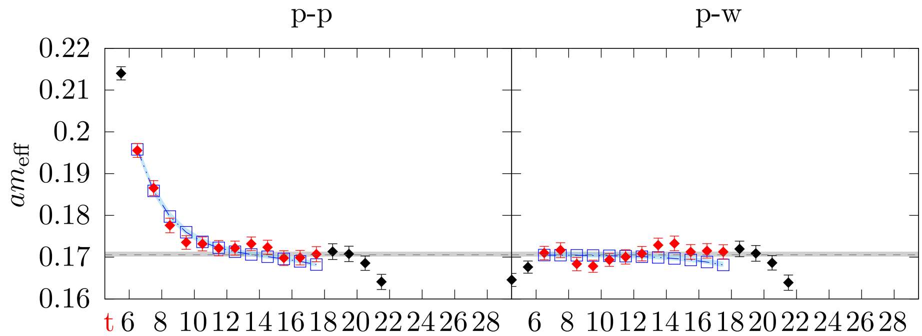

Figure 4.5 *Ensemble M3 pion mass:* $am_\pi = 0.17056(59)$; $m_\pi = 406.5(2.0)$ *MeV; 2-state fit; Hotelling p-value = 0.522; as described in fig 4.1.*

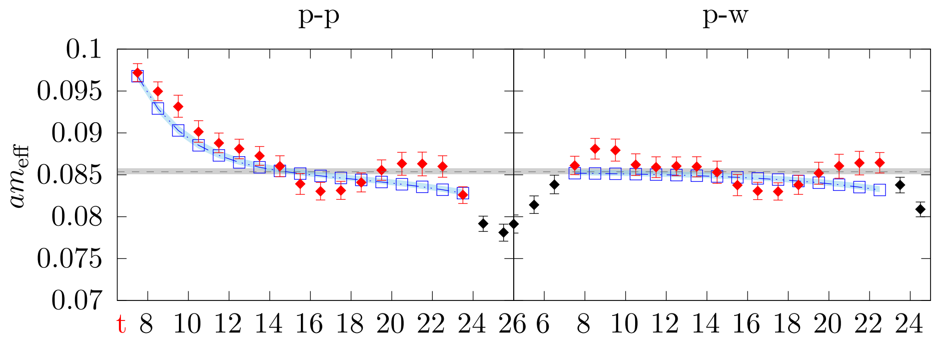

Figure 4.6 *Ensemble F1M pion mass:* $am_\pi = 0.08536(33)$; $m_\pi = 231.2(1.3)$ *MeV; 2-state fit; Hotelling p-value = 0.376; as described in fig 4.1.*

4.1.2 Imposing the constraint $f_0(0) = f_+(0)$

Data for both form factors on all ensembles are fitted simultaneously so that we can impose the chiral continuum limit constraint (1.242)

$$f_0^{(\mathrm{cont})}(0) = f_+^{(\mathrm{cont})}(0) \ . \tag{4.24}$$

The fit form is deliberately constructed as the sum of a continuum piece, $f_X^{(\mathrm{cont})}$, and a lattice piece, $f_X^{(\mathrm{lat})}$ (containing the pion mass mistuning and lattice spacing dependency), with a view to imposing (4.24) as a constraint in the fit. Using (1.204) and the physical masses of the D_s and the K, we define

$$E_0 \equiv E_L \Big|_{q^2=0} = \frac{\left(M_{D_s}^{\mathrm{p}}\right)^2 + \left(M_K^{\mathrm{p}}\right)^2}{2M_{D_s}^{\mathrm{p}}} \ . \tag{4.25}$$

Imposing (4.24) as the constraint and rearranging for $c_{+,0}$, we can impose the constraint in the fit by making $c_{+,0}$ the derived constant

$$c_{+,0} = \frac{E_0 + \Delta_{xy,+}}{E_0 + \Delta_{xy,0}} \left[c_{0,0} + \sum_{n=1}^{n_{E,0}} e_{0,n-1} \left(\frac{E_0}{\Lambda}\right)^n \right] - \sum_{n=1}^{n_{E,+}} e_{+,n-1} \left(\frac{E_0}{\Lambda}\right)^n \ . \tag{4.26}$$

It is important to note that at q_0, identical information is present in the data points for f_0 and f_+, because they are constructed from the same linear combinations of $f_\parallel$ and $f_\perp$ (see § 1.4.3).

This places an important restriction on the data points that can be used in the global fit. For points "near" q_0, the data for either f_0 or f_+ can be used – but not both. That is, $q \to q_0 \implies f_0 \to f_+$, hence attempts to use both datapoints in the fit prevent the correlation matrix from being invertible.

In practice, of the 58 data points available (32 for f_0 and 26 for f_+), the five data points for f_0 $(n^2 = 4)$ on ensembles C1, C2, M1, M2 and M3 were not sufficiently independent from the corresponding data points for f_+ $(n^2 = 4)$ to include both in the global fit.

For clarity of presentation, the sections below present global fit results for the 53 data points remaining after excluding these 5 data points. Details of other global fit options considered are deferred to § 4.4.

4.1.3 Fit covariance matrix

The estimate of the covariance matrix for the global fit is constructed from 10,000 bootstrap replicas per (2.57).

In the large statistics limit, there cannot be correlations between data points on different ensembles. If the full covariance matrix is constructed this is what is found – i.e. numerically small correlations across ensembles (compared with the correlations within ensembles). These numerical fluctuations are excluded by constructing the correlation matrix as a block diagonal per ensemble.

Within each ensemble, the data points are sorted first by form factor, then by Fourier momentum. Changing the sort order made no material difference to the fit. This sort order was retained in order to ensure reproducibility.

The condition numbers (see § 2.5.3) of the block diagonal components of the correlation matrix used in the global fit and for the full matrix itself (table 4.2) indicate that errors in the numerical inverse should be low, giving confidence in the fit cost function and p-value.

Name	κ^{-1}	N_{samples}	N_{data}
C1	1.97×10^{-3}	160	8
C2	2.23×10^{-3}	128	8
F1M	6.44×10^{-4}	72	13
M1	2.53×10^{-3}	128	8
M2	1.72×10^{-3}	128	8
M3	1.35×10^{-3}	120	8
Global	4.21×10^{-3}	160	53

Table 4.2 *Reciprocal condition numbers (see § 2.5.3) for the block diagonal components of the full covariance matrix for each ensemble. 'Global' is the reciprocal condition number for the full covariance matrix used in the fit, i.e. with cross-ensemble components set to 0. The numbers of measurement samples $N_{samples}$ and data points N_{data} entering the fit is shown for each ensemble. Conservative estimates of Hotelling p-value in the global fit are based on the maximum number of samples, 160.*

In § 2.4.3, the number of independent samples enters the computation of the Hotelling p-value (2.52). We seek a prescription for how to report p-values in this case when combining datasets with different underlying numbers of samples.

We look at the transformation from Hotelling's t^2 statistic into the f-statistic (2.51) (dropping the dashes)

$$f = \frac{n-p}{p\,(n-1)} t^2 \,. \tag{4.27}$$

Differentiating with respect to the number of samples n

$$\frac{\partial f}{\partial n} = \frac{p-1}{p\,(n-1)^2}\, t^2 \tag{4.28}$$

$$> 0 \qquad \text{for } p > 1\,, \tag{4.29}$$

i.e. for any given number of fit degrees of freedom $p > 1$ and test statistic t^2, the f-statistic increases for larger numbers of samples n. Given that the p-value (2.52) is an integral from f to infinity of the F-distribution (which is positive everywhere), larger f-statistics result in smaller Hotelling p-values.

Thus, our prescription is to report conservative p-values using the largest number of samples contributing to a combined dataset and accept or reject our null hypothesis based on the usual criteria (accept for $p \geq 0.05$ in this thesis).

4.2 Chiral continuum correlated fit results

Fit results for the preferred fit, a fully correlated fit to a linear fit form with $n_{E,X} = 1$, are shown in tables: 4.3 parameters; 4.4 statistical summary; and 4.5 form factors at q_0 and q^2_{max}. Discussion of other options is deferred to § 4.4.

form factor	c_0	c_1	d_0	e_0
f_0	0.781(20)	0.328(83)	-0.224(58)	0.128(14)
f_+	0.829(11)	0.180(72)	-0.184(46)	-0.150(11)

Table 4.3 *Global chiral continuum fit results. Parameters match fit form (4.1). Parameter $c_{+,0}$ (blue) is implemented as a constraint per (4.26), not a free parameter. The expansion in E_L/Λ is linear, i.e. $n_{E,X} = 1$.*

Table 4.4 shows that the global fit has an acceptable Hotelling p-value. As noted at the end of § 4.1.2, 5 data points have been cut from the fit (on the basis they are not independent) leaving 53 data points in the fit.

N_{data}	N_{param}	ν	t_ν^2	Hotelling p-value
53	7	46	2.04	0.0543

Table 4.4 *Statistical summary of chiral continuum fit: number of data points N_{data}; number of parameters N_{param}; number of degrees of freedom $\nu = N_{data} - N_{param}$; Hotelling test statistic per degree of freedom t_ν^2; and Hotelling p-value.*

The correlation matrix for the fitted parameters is shown in fig 4.7. For parameters c_1 (parameterising the pion mass mis-tuning) and d_0 (parameterising discretisation errors) we observe that correlations appear to be independent of form factor (i.e. rows or columns involving c_1 or d_0 repeat twice) – i.e. input pion masses and discretisation effects are global in nature and positively correlated.

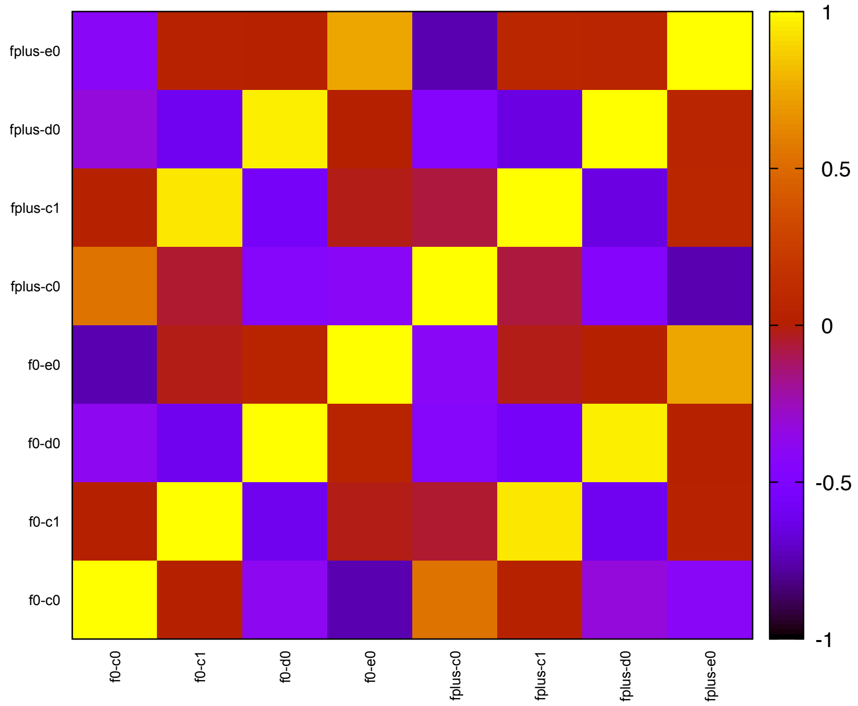

Figure 4.7 *Correlation matrix of fitted parameters. Parameters names consist of the form factor ('f0' for f_0 or 'fplus' for f_+) followed by a hyphen and the parameter name.*

Table 4.5 shows form factors extrapolated to kinematic points q_0 and q^2_{max}.

$f_X\left(q^2\right)$	result(stat)	$\delta\%$
$f_0\left(0\right)=f_+\left(0\right)$	0.6557(75)	1.1%
$f_0\left(q^2_{\text{max}}\right)$	1.000(10)	1.0%
$f_+\left(q^2_{\text{max}}\right)$	1.592(16)	1.0%

Table 4.5 *Form factors at kinematic points $q_0 = 0$ and q^2_{max} from chiral continuum fit results in table 4.3. The result for each form factor $f_X\left(q^2\right)$ is shown with statistical errors in brackets. The $\delta\%$ column shows the relative statistical error expressed as a percentage.*

Form factor fit results covering the entire kinematic range are shown in fig 4.8 and fig 4.9. Data points shown are the raw data points entering the fit. The continuum fit result $f_X^{(\text{cont})}$ (4.2) is the brick-red line with the blue statistical error band.

The kinematic point q_0 – associated with maximum recoil of a physical-mass final-state kaon, $E^{\text{p}}_{K,\text{max}} \simeq 1.0466$ GeV [using (1.204) and data from § 4.1] – is indicated with the vertical dotted line. The vertical dashed line indicates the physical zero recoil point $q^{(\text{p})2}_{\text{max}}$, where $E^{\text{p}}_K = m^{\text{p}}_K$.

It is worth noting that the leftmost six data points in fig 4.8 are zero-momentum kaons (one for each ensemble). Reading off their masses from the horizontal scale, we see they are all heavier than physical (vertical dashed line).

The rightmost 5 data points in fig 4.9 for the ensembles C1, C2, M1, M2 and M3 lie close to q_0 and just outside the physical ($q^2 \geq 0$) region. For reasons explained at the end of § 4.1.2, they are not independent from the corresponding data points for f_0, which is why they have been excluded from fig 4.8.

The coloured, dashed trend lines are the full prediction $f_X = f_X^{(\text{cont})} + f_X^{(\text{lat})}$ (4.1) for each ensemble (matching the colour in the legend). That is the coloured trend lines show the continuum fit form with the lattice components included: pion mass mis-tuning; chiral logs; finite volume corrections; and discretisation effects.

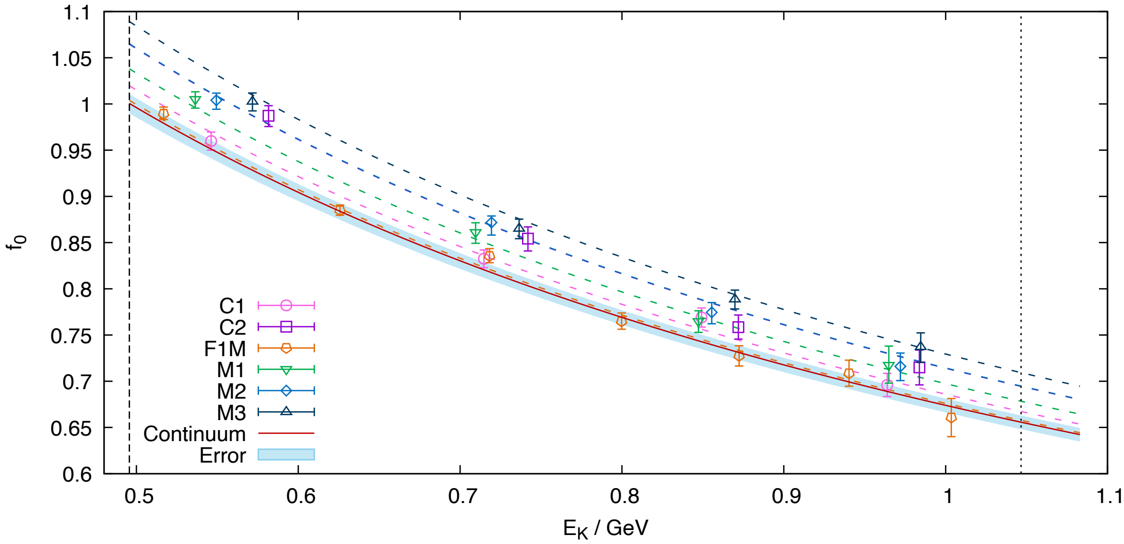

Figure 4.8 *Data points entering the chiral continuum fit for scalar form factor f_0. The form factor is shown on the vertical axis, with the energy of the final-state kaon E_K in GeV on the horizontal axis. Statistical errors only (blue band) are shown for the continuum fit result (brick red). Coloured, dashed trend lines show $f_X = f_X^{(cont)} + f_X^{(lat)}$ for each ensemble. The trend line for the C2 ensemble is underneath the trend line for the M2 ensemble. The vertical dotted line indicates $E^p_{K,max}$ (i.e. q_0).*

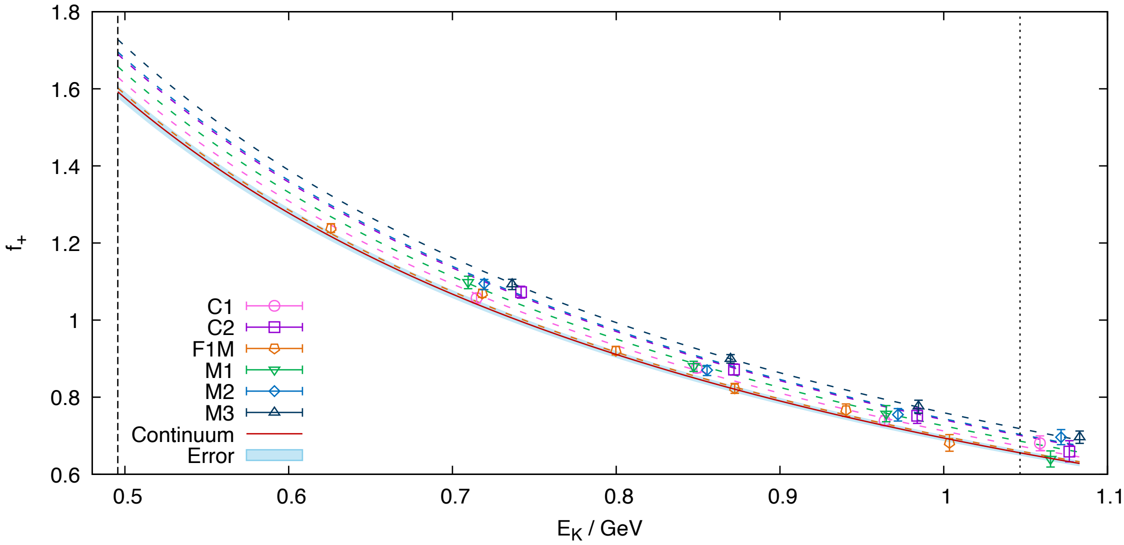

Figure 4.9 *Data points entering the chiral continuum fit for vector form factor f_+ (and otherwise as described in figure 4.8). The trend for ensemble C2 is visible immediately underneath the M2 trend.*

In order to more clearly show the compatibility of each data point with the chiral continuum fit result, in figures 4.10 and 4.11 the data points adjusted by the fitted lattice corrections $f_X^{\text{(lat)}}$ (4.2) are shown – with the pole removed (which makes better use of the vertical scale). That is we plot adjusted data points f'_X

$$f'_X = \left(\frac{E_L + \Delta_{xy,X}}{\Lambda}\right)\left(f_X - f_X^{\text{(lat)}}\right) . \tag{4.30}$$

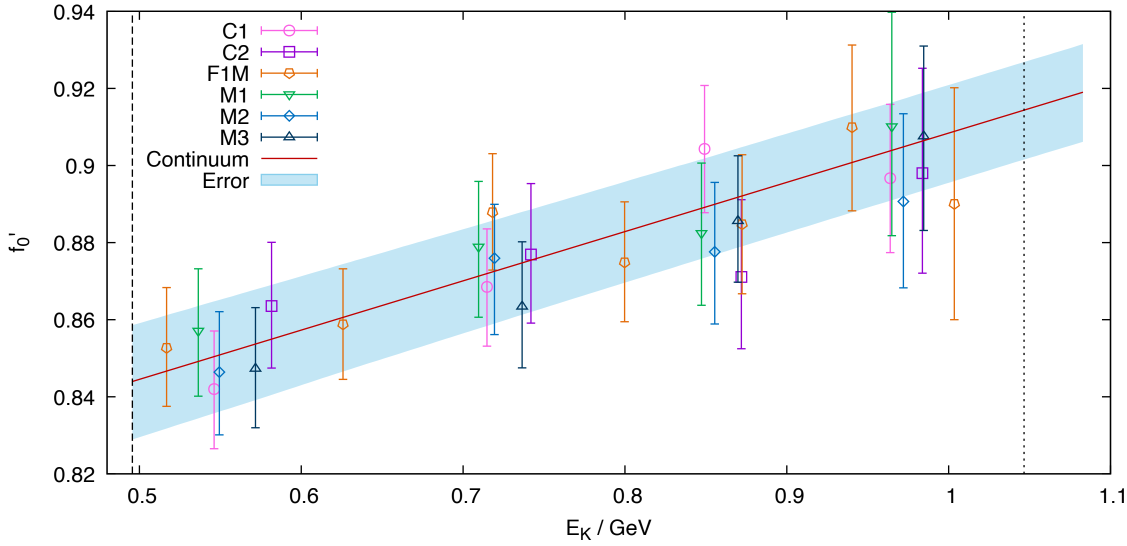

Figure 4.10 *Plot of adjusted data points f'_0 (4.30) – i.e. adjusted by $f_0^{(lat)}$ and with the pole removed (otherwise as described in fig 4.8). These data points agree very well with the chiral continuum fit.*

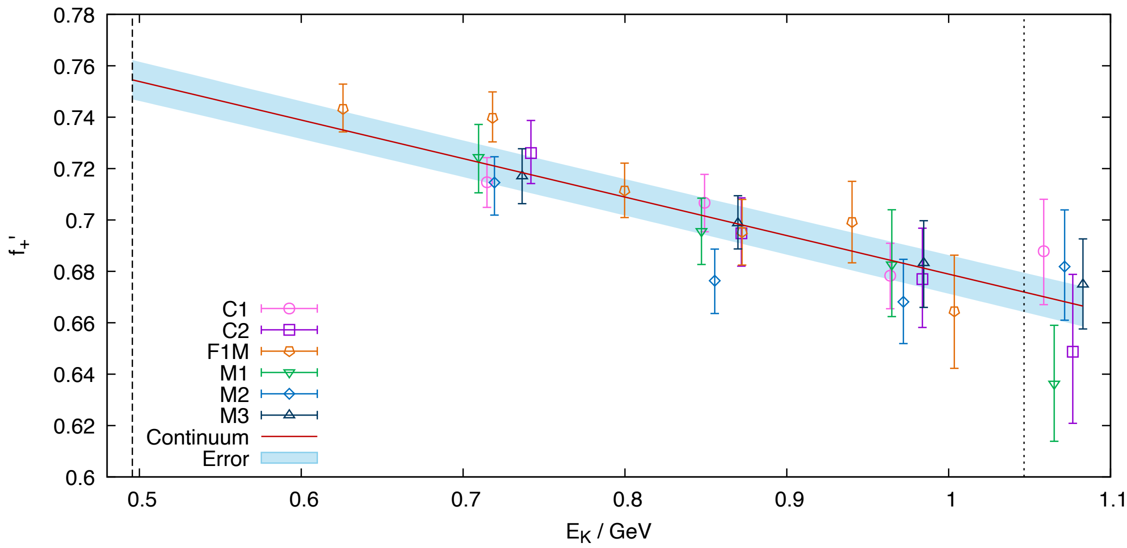

Figure 4.11 *Plot of adjusted data points f'_+ (4.30) – i.e. adjusted by $f_+^{(lat)}$ and with the pole removed (otherwise as described in fig 4.8). There is a moderate increase in tension with the global fit, however there is still very good agreement.*

The adjusted data points agree very well with the chiral continuum fit. More of a spread is observed in the data points near q_0, however, this is unsurprising given that these data points are constructed from 2- and 3-point functions with the greatest Fourier momenta, i.e. the least precise data in this data set.

The data points entering the chiral continuum fit were examined very closely, with a large number of alternate fits attempted in order to extract the $f_\parallel$ and $f_\perp$ data contributing to these data points. It was not possible to improve the quality of this fit by improving the quality of the underlying fits. Thus, it was concluded that the spread of data points here are statistical in nature and a function of the limited data available for this study. An estimate of systematic error due to underlying fit choices (amongst other things) is made in the next section.

4.3 Systematic uncertainty

Systematic uncertainty is quantified by constructing a set of alternate global fits and examining their impact on the global fit result. Alternate fits probe:

- Finite volume corrections;
- Pole locations;
- Renormalisation;
- Underlying matrix element fits; and
- Data cuts.

Fit alternatives (a)–(g) consist of reasonable alternative choices that could have been made to the reference fit. The systematic uncertainties arising from each are added in quadrature to arrive at the systematic error quoted for the final result.

(a) Omit the finite volume correction term δf^{FV} (1.269)

$$\delta f^{\mathrm{FV}}(M) = \frac{4M}{L} \sum_{|\mathbf{n}|\neq 0} \frac{K_1\left(|\mathbf{n}|ML\right)}{|\mathbf{n}|} \,. \tag{4.31}$$

(b) Make reasonable changes to both the vector and scalar pole masses entering the fit. Since both the strange and charm quark fields are tuned to their physical masses, the mass of the light is used to interpolate between the pole mass that should enter the fit and the equivalent meson with $\ell \to s$. That is, an approximate simulated $M^{\text{sim}}_{D^*_x}$ mass is computed using residual masses am_{res} from [4, 99]

$$M^{\text{sim}}_{D^*_x} = \frac{am_\ell + am_{\text{res}}}{am_s + am_{\text{res}}} \left(M_{D^*_{xs}} - M_{D^*_x}\right) + M_{D^*_x} \,. \tag{4.32}$$

Ensemble	am_{res}	ℓ/s bare	$M^{\text{sim}}_{D^*_0}$	$\Delta_{\ell s,0}$	$M^{\text{sim}}_{D^*}$	$\Delta_{\ell s,+}$
C1	0.003154	0.23	2337.2	327.6	2032.4	-10.65
C2	0.003154	0.37	2333.6	313.2	2047.1	-5.64
M1	0.0006697	0.18	2338.4	331.7	2027.6	-12.96
M2	0.0006697	0.26	2336.4	325.8	2035.7	-8.14
M3	0.0006697	0.34	2334.4	317.1	2043.9	-6.05
F1M	0.0002356	0.11	2340.3	339.3	2019.6	-15.96
extremal				313.2		-5.64

Table 4.6 *For each ensemble, the residual mass am_{res} and the ratio from (4.32) in ℓ/s bare are shown. For each of the scalar and vector channels, the estimate of simulated pole mass $M_{D^*_x}$ and pole term $\Delta_{\ell s,X}$ are shown. The extremal values of $\Delta_{\ell s,X}$ (final column) are used for pole location fit variations.*

(c) The vector pole $\Delta_{\ell s,+}$ is shifted to the extremal value from table 4.6 while keeping the scalar pole at its physical value. It is instructive to see the contribution to (b) arising from shifts to the vector pole. However, this alternative is not included in the systematic uncertainty estimate to avoid double counting.

(d) The scalar pole $\Delta_{\ell s,0}$ is shifted to the extremal value from table 4.6 while keeping the vector pole at its physical value. Again, it is instructive to see the contribution to (b) arising from shifts to the scalar pole. However, this alternative is not included in the systematic uncertainty estimate to avoid double counting.

(e) Assess the impact of the alternate $Z_{V,\text{hh}}$ fits shown in table 4.7. This alternative extracts $Z_{V,hh}$ using (2.95) for the heavy action on the medium ensembles using the light spectator (instead of the strange) and a wall separation $\Delta T/a = 20$ (instead of 24). Full details, see appendix A.9.

	heavy			light			mixed
Name	aE_0 $[D_s]$	p-value	Z_V	aE_0 $[K]$	p-value	Z_V	Z_V
M1	0.82568(57)	0.71	0.9964(80)	0.22449(85)	0.63	0.7412(51)	0.8532(76)
M2	0.82567(68)	0.078	1.0211(82)	0.23064(55)	0.82	0.7549(60)	0.8809(80)
M3	0.82554(62)	1.00	1.0022(96)	0.23852(68)	0.348	0.7414(57)	0.8636(79)

Table 4.7 *Alternative fit option (e). Mostly nonperturbative renormalisation results for medium ensembles using the light spectator to extract* $Z_{V,hh}$*, for comparison with reference renormalisation results in table 2.12.* Z_V *is computed per (1.182) taking* $\rho = 1$*, i.e.* $Z_{V,m} = \sqrt{Z_{V,h} Z_{V,\ell}}$*. Error propagation for* $Z_{V,m}$ *comes from the bootstrap.*

(f) As mentioned in § 3.1.1, one of the criteria for matrix element fit selection is that multiple choices must be possible while retaining compatible (i.e. within 1-σ) matrix element results. This alternative assesses global fit sensitivity to differing underlying matrix element fit results on $C1$, per table 4.8. The alternate fit range choices are listed in table 4.10.

n^2	aE_K	$(aq)^2$	$\langle K \vert \mathcal{V}_4 \vert D_s \rangle$	$\langle K \vert \mathcal{V}_i \vert D_s \rangle$	$f_\parallel \sqrt{a}$	$f_\perp / \sqrt{a}$	f_0	f_+
0	0.30601(47)	0.6368(11)	1.355(15)		0.9119(99)		0.961(10)	0.6137(67)
1	0.40046(35)	0.42829(90)	1.138(21)	0.4457(95)	0.766(14)	1.146(24)	0.813(14)	1.058(17)
2	0.47578(29)	0.26197(78)	1.088(25)	0.3485(71)	0.732(17)	0.896(18)	0.764(15)	0.871(15)
3	0.54006(26)	0.12005(69)	0.953(34)	0.2965(74)	0.641(23)	0.762(19)	0.677(19)	0.721(18)
4	0.59320(23)	0.00271(62)	1.002(47)	0.274(10)	0.674(32)	0.705(26)	0.695(24)	0.696(24)

Table 4.8 *Form factor results for alternate fits (f) on ensemble C1 for comparison with table 4.9. For each integer lattice momentum* n^2*, the kaon energy* aE_K*,* D_s *mass* am_{D_s} *and vertex momentum* $(aq)^2$ *are shown. The renormalised temporal and spatial matrix elements* $\langle K|\mathcal{V}_4|D_s\rangle$ *and* $\langle K|\mathcal{V}_i|D_s\rangle$ *are then used to compute* $f_\parallel$*,* $f_\perp$*,* f_0 *and* f_+ *per (3.18), (3.19), (3.21) and (3.22).*

n^2	aE_K	$(aq)^2$	$\langle K \vert \mathcal{V}_4 \vert D_s \rangle$	$\langle K \vert \mathcal{V}_i \vert D_s \rangle$	$f_\parallel \sqrt{a}$	$f_\perp / \sqrt{a}$	f_0	f_+
0	0.30601(47)	0.6368(11)	1.353(14)		0.9108(92)		0.9599(98)	0.6129(62)
1	0.40046(35)	0.42829(90)	1.175(14)	0.4312(68)	0.7909(94)	1.109(18)	0.8325(96)	1.057(13)
2	0.47578(29)	0.26197(78)	1.095(16)	0.3493(74)	0.737(11)	0.898(19)	0.769(10)	0.876(13)
3	0.54006(26)	0.12005(69)	0.987(22)	0.2991(71)	0.664(15)	0.769(18)	0.696(13)	0.739(13)
4	0.59320(23)	0.00271(62)	0.969(35)	0.273(11)	0.652(24)	0.703(27)	0.680(19)	0.681(19)

Table 4.9 *Form factor results for reference fits on ensemble C1 (repeat of table 3.13) (same format as table 4.8).*

n^2	reference		alternate	
	$\Delta T/a$	t	$\Delta T/a$	t
$\langle K\|\gamma_4\|D_s\rangle$				
0	16, 20 and 24	6-11, 6-14 and 6-18	20, 24 and 28	9-14, 11-18 and 13-18
1	16, 20 and 24	8-10, 9-14 and 10-18	20, 24 and 28	11-12, 14-15 and 13-17
2	16 and 20	6-11 and 6-14	20, 24 and 28	8-12, 12-16 and 16-19
3	16 and 20	6-11 and 6-14	20, 24 and 28	8-14, 12-16 and 16-19
4	16 and 20	6-10 and 6-14	20 and 24	8-14 and 12-16
$\langle K\|\gamma_i\|D_s\rangle$				
1	16, 20 and 24	9-11, 9-15 and 9-19	20, 24 and 28	12-14, 15-17 and 13-17
2	16 and 20	8-11 and 9-15	16, 20 and 24	8-11, 9-15 and 8-19
3	16, 20 and 24	7-11, 7-14 and 7-18	16, 20 and 24	8-11, 9-15 and 8-19
4	16 and 20	7-11 and 9-15	16, 20 and 24	7-11, 9-15 and 8-19

Table 4.10 *Comparison of the fit ranges (wall separations $\Delta T/a$ and timeslices t) at each integer lattice momentum n^2 between the reference fit and alternate fit (l) on ensemble C1.*

(g) Omit the data points with the highest integer lattice momentum n^2 on both coarse ensembles, i.e. the last rows of tables 3.13 and 3.14. Note that many alternative fits were tested dropping different data points from different ensembles – there was no qualitative difference to the fit results and this is included as a representative example.

4.3.1 Data cuts

Alternatives (h)–(m) consist of omitting all data points on one or more ensembles. These data cuts were considered unrepresentative of systematic effects and were excluded from the final systematic uncertainty and in many cases the resulting fit p-values are marginal. It is, nevertheless, instructive to note that for many of these fits the impact on the global fit result is substatistical. For the most extreme data cuts, the effect is only mildly greater than statistical error.

An alternate fit omitting all the data points on the fine ensemble (F1M) is not included, as to do so would omit an entire lattice spacing – the finest lattice spacing – consisting of data with the lightest pions. Eliminating the F1M data from the global fit would mean disregarding the most expensive data to produce (in computer time) which is also closest to the chiral continuum limit. This was also considered unrepresentative of systematic effects and excluded from the set of 'reasonable' alternate fits.

(h) Omit all data points on the C1 ensemble, i.e. half of the coarse lattice spacing data and approximately 1/6th of the entire data set. After this cut only a single coarse ensemble remains, hence all of the chiral, light-mass dependence in the global fit is determined from the medium ensembles.

(i) Similar to (h), but omit all data points on the C2 ensemble.

(j) Omit all data points on the M1 ensemble, i.e. 1/3rd of the medium lattice spacing data and 1/6th of the data set. Two medium and two coarse ensembles remain after the cut, the effect of which is benign.

(k) Similar to (j), but omit all data points on the M2 ensemble.

(l) Similar to (j), but omit all data points on the M3 ensemble.

(m) Omit data from all the medium ensembles, M1, M2 and M3, i.e. omit approximately half the data set and an entire lattice spacing. Data from finer and coarser lattice spacings and for both heavier and lighter simulated pion masses remain.

4.3.2 Residual discretisation effects

(n) The chiral continuum fit form (4.3) includes a term for discretisation effects of $\mathcal{O}(a^2)$. For the single, $\mathcal{O}(a)$ improved DWF action used in this thesis, residual discretisation effects not included in the model are expected to be of $\mathcal{O}(a^4)$.

In order to quantify residual discretisation effects, the fit ansatz was modified to include an additional term $d_{X,2}a^4$. However, to the level of statistical precision of the result, no residual discretisation term could be resolved in the fit.

As a check, a power counting estimate of residual discretisation effects is made following the procedure outlined by [86, 110]:

- $d_{X,2}$ takes the same magnitude as d_X;
- the relevant scale that enters is $\Lambda_{\text{QCD}} = 500$ MeV; and
- discretisation effects are constrained by the finest ensemble.

Results for the power counting estimate are shown in table 4.11. Given the negligible size of these effects and the negative result in the fit, residual discretisation effects are not included in the final systematic error.

$f_X\left(q^2\right)$	result(stat)(disc)	δ_{disc}
$f_+\left(q^2_{\text{max}}\right)$	$1.592(16)_{\text{stat}}(0)_{\text{disc}}$	0.03%
$f_0\left(q^2_{\text{max}}\right)$	$1.000(10)_{\text{stat}}(0)_{\text{disc}}$	0.03%
$f_0(0) = f_+(0)$	$0.6557(75)_{\text{stat}}(2)_{\text{disc}}$	0.03%

Table 4.11 *Residual discretisation effects from power counting estimate for form factors f_0 and f_+ at the kinematic points q_0 and q^2_{max}. Form factor result, statistical and discretisation errors shown in 'result(stat)(disc)', relative discretisation error per (4.33) in 'δ_{disc}'.*

4.3.3 Systematic uncertainty results

The relative error introduced by each of the alternative fits (x) is constructed for each fit $\delta f_X^{(x)}$ as a function of the final-state kaon energy E_K, where at each energy $f_X^{(x)}$ (the form factor for fit x) is compared with the reference fit using

$$\delta f_X^{(x)}\left(E_K\right) = \frac{\left|f_X^{(x)}\left(E_K\right) - f_X\left(E_K\right)\right|}{f_X\left(E_K\right)} . \tag{4.33}$$

The results are shown in figures 4.12 and 4.13, where the grey background indicates the statistical error, and dashed and dotted lines indicate alternatives not included in final systematic error result.

As set out in § 4.3, alternatives (h) and (m) involve large data cuts which would be expected to differ significantly from the preferred fit results. Reassuringly these alternatives yield results only marginally greater than 1σ from the preferred fit. Option h (dashed violet line), excluding data for the C1 ensemble, has a slightly greater than statistical effect in f_0 and f_+ for higher kaon energies. The effect of option m (dashed blue line), excluding data for the medium ensembles (M1, M2 and M3), is marginally greater than statistical in the extrapolation region of f_0, i.e. low kaon energies.

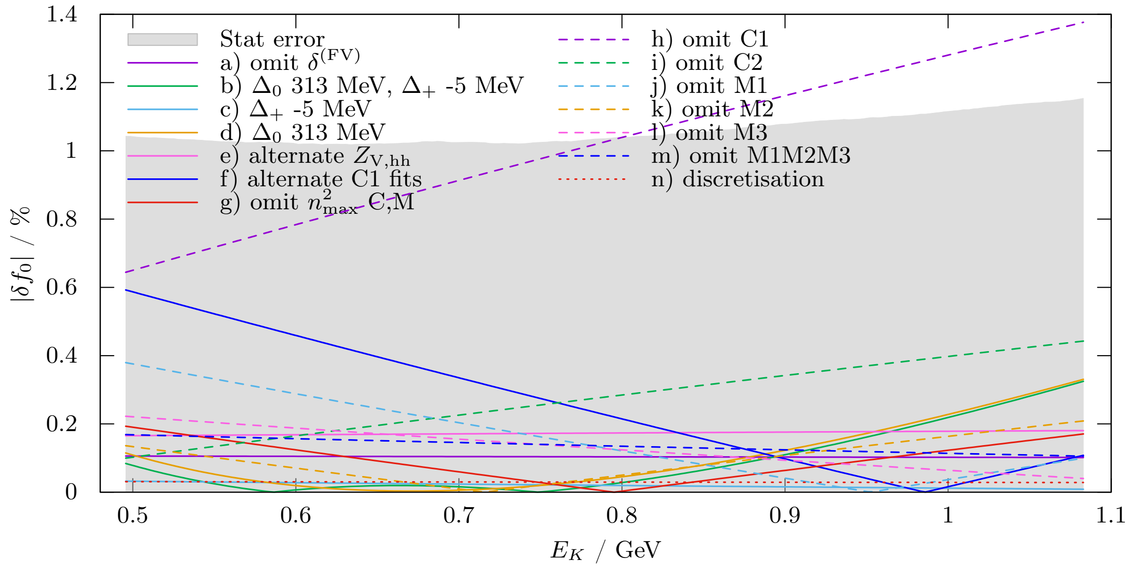

Figure 4.12 *Relative error $\delta f_0^{(x)}(E_K)$ (vertical axis, %) (4.33) associated with each alternate fit choice (x) as a function of final-state kaon energy E_K (horizontal axis, GeV). The grey band is the statistical error of the reference fit. Dashed lines indicate alternatives not included in the final fit systematic uncertainty relative error (see § 4.3).*

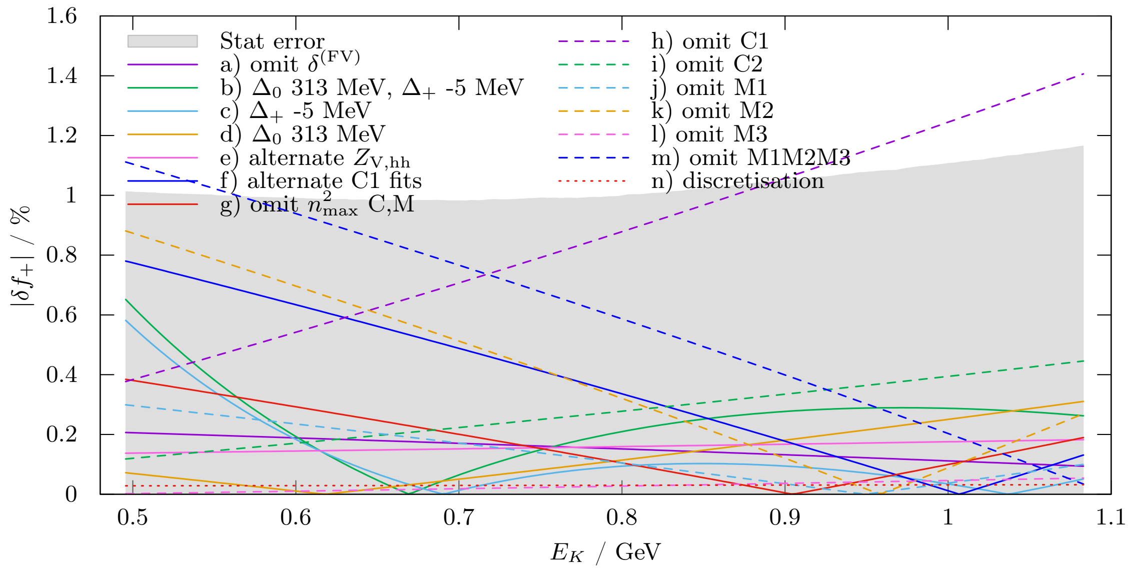

Figure 4.13 *Relative error $\delta f_+^{(x)}(E_K)$ (otherwise as described in fig 4.13).*

The fit characteristics are summarised in table 4.12. Hotelling p-values for some alternatives are marginally below threshold ($\alpha = 0.05$), although the fit form factor results are nevertheless compatible with the reference fit.

The largest contribution to systematic error comes from the use of alternative matrix elements fits (solid blue line). As expected, in the low kaon energy region of f_+ (i.e. the extrapolation region where there is no data point for $f_+(q^2_{\mathrm{max}})$) an increased sensitivity to the pole locations is seen. All of these effects are substatistical, indicating good control over potential sources of systematic error.

In conclusion, systematic error is dominated by statistical error.

	t^2	ν	t^2_ν	p-H	$f_0(0)$	$f_0(q^2_{\mathrm{max}})$	$f_+(q^2_{\mathrm{max}})$
Ref	93.783	46	2.03877	0.0542715	0.6557(75)	1.000(10)	1.592(16)
a	86.850	46	1.88805	0.10001	0.6564(75)	1.002(10)	1.596(16)
b	96.910	46	2.10676	0.0406097	0.6575(74)	1.001(10)	1.582(16)
c	95.562	46	2.07744	0.0460657	0.6556(74)	1.000(10)	1.583(16)
d	94.834	46	2.06162	0.0492766	0.6576(74)	1.002(10)	1.591(16)
e	93.231	46	2.02677	0.0570727	0.6545(76)	0.999(11)	1.590(17)
f	93.852	46	2.04028	0.0539274	0.6553(77)	1.006(11)	1.605(17)
g	83.787	41	2.04359	0.0401691	0.6547(77)	1.002(10)	1.598(16)
h	79.418	38	2.08997	0.06662	0.6469(98)	0.994(14)	1.586(21)
i	80.471	38	2.11768	0.0249405	0.6585(84)	1.001(12)	1.594(18)
j	83.651	38	2.20136	0.0170139	0.6562(78)	0.997(11)	1.588(17)
k	58.731	38	1.54556	0.241283	0.6545(77)	1.002(11)	1.606(17)
l	83.115	38	2.18724	0.0181603	0.6560(79)	1.003(11)	1.592(17)
m	43.091	22	1.9587	0.0350672	0.6564(98)	1.002(14)	1.610(22)

Table 4.12 *Fit characteristics for the reference fit, followed by each alternative fit. Columns are: test statistic t^2; degrees of freedom ν; test statistic per degree of freedom t^2_ν; Hotelling p-value p-H; $f_0(0) = f_+(0)$; $f_0(q^2_{max})$; and $f_+(q^2_{max})$.*

4.3.4 Final systematic uncertainty

The previous section quantified the sources of systematic uncertainty and determined that they are substatistical effects. The systematic errors of alternate fits (a), (b), (e), (f) and (g) are added in quadrature and quoted as the systematic error. The statistical and systematic errors are added in quadrature to form the total error. These are plotted as a function of final-state kaon energy in figures 4.14 and 4.15.

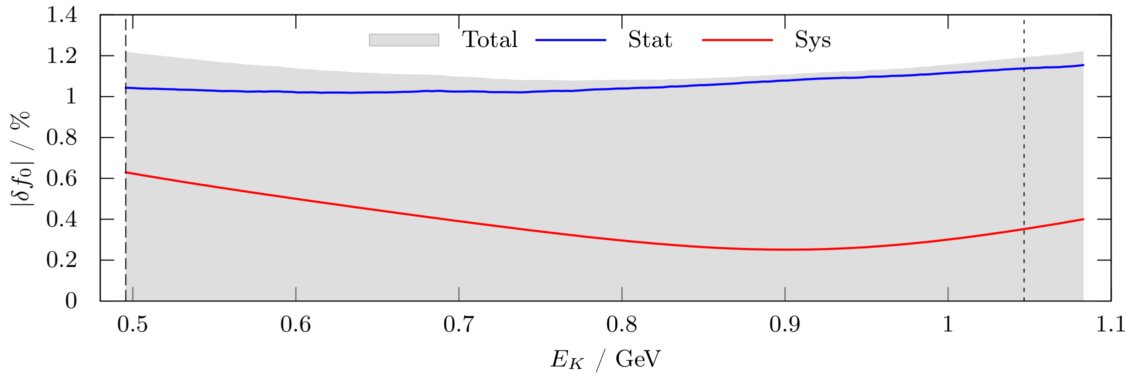

Figure 4.14 *Error budget for form factor f_0. Vertical scale shows relative error (%) for total (grey shading), statistical (blue) and systematic (red) errors as a function of final-state kaon energy E_K (horizontal axis, GeV). q^2_{max} and q_0 are indicated by the dashed and dotted vertical lines respectively.*

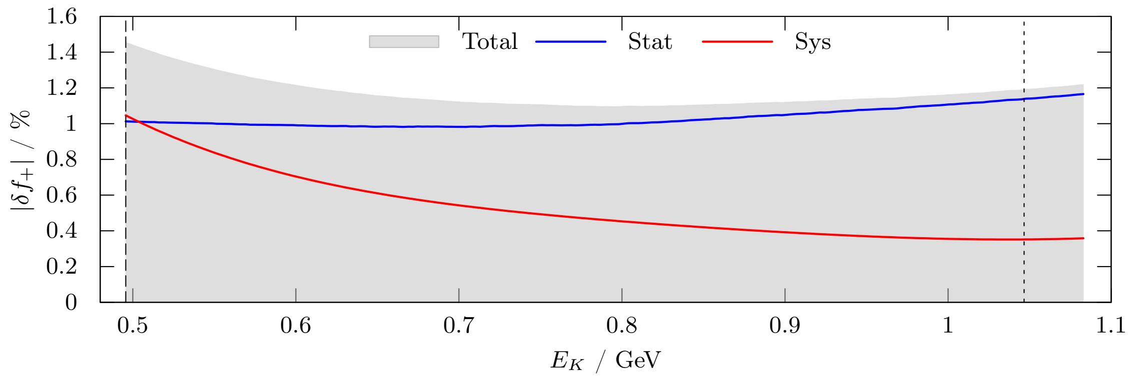

Figure 4.15 *Error budget for form factor f_+ (otherwise as described in fig 4.14).*

The statistical error is very similar across both form factors, varying between ∼1–1.2% and showing a very mild increase towards q_0. Statistical error dominates systematic error which varies between ∼0.3–1.0%. There is a very small region in f_+ near $q^2_{\rm max}$ where systematic errors are marginally greater than statistical errors. Total error varies between ∼1.1–1.5%.

Systematic error is larger in f_+ than f_0 showing a mild uptick in f_0 near q_0. Both form factors show an increase in statistical error in f_+ near $q^2_{\rm max}$ that is larger in f_+ than f_0.

Results at q_0 and q^2_{max} are shown in table 4.13.

$f_X\,(q^2)$	result(stat)(sys)	δ_{stat}	δ_{sys}	(total)	δ_{total}
$f_+\,(q^2_{\text{max}})$	$1.592(16)_{\text{stat}}(17)_{\text{sys}}$	1.0 %	1.0 %	$(23)_{\text{total}}$	1.5 %
$f_0\,(q^2_{\text{max}})$	$1.000(10)_{\text{stat}}(6)_{\text{sys}}$	1.0 %	0.63 %	$(12)_{\text{total}}$	1.2 %
$f_0\,(0) = f_+\,(0)$	$0.6557(75)_{\text{stat}}(23)_{\text{sys}}$	1.1 %	0.35 %	$(78)_{\text{total}}$	1.2 %

Table 4.13 *Statistical and systematic error budget for form factors f_0 and f_+ at the kinematic points q_0 and q^2_{max}. Form factor result, statistical and systematic errors shown in 'result(stat)(sys)', statistical and systematic relative error per (4.33) in 'δ_{stat}' and 'δ_{sys}'. Statistical and systematic errors are added in quadrature to form '(total)' error, shown as relative error in 'δ_{total}'.*

4.4 Alternative fit strategies

Having presented the preferred analysis, we return to the discussion of the choice to eliminate five data points from the fit and the alternatives considered.

The components of the scaled cost function (2.81) are

$$\Phi_i = \sum_j \left(L^T\right)_{ij} S^{-1}_{jj} \left(y_j - f_j\right) . \tag{4.34}$$

That is, each component Φ_i is scaled by S in order that the cost is in units of standard deviation and multiplied by the Cholesky decomposition of the inverse correlation matrix L so that correlations are accounted for.

When the full data set of 58 data points is fitted to a linear global fit model, the Hotelling p-value is 0. Examining the Φ_i, four data points are responsible for the 0 p-value, which is listed in table 4.14.

Ensemble	Form factor	n^2	Φ_i
C2	f_0	4	8.35
M1	f_0	4	-7.06
M2	f_0	4	-7.18
M3	f_0	4	-4.38

Table 4.14 *Data points from the full data set with large contribution to the fit cost function Φ_i (4.34).*

The options evaluated to deal with this issue were:

1. Drop these data points from the fit, together with the f_0 data point for C1 at $n^2 = 4$ (see discussion in § 4.1.2). This is the preferred fit.

2. Use Ledoit and Wolf shrinkage [111, 112] to condition the covariance matrix. Using this method, the estimate of the correlation matrix $\hat{\rho}$ is adjusted towards $\mathbb{1}$ where for a small parameter λ

$$\hat{\rho}_{\text{shrink}} = \lambda \mathbb{1} + (1 - \lambda)\,\hat{\rho}\,. \tag{4.35}$$

   It was found that $\lambda = 0.005$ was sufficient to produce an acceptable p-value (appendix A.6.1).

3. Fit to a model with more terms $n_{E,X}$ in the expansion of E_L/Λ. It was found that setting $n_{E,+} = 3$ while leaving $n_{E,0} = 1$ resulted in an acceptable p-value for the fit (appendix A.6.2).

Using a linear model and dropping the five data points from the fit is the best motivated of these three options. There is little evidence of curvature after pole removal (fig 4.11) and the data points at $n^2 = 4$ are the least precise, so little information is lost by discarding them.

In addition to the lack of evident curvature, the correlation matrix of the cubic f_+ model (fig A.50) shows that the parameters in the E_L/Λ expansion are highly correlated. It would appear more likely that the additional terms derived in this fit are artefacts of the correlation matrix, arising from the limited statistics of the underlying data points entering the fit.

The full Ledoit and Wolf procedure was not used to optimise the shrinkage term. Instead, a numerically small shrinkage factor λ was applied. This option was eliminated on the basis that it is preferable to use a covariance matrix that derives from the data – without adjusting its eigenvalue spectrum. By doing so any questions as to whether reported p-values are correct are avoided because there is a well-motivated reason for using the Hotelling distribution in its calculation.

Each analysis was performed end to end and results for the two alternative fit strategies can be seen in appendix A.6. The results were numerically compatible (table 4.15) – except for the cubic f_+ model in the region near $f_+\left(q^2_{\text{max}}\right)$, which is an extrapolation. In all cases, the sensitivity to systematic effects were qualitatively similar.

	fit	$f_0(0) = f_+(0)$	$f_0\left(q^2_{\text{max}}\right)$	$f_+\left(q^2_{\text{max}}\right)$
1.	preferred	0.6557(75)	1.000(10)	1.592(16)
2.	shrink	0.6556(75)	1.001(10)	1.593(15)
3.	cubic f_+	0.6533(76)	0.997(11)	1.550(20)

Table 4.15 *Results(statistical error) at kinematic points q_0 and q^2_{max} for the preferred fit and two alternatives. The results are compatible, except for the cubic f_+ model where the curvature in the model leads to a 2-σ discrepancy at $f_+\left(q^2_{max}\right)$. Note that this region is an extrapolation as we do not have access to data points for $f_+\left(q^2_{max}\right)$.*

Chapter 5

Conclusion and phenomenological implications

This section discusses the overall findings in this thesis and how they fit into the wider context.

Starting with the most directly relevant results for the exclusive semileptonic decay $D_s \to K$, the result from this thesis is compared with:

- The one theoretical prediction available from Fermilab Lattice and MILC Collaborations (Fermilab/MILC) published on 31 May 2023 [87] in § 5.1.
- The one experimental result from BESIII in 2019 [113] in § 5.2.

The discussion in § 5.3 examines theoretical predictions and experimental results available for other charm decays not presented in this thesis such as exclusive semileptonic $D \to \pi$ and $D \to K$ decays.

The outlook for the field as a result of this work is discussed in § 5.4.

5.1 Comparison with theoretical prediction

Table 5.1 compares the result in this thesis at q_0 and q^2_{max} to the one other theoretical prediction in the literature for $D_s \to K$ form factors, from Fermilab Lattice and MILC Collaborations (Fermilab/MILC) published on 31 May 2023 [87]. In both cases, these are predictions for isospin symmetric QCD with degenerate light quarks of equal mass $m_\ell = (m_u + m_d)/2$ and ignoring quantum electrodynamics (QED) effects. They can thus be compared directly.

	fit result		Fermilab/MILC [87]	
$f_X(q^2)$	result(total)	δ	result(stat+sys)	δ
$f_+(q^2_{\mathrm{max}})$	$1.592(23)_{\mathrm{total}}$	1.5%	1.576(16)	0.99%
$f_0(q^2_{\mathrm{max}})$	$1.000(12)_{\mathrm{total}}$	1.2%	0.9843(30)	0.30%
$f_0(0) = f_+(0)$	$0.6557(78)_{\mathrm{total}}$	1.2%	0.6307(29)	0.46%

Table 5.1 *Comparison of the fit result in this study at q_0 and q^2_{max} with Fermilab/MILC 31 May 2023 [87]. δ is total relative error %.*

5.1.1 Precision

The Fermilab/MILC prediction is a factor 1.5–4× more precise than this study, varying over the kinematic range. The inclusion of ensembles with physical pion masses will have contributed to this increased precision.

The Fermilab/MILC prediction also included 24–36 sources per configuration with 697–1352 configurations per ensemble, i.e. $\mathcal{O}(200)\times$ the statistics of the work in this thesis. However, the use of different actions means these statistical counts cannot be compared directly in a meaningful way.

What can be said to compare the statistics of the two studies is that Fermilab/MILC found it necessary to employ Ledoit and Wolf shrinkage [111, 112] to adjust the fit covariance matrices whereas the statistics of this thesis allowed the sample covariance matrices to be constructed directly from the data without adjustment. Fermilab/MILC's use of linear shrinkage estimators and novel nonlinear estimation techniques are used to contend with marginal statistics.

The data from the 2- and 3-point functions underpinning this thesis are more precisely known at smaller Fourier momenta, i.e. near q^2_{max}. Nevertheless, after the global fit, the statistical precision near q^2_{max} is only marginally better than near q_0 (around 1% in both cases). This reflects the accuracy of the covariance matrices employed in the fit, weighing the more precise data more heavily in the minimisation of the global cost function. Including systematic effects, we have a slight increase in total error in f_+ near q^2_{max}. This region is an extrapolation as we do not have access to f_+ at exactly $q^2_{\rm max}$ on the lattice.

Fermilab/MILC's form factor determination has a much more pronounced inflation of relative error at $f_0\left(q^2_{\rm max}\right)$, being twice the relative error of $f_0\left(0\right)$ and $f_0\left(q^2_{\rm max}\right)$. It is possible that the greater statistical accuracy of the measurements entering the fit make the effects of the extrapolation at this point more apparent.

The relative effect of the extrapolation in f_+ appears milder at the precision of this thesis. Figures 4.14 and 4.15 show that the result from this study has a moderate uptick in relative error at each end of the kinematic range, but with an uptick near $q^2_{\rm max}$ that is more pronounced in f_+ than f_0.

As noted in § 3.2.2, this work has an advantage over other studies such as [87]. The range of wall separations for 3-point data is wide enough to ensure R_3 ratio results without excited state contamination are produced. We are, therefore, certain the ground-state matrix elements of interest are being extracted, even though those matrix elements are extracted at narrower wall separations to minimise statistical error.

5.1.2 Central value

In figure 5.1 we show (left to right across each of the three panels):

1. The experimental result from BESIII [113].
2. The theoretical prediction in this thesis.
3. The theoretical prediction from Fermilab/MILC [87].

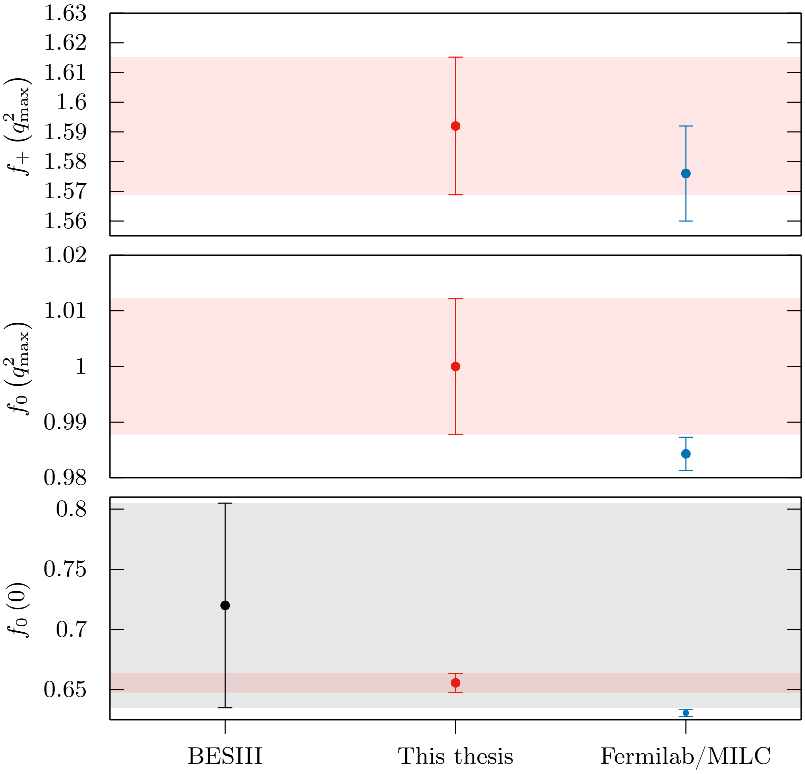

Figure 5.1 *Comparison of the theoretical prediction in this thesis (center) with the theoretical prediction from Fermilab/MILC [87] (right) and the experimental result from BESIII [113] (left). The BESIII result is only available at q_0 and is shown in the bottom panel as the black data point with grey error band. Results from this thesis are shown as red data points with pink error bands. Fermilab/MILC results are the blue data points. Errors bands are total error.*

For $f_+ (q^2_{max})$ (fig 5.1 top panel) the two predictions agree. Similarly the two predictions agree at the level of $\sim 1\sigma$ for $f_0 (q^2_{max})$ (middle panel).

The experimental result is only available for the kinematic point q_0 (bottom panel) and has large uncertainty of $\sim 12\%$. Both lattice predictions for $f_0 (0)$ agree with the BESIII result (grey band), but are in mild tension with each other at $\sim 3\sigma$. The Fermilab/MILC prediction at q_0 is $3\times$ more precise than this thesis and sits marginally more than 1σ from the BESIII result. Both theoretical predictions are much more precise than the experimental result, with both suggesting a value towards the lower end of the 1σ confidence interval in the experimental result.

This is quite a significant agreement for two independent theoretical predictions using different actions and independent analyses employing quite different methods, e.g.: bayesian fits with priors vs no priors; shrinkage vs no shrinkage; χ^2

vs Hotelling distributions; and z-expansion vs no z-expansion. It is worth noting (although beyond the scope of this thesis to explain) that the staggered fermion action in the Fermilab/MILC study has the complication that the spatial and temporal vector currents are treated differently.

The 3σ tension at $f_+(0)$ occurs in the region where the underlying lattice data are least precise – although the constraint $f_+(0) = f_0(0)$ improves the accuracy of fit results near q_0. Given the constraints imposed by time limitations on this thesis, a 3σ tension does not warrant a detailed analysis at this point. Rather, it would be prudent to address the limitations by:

1. Introducing ensembles with physical mass pions;
2. Increasing the statistics of this study; and
3. Analysing the $D \to \pi$ and $D \to K$ data.

Once this is done, remaining tensions can be explored. Knowledge of the additional $D \to \pi$ and $D \to K$ form factors would also allow comparison with a larger number of theoretical predictions – where the experimental result is known with greater precision.

5.2 Comparison with experimental result and extraction of $|V_{cd}|$

The one experimental result in the literature is from BESIII in 2019 [113]. They quote their measured result for the product

$$|V_{cd}|f_+(0)^{\mathrm{BESIII}} = 0.162(19)_{\mathrm{stat}}(03)_{\mathrm{sys}} \tag{5.1}$$

and using $|V_{cd}| = 0.22492(50)$ from PDG they state their experimental determination of the form factor f_+ at q_0

$$f_+(0)^{\mathrm{BESIII}} = 0.720(84)_{\mathrm{stat}}(13)_{\mathrm{sys}}\,. \tag{5.2}$$

The experimental uncertainties at $\sim 12\%$ are large – much larger than strong isospin breaking effects at around 1% and QED corrections at around 0.5% [87]. Given the lack of precision, we simply note that strong isospin breaking and QED effects are subleading and have not been included in the lattice prediction.

Combining the BESIII result (5.1) with the prediction for $f_+(0)$ from this thesis multiplicatively (assuming no correlations) we obtain as the prediction for $|V_{cd}|$

$$|V_{cd}| = 0.247(29)_{\text{expt}}(03)_{\text{theory}} \,. \tag{5.3}$$

As of 2022, PDG quotes the value for $|V_{cd}|$ from semileptonic decays $|V_{cd}|^{\text{PDG}}_{\text{semi}}$

$$|V_{cd}|^{\text{PDG}}_{\text{semi}} = 0.2330(29)_{\text{expt}}(133)_{\text{theory}} \tag{5.4}$$

and the value from leptonic decays $|V_{cd}|^{\text{PDG}}_{\text{lep}}$

$$|V_{cd}|^{\text{PDG}}_{\text{lep}} = 0.2181(49)_{\text{expt}}(07)_{\text{theory}} \,, \tag{5.5}$$

both of which match the value from this thesis within 1σ.

At 1.2%, the relative theory error from this work is around $4\frac{1}{2}\times$ smaller than the relative theory error for the current PDG semileptonic determination at 5.7%.

5.3 Charm semileptonic decays

The work presented in this thesis focuses on the $D_s \to K$ channel of exclusive semileptonic decays, for which experimental results became available from BESIII in 2019 [113].

Other charm semileptonics programs (listed below), have hitherto focussed on the $D \to \pi$ and $D_s \to \pi$ channels, owing to the availability of experimental results. It is useful, therefore, to survey contemporary lattice predictions available from other collaborations. These are summarised in fig 5.2, grouped by the number of flavours N_f in the sea, following the Flavour Lattice Averaging Group (FLAG) [114]:

- $N_f = 2$ – ETM collaboration [115].
- $N_f = 2 + 1$:

- Fermilab Lattice Collaboration, MILC Collaboration, and HPQCD Collaboration [116, 117],
- HPQCD Collaboration [118–121],
- JLQCD Collaboration [122].

- $N_f = 2 + 1 + 1$:
  - ETM collaboration [123, 124],
  - HPQCD Collaboration [125],
  - Fermilab/MILC [87] (the result discussed in § 5.1 also included results for $D \to \pi$ and $D \to K$).

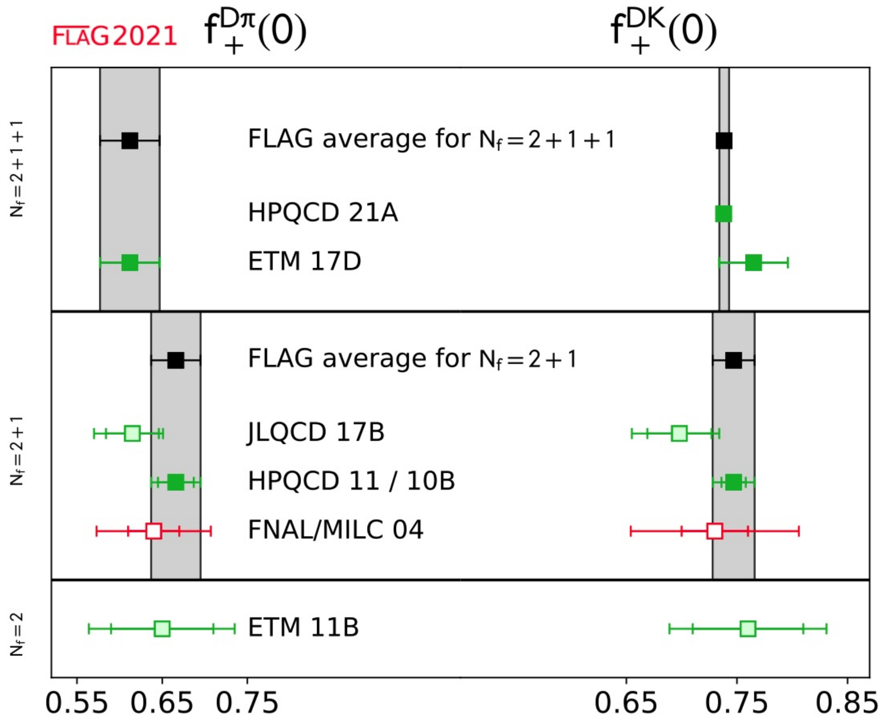

Figure 5.2 *Summary of lattice predictions for $D \to \pi$ and $D \to K$ form factors from the FLAG 2021 review [114].*

Of immediate relevance is the $D \to \pi$ channel, which differs from the $D_s \to K$ channel presented in this thesis only by the spectator; light or strange, respectively. That is, both channels involve the same charm to light weak decay mediated by the $W^{\pm}_{\mu}$.

Fermilab/MILC observe [87] that in the calculation of the form factors for hadronic matrix elements for these two channels, only the mass of the valence spectator quarks differ. Fermilab/MILC's results – and available experimental results from BESIII – for these two channels differ by only 2%.

The work in this thesis forms part of the RBC/UKQCD Collaboration's wider charm semileptonic programme. The methods developed here will be applied to the $D \to \pi$ and $D_s \to \pi$ channels, for which data have already been produced on the ensembles presented here. Further data generation is underway for all three channels (i.e. including $D_s \to K$), including lattices with physical mass pions.

Related work [126, 127] is also ongoing for inclusive heavy meson decays (i.e. decays involving all possible final states). However, inclusive semileptonic decays are not planned as part of RBC/UKQCD's programme of work.

5.4 Outlook

We see from (5.4) that error in the current PDG semileptonic determination $|V_{cd}|^{\text{PDG}}_{\text{semi}}$ is theory dominated. FLAG's 2021 review [114] shows this is more generally true, i.e. that charmed "meson decay errors are largely theory-dominated, save for the $D \to K$ mode for $N_f = 2 + 1 + 1$."

We show that the theory error on the prediction for $|V_{cd}|$ is $4\frac{1}{2}\times$ smaller than that of the currently published value for $|V_{cd}|^{\text{PDG}}_{\text{semi}}$. If the experimental error in this $D_s \to K$ channel could be reduced over the foreseeable planning horizon, e.g. in the next decade, then this could become the most precise channel for determining $|V_{cd}|$.

The kinematics of these decays (i.e. the $\sqrt{E_P - m_P}$ term in the differential decay rate) are such that higher q^2 events are suppressed. Experiment then will always be able to produce more data – and thus results with smaller errors – near $q^2 = 0$.

Lattice QCD, however, as shown here, is able to produce data with smaller statistical errors at lower spatial momenta, i.e. near q^2_{max}. It would be anticipated that increasing the statistics of this study, adding physical mass pions and producing data at lower spatial momenta would result in higher precision form factor predictions near q^2_{max} than $q^2 = 0$.

There are two clear steps experimentalists could contribute in the effort to determine $|V_{cd}|_{\text{semi}}$ with the smallest possible error:

1. Increase precision of $|V_{cd}| f_+ (q^2)$ measurements in the $D_s \to K$ channel.
2. Provide results for this channel for non-zero q^2 bins.

Exactly which q^2 bins are most important will depend on the relative size of experimental vs theoretical errors and thus vary over time.

Appendix A

Appendices

A.1 Ensemble M1 matrix element fits

Results are presented here for matrix element fits deferred from § 3.3.1.

M1 matrix elements $n^2 = 1$

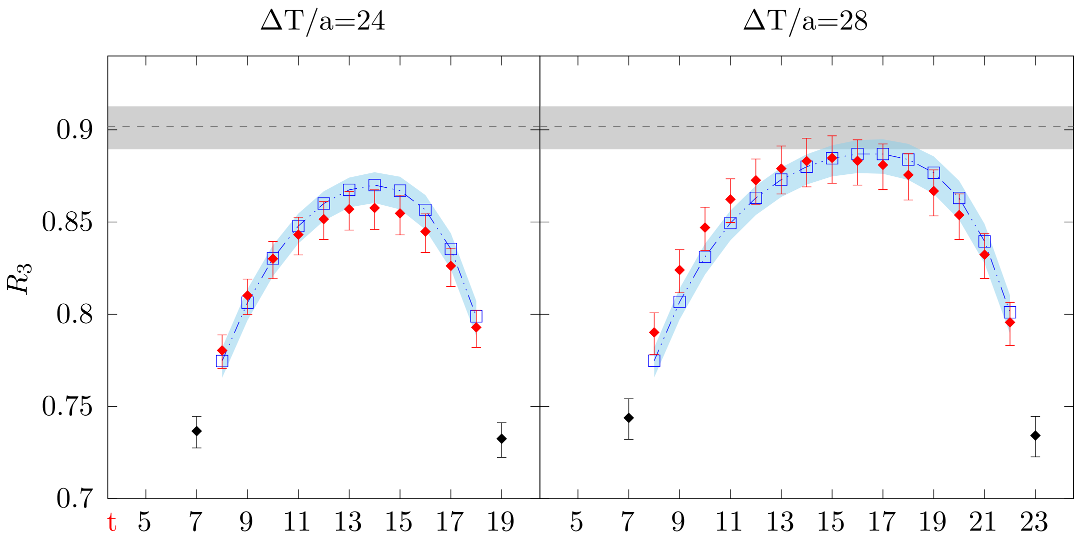

Figure A.1 *Temporal component of mostly nonperturbatively renormalised ratio R_3 vs t, for $D_s \to K$ at $n^2 = 1$ on ensemble M1. Simultaneous fit to wall separations $\Delta T/a$ 24 and 28 on timeslices 8-18 and 8-22, respectively. The grey band is the matrix element $\langle K|\gamma_4\left(n^2=1\right)|D_s\rangle = 0.902(12)$. Hotelling p-value for the fit is 0.230, with excited-state matrix elements shown in table 3.2.*

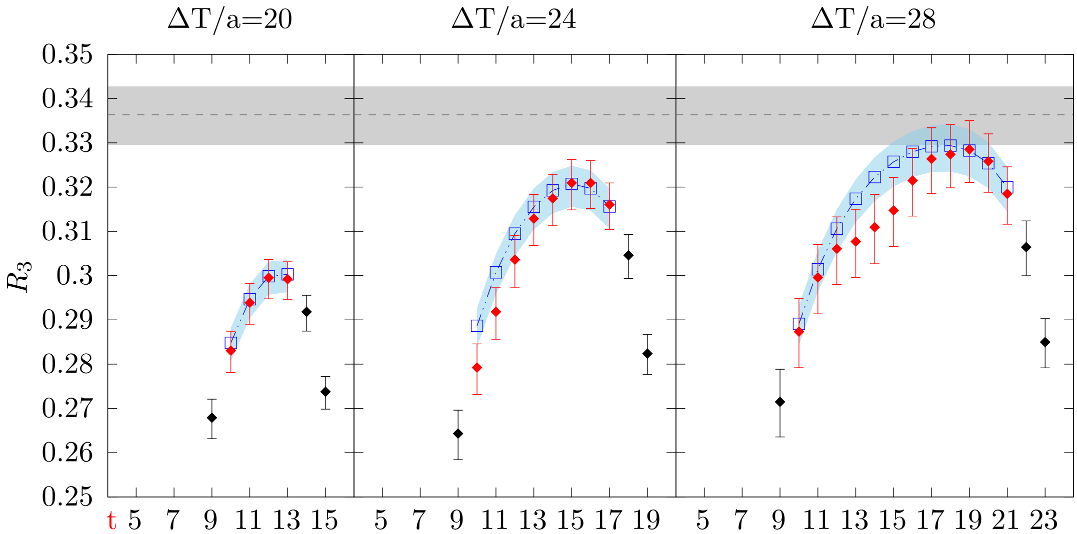

Figure A.2 *Spatial component of mostly nonperturbatively renormalised ratio R_3 vs t, for $D_s \to K$ at $n^2 = 1$ on ensemble M1. Simultaneous fit to wall separations $\Delta T/a$ 20, 24 and 28 on timeslices 10-13, 10-17 and 10-21, respectively. The grey band is the matrix element $\langle K|\gamma_i\left(n^2=1\right)|D_s\rangle = 0.3363(66)$. Hotelling p-value for the fit is 0.334, with excited-state matrix elements shown in table 3.2.*

M1 matrix elements $n^2 = 2$

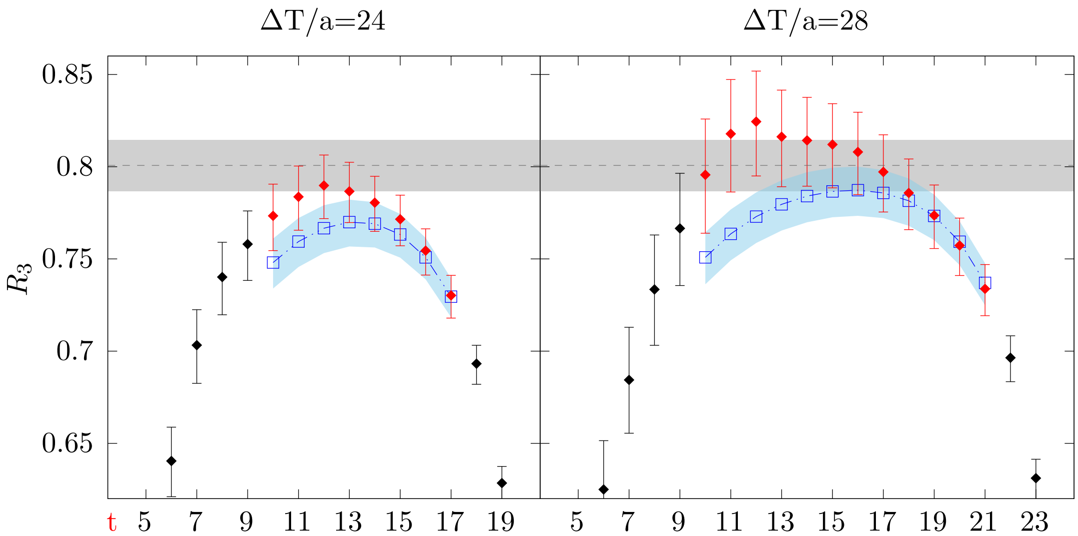

Figure A.3 *Temporal component of mostly nonperturbatively renormalised ratio R_3 vs t, for $D_s \to K$ at $n^2 = 2$ on ensemble M1. Simultaneous fit to wall separations $\Delta T/a$ 24 and 28 on timeslices 10-17 and 10-21, respectively. The grey band is the matrix element $\langle K|\gamma_4\left(n^2=2\right)|D_s\rangle = 0.801(14)$. Hotelling p-value for the fit is 0.296, with excited-state matrix elements shown in table 3.2.*

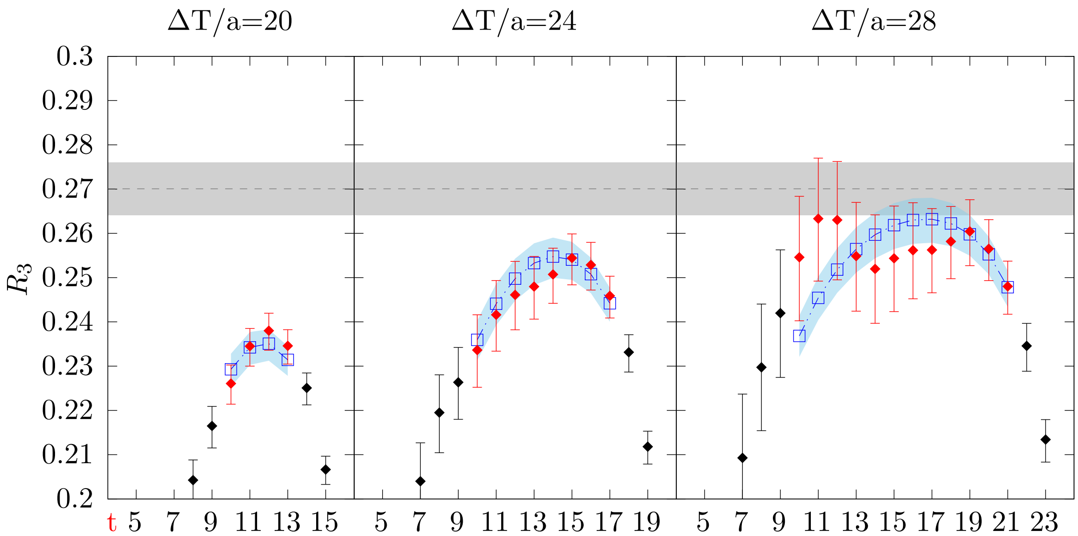

Figure A.4 *Spatial component of mostly nonperturbatively renormalised ratio R_3 vs t, for $D_s \to K$ at $n^2 = 2$ on ensemble M1. Simultaneous fit to wall separations $\Delta T/a$ 20, 24 and 28 on timeslices 10-13, 10-17 and 10-21, respectively. The grey band is the matrix element $\langle K|\gamma_i\left(n^2=2\right)|D_s\rangle = 0.2701(59)$. Hotelling p-value for the fit is 0.58, with excited-state matrix elements shown in table 3.2.*

M1 matrix elements $n^2 = 3$

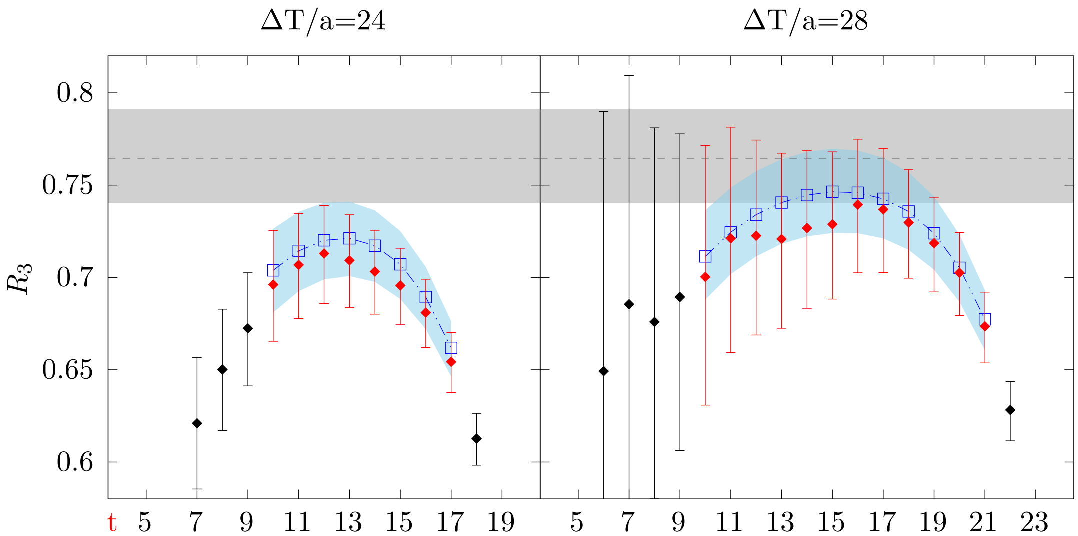

Figure A.5 *Temporal component of mostly nonperturbatively renormalised ratio R_3 vs t, for $D_s \to K$ at $n^2 = 3$ on ensemble M1. Simultaneous fit to wall separations $\Delta T/a$ 24 and 28 on timeslices 10-17 and 10-21, respectively. The grey band is the matrix element $\langle K|\gamma_4\left(n^2=3\right)|D_s\rangle = 0.765(25)$. Hotelling p-value for the fit is 0.169, with excited-state matrix elements shown in table 3.2.*

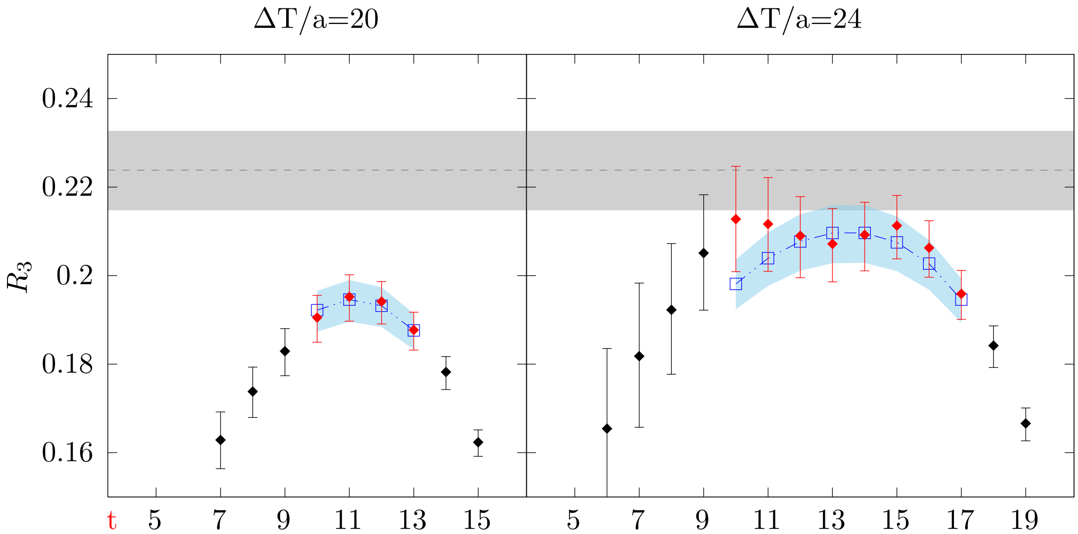

Figure A.6 *Spatial component of mostly nonperturbatively renormalised ratio R_3 vs t, for $D_s \to K$ at $n^2 = 3$ on ensemble M1. Simultaneous fit to wall separations $\Delta T/a$ 20 and 24 on timeslices 10-13 and 10-17, respectively. The grey band is the matrix element $\langle K|\gamma_i\left(n^2=3\right)|D_s\rangle = 0.2238(89)$. Hotelling p-value for the fit is 0.27, with excited-state matrix elements shown in table 3.2.*

M1 matrix elements $n^2 = 4$

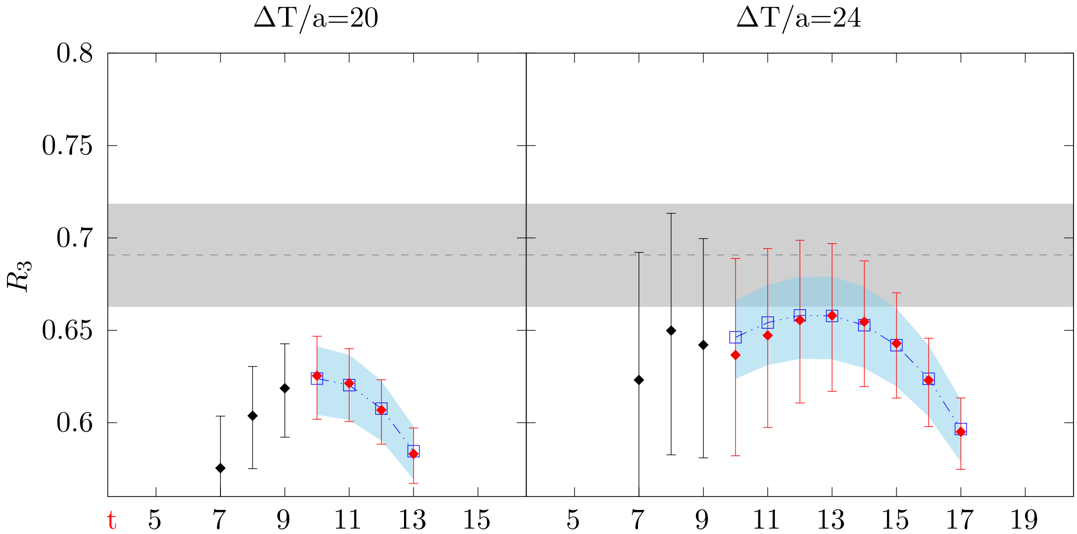

Figure A.7 *Temporal component of mostly nonperturbatively renormalised ratio R_3 vs t, for $D_s \to K$ at $n^2 = 4$ on ensemble M1. Simultaneous fit to wall separations $\Delta T/a$ 20 and 24 on timeslices 10-13 and 10-17, respectively. The grey band is the matrix element $\langle K|\gamma_4\left(n^2 = 4\right)|D_s\rangle = 0.691(28)$. Hotelling p-value for the fit is 1.00, with excited-state matrix elements shown in table 3.2.*

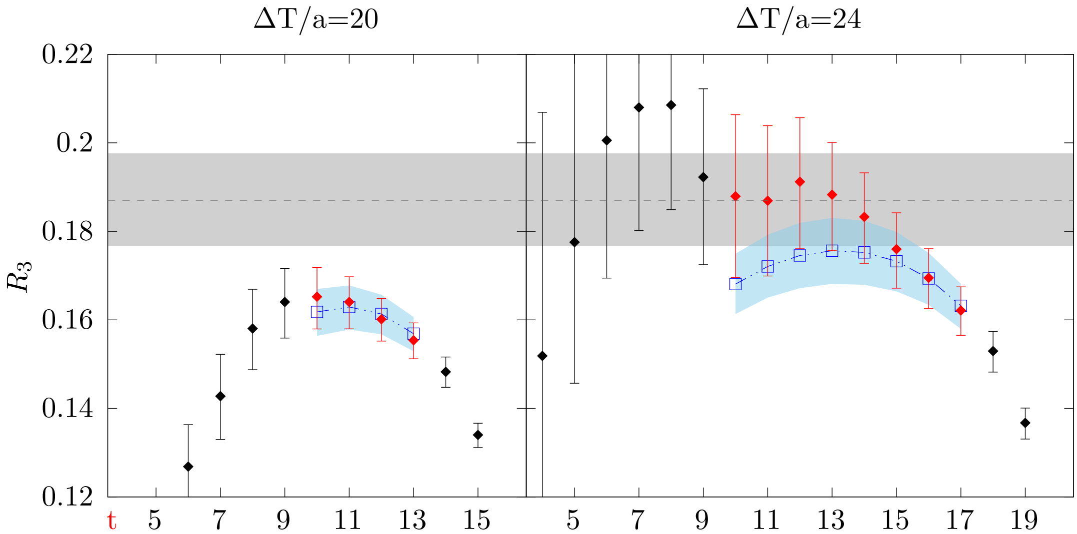

Figure A.8 *Spatial component of mostly nonperturbatively renormalised ratio R_3 vs t, for $D_s \to K$ at $n^2 = 4$ on ensemble M1. Simultaneous fit to wall separations $\Delta T/a$ 20 and 24 on timeslices 10-13 and 10-17, respectively. The grey band is the matrix element $\langle K|\gamma_i\left(n^2 = 4\right)|D_s\rangle = 0.187(10)$. Hotelling p-value for the fit is 0.35, with excited-state matrix elements shown in table 3.2.*

A.2 Ensemble M2 matrix element fits

Results are presented here for matrix element fits deferred from § 3.3.2.

M2 matrix elements $n^2 = 1$

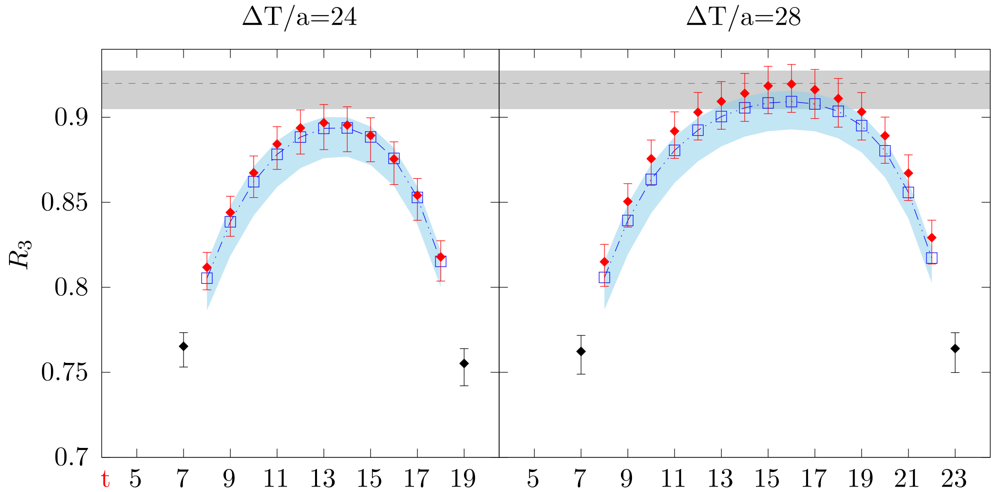

Figure A.9 *Temporal component of mostly nonperturbatively renormalised ratio R_3 vs t, for $D_s \to K$ at $n^2 = 1$ on ensemble M2. Simultaneous fit to wall separations $\Delta T/a$ 24 and 28 on timeslices 8-18 and 8-22, respectively. The grey band is the matrix element $\langle K|\gamma_4 \left(n^2 = 1\right)|D_s\rangle = 0.920(11)$. Hotelling p-value for the fit is 0.725, with excited-state matrix elements shown in table 3.3.*

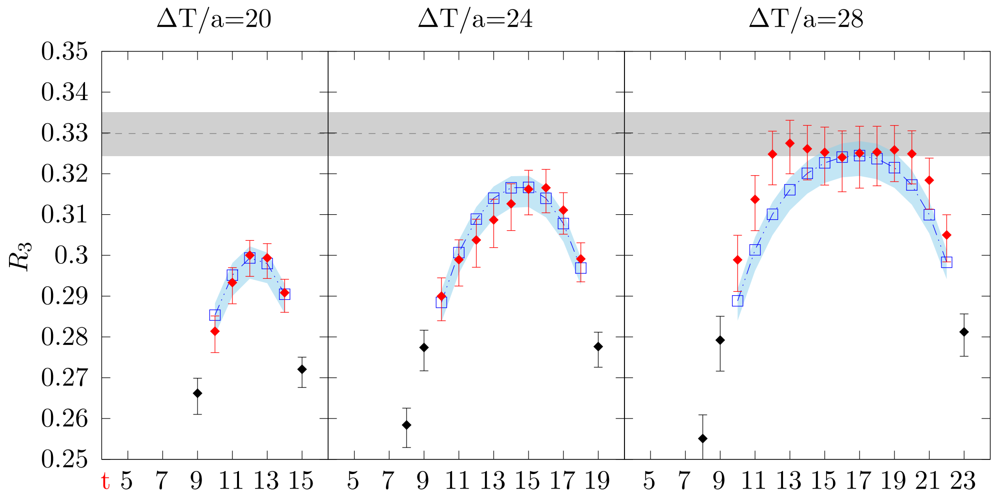

Figure A.10 *Spatial component of mostly nonperturbatively renormalised ratio R_3 vs t, for $D_s \to K$ at $n^2 = 1$ on ensemble M2. Simultaneous fit to wall separations $\Delta T/a$ 20, 24 and 28 on timeslices 10-14, 10-18 and 10-22, respectively. The grey band is the matrix element $\langle K|\gamma_i \left(n^2 = 1\right)|D_s\rangle = 0.3298(54)$. Hotelling p-value for the fit is 0.145, with excited-state matrix elements shown in table 3.3.*

M2 matrix elements $n^2 = 2$

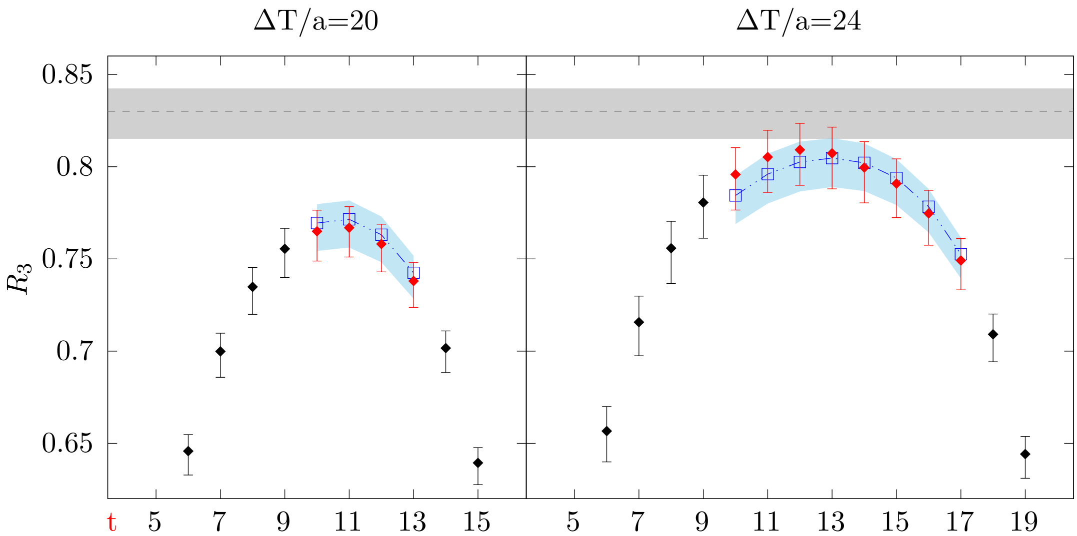

Figure A.11 *Temporal component of mostly nonperturbatively renormalised ratio R_3 vs t, for $D_s \to K$ at $n^2 = 2$ on ensemble M2. Simultaneous fit to wall separations $\Delta T/a$ 20 and 24 on timeslices 10-13 and 10-17, respectively. The grey band is the matrix element $\langle K|\gamma_4\left(n^2=2\right)|D_s\rangle = 0.830(14)$. Hotelling p-value for the fit is 0.49, with excited-state matrix elements shown in table 3.3.*

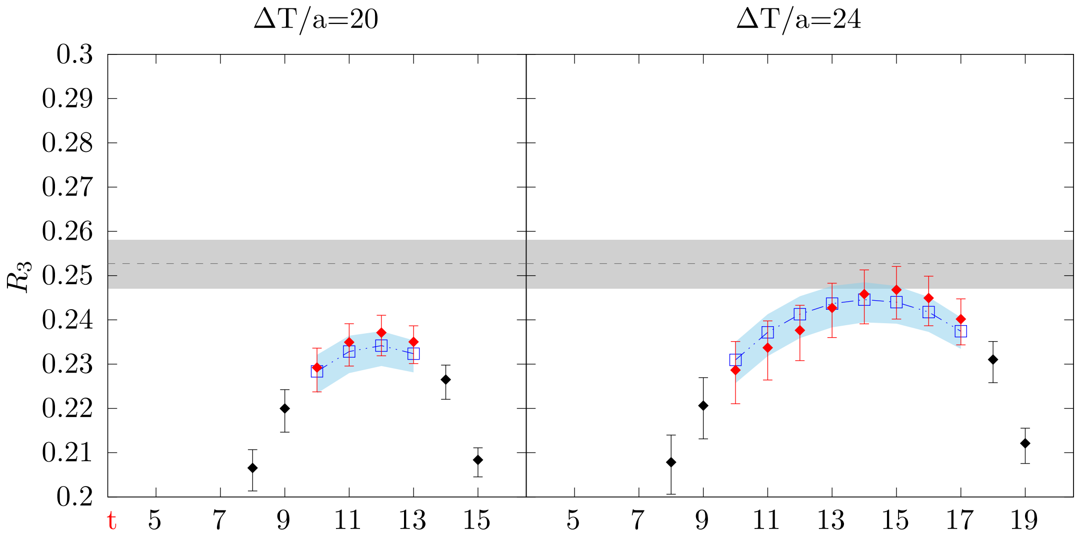

Figure A.12 *Spatial component of mostly nonperturbatively renormalised ratio R_3 vs t, for $D_s \to K$ at $n^2 = 2$ on ensemble M2. Simultaneous fit to wall separations $\Delta T/a$ 20 and 24 on timeslices 10-13 and 10-17, respectively. The grey band is the matrix element $\langle K|\gamma_i\left(n^2=2\right)|D_s\rangle = 0.2527(55)$. Hotelling p-value for the fit is 0.85, with excited-state matrix elements shown in table 3.3.*

M2 matrix elements $n^2 = 3$

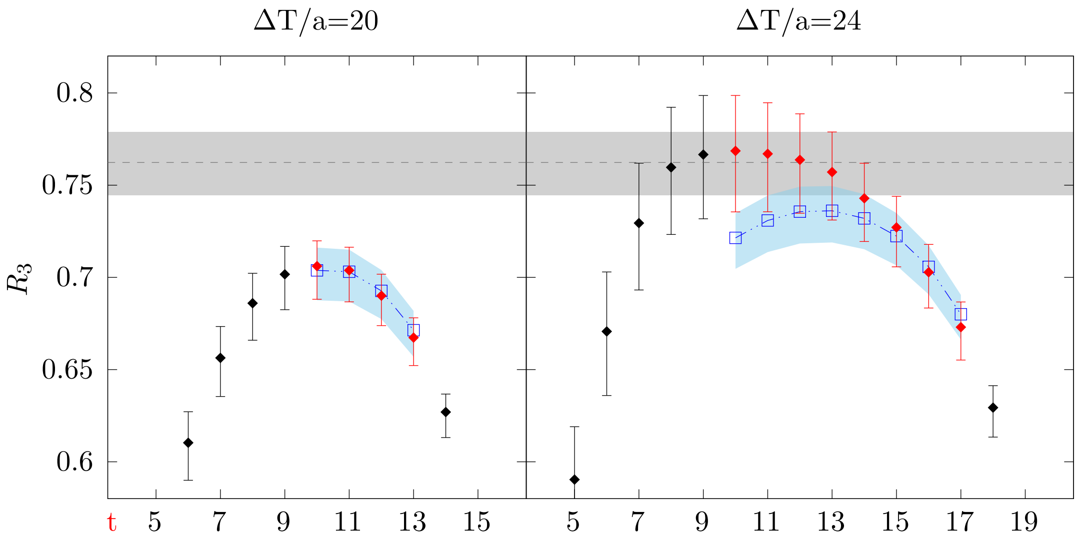

Figure A.13 *Temporal component of mostly nonperturbatively renormalised ratio R_3 vs t, for $D_s \to K$ at $n^2 = 3$ on ensemble M2. Simultaneous fit to wall separations $\Delta T/a$ 20 and 24 on timeslices 10-13 and 10-17, respectively. The grey band is the matrix element $\langle K|\gamma_4\left(n^2 = 3\right)|D_s\rangle = 0.762(17)$. Hotelling p-value for the fit is 0.37, with excited-state matrix elements shown in table 3.3.*

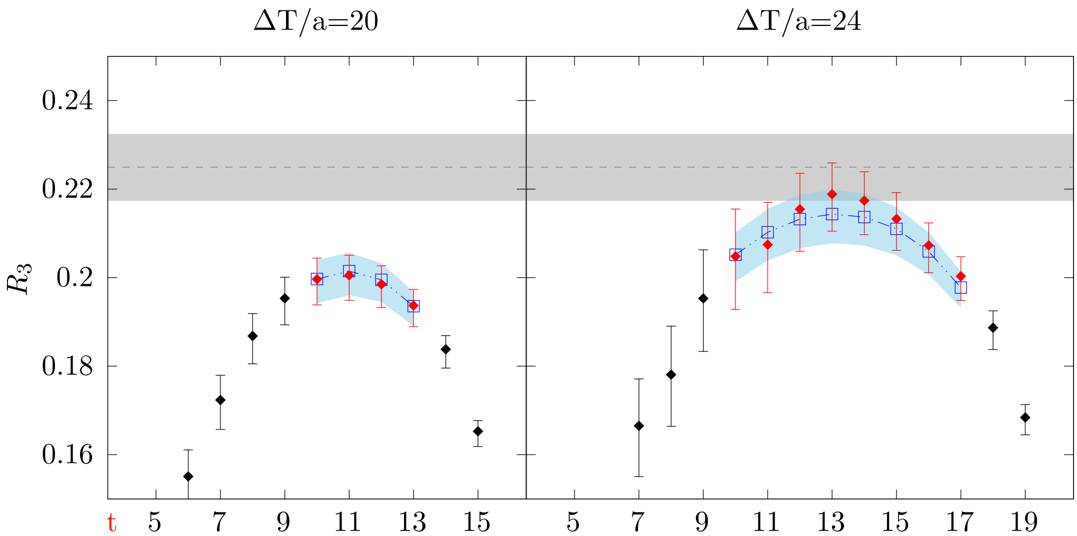

Figure A.14 *Spatial component of mostly nonperturbatively renormalised ratio R_3 vs t, for $D_s \to K$ at $n^2 = 3$ on ensemble M2. Simultaneous fit to wall separations $\Delta T/a$ 20 and 24 on timeslices 10-13 and 10-17, respectively. The grey band is the matrix element $\langle K|\gamma_i\left(n^2 = 3\right)|D_s\rangle = 0.2250(75)$. Hotelling p-value for the fit is 0.60, with excited-state matrix elements shown in table 3.3.*

M2 matrix elements $n^2 = 4$

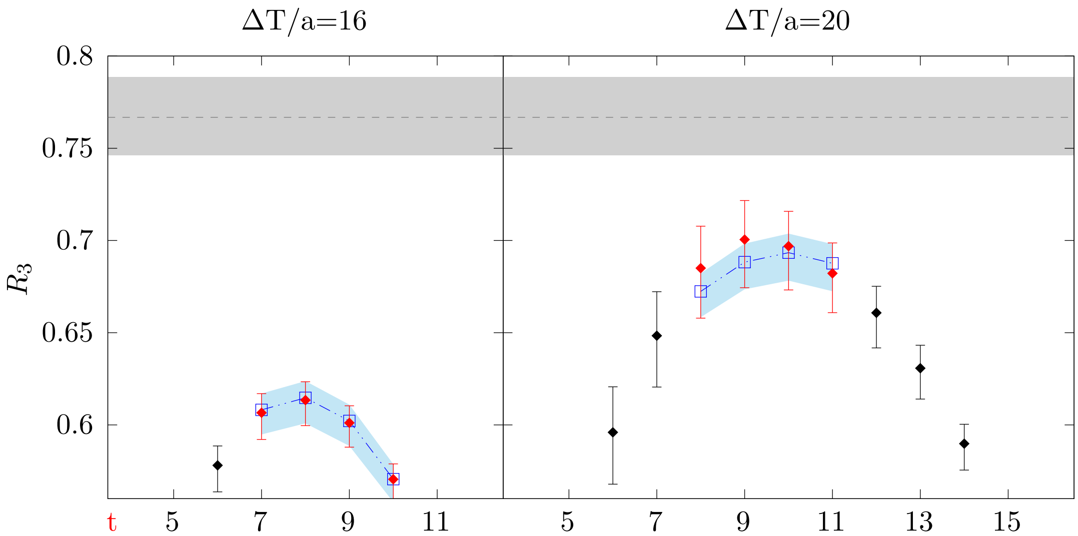

Figure A.15 *Temporal component of mostly nonperturbatively renormalised ratio R_3 vs t, for $D_s \to K$ at $n^2 = 4$ on ensemble M2. Simultaneous fit to wall separations $\Delta T/a$ 16 and 20 on timeslices 7-10 and 8-11, respectively. The grey band is the matrix element $\langle K|\gamma_4\left(n^2 = 4\right)|D_s\rangle = 0.767(21)$. Hotelling p-value for the fit is 0.22, with excited-state matrix elements shown in table 3.3.*

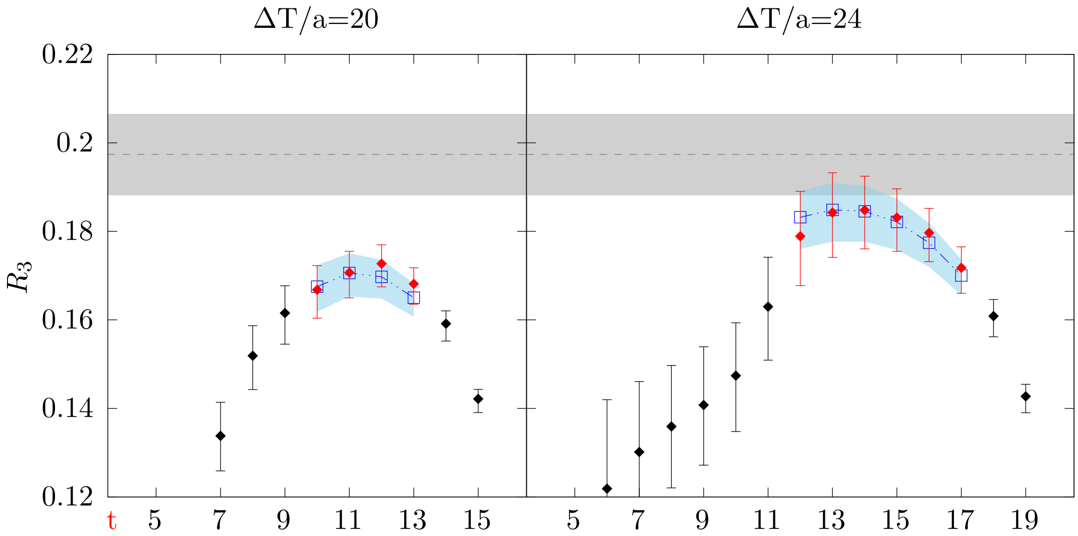

Figure A.16 *Spatial component of mostly nonperturbatively renormalised ratio R_3 vs t, for $D_s \to K$ at $n^2 = 4$ on ensemble M2. Simultaneous fit to wall separations $\Delta T/a$ 20 and 24 on timeslices 10-13 and 12-17, respectively. The grey band is the matrix element $\langle K|\gamma_i\left(n^2 = 4\right)|D_s\rangle = 0.1974(91)$. Hotelling p-value for the fit is 0.27, with excited-state matrix elements shown in table 3.3.*

A.3 Ensemble M3 matrix element fits

M3 matrix elements $n^2 = 1$

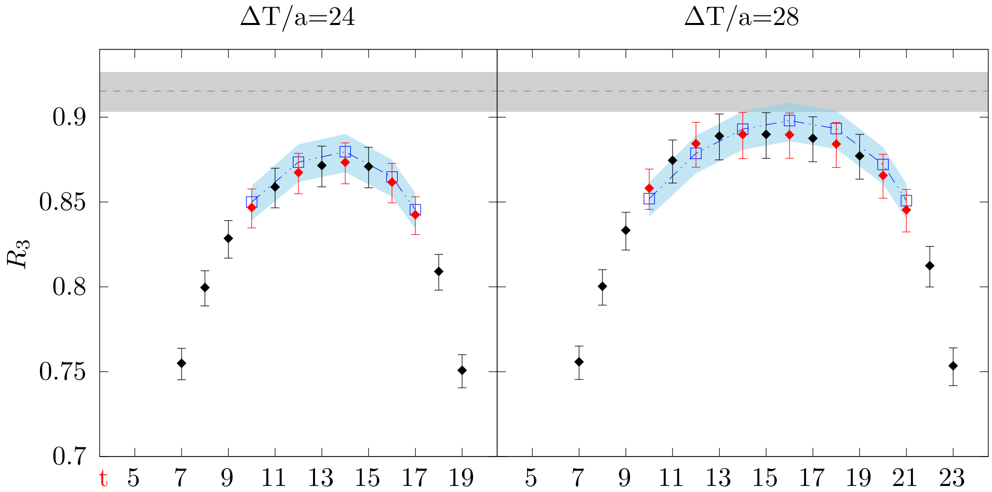

Figure A.17 *Temporal component of mostly nonperturbatively renormalised ratio R_3 vs t, for $D_s \to K$ at $n^2 = 1$ on ensemble M3. Simultaneous fit to wall separations $\Delta T/a$ 24 and 28 on timeslices 10-16:2;17 and 10-20:2;21, respectively. The grey band is the matrix element $\langle K|\gamma_4\left(n^2 = 1\right)|D_s\rangle = 0.915(12)$. Hotelling p-value for the fit is 0.41, with excited-state matrix elements shown in table 3.4.*

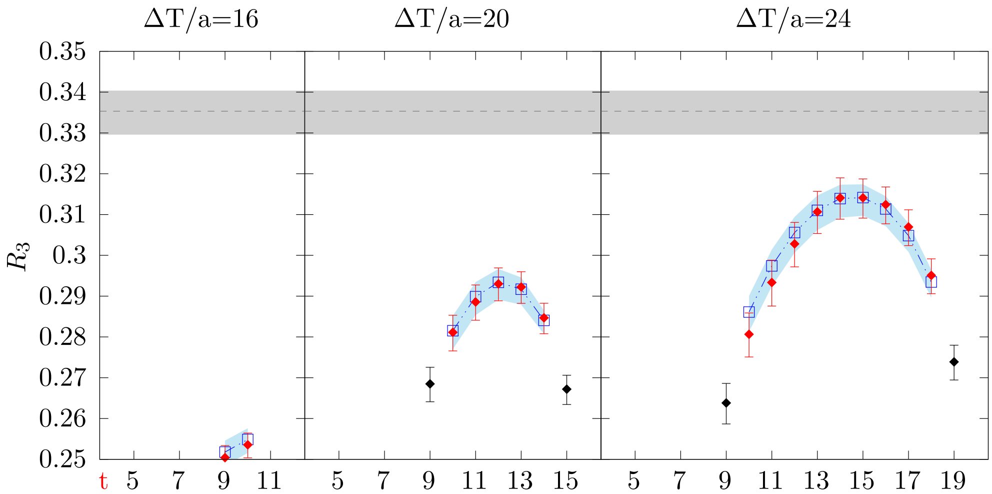

Figure A.18 *Spatial component of mostly nonperturbatively renormalised ratio R_3 vs t, for $D_s \to K$ at $n^2 = 1$ on ensemble M3. Simultaneous fit to wall separations $\Delta T/a$ 16, 20 and 24 on timeslices 9;10, 10-14 and 10-18, respectively. The grey band is the matrix element $\langle K|\gamma_i\left(n^2 = 1\right)|D_s\rangle = 0.3353(54)$. Hotelling p-value for the fit is 0.53, with excited-state matrix elements shown in table 3.4.*

M3 matrix elements $n^2 = 2$

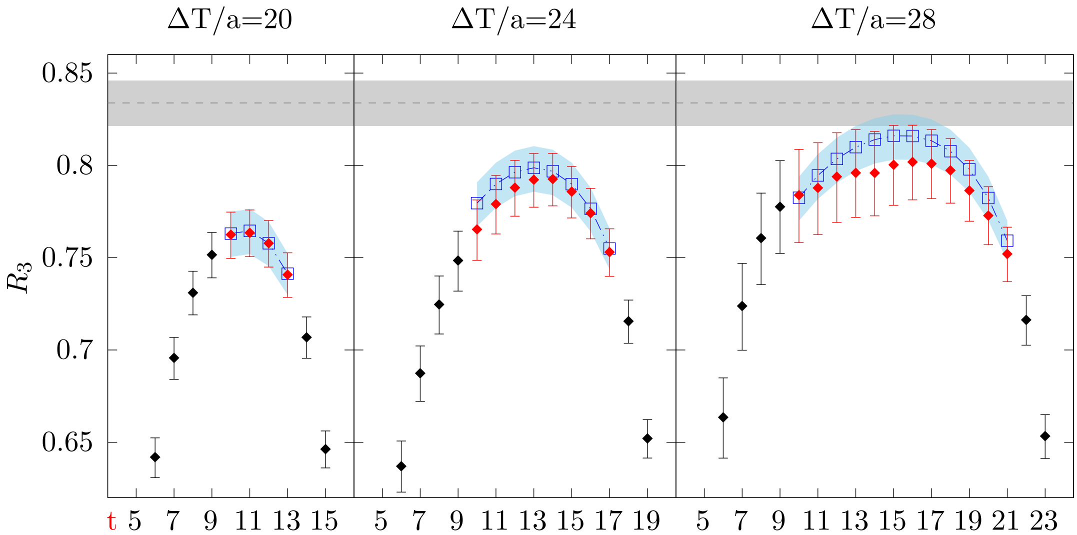

Figure A.19 *Temporal component of mostly nonperturbatively renormalised ratio R_3 vs t, for $D_s \to K$ at $n^2 = 2$ on ensemble M3. Simultaneous fit to wall separations $\Delta T/a$ 20, 24 and 28 on timeslices 10-13, 10-17 and 10-21, respectively. The grey band is the matrix element $\langle K|\gamma_4 \left(n^2 = 2\right)|D_s\rangle = 0.834(12)$. Hotelling p-value for the fit is 0.525, with excited-state matrix elements shown in table 3.4.*

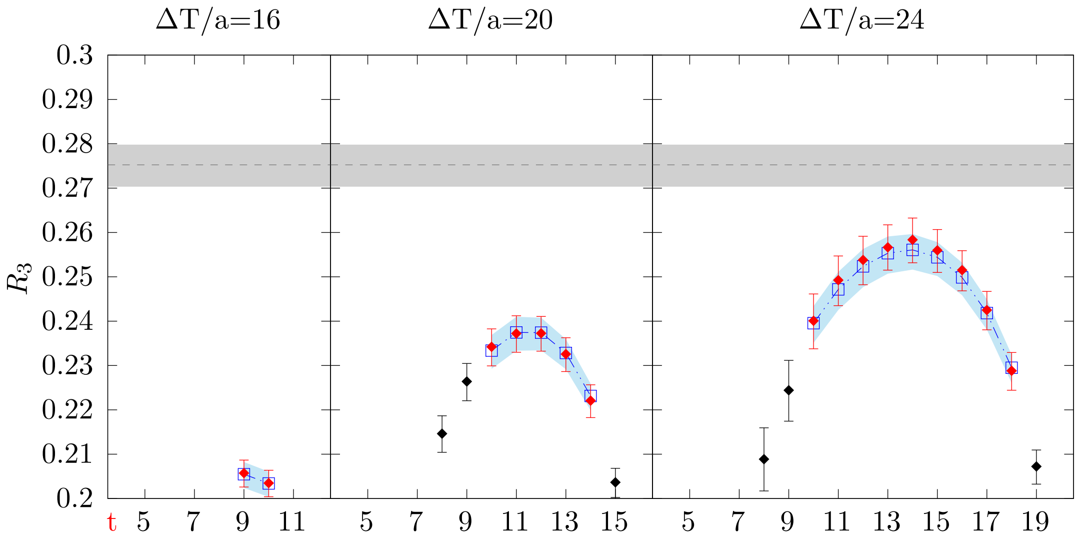

Figure A.20 *Spatial component of mostly nonperturbatively renormalised ratio R_3 vs t, for $D_s \to K$ at $n^2 = 2$ on ensemble M3. Simultaneous fit to wall separations $\Delta T/a$ 16, 20 and 24 on timeslices 9;10, 10-14 and 10-18, respectively. The grey band is the matrix element $\langle K|\gamma_i \left(n^2 = 2\right)|D_s\rangle = 0.2752(47)$. Hotelling p-value for the fit is 0.55, with excited-state matrix elements shown in table 3.4.*

M3 matrix elements $n^2 = 3$

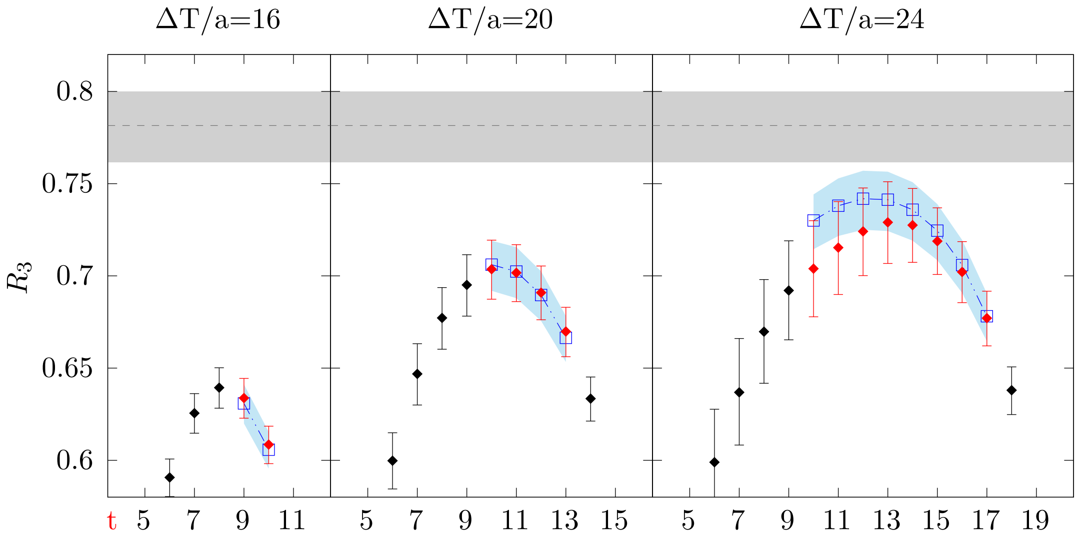

Figure A.21 *Temporal component of mostly nonperturbatively renormalised ratio R_3 vs t, for $D_s \to K$ at $n^2 = 3$ on ensemble M3. Simultaneous fit to wall separations $\Delta T/a$ 16, 20 and 24 on timeslices 9;10, 10-13 and 10-17, respectively. The grey band is the matrix element $\langle K|\gamma_4 \left(n^2 = 3\right)|D_s\rangle = 0.782(19)$. Hotelling p-value for the fit is 0.98, with excited-state matrix elements shown in table 3.4.*

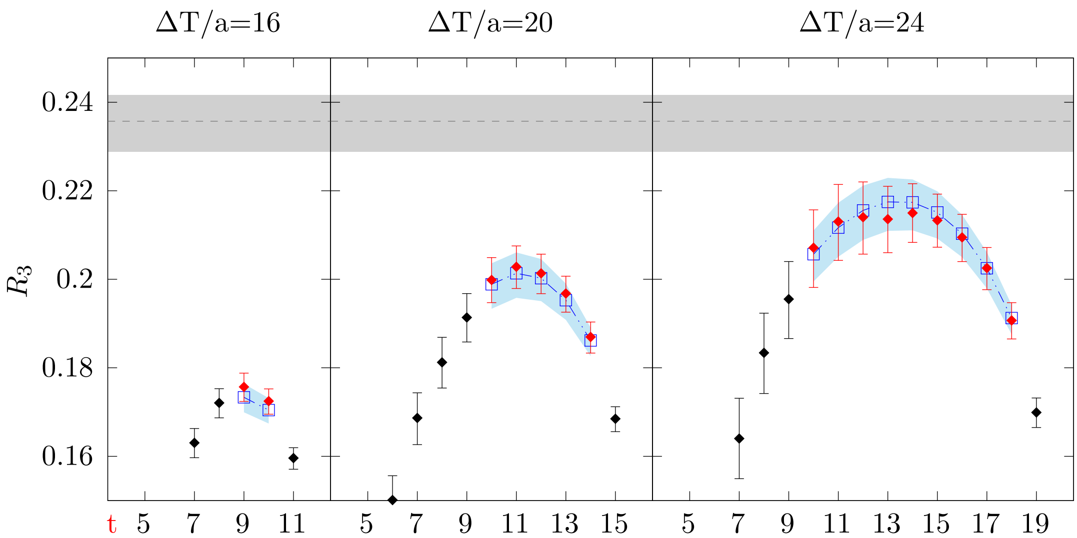

Figure A.22 *Spatial component of mostly nonperturbatively renormalised ratio R_3 vs t, for $D_s \to K$ at $n^2 = 3$ on ensemble M3. Simultaneous fit to wall separations $\Delta T/a$ 16, 20 and 24 on timeslices 9;10, 10-14 and 10-18, respectively. The grey band is the matrix element $\langle K|\gamma_i \left(n^2 = 3\right)|D_s\rangle = 0.2357(64)$. Hotelling p-value for the fit is 0.70, with excited-state matrix elements shown in table 3.4.*

M3 matrix elements $n^2 = 4$

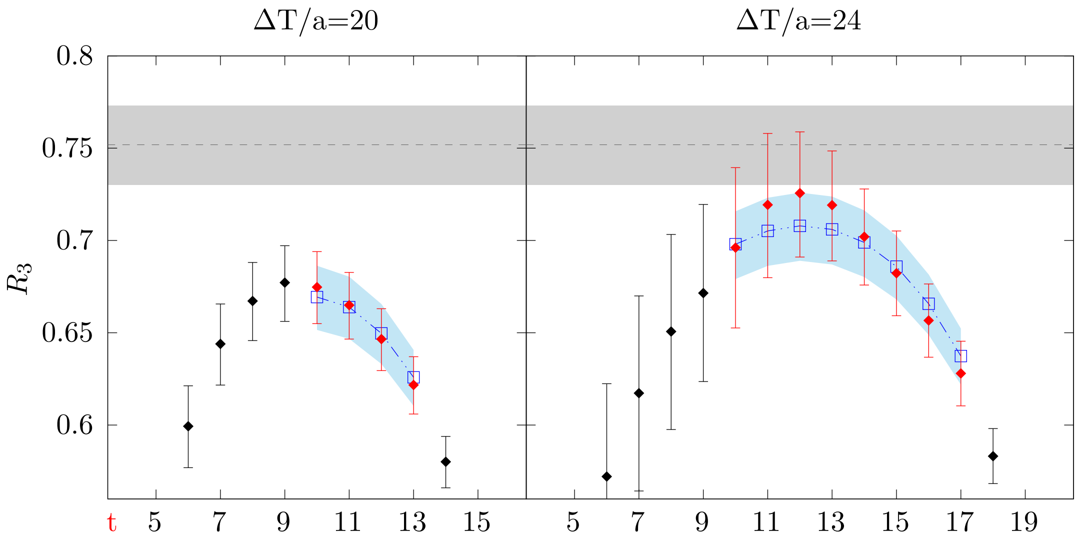

Figure A.23 *Temporal component of mostly nonperturbatively renormalised ratio R_3 vs t, for $D_s \to K$ at $n^2 = 4$ on ensemble M3. Simultaneous fit to wall separations $\Delta T/a$ 20 and 24 on timeslices 10-13 and 10-17, respectively. The grey band is the matrix element $\langle K|\gamma_4\left(n^2=4\right)|D_s\rangle = 0.752(21)$. Hotelling p-value for the fit is 0.66, with excited-state matrix elements shown in table 3.4.*

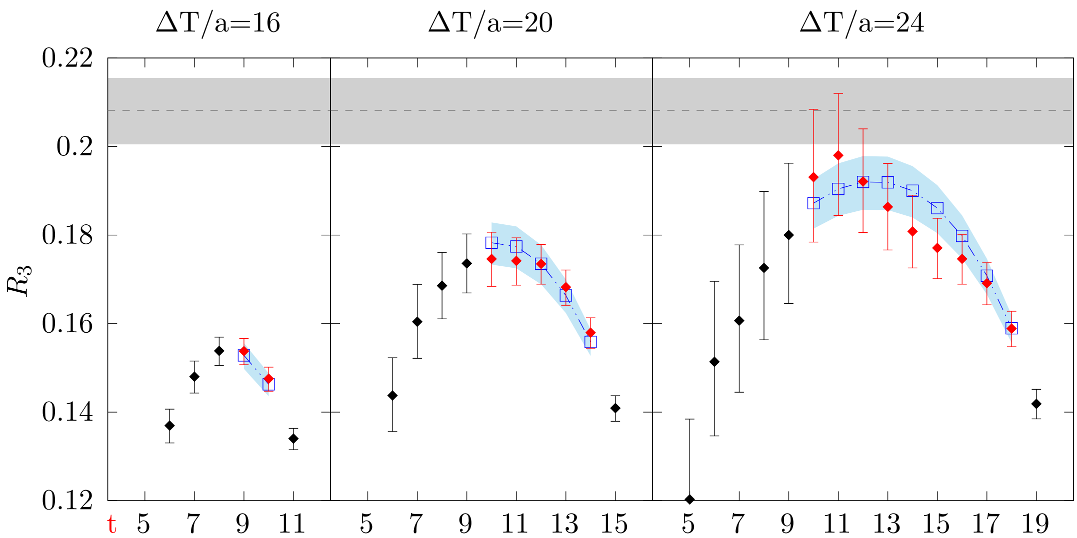

Figure A.24 *Spatial component of mostly nonperturbatively renormalised ratio R_3 vs t, for $D_s \to K$ at $n^2 = 4$ on ensemble M3. Simultaneous fit to wall separations $\Delta T/a$ 16, 20 and 24 on timeslices 9;10, 10-14 and 10-18, respectively. The grey band is the matrix element $\langle K|\gamma_i\left(n^2=4\right)|D_s\rangle = 0.2082(75)$. Hotelling p-value for the fit is 0.65, with excited-state matrix elements shown in table 3.4.*

A.4 Ensemble C1 matrix element fits

Results are presented here for matrix element fits deferred from § 3.3.4.

C1 matrix elements $n^2 = 1$

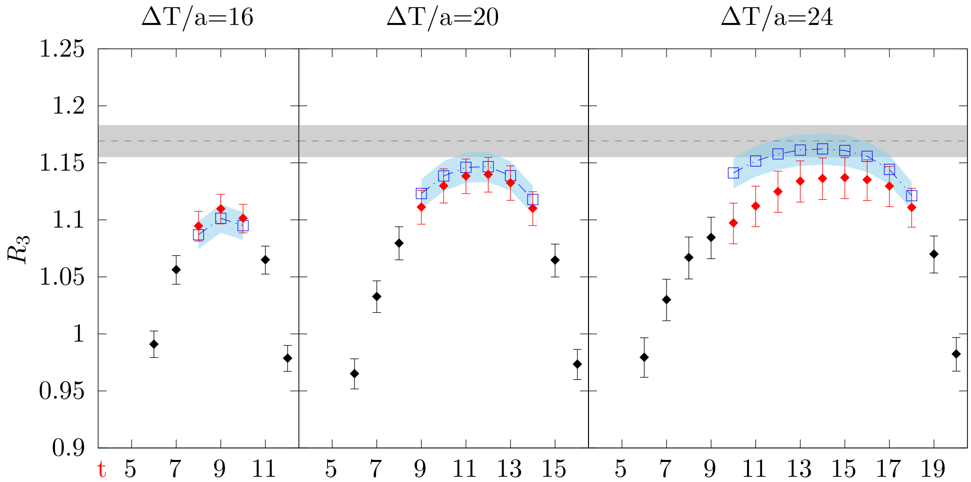

Figure A.25 *Temporal component of mostly nonperturbatively renormalised ratio* R_3 *vs t, for* $D_s \to K$ *at* $n^2 = 1$ *on ensemble C1. Simultaneous fit to wall separations* $\Delta T/a$ *16, 20 and 24 on timeslices 8-10, 9-14 and 10-18, respectively. The grey band is the matrix element* $\langle K|\gamma_4\left(n^2=1\right)|D_s\rangle = 1.169(14)$*. Hotelling p-value for the fit is 0.246, with excited-state matrix elements shown in table 3.5.*

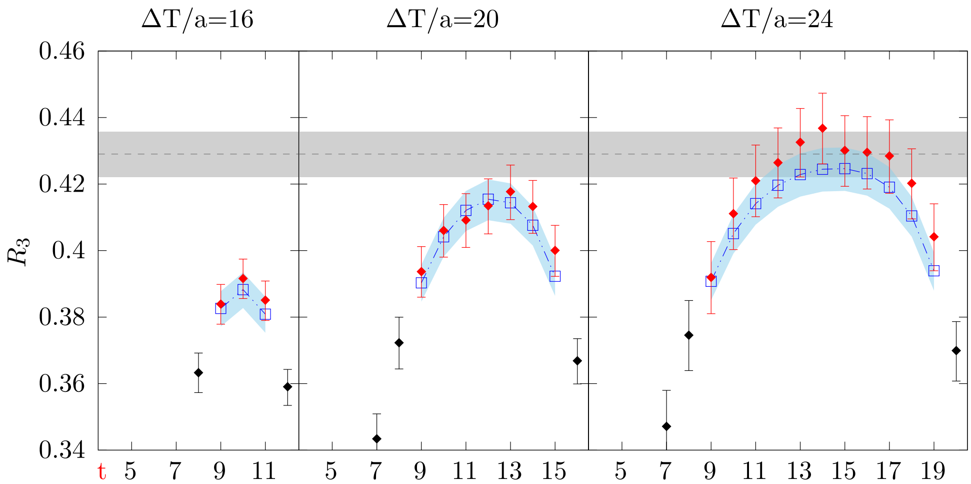

Figure A.26 *Spatial component of mostly nonperturbatively renormalised ratio* R_3 *vs t, for* $D_s \to K$ *at* $n^2 = 1$ *on ensemble C1. Simultaneous fit to wall separations* $\Delta T/a$ *16, 20 and 24 on timeslices 9-11, 9-15 and 9-19, respectively. The grey band is the matrix element* $\langle K|\gamma_i\left(n^2=1\right)|D_s\rangle = 0.4290(68)$*. Hotelling p-value for the fit is 0.213, with excited-state matrix elements shown in table 3.5.*

C1 matrix elements $n^2 = 2$

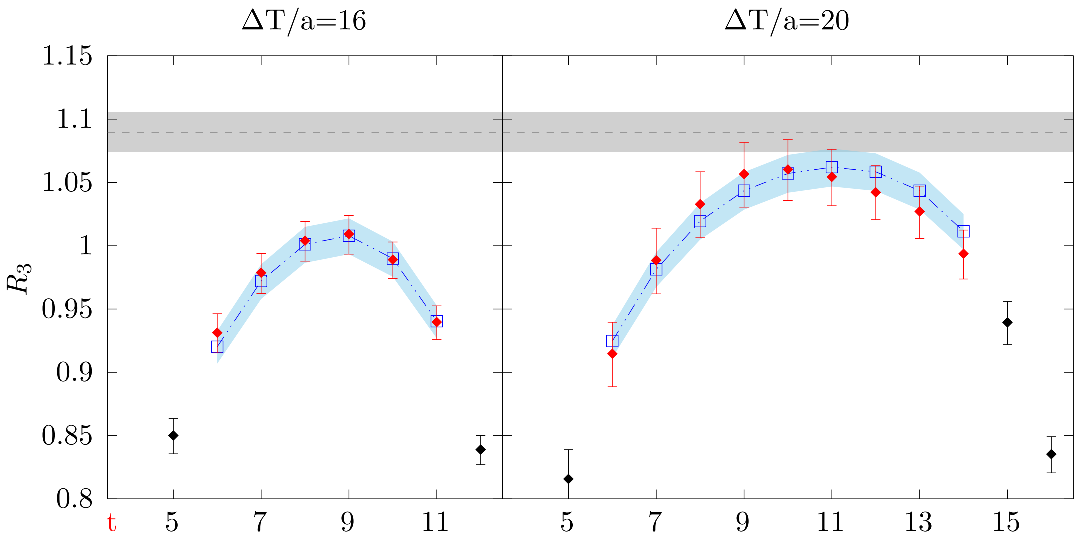

Figure A.27 *Temporal component of mostly nonperturbatively renormalised ratio R_3 vs t, for $D_s \to K$ at $n^2 = 2$ on ensemble C1. Simultaneous fit to wall separations $\Delta T/a$ 16 and 20 on timeslices 6-11 and 6-14, respectively. The grey band is the matrix element $\langle K|\gamma_4\left(n^2=2\right)|D_s\rangle = 1.090(16)$. Hotelling p-value for the fit is 0.42, with excited-state matrix elements shown in table 3.5.*

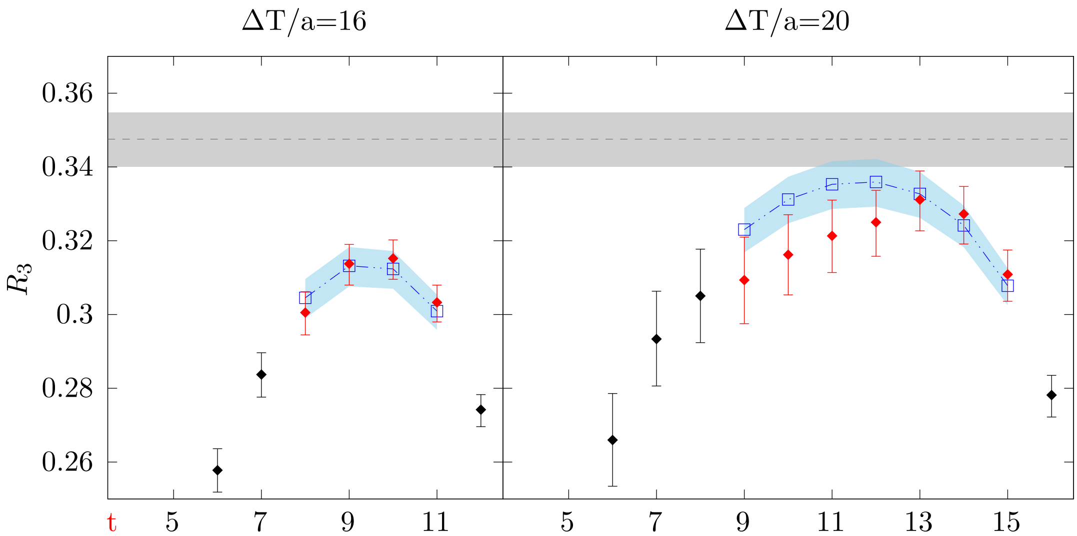

Figure A.28 *Spatial component of mostly nonperturbatively renormalised ratio R_3 vs t, for $D_s \to K$ at $n^2 = 2$ on ensemble C1. Simultaneous fit to wall separations $\Delta T/a$ 16 and 20 on timeslices 8-11 and 9-15, respectively. The grey band is the matrix element $\langle K|\gamma_i\left(n^2=2\right)|D_s\rangle = 0.3475(74)$. Hotelling p-value for the fit is 0.38, with excited-state matrix elements shown in table 3.5.*

C1 matrix elements $n^2 = 3$

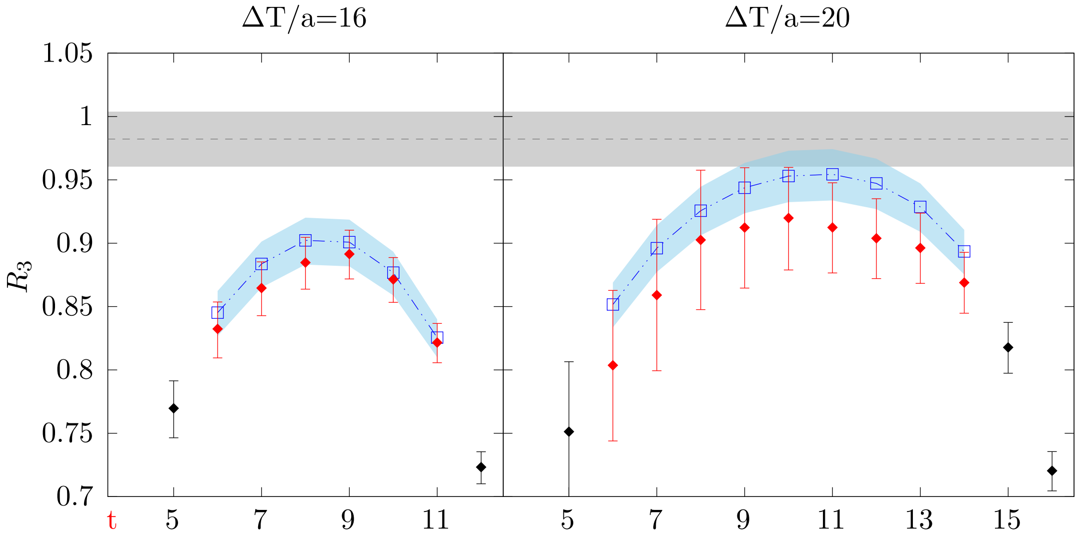

Figure A.29 *Temporal component of mostly nonperturbatively renormalised ratio R_3 vs t, for $D_s \to K$ at $n^2 = 3$ on ensemble C1. Simultaneous fit to wall separations $\Delta T/a$ 16 and 20 on timeslices 6-11 and 6-14, respectively. The grey band is the matrix element $\langle K|\gamma_4\left(n^2=3\right)|D_s\rangle = 0.982(22)$. Hotelling p-value for the fit is 0.62, with excited-state matrix elements shown in table 3.5.*

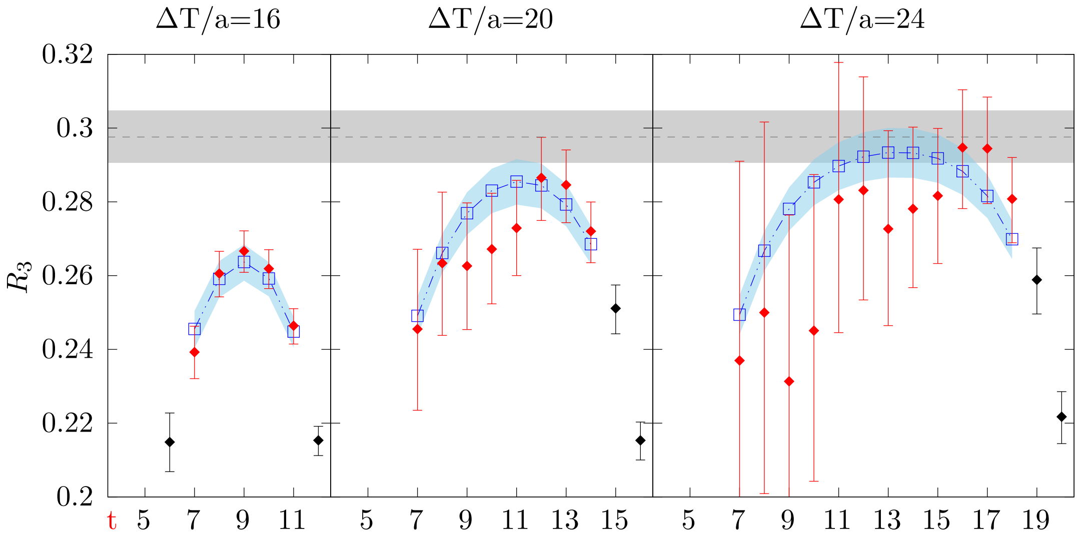

Figure A.30 *Spatial component of mostly nonperturbatively renormalised ratio R_3 vs t, for $D_s \to K$ at $n^2 = 3$ on ensemble C1. Simultaneous fit to wall separations $\Delta T/a$ 16, 20 and 24 on timeslices 7-11, 7-14 and 7-18, respectively. The grey band is the matrix element $\langle K|\gamma_i\left(n^2=3\right)|D_s\rangle = 0.2976(71)$. Hotelling p-value for the fit is 0.521, with excited-state matrix elements shown in table 3.5.*

C1 matrix elements $n^2 = 4$

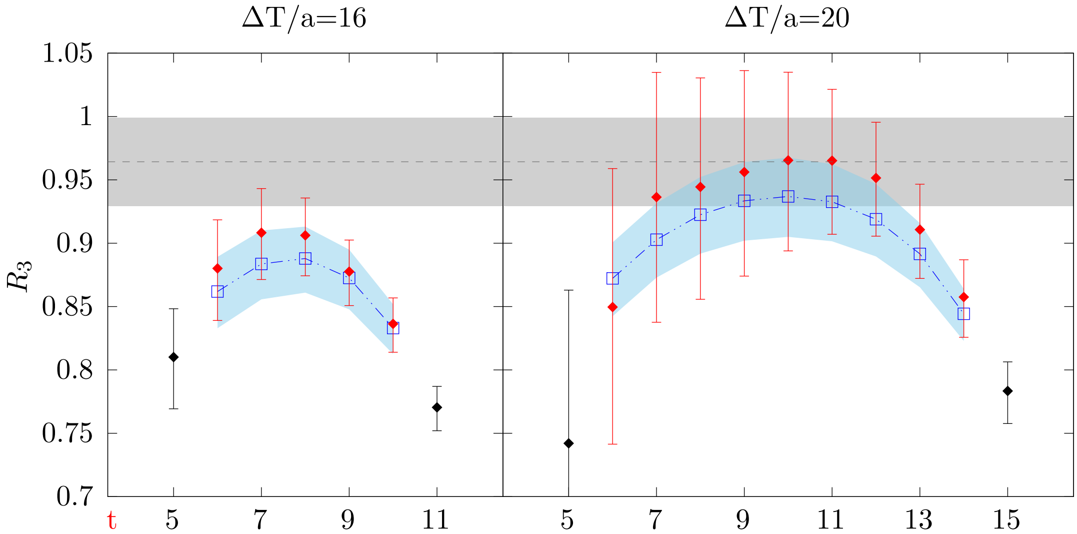

Figure A.31 *Temporal component of mostly nonperturbatively renormalised ratio R_3 vs t, for $D_s \to K$ at $n^2 = 4$ on ensemble C1. Simultaneous fit to wall separations $\Delta T/a$ 16 and 20 on timeslices 6-10 and 6-14, respectively. The grey band is the matrix element $\langle K|\gamma_4\left(n^2=4\right)|D_s\rangle = 0.964(35)$. Hotelling p-value for the fit is 0.49, with excited-state matrix elements shown in table 3.5.*

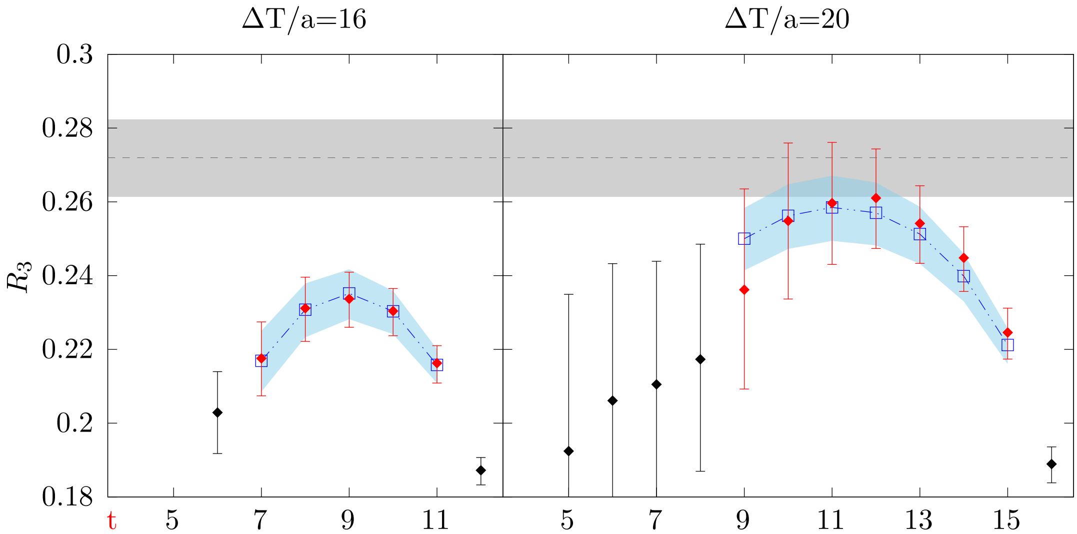

Figure A.32 *Spatial component of mostly nonperturbatively renormalised ratio R_3 vs t, for $D_s \to K$ at $n^2 = 4$ on ensemble C1. Simultaneous fit to wall separations $\Delta T/a$ 16 and 20 on timeslices 7-11 and 9-15, respectively. The grey band is the matrix element $\langle K|\gamma_i\left(n^2=4\right)|D_s\rangle = 0.272(10)$. Hotelling p-value for the fit is 0.91, with excited-state matrix elements shown in table 3.5.*

A.5 Ensemble C2 matrix element fits

Results are presented here for matrix element fits deferred from § 3.3.5.

C2 matrix elements $n^2 = 1$

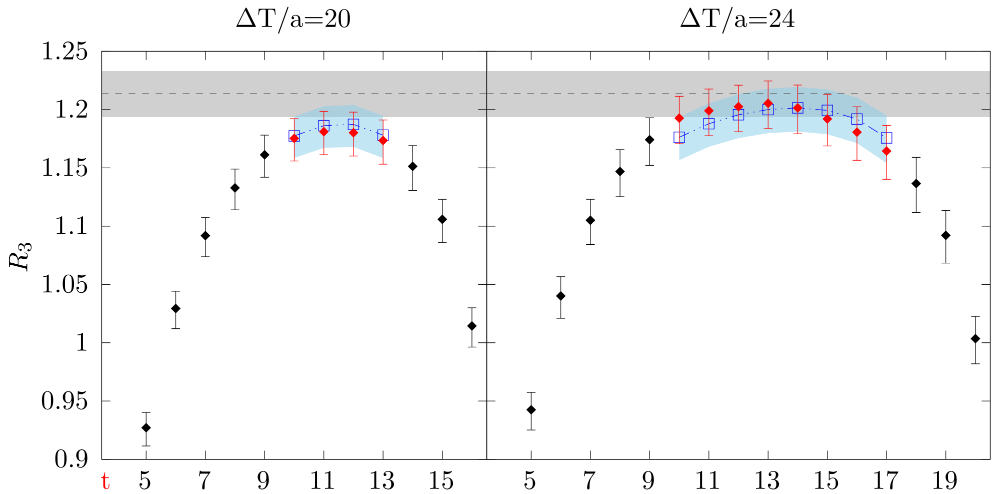

Figure A.33 *Temporal component of mostly nonperturbatively renormalised ratio R_3 vs t, for $D_s \to K$ at $n^2 = 1$ on ensemble C2. Simultaneous fit to wall separations $\Delta T/a$ 20 and 24 on timeslices 10-13 and 10-17, respectively. The grey band is the matrix element $\langle K|\gamma_4\left(n^2=1\right)|D_s\rangle = 1.214(20)$. Hotelling p-value for the fit is 0.46, with excited-state matrix elements shown in table 3.6.*

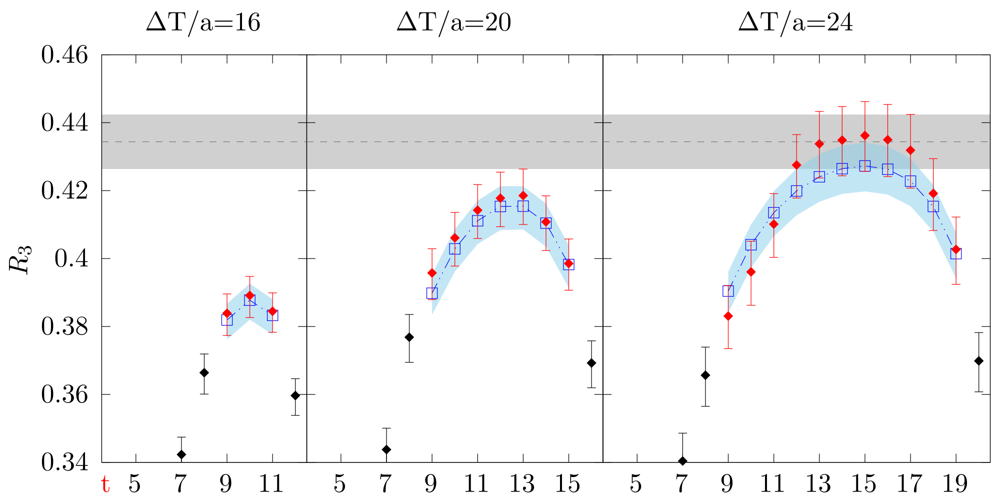

Figure A.34 *Spatial component of mostly nonperturbatively renormalised ratio R_3 vs t, for $D_s \to K$ at $n^2 = 1$ on ensemble C2. Simultaneous fit to wall separations $\Delta T/a$ 16, 20 and 24 on timeslices 9-11, 9-15 and 9-19, respectively. The grey band is the matrix element $\langle K|\gamma_i\left(n^2=1\right)|D_s\rangle = 0.4344(80)$. Hotelling p-value for the fit is 0.189, with excited-state matrix elements shown in table 3.6.*

C2 matrix elements $n^2 = 2$

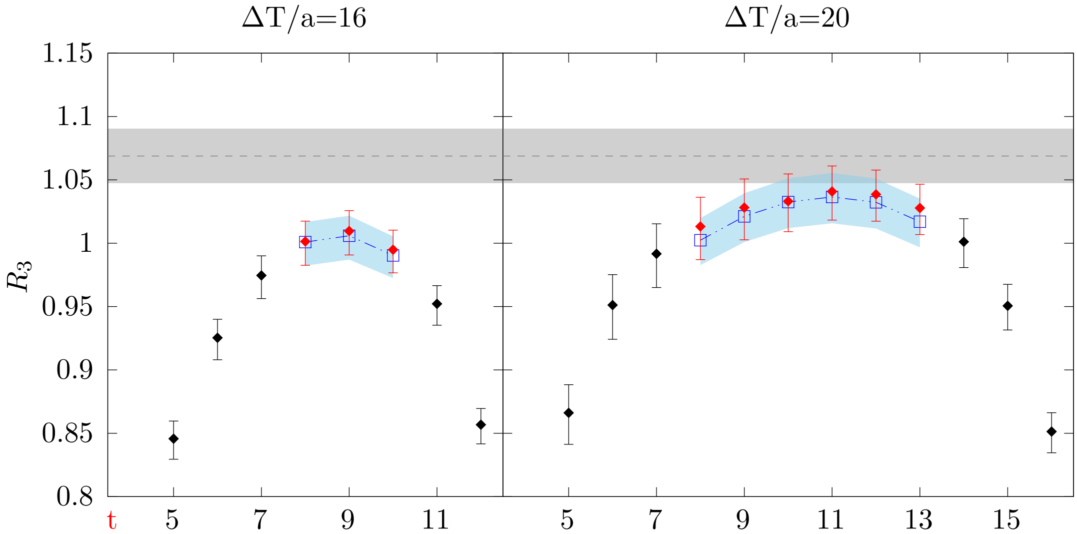

Figure A.35 *Temporal component of mostly nonperturbatively renormalised ratio R_3 vs t, for $D_s \to K$ at $n^2 = 2$ on ensemble C2. Simultaneous fit to wall separations $\Delta T/a$ 16 and 20 on timeslices 8-10 and 8-13, respectively. The grey band is the matrix element $\langle K|\gamma_4\left(n^2 = 2\right)|D_s\rangle = 1.069(21)$. Hotelling p-value for the fit is 0.32, with excited-state matrix elements shown in table 3.6.*

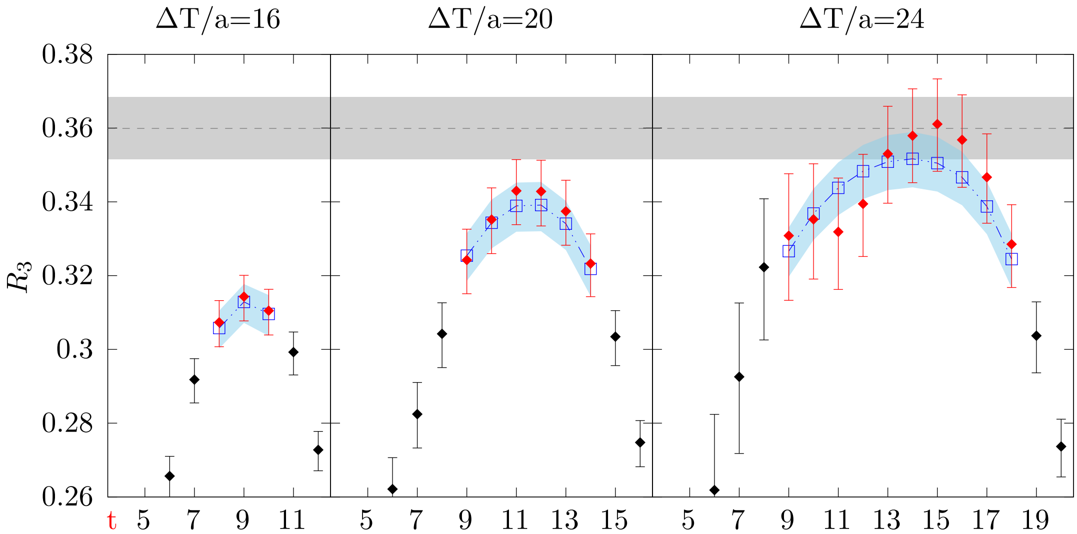

Figure A.36 *Spatial component of mostly nonperturbatively renormalised ratio R_3 vs t, for $D_s \to K$ at $n^2 = 2$ on ensemble C2. Simultaneous fit to wall separations $\Delta T/a$ 16, 20 and 24 on timeslices 8-10, 9-14 and 9-18, respectively. The grey band is the matrix element $\langle K|\gamma_i\left(n^2 = 2\right)|D_s\rangle = 0.3599(84)$. Hotelling p-value for the fit is 0.84, with excited-state matrix elements shown in table 3.6.*

C2 matrix elements $n^2 = 3$

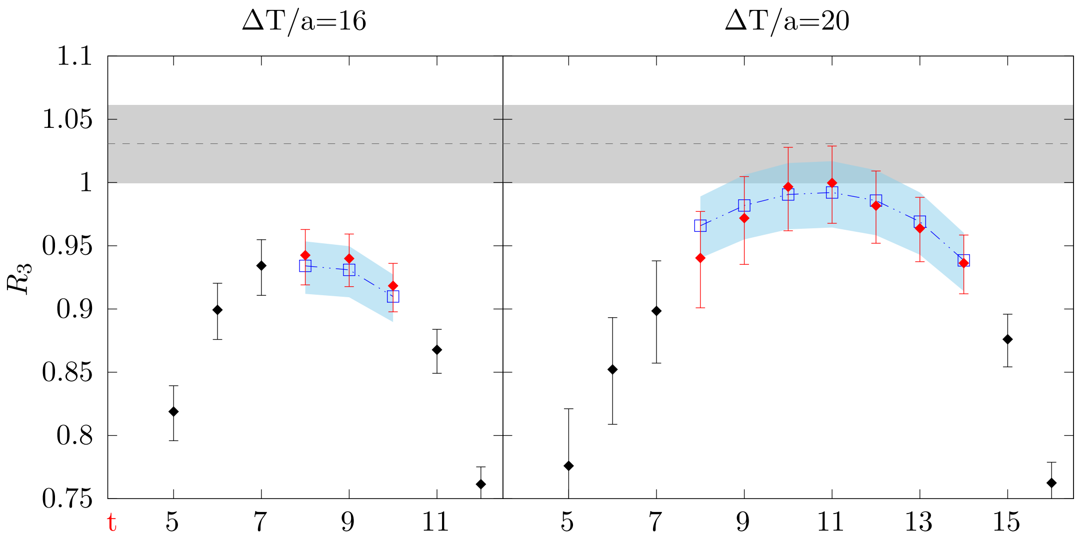

Figure A.37 *Temporal component of mostly nonperturbatively renormalised ratio R_3 vs t, for $D_s \to K$ at $n^2 = 3$ on ensemble C2. Simultaneous fit to wall separations $\Delta T/a$ 16 and 20 on timeslices 8-10 and 8-14, respectively. The grey band is the matrix element $\langle K|\gamma_4\left(n^2=3\right)|D_s\rangle = 1.031(31)$. Hotelling p-value for the fit is 0.098, with excited-state matrix elements shown in table 3.6.*

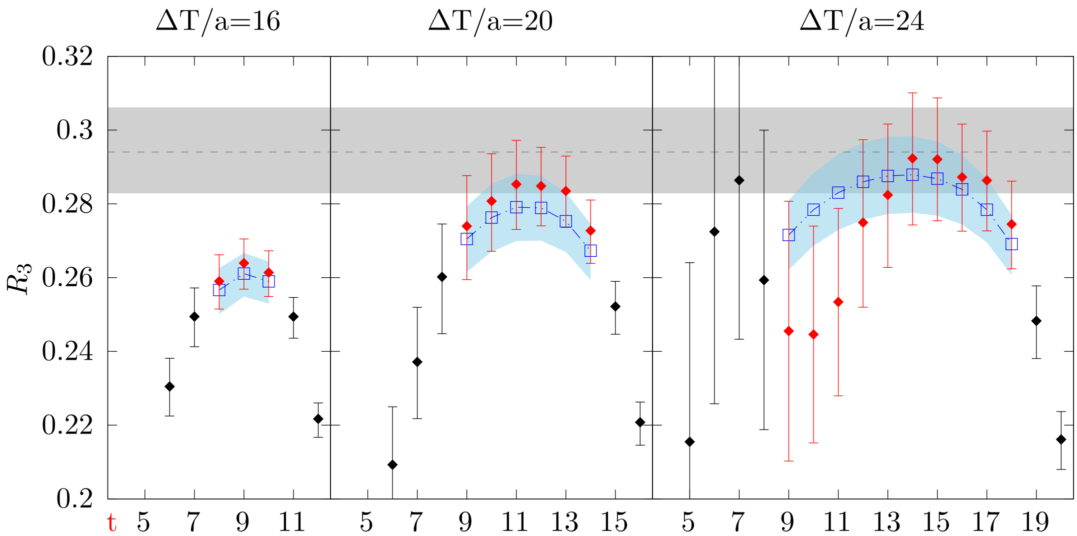

Figure A.38 *Spatial component of mostly nonperturbatively renormalised ratio R_3 vs t, for $D_s \to K$ at $n^2 = 3$ on ensemble C2. Simultaneous fit to wall separations $\Delta T/a$ 16, 20 and 24 on timeslices 8-10, 9-14 and 9-18, respectively. The grey band is the matrix element $\langle K|\gamma_i\left(n^2=3\right)|D_s\rangle = 0.294(12)$. Hotelling p-value for the fit is 0.78, with excited-state matrix elements shown in table 3.6.*

C2 matrix elements $n^2 = 4$

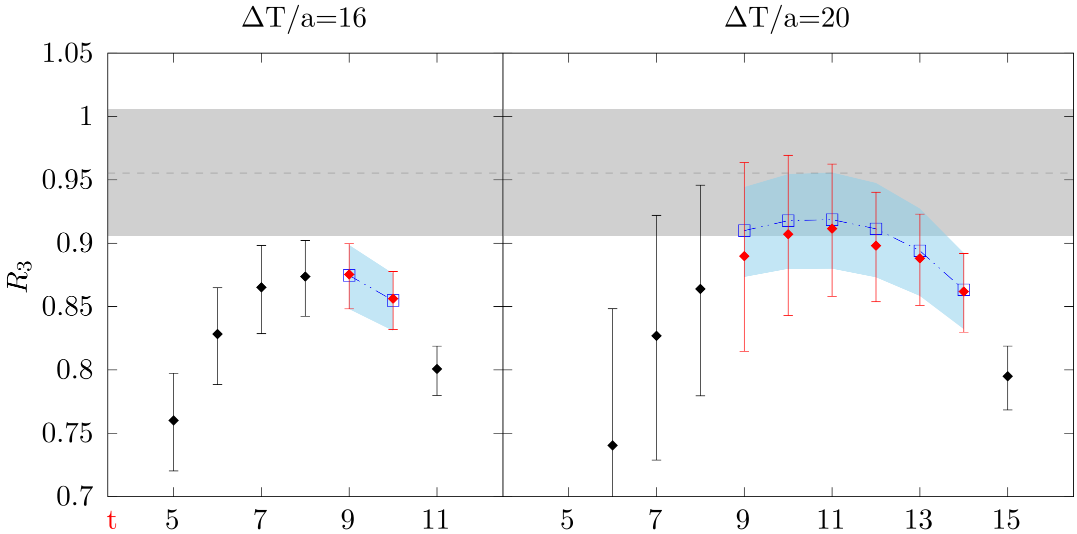

Figure A.39 *Temporal component of mostly nonperturbatively renormalised ratio R_3 vs t, for $D_s \to K$ at $n^2 = 4$ on ensemble C2. Simultaneous fit to wall separations $\Delta T/a$ 16 and 20 on timeslices 9;10 and 9-14, respectively. The grey band is the matrix element $\langle K|\gamma_4\left(n^2=4\right)|D_s\rangle = 0.955(50)$. Hotelling p-value for the fit is 0.66, with excited-state matrix elements shown in table 3.6.*

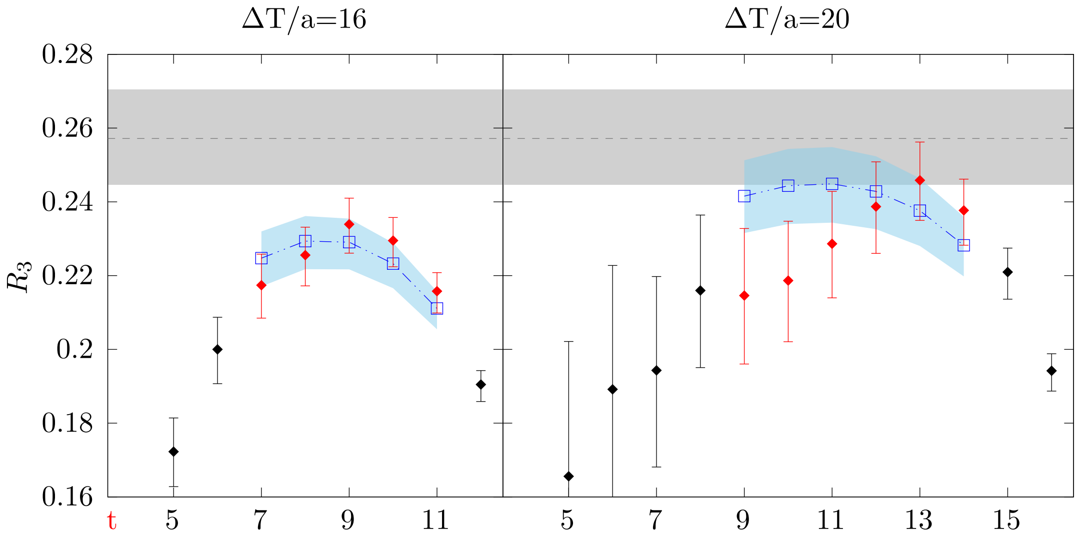

Figure A.40 *Spatial component of mostly nonperturbatively renormalised ratio R_3 vs t, for $D_s \to K$ at $n^2 = 4$ on ensemble C2. Simultaneous fit to wall separations $\Delta T/a$ 16 and 20 on timeslices 7-11 and 9-14, respectively. The grey band is the matrix element $\langle K|\gamma_i\left(n^2=4\right)|D_s\rangle = 0.257(13)$. Hotelling p-value for the fit is 0.145, with excited-state matrix elements shown in table 3.6.*

A.6 Alternate chiral continuum fits

Results presented in the main body of the thesis are for the preferred strategy. However, as set out is § 4.4, other global fit strategies are possible:

1. In § A.6.1 we present results using linear shrinkage in the estimation of the covariance matrix.
2. In § A.6.2 we present results using more terms in the global fit ansatz.

In each case the analysis follows the procedure described in the main body of the text. We present here the data tables and figures which differ from the main text.

A.6.1 Linear model with shrinkage 0.005

Covariance matrix

Name	κ^{-1}	N_{samples}
C1	9.35×10^{-6}	160
C2	1.13×10^{-5}	128
F1M	6.44×10^{-4}	72
M1	4.59×10^{-5}	128
M2	3.77×10^{-5}	128
M3	1.10×10^{-4}	120
global	5.05×10^{-3}	160

Table A.1 *Reciprocal condition numbers (see § 2.5.3) for the block diagonal components of the full covariance matrix for each ensemble. 'Global' is the reciprocal condition number for the full covariance matrix used in the fit, i.e. with cross-ensemble components set to 0. The number of samples $N_{samples}$ varies on each ensemble. Conservative estimates of the Hotelling p-value in the global fit are based on the maximum number of samples, 160.*

Linear continuum fit with shrinkage

form factor	c_0	c_1	d_0	e_0
f_0	0.781(19)	0.324(82)	-0.224(57)	0.127(14)
f_+	0.830(10)	0.175(67)	-0.184(44)	-0.151(10)

Table A.2 *Global chiral continuum fit results. Parameters match fit form (4.1). Parameter $c_{+,0}$ (blue) is implemented as a constraint per (4.26), not a free parameter. The expansion in E_L/Λ is linear, i.e. $n_{E,X} = 1$. Ledoit and Wolf shrinkage is applied to the covariance matrix with $\lambda = 0.005$.*

N_{data}	N_{param}	ν	t^2_ν	Hotelling p-value
58	7	51	1.84	0.156

Table A.3 *Statistical summary of chiral continuum fit: number of data points N_{data}; number of parameters N_{param}; number of degrees of freedom $\nu = N_{data} - N_{param}$; Hotelling test statistic per degree of freedom t^2_ν; and Hotelling p-value.*

$f_X\left(q^2\right)$	result(stat)	$\delta\%$
$f_0(0) = f_+(0)$	0.6556(75)	1.1%
$f_0\left(q^2_{\text{max}}\right)$	1.001(10)	1.0%
$f_+\left(q^2_{\text{max}}\right)$	1.593(15)	0.9%

Table A.4 *Form factors at kinematic points $q_0 = 0$ and q^2_{max} from chiral continuum fit results in table A.2. The result for each form factor $f_X\left(q^2\right)$ is shown with statistical errors in brackets. The $\delta\%$ column shows the relative statistical error expressed as a percentage.*

Correlation matrix

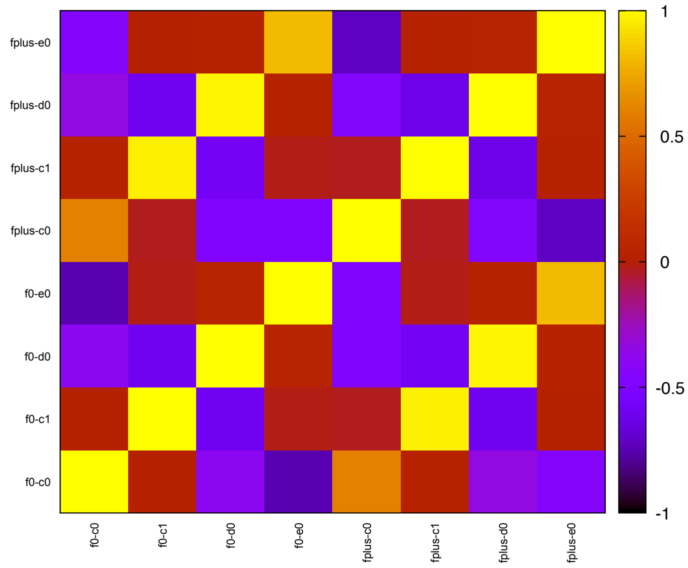

Figure A.41 *Correlation matrix of fitted parameters*

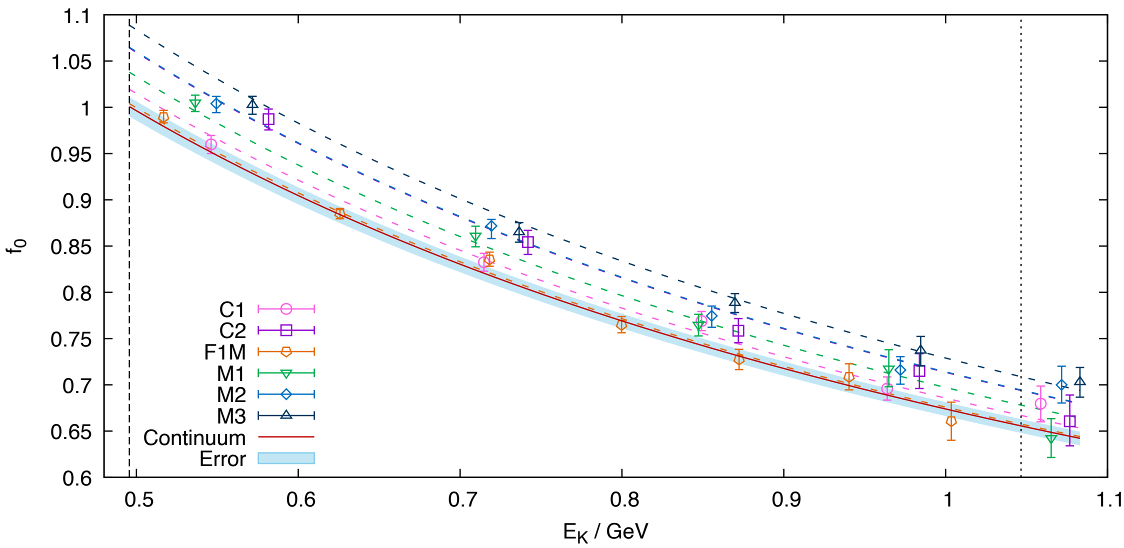

Figure A.42 *Data points entering the chiral continuum fit for scalar form factor f_0. The form factor is shown on the vertical axis, with the energy of the final-state kaon E_K in GeV on the horizontal axis. Statistical errors only are shown for the continuum fit result (blue). Coloured, dashed trend lines show $f_X = f_X^{(cont)} + f_X^{(lat)}$ for each ensemble. The trend line for the C2 ensemble is underneath the trend line for the M2 ensemble. The vertical dotted line indicates $E_{K,max}^p$ (i.e. q_0).*

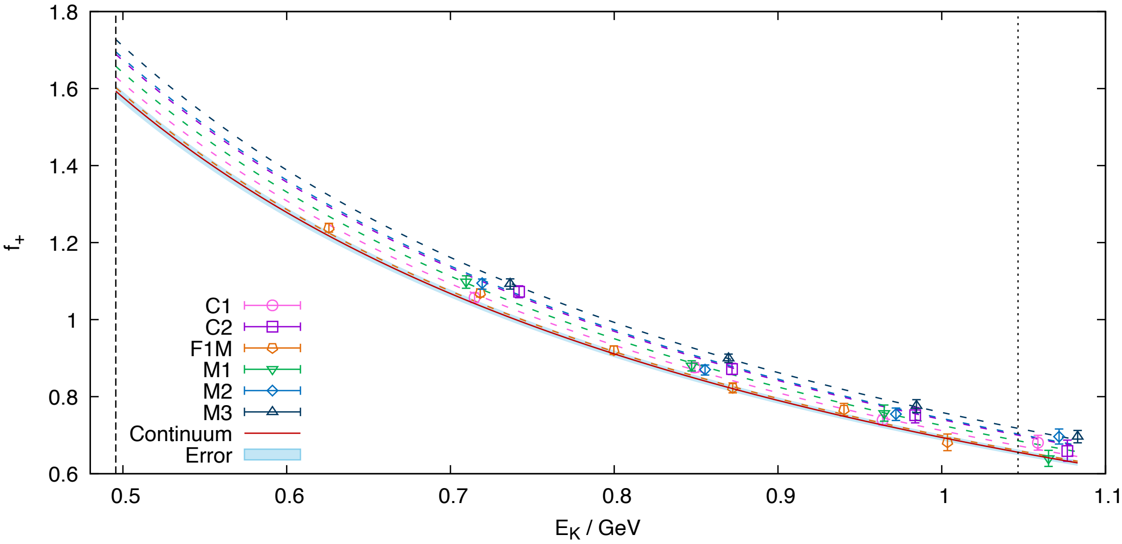

Figure A.43 *Data points entering the chiral continuum fit for vector form factor f_+ (and otherwise as described in figure A.42). The trend line for ensemble C2 is visible immediately underneath the trend line for M2.*

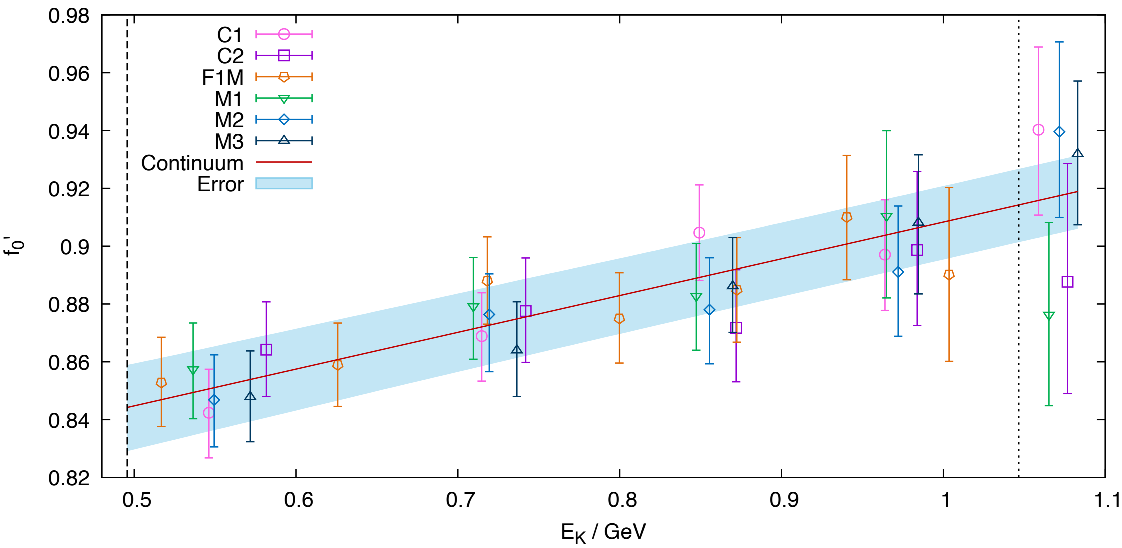

Figure A.44 *Plot of adjusted data points f_0' (4.30) – i.e. adjusted by $f_0^{(lat)}$ and with the pole removed – and otherwise as described in fig A.42. These data points agree very well with the chiral continuum fit.*

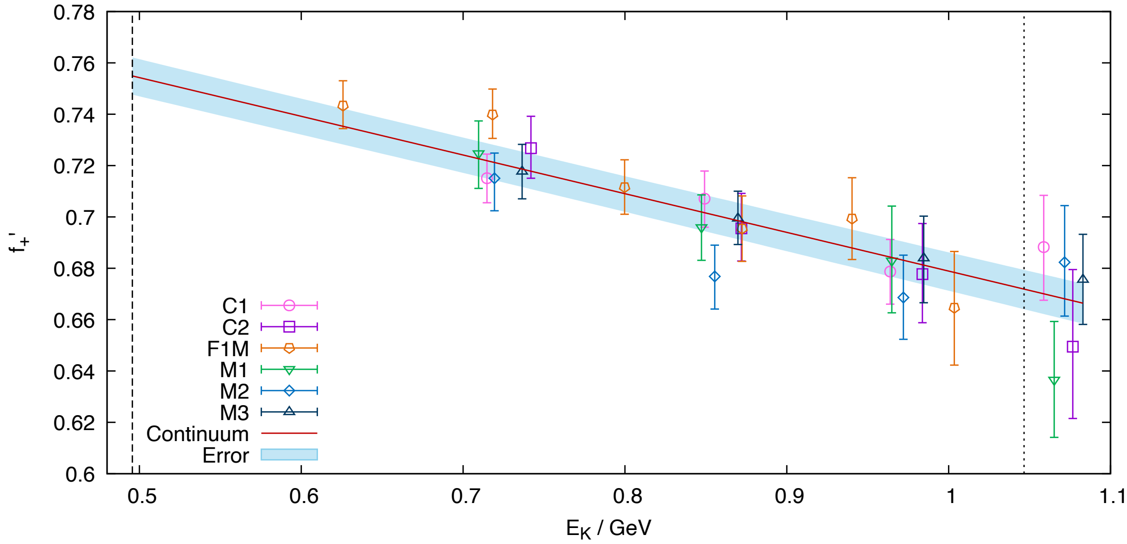

Figure A.45 *Plot of adjusted data points f_+' (4.30) – i.e. adjusted by $f_+^{(lat)}$ and with the pole removed – and otherwise as described in fig A.42. There is a moderate increase in tension with the global fit, however there is still very good agreement.*

Systematic uncertainty results

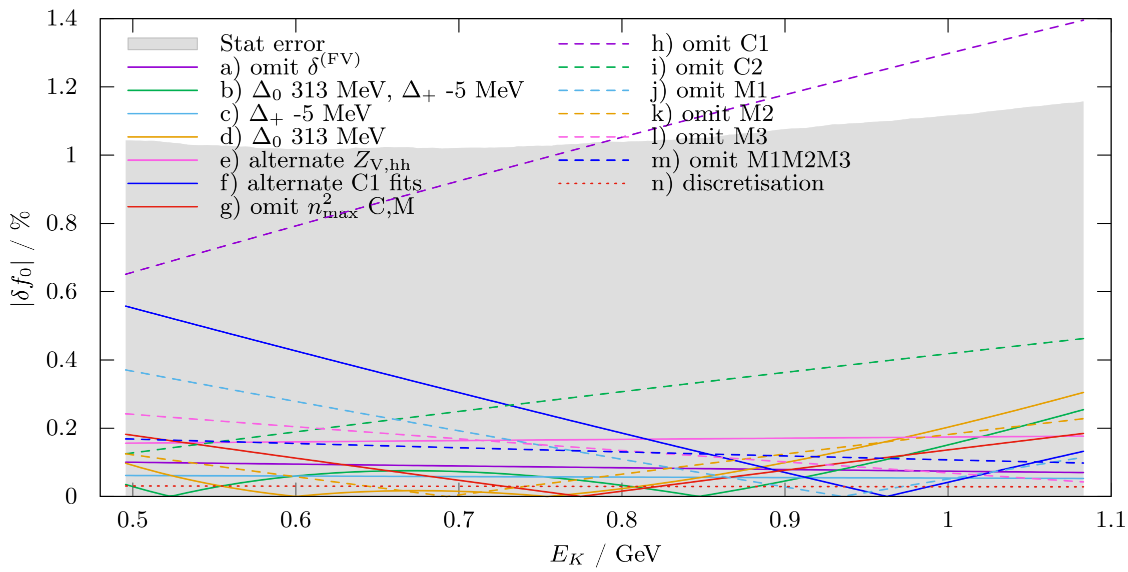

Figure A.46 *Relative error $\delta f_0^{(x)}(E_K)$ (vertical axis, %) (4.33) associated with each alternate fit choice (x) as a function of final-state kaon energy E_K (horizontal axis, GeV). The grey band is the statistical error of the reference fit. Dashed lines indicate alternatives not included in the final fit systematic uncertainty relative error (see § 4.3).*

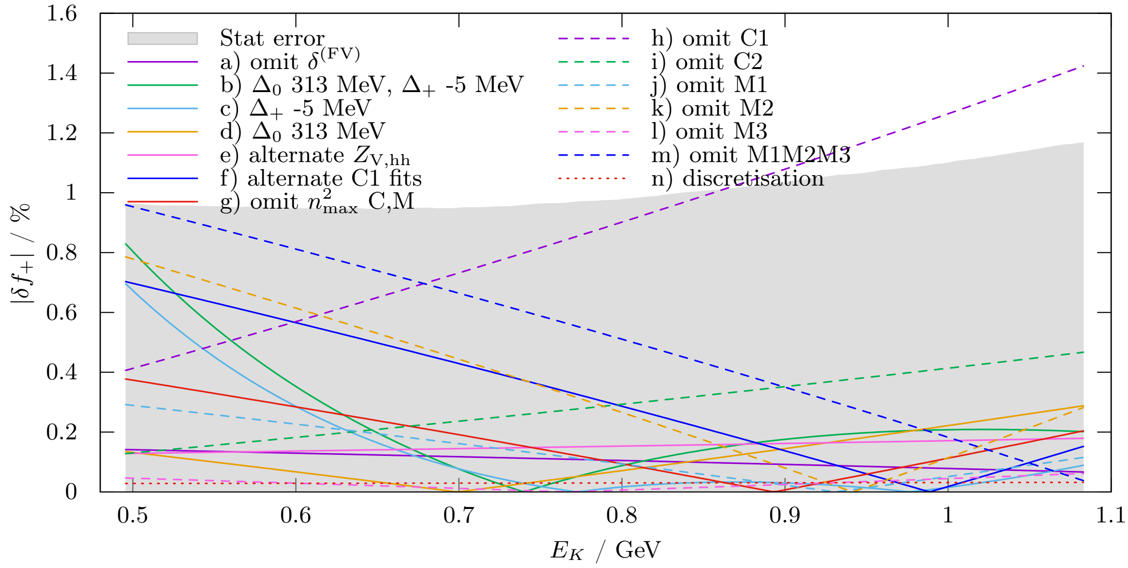

Figure A.47 *Relative error $\delta f_+^{(x)}(E_K)$ (otherwise as described in fig A.47).*

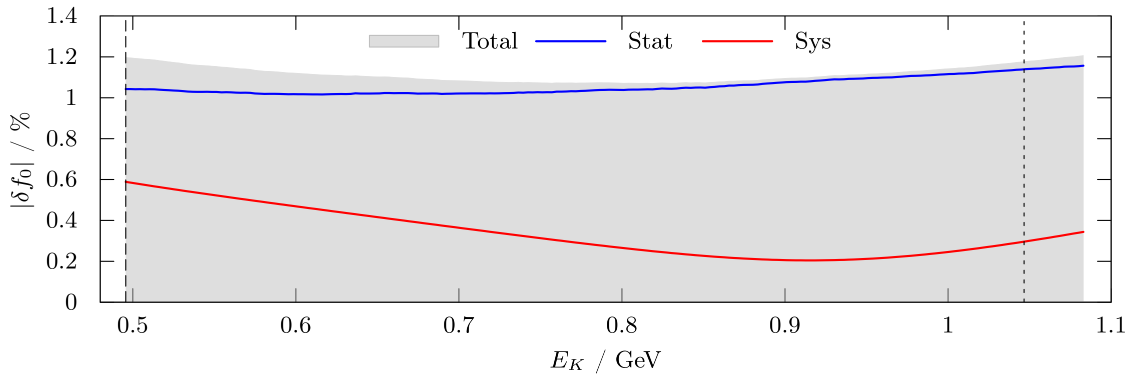

Figure A.48 *Error budget for form factor f_0. Vertical scale shows relative error (%) for total (grey shading), statistical (blue) and systematic (red) errors as a function of final-state kaon energy E_K (horizontal axis, GeV). q^2_{max} and q_0 are indicated by the dashed and dotted vertical lines respectively.*

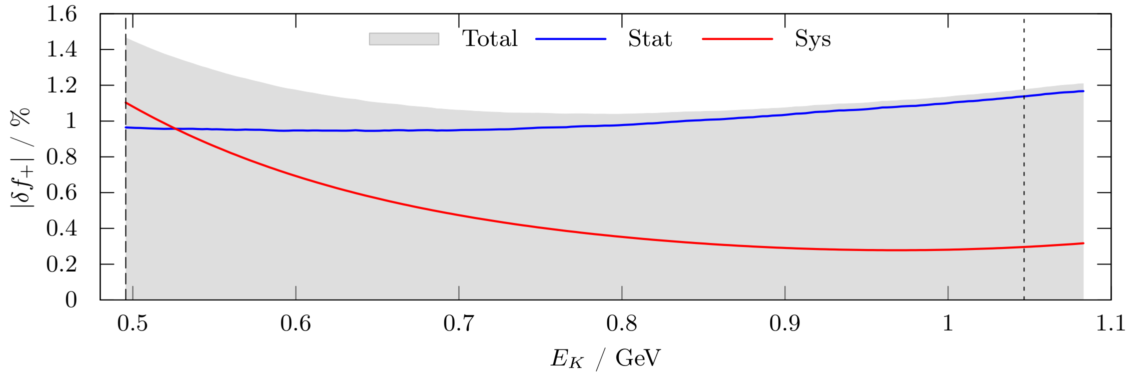

Figure A.49 *Error budget for form factor f_+ (otherwise as described in fig A.48).*

	t^2	ν	t^2_ν	p-H	$f_0(0)$	$f_0(q^2_{\mathrm{max}})$	$f_+(q^2_{\mathrm{max}})$
Ref	93.955	51	1.84226	0.155862	0.6556(75)	1.001(10)	1.593(15)
a	83.913	51	1.64537	0.2971	0.6561(75)	1.002(10)	1.595(15)
b	98.248	51	1.92645	0.114604	0.6570(73)	1.001(10)	1.580(15)
c	96.241	51	1.88708	0.132607	0.6553(74)	1.000(10)	1.582(15)
d	95.524	51	1.87303	0.139573	0.6573(74)	1.002(10)	1.591(15)
e	92.744	51	1.81851	0.169441	0.6545(76)	0.999(11)	1.591(16)
f	94.191	51	1.84689	0.153319	0.6550(77)	1.006(11)	1.604(16)
g	78.358	41	1.91119	0.0703837	0.6546(77)	1.003(10)	1.599(17)
h	80.057	42	1.90614	0.159062	0.6468(98)	0.994(14)	1.587(20)
i	77.230	42	1.83881	0.0988414	0.6585(84)	1.002(12)	1.595(17)
j	83.379	42	1.98523	0.0543663	0.6562(78)	0.997(11)	1.588(16)
k	59.870	42	1.42548	0.396642	0.6543(77)	1.002(11)	1.606(16)
l	85.043	42	2.02484	0.0459162	0.6560(79)	1.003(11)	1.592(16)
m	41.117	24	1.71324	0.0896853	0.6563(98)	1.002(14)	1.608(21)

Table A.5 *Fit characteristics for alternate fits: test statistic t^2; degrees of freedom ν; test statistic per degree of freedom t^2_ν; Hotelling p-value p-H; $f_0(0) = f_+(0)$; $f_0\left(q^2_{max}\right)$; and $f_+\left(q^2_{max}\right)$ – i.e. form factors at q_0 and q^2_{max}. The test statistic is above the $\alpha = 0.05$ significance level in all cases except (g) which is marginal due to the greatly reduced degrees of freedom in the fit excluding all coarse data points.*

A.6.2 Cubic model

In the cubic model we make two changes compared with the reference fit:

- We use all 58 data points
  - i.e. including $f_0\,(n^2 = 4)$ for ensembles C2, M1, M2 and M3
- We include two more terms in the fit ansatz for f_+ (4.1)
  - i.e. $n_{E,+} = 3$

Covariance matrix

Name	κ^{-1}	N_{samples}	N_{data}
C1	9.35×10^{-6}	160	9
C2	1.13×10^{-5}	128	9
F1M	6.44×10^{-4}	72	13
M1	4.59×10^{-5}	128	9
M2	3.77×10^{-5}	128	9
M3	1.10×10^{-4}	120	9
global	5.09×10^{-5}	160	58

Table A.6 *Reciprocal condition numbers (§ 2.5.3) for block diagonal components of the covariance matrix for each ensemble for comparison with the reference fit, table 4.2 (as described there).*

Fully correlated continuum fit results

A fully-correlated global fit was run using the inputs described in the previous section. The maximum number of energy levels $e_{X,n}$ the fitter was able to resolve was three for the f_+ form factor and one for the f_0 form factor.

Fit results are shown in tables A.7 parameters, A.8 statistical summary and A.9 form factors at q_0 and q^2_{max}.

form factor	c_0	c_1	d_0	e_0	e_1	e_2
f_0	0.777(20)	0.326(83)	-0.208(58)	0.128(14)		
f_+	0.553(65)	0.305(70)	-0.151(45)	0.81(22)	-1.10(26)	0.41(10)

Table A.7 *Global chiral continuum fit results. Parameters match fit form (4.1). Parameter $c_{+,0}$ (blue) is implemented as a constraint per (4.26), not a free parameter. It was necessary to include 3 terms in the expansion of E_L/Λ for f_+, i.e. $n_{E,+} = 3$, $n_{E,0} = 1$.*

N_{data}	N_{param}	ν	t^2_ν	Hotelling p-value
58	9	49	1.71	0.2192

Table A.8 *Statistical summary of chiral continuum fit: number of data points N_{data}; number of parameters N_{param}; number of degrees of freedom $\nu = N_{data} - N_{param}$; Hotelling test statistic per degree of freedom t^2_ν; and Hotelling p-value.*

$f_X(q^2)$	result(stat)	$\delta\%$
$f_0(0) = f_+(0)$	0.6533(76)	1.2%
$f_0(q^2_{\text{max}})$	0.997(11)	1.1%
$f_+(q^2_{\text{max}})$	1.550(20)	1.3%

Table A.9 *Form factors at kinematic points $q_0 = 0$ and q^2_{max} from chiral continuum fit results in table A.7. The result for each form factor $f_X(q^2)$ is shown with statistical errors in brackets. The $\delta\%$ column shows the relative statistical error expressed as a percentage.*

Correlation matrix

The correlation matrix for the fitted parameters is shown in table A.50. The block submatrix excluding coefficients $f_{+,n}$ appears relatively unchanged cf fig 4.7.

In the new components of the correlation matrix, strong correlation (both positive and negative) was observed amongst the coefficients e_n and c_0 for form factor f_+. This is perhaps unsurprising as these all relate to the expansion in terms of kaon energies.

However the alternating sign of the coefficients in the energy expansion and the very strong correlations support the view that this fit is fitting noise in the correlation matrix which is an artefact of the limited statistics – rather than underlying physics.

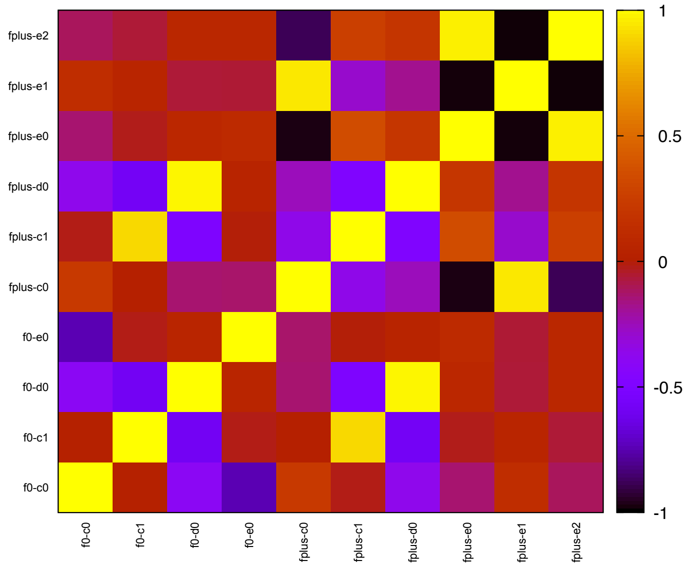

Figure A.50 *Correlation matrix of fitted parameters for comparison with fig 4.7 (and as described there). The sub matrix excluding coefficients $f_{+,n}$ appears relatively unchanged, however there are strong correlations amongst for factor f_+ parameters c_0 and e_n.*

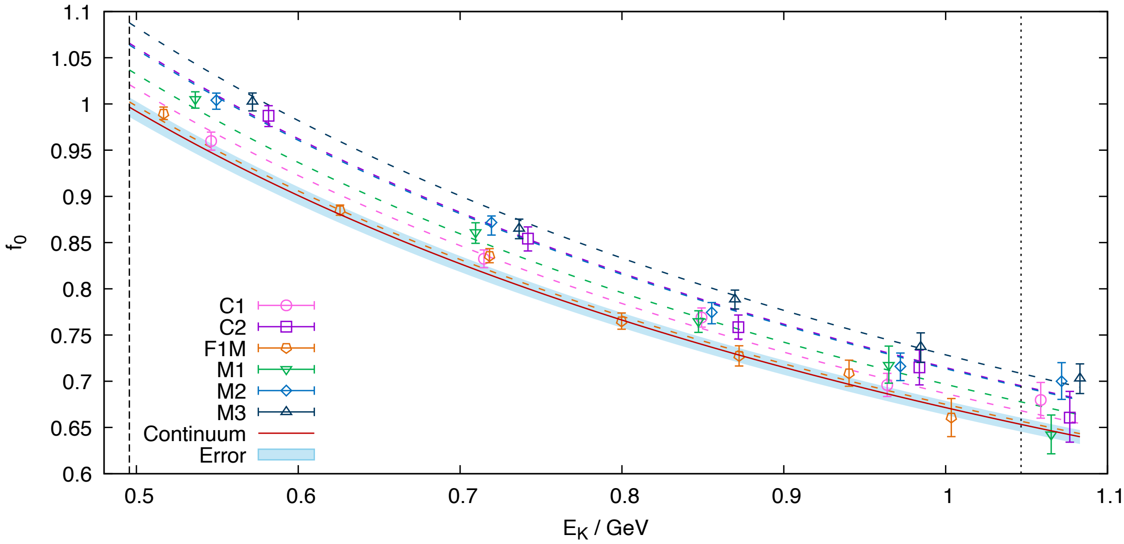

Figure A.51 *Data points entering the chiral continuum fit for scalar form factor f_0. The form factor is shown on the vertical axis, with the energy of the final-state kaon E_K in GeV on the horizontal axis. Statistical errors only are shown for the continuum fit result (blue). Coloured, dashed trend lines show $f_X = f_X^{(cont)} + f_X^{(lat)}$ for each ensemble. The trend line for the C2 ensemble is visible slightly above the trend line for the M2 ensemble. The vertical dotted line indicates $E_{K,max}^p$ (i.e. q_0).*

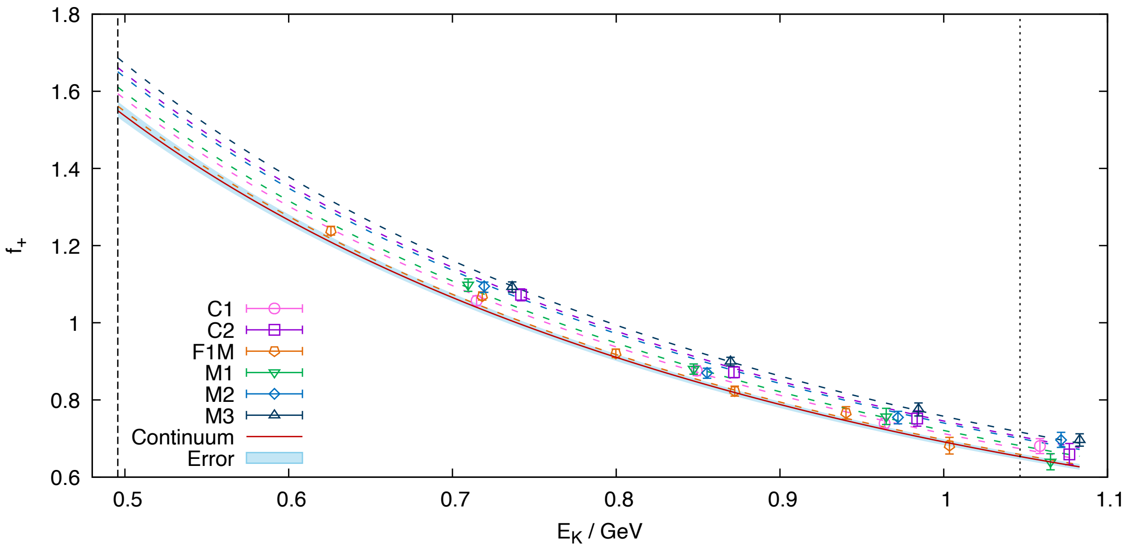

Figure A.52 *Data points entering the chiral continuum fit for vector form factor f_+ (and otherwise as described in figure A.51).*

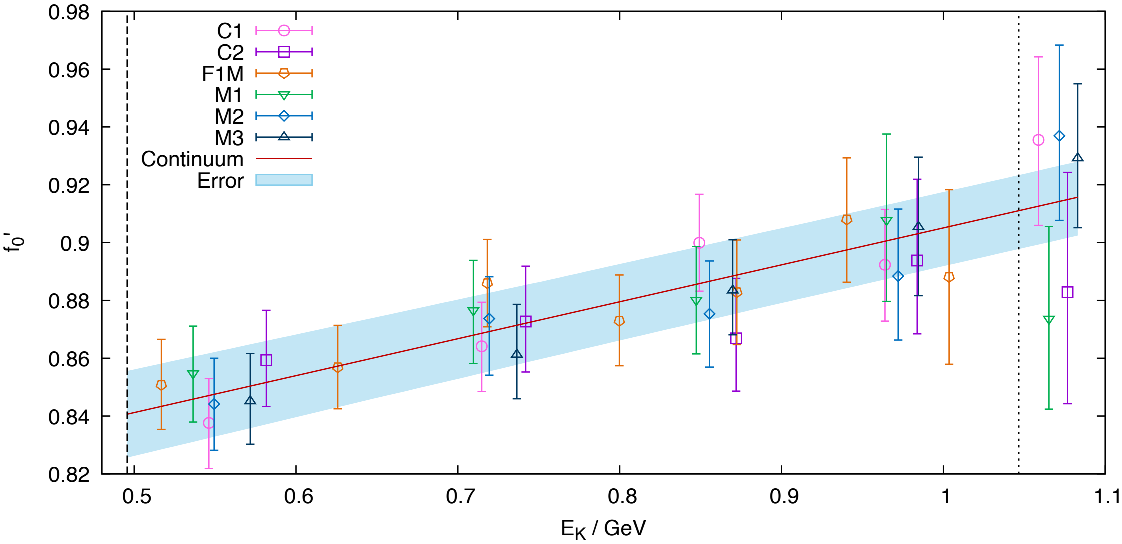

Figure A.53 *Plot of adjusted data points* f_0' (4.30) *– i.e. adjusted by* $f_0^{(lat)}$ *and with the pole removed – and otherwise as described in fig A.51. These data points agree very well with the chiral continuum fit.*

The adjusted data points agree very well with the chiral continuum fit. There is more of a spread in the data points near q_0, although this is unsurprising given that these data points are constructed from 2- and 3-point functions with the greatest Fourier momenta, i.e. the least precise data in this data set.

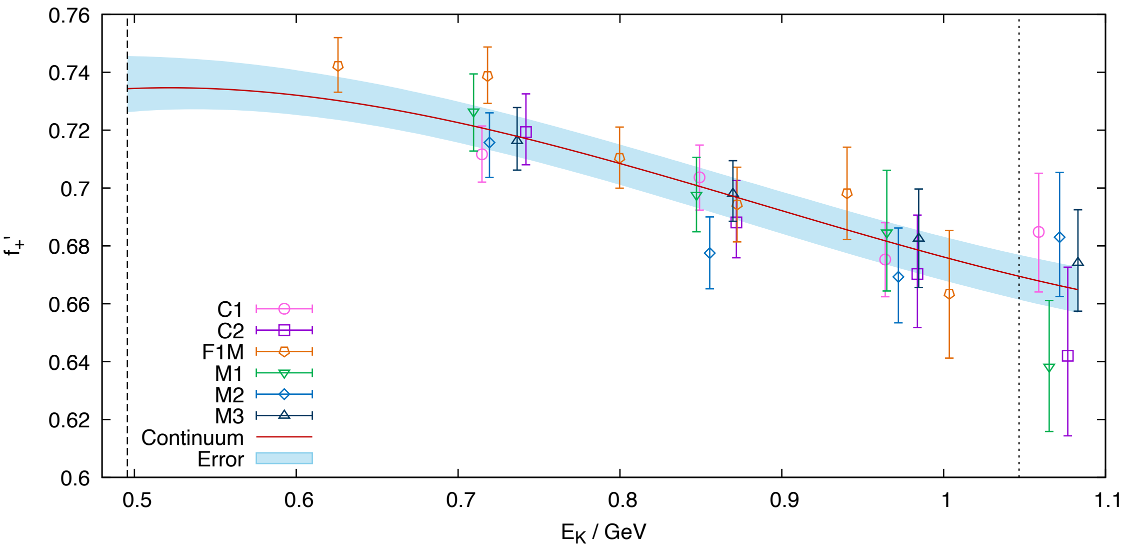

Figure A.54 *Plot of adjusted data points* f_+' (4.30) *– i.e. adjusted by* $f_+^{(lat)}$ *and with the pole removed – and otherwise as described in fig A.51. There is a moderate increase in tension with the global fit, however there is still very good agreement.*

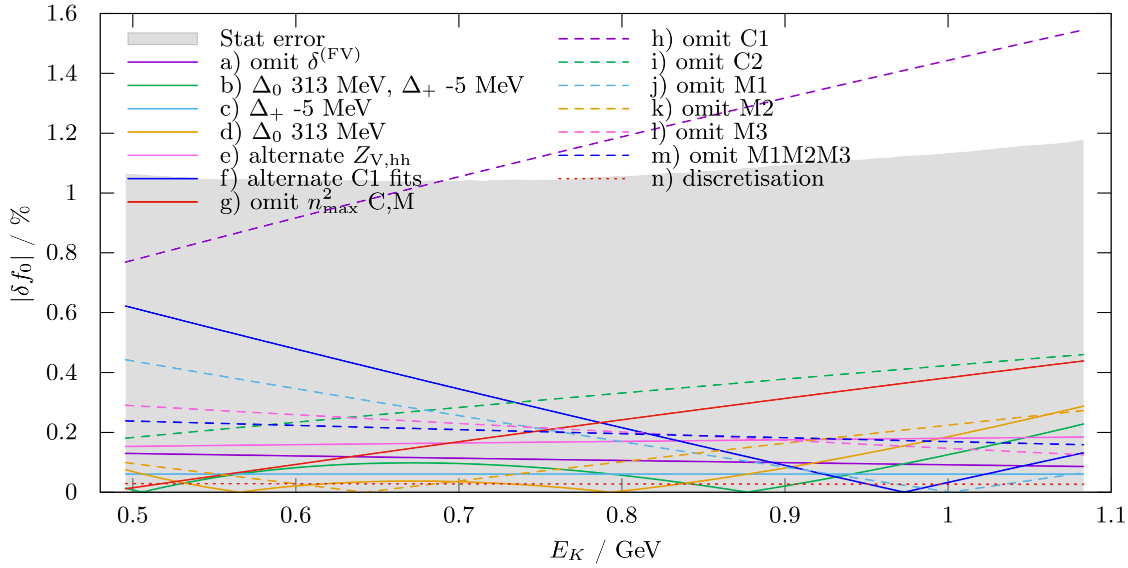

Figure A.55 *Relative error $\delta f_0^{(x)}(E_K)$ (vertical axis, %) (4.33) associated with each alternate fit choice (x) as a function of final-state kaon energy E_K (horizontal axis, GeV). The grey band is the statistical error of the reference fit. Dashed lines indicate alternatives not included in the final fit systematic uncertainty relative error (see § 4.3).*

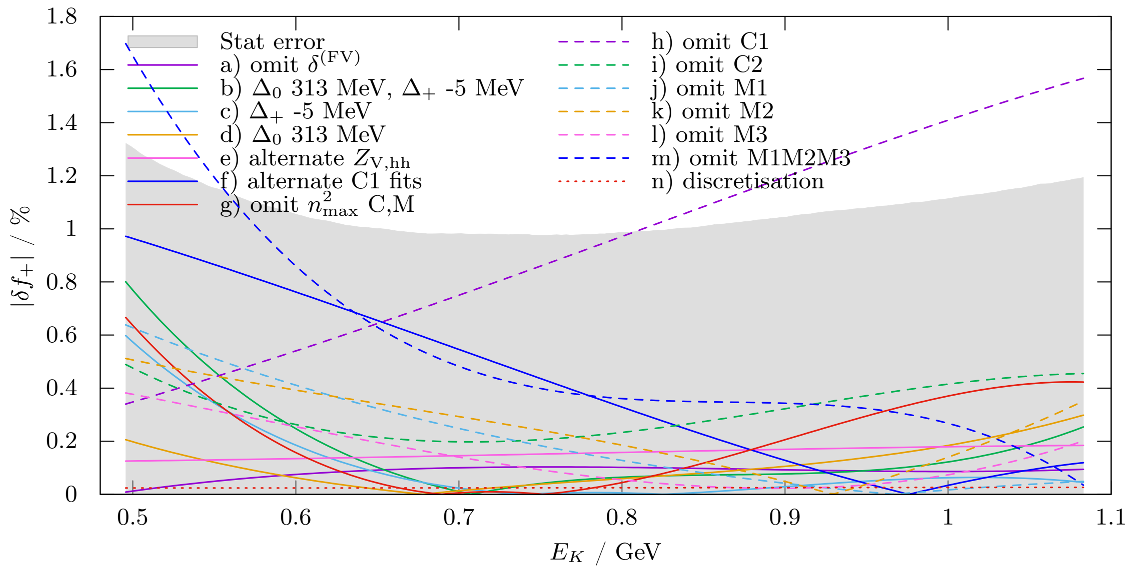

Figure A.56 *Relative error $\delta f_+^{(x)}(E_K)$ (otherwise as described in fig A.56).*

	t^2	ν	t^2_ν	p-H	$f_0\,(0)$	$f_0\,(q^2_{\text{max}})$	$f_+\,(q^2_{\text{max}})$
Ref	83.945	49	1.71317	0.219195	0.6533(76)	0.997(11)	1.550(20)
a	87.927	49	1.79443	0.166035	0.6539(76)	0.998(11)	1.550(27)
b	84.677	49	1.72812	0.208566	0.6545(74)	0.997(11)	1.537(20)
c	84.533	49	1.72518	0.210622	0.6529(75)	0.996(11)	1.540(20)
d	83.972	49	1.71372	0.218795	0.6549(74)	0.997(11)	1.546(20)
e	83.425	49	1.70257	0.226971	0.6521(77)	0.995(11)	1.548(21)
f	80.917	49	1.65138	0.267294	0.6527(77)	1.003(11)	1.565(21)
g	69.686	39	1.78683	0.105592	0.6506(77)	0.996(11)	1.539(25)
h	64.426	40	1.61066	0.329268	0.6435(98)	0.989(15)	1.544(24)
i	74.826	40	1.87066	0.079173	0.6562(84)	0.998(12)	1.557(28)
j	75.815	40	1.89538	0.0715868	0.6535(78)	0.992(11)	1.540(23)
k	55.512	40	1.38782	0.411936	0.6517(78)	0.998(11)	1.558(23)
l	75.313	40	1.88284	0.0753529	0.6542(79)	0.999(11)	1.556(21)
m	43.092	22	1.95875	0.0350603	0.6544(99)	0.999(14)	1.576(41)

Table A.10 *Fit characteristics for alternate fits: test statistic t^2; degrees of freedom ν; test statistic per degree of freedom t^2_ν; Hotelling p-value p-H; $f_0\,(0) = f_+\,(0)$; $f_0\left(q^2_{max}\right)$; and $f_+\left(q^2_{max}\right)$ – i.e. form factors at q_0 and q^2_{max}. The test statistic is above the $\alpha = 0.05$ significance level in all cases except (g) which is marginal due to the greatly reduced degrees of freedom in the fit excluding all coarse data points.*

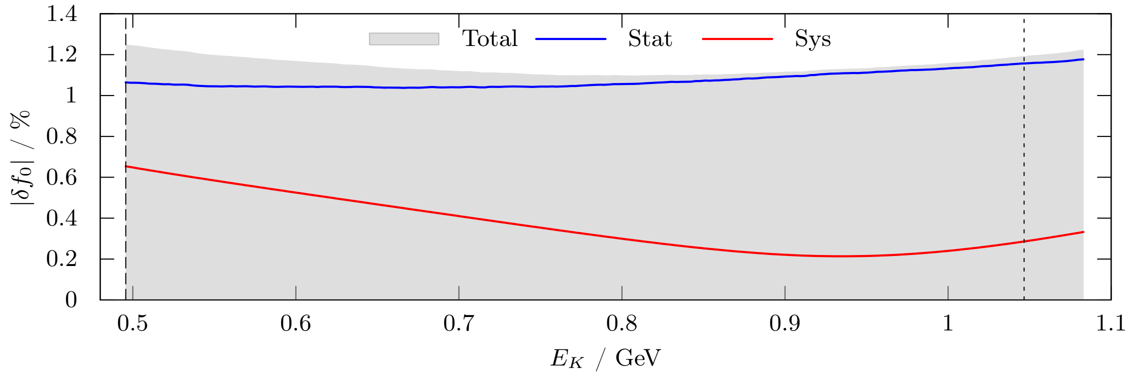

Figure A.57 *Error budget for form factor f_0. Vertical scale shows relative error (%) for total (grey shading), statistical (blue) and systematic (red) errors as a function of final-state kaon energy E_K (horizontal axis, GeV). q^2_{max} and q_0 are indicated by the dashed and dotted vertical lines respectively.*

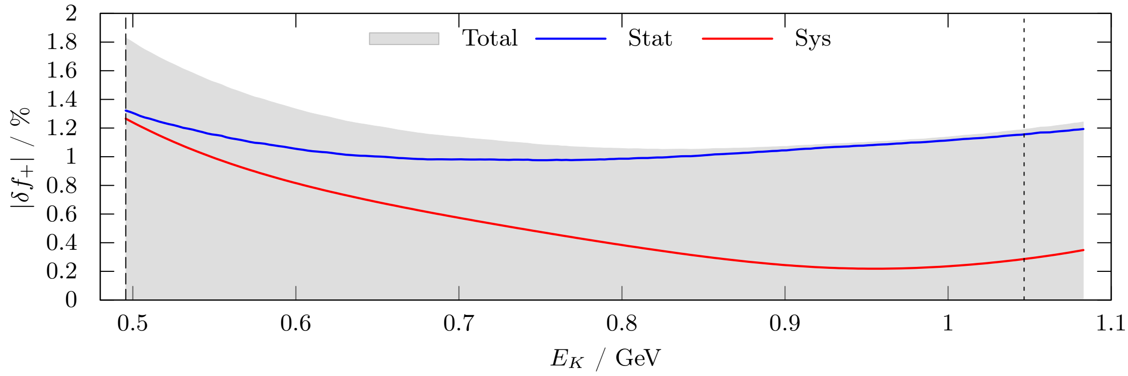

Figure A.58 *Error budget for form factor f_+ (otherwise as described in fig A.57).*

A.7 D_s fit stability tables, ensemble F1M

Tables A.11 and A.12 show the stability of the D_s fits on ensemble F1M over a range of fit start and stop times. Each fit is a simultaneous, 2-state fit to both the point- and wall-source correlation functions, both with point-sinks and using a cosh model (2.86).

Both tables contain the same columns:

- **Fit** – Fit ranges for the point- and wall-source correlation functions (both point-sink) respectively.

- **E0, E1** – Ground and 1st excited-state energies respectively.

- **g5P0, g5P1, g5W** – overlap coefficients $A_{\mathrm{P},0}$, $A_{\mathrm{P},1}$, $A_{\mathrm{W},0}$ and $A_{\mathrm{W},1}$ respectively.

- χ^2/dof – test statistic t^2 (2.45).

- **pvalue** – p-value when using the χ^2 distribution.

- **pvalueH** – p-value when using the Hotelling distribution.

In Table A.11 the start and stop times are varied for the fit to the point-source correlation function, while holding the fit times to the wall-source correlation function constant at $[13, 29]$.

Fit	E0	E1	g5P0	g5P1	g5W0	g5W1	$\chi^2/$dof	pvalue	pvalueH
[11-27], [13-29]	0.72837(26)	1.028(11)	45.96(16)	75.8(3.8)	53466(300)	-40287(4700)	1.40	0.0778	0.65
[11-28], [13-29]	0.72836(26)	1.026(11)	45.98(16)	75.3(3.7)	53467(290)	-40247(4700)	1.38	0.0819	0.69
[11-29], [13-29]	0.72826(25)	1.024(10)	45.88(14)	74.6(3.6)	53605(290)	-39014(4600)	1.44	0.0549	0.67
[12-27], [13-29]	0.72850(26)	1.004(15)	45.90(16)	65.8(5.3)	53765(340)	-38116(4400)	1.24	0.1794	0.74
[12-28], [13-29]	0.72849(26)	1.002(15)	45.93(16)	65.4(5.2)	53769(340)	-38148(4400)	1.23	0.1871	0.77
[12-29], [13-29]	0.72841(26)	0.999(15)	45.84(15)	64.5(5.0)	53907(330)	-37117(4300)	1.27	0.1502	0.77
[13-27], [13-29]	0.72886(29)	0.980(14)	46.05(17)	55.3(4.5)	54241(360)	-41579(4600)	0.81	0.734	0.96
[13-28], [13-29]	0.72885(29)	0.979(14)	46.07(17)	55.1(4.4)	54244(350)	-41651(4500)	0.81	0.738	0.97
[13-29], [13-29]	0.72870(28)	0.978(14)	45.93(16)	55.4(4.5)	54377(360)	-39808(4400)	0.96	0.529	0.93
[14-27], [13-29]	0.72886(29)	0.974(17)	46.06(17)	53.0(5.6)	54244(360)	-40795(4700)	0.83	0.709	0.95
[14-28], [13-29]	0.72885(29)	0.975(17)	46.08(17)	53.4(5.7)	54246(350)	-41094(4700)	0.84	0.702	0.95
[14-29], [13-29]	0.72871(28)	0.969(16)	45.96(16)	52.1(5.3)	54366(360)	-38947(4400)	0.95	0.531	0.92

Table A.11 *Stability of the D_s fit at zero momentum on the F1M ensemble over a range of fit start and stop times for the point-source correlation function while keeping the wall-source correlation function fit times constant. Columns are described in the text above this figure.*

In Table A.12 the start and stop times are varied for the fit to the wall-source correlation function, while holding the fit times to the point-source correlation function constant at $[13, 28]$.

Fit	E0	E1	g5P0	g5P1	g5W0	g5W1	χ^2/dof	pvalue	pvalueH
[13-28], [11-28]	0.72823(27)	0.978(14)	45.71(16)	58.2(4.8)	53903(350)	-30131(2500)	1.12	0.305	0.85
[13-28], [11-29]	0.72837(26)	0.976(15)	45.79(16)	57.4(4.7)	53921(360)	-30424(2500)	1.27	0.1518	0.77
[13-28], [11-30]	0.72834(26)	0.974(14)	45.78(16)	56.6(4.6)	53963(370)	-30357(2400)	1.46	0.0497	0.66
[13-28], [12-28]	0.72834(28)	0.980(15)	45.77(16)	58.1(4.8)	53982(350)	-32400(3400)	1.12	0.301	0.83
[13-28], [12-29]	0.72850(27)	0.979(15)	45.86(16)	57.4(4.8)	54028(360)	-33513(3400)	1.25	0.1739	0.76
[13-28], [12-30]	0.72853(27)	0.978(14)	45.88(16)	56.7(4.6)	54106(370)	-34722(3300)	1.37	0.0888	0.70
[13-28], [13-28]	0.72871(30)	0.980(14)	45.99(17)	55.7(4.5)	54196(350)	-40076(4500)	0.77	0.790	0.97
[13-28], [13-29]	0.72885(29)	0.979(14)	46.07(17)	55.1(4.4)	54244(350)	-41651(4500)	0.81	0.738	0.97
[13-28], [13-30]	0.72886(29)	0.978(14)	46.09(17)	54.4(4.4)	54318(360)	-42789(4500)	0.99	0.480	0.91
[13-28], [14-28]	0.72866(32)	0.973(17)	45.96(18)	54.0(5.2)	54185(350)	-37002(6600)	0.79	0.764	0.96
[13-28], [14-29]	0.72883(29)	0.975(18)	46.06(17)	54.1(5.3)	54240(350)	-39893(6800)	0.84	0.696	0.95
[13-28], [14-30]	0.72886(29)	0.978(17)	46.09(17)	54.5(5.3)	54318(360)	-42844(6800)	1.03	0.426	0.88
[13-28], [15-28]	0.72868(31)	0.990(24)	46.06(20)	58.9(7.5)	54171(350)	-48229(13000)	0.73	0.826	0.97
[13-28], [15-29]	0.72887(29)	0.988(24)	46.14(19)	57.4(7.3)	54238(350)	-48323(12000)	0.83	0.705	0.95
[13-28], [15-30]	0.72890(29)	0.991(23)	46.17(19)	58.0(7.3)	54313(350)	-52005(13000)	1.02	0.435	0.87
[13-28], [16-28]	0.72880(33)	1.004(28)	46.15(21)	63.0(9.5)	54226(340)	-60269(20000)	0.71	0.84	0.97
[13-28], [16-29]	0.72899(31)	1.002(28)	46.23(20)	61.7(9.1)	54294(340)	-61000(20000)	0.81	0.724	0.94
[13-28], [16-30]	0.72898(31)	1.000(27)	46.22(20)	60.6(8.7)	54351(350)	-60031(19000)	1.04	0.406	0.84

Table A.12 *Stability of the D_s fit at zero momentum on the F1M ensemble over a range of fit start and stop times for the wall-source correlation function while keeping the point-source correlation function fit times constant. Columns are described in the text above fig A.11.*

A.8 Lattice dispersion relation

This section summarises an exploratory study which was performed to test whether the lattice dispersion relation was a suitable model for the ground- and first excited-state energies extracted from 2-state kaon fits on each ensemble at each of the momenta covered in this thesis.

The method used for this study is:

1. Fit the kaon 2-point correlation function data separately for each momentum on each ensemble.
2. Each fit is a simultaneous fit of the kaon point- and wall-source two point correlation function data (each with a point-sink).
3. Each fit is repeated multiple times, varying the fit start and stop times in small increments.
4. Fits which do not have an acceptable Hotelling p-value are rejected.

As a result, an ensemble of ground-state energies (masses) aE_0 and first excited-state energies aE_1 for the kaon at each momentum on each ensemble are obtained.

Please note:

- This exploratory study was performed before the final fit ranges were chosen for the main body of this thesis.
- Data from these fits do not enter the analysis in the main body of this thesis.

Next, the ensemble of results according to this procedure are plotted:

1. Two plots are produced per ensemble:
   (a) One plot for the ground-state energies (masses) aE_0.
   (b) A separate plot for the first excited-state energies aE_1.
2. All fits for the same integer lattice momentum n^2 are grouped together.
3. Within each n^2:
   (a) Fits are ordered by decreasing p-value left to right.
   (b) Results are spaced equally.
   (c) I.e. for each n^2 there are multiple fit results, all of which are valid.
4. Each fit is colour coded by the initial fit time t_i for the point-source correlation function:
   - The two plots for each ensemble share the same legend – data points for the same t_i share the same colour across each of the two plots.
   - In some cases, the legend contains rows with no corresponding data points shown.
5. Each fit is labelled (immediately above each data point) with three numbers separated by underscores:
   (a) The final fit time for the point data $t_{f,\mathrm{P}}$.
   (b) The initial fit time for the wall data $t_{i,\mathrm{W}}$.
   (c) The final fit time for the wall data $t_{f,\mathrm{W}}$.

6. One of the $n^2 = 0$ data points is chosen as a reference fit for each ensemble.
   - The fitted energy for $n^2 = 0$ and the reference fit t_i are shown, and labelled inside the bottom right edge of each figure.
7. The reference energy boosted to each momentum using the lattice dispersion relation is shown in pink.
   - Central value only (no error bars).
8. Similarly, the grey dashed line plots the reference energy boosted to each momentum using the continuum dispersion relation.

A.8.1 Results

Results are presented for each ensemble in sections A.8.3 to A.8.8 which follow, and are qualitatively similar across all ensembles:

1. For the ground-state energies (masses):
   - Figures A.59, A.61, A.63, A.65, A.67 and A.69.
   - The dispersion relation is compatible with a wide range of fits.
   - I.e. most of the fits at most momenta.
2. For the first excited-state energies:
   - Figures A.60, A.62, A.64, A.66, A.68 and A.70.
   - The dispersion relation is compatible with a wide range of fits.
   - Though fewer than for the ground state energies.
   - I.e. we see evidence of excited-state contamination in the excited state energies – which is what we would expect from a two-state fit.

Kaon energies extracted from separate fits at each momenta on each ensemble are compatible with the lattice dispersion relation, albeit with some error in the excited-state energies.

A.8.2 Conclusion

Based on the results presented in § A.8.1, we conclude that it would be reasonable to use the lattice dispersion relation in a simultaneous fit of kaon data across multiple momenta, especially where (as outlined in § 3.2.1) the higher momenta kaon data are difficult to fit independently.

Enforcing the use of the lattice dispersion relation in the kaon fits introduces lattice artefacts into the analysis. However, the global fit includes terms which quantify discretisation effects such as these, so taking the chiral continuum limit still gives the correct result.

A.8.3 Kaon fits – lattice dispersion ensemble F1M

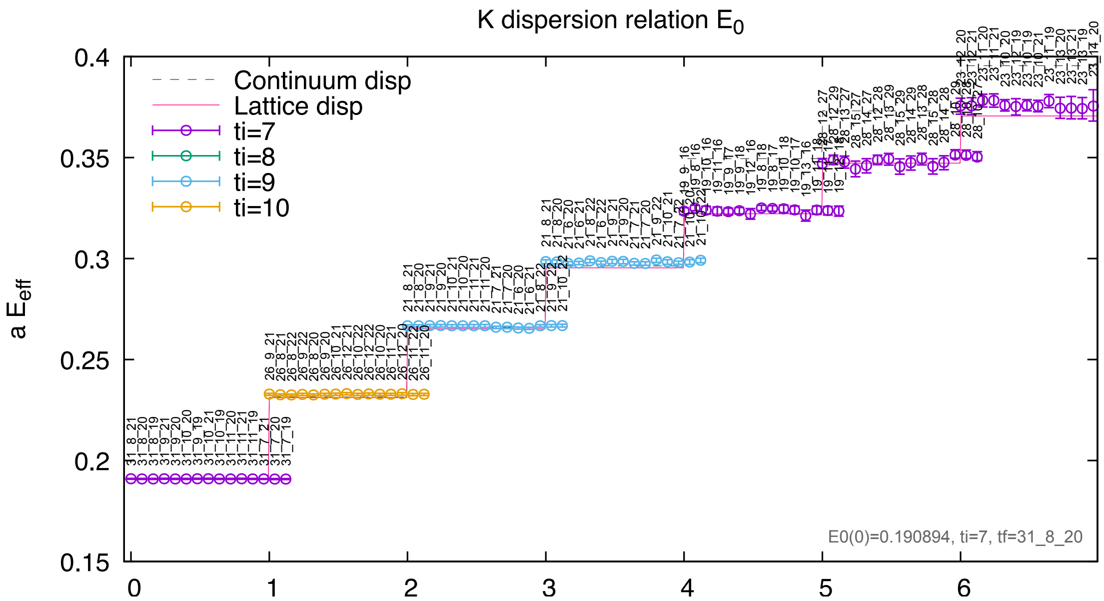

Figure A.59 *Ground state kaon energies (masses) extracted from simultaneous fits to point- and wall-source correlation functions at each integer lattice momentum n^2 for a range of fit times on ensemble F1M. Lattice and continuum dispersion relations plotted per § A.8.*

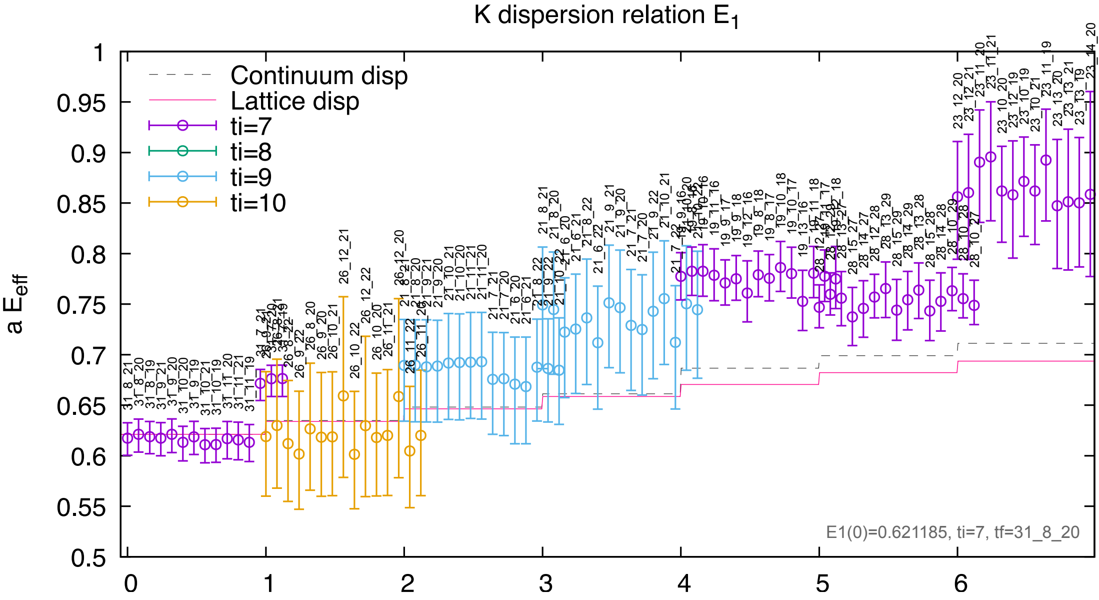

Figure A.60 *First excited-state kaon energies extracted from simultaneous fits to point- and wall-source correlation functions at each integer lattice momentum n^2 for a range of fit times on ensemble F1M. Lattice and continuum dispersion relations plotted per § A.8.*

A.8.4 Kaon fits – lattice dispersion ensemble M1

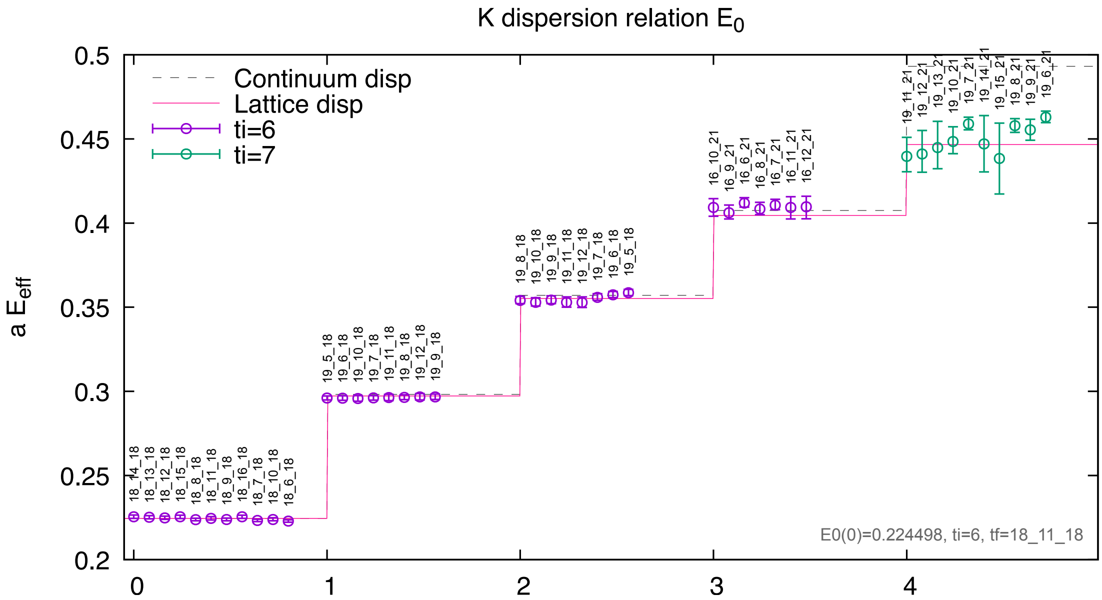

Figure A.61 *Ground state kaon energies (masses) extracted from simultaneous fits to point- and wall-source correlation functions at each integer lattice momentum n^2 for a range of fit times on ensemble M1. Lattice and continuum dispersion relations plotted per § A.8.*

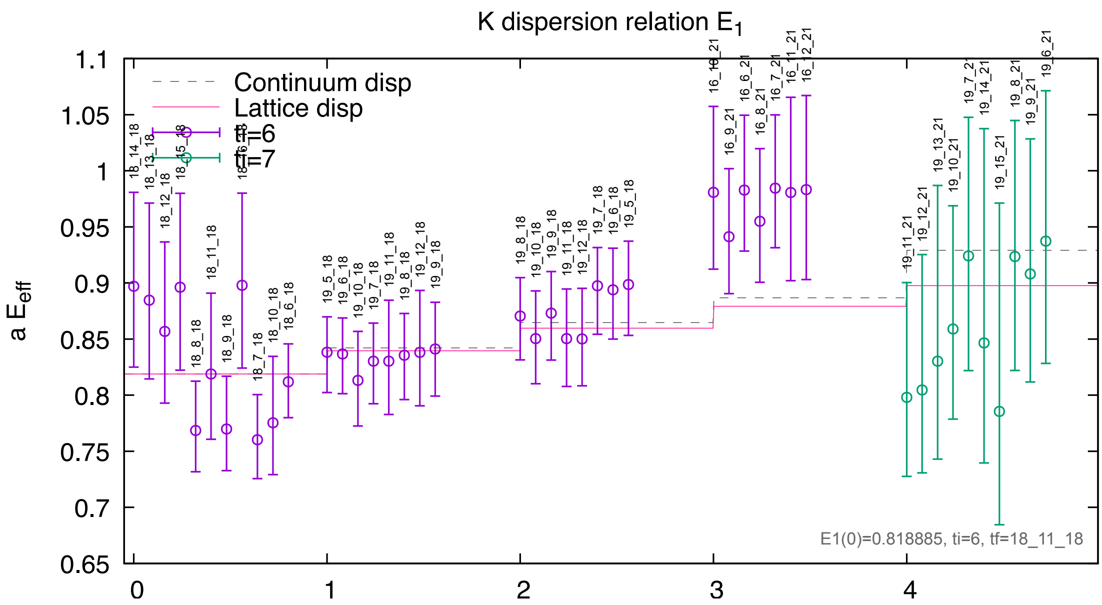

Figure A.62 *First excited-state kaon energies extracted from simultaneous fits to point- and wall-source correlation functions at each integer lattice momentum n^2 for a range of fit times on ensemble M1. Lattice and continuum dispersion relations plotted per § A.8.*

A.8.5 Kaon fits – lattice dispersion ensemble M2

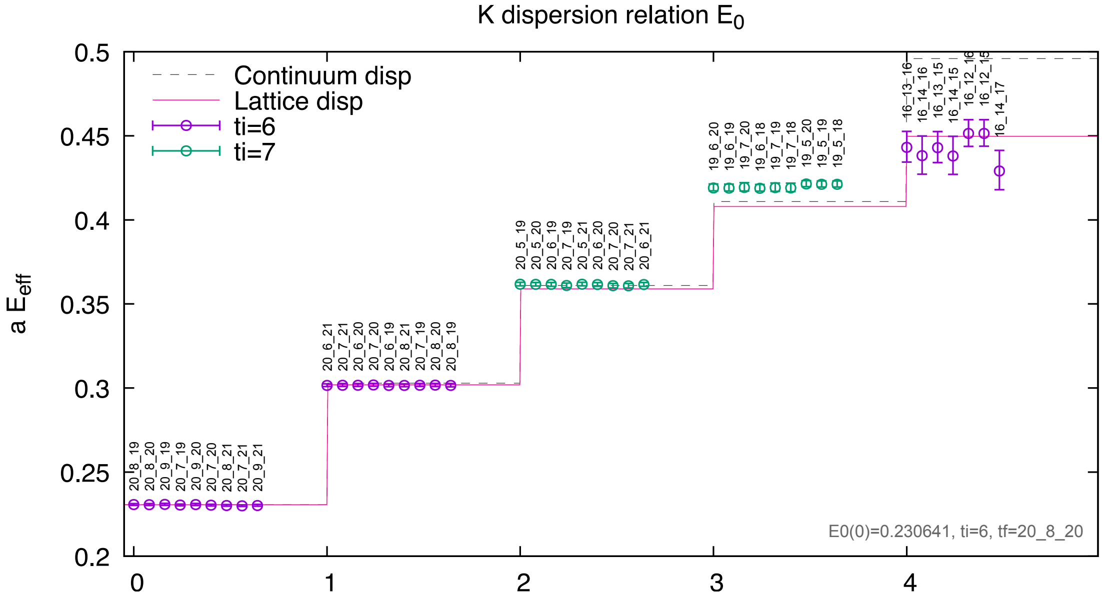

Figure A.63 *Ground state kaon energies (masses) extracted from simultaneous fits to point- and wall-source correlation functions at each integer lattice momentum n^2 for a range of fit times on ensemble M2. Lattice and continuum dispersion relations plotted per § A.8.*

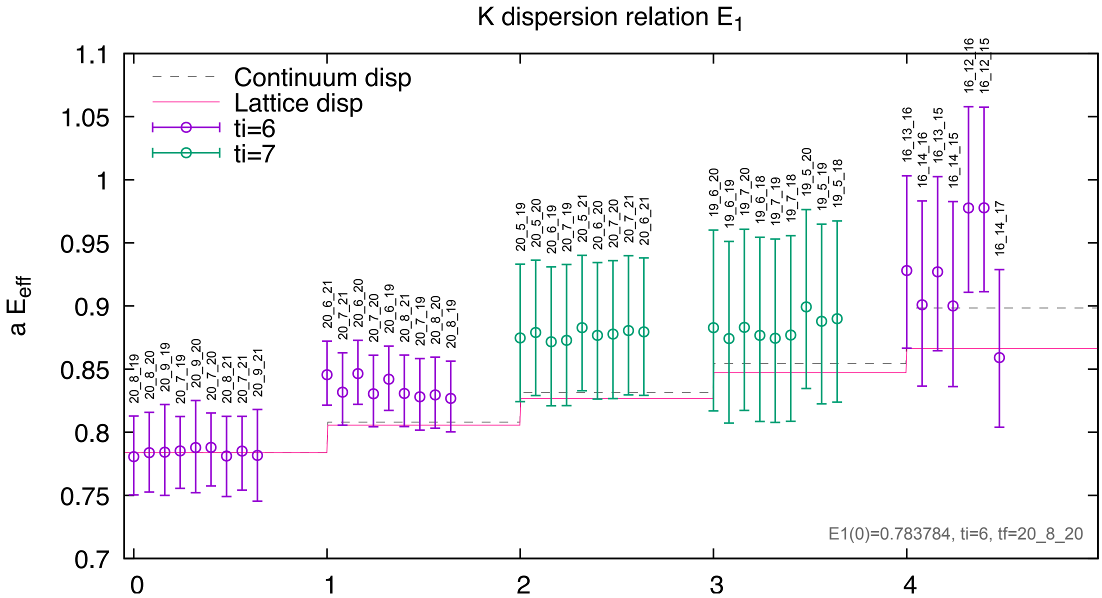

Figure A.64 *First excited-state kaon energies extracted from simultaneous fits to point- and wall-source correlation functions at each integer lattice momentum n^2 for a range of fit times on ensemble M2. Lattice and continuum dispersion relations plotted per § A.8.*

A.8.6 Kaon fits – lattice dispersion ensemble M3

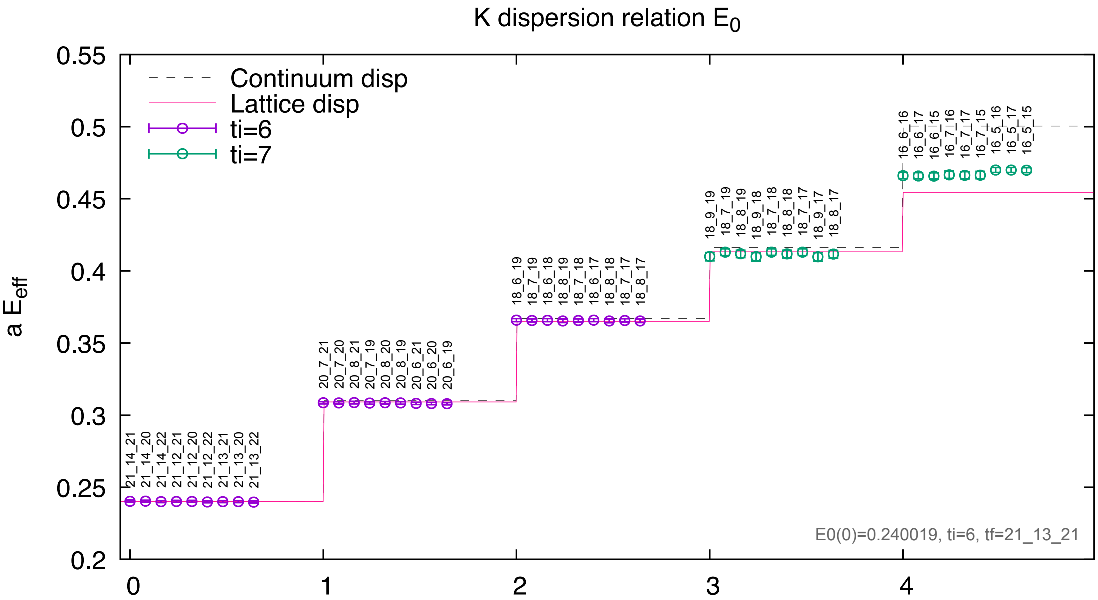

Figure A.65 *Ground state kaon energies (masses) extracted from simultaneous fits to point- and wall-source correlation functions at each integer lattice momentum n^2 for a range of fit times on ensemble M3. Lattice and continuum dispersion relations plotted per § A.8.*

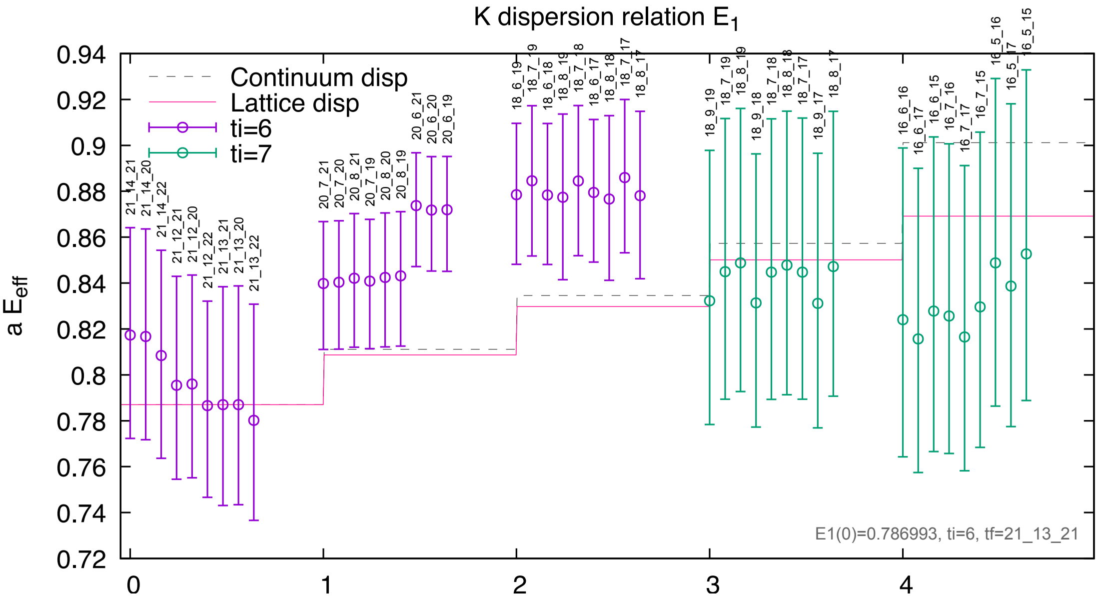

Figure A.66 *First excited-state kaon energies extracted from simultaneous fits to point- and wall-source correlation functions at each integer lattice momentum n^2 for a range of fit times on ensemble M3. Lattice and continuum dispersion relations plotted per § A.8.*

A.8.7 Kaon fits – lattice dispersion ensemble C1

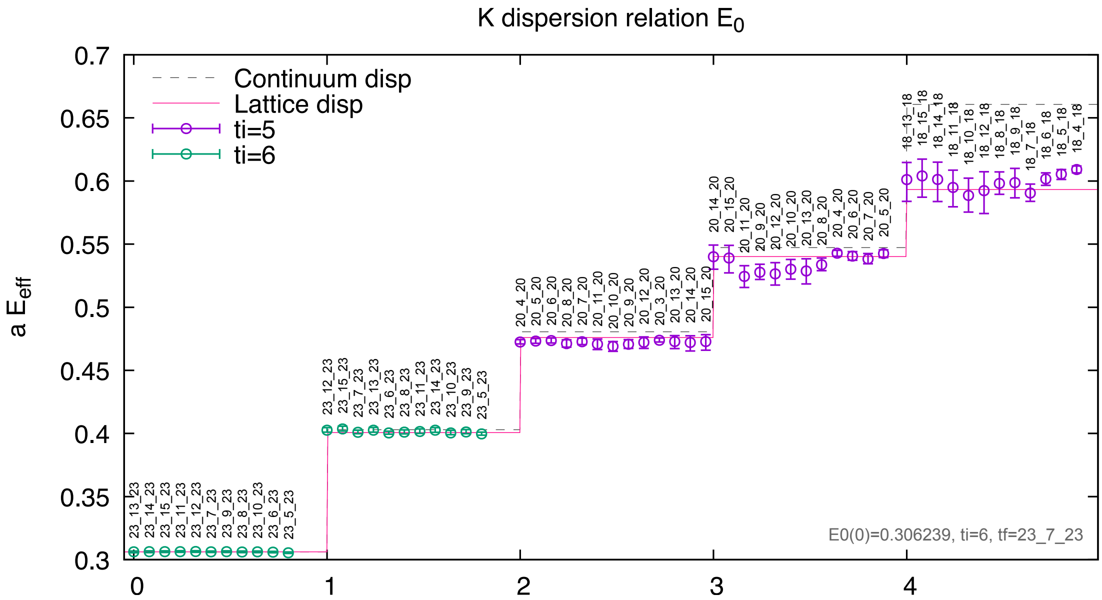

Figure A.67 *Ground state kaon energies (masses) extracted from simultaneous fits to point- and wall-source correlation functions at each integer lattice momentum n^2 for a range of fit times on ensemble C1. Lattice and continuum dispersion relations plotted per § A.8.*

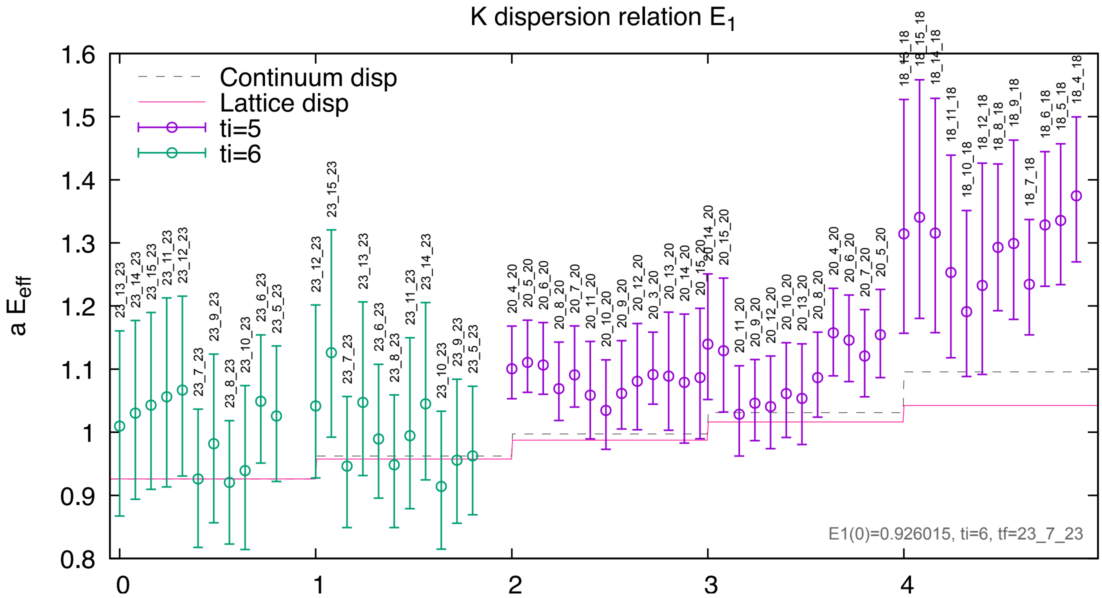

Figure A.68 *First excited-state kaon energies extracted from simultaneous fits to point- and wall-source correlation functions at each integer lattice momentum n^2 for a range of fit times on ensemble C1. Lattice and continuum dispersion relations plotted per § A.8.*

A.8.8 Kaon fits – lattice dispersion ensemble C2

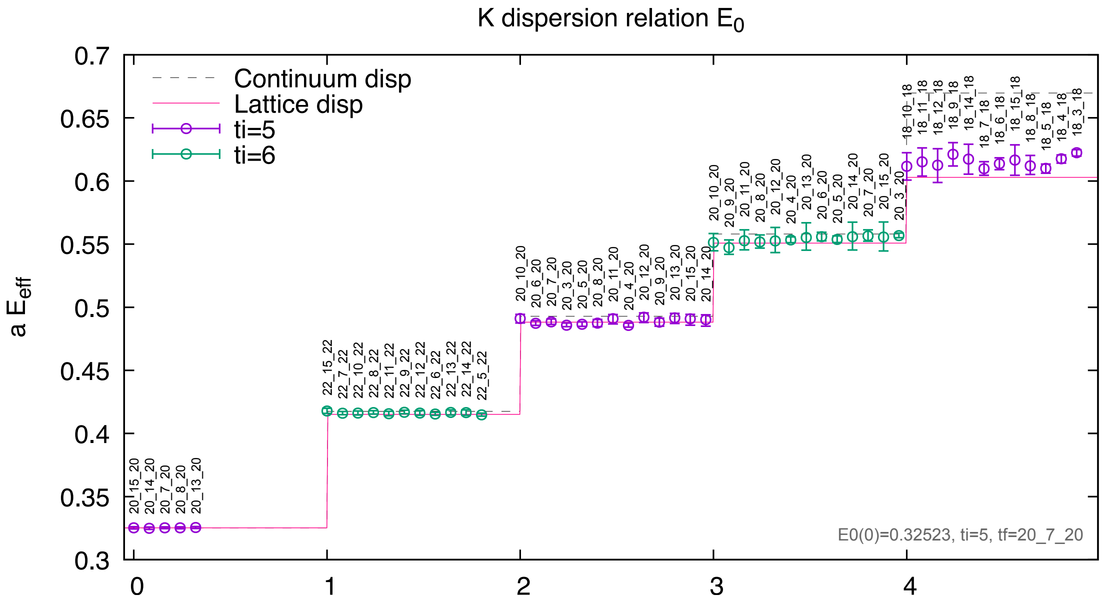

Figure A.69 *Ground state kaon energies (masses) extracted from simultaneous fits to point- and wall-source correlation functions at each integer lattice momentum n^2 for a range of fit times on ensemble C2. Lattice and continuum dispersion relations plotted per § A.8.*

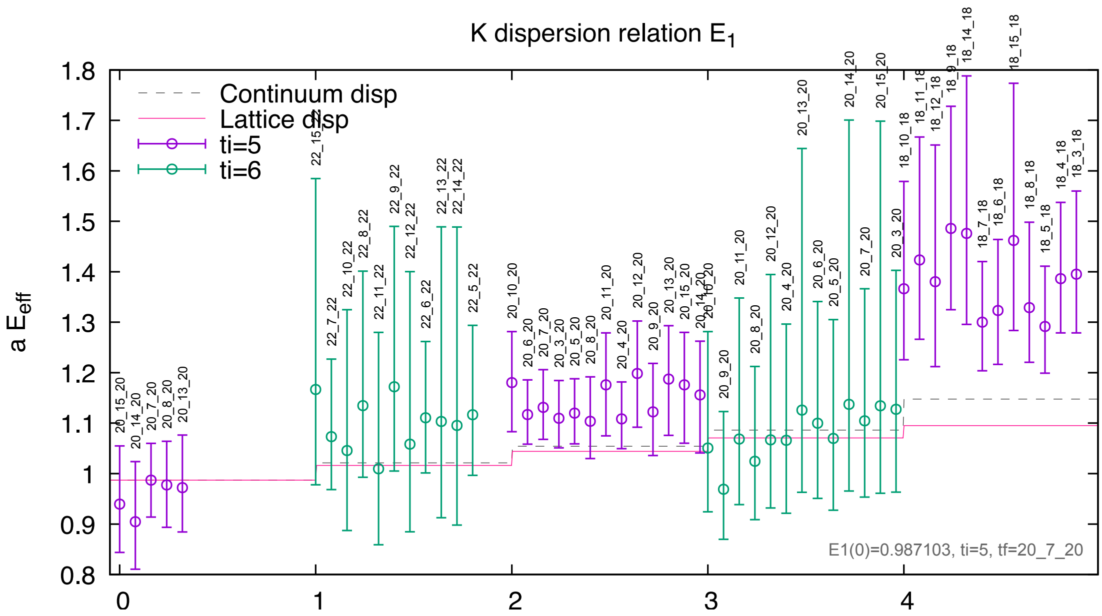

Figure A.70 *First excited-state kaon energies extracted from simultaneous fits to point- and wall-source correlation functions at each integer lattice momentum n^2 for a range of fit times on ensemble C2. Lattice and continuum dispersion relations plotted per § A.8.*

A.9 Alternate renormalisation

The value extracted for $Z_{V,\mathrm{hh}}$ on the M2 ensemble, 1.0211(82), is not compatible with $Z_{V,\mathrm{hh}}$ extracted from the other medium ensembles, 0.9964(80) and 1.0022(96) for M1 and M3 respectively.

Table A.13 presents the alternative of extracting $Z_{V,\mathrm{hh}}$ from (2.95) using a light spectator (instead of strange) and a wall separation $\Delta T/a = 20$ (instead of 24). Comparing the rightmost column in table A.13 with corresponding rows from the same column in table A.13, shows $\sim 1\sigma$ difference between $Z_{V,\mathrm{mixed}} = \sqrt{Z_{V,\mathrm{hh}} Z_{V,\mathrm{ll}}}$ for M1, with closer agreement for M2 and M3.

We conclude that at the level of statistics in this study, we cannot eliminate this tension. Instead we quantify the effect of making this alternative renormalisation choice, including this as fit alternative (m) in the fit systematics analysis in § 4.3.

	heavy			light			mixed
Name	aE_0 $[D_s]$	p-value	Z_V	aE_0 $[K]$	p-value	Z_V	Z_V
M1	0.82568(57)	0.71	0.9964(80)	0.22449(85)	0.63	0.7412(51)	0.8532(76)
M2	0.82567(68)	0.078	1.0211(82)	0.23064(55)	0.82	0.7549(60)	0.8809(80)
M3	0.82554(62)	1.00	1.0022(96)	0.23852(68)	0.348	0.7414(57)	0.8636(79)

Table A.13 *Alternative mostly non-perturbative renormalisation results for medium ensembles. The heavy action is extracted using a light spectator and a wall separation $\Delta T/a = 20$. This is a repeat of table 4.7 (and is described there) for comparison with table A.14.*

	heavy			light			mixed
Name	aE_0 $[D_s]$	p-value	Z_V	aE_0 $[K]$	p-value	Z_V	Z_V
C1	1.10403(61)	0.623	1.037(13)	0.30620(47)	0.411	0.7113(58)	0.8590(74)
C2	1.10465(74)	0.429	1.036(14)	0.32522(57)	0.062	0.7319(59)	0.8709(82)
M1	0.82568(57)	0.71	0.9964(80)	0.22449(85)	0.63	0.7412(51)	0.8594(51)
M2	0.82567(68)	0.078	1.0211(82)	0.23064(55)	0.82	0.7549(60)	0.8780(58)
M3	0.82554(62)	1.00	1.0022(96)	0.23852(68)	0.348	0.7414(57)	0.8620(62)
F1M	0.72911(21)	0.59	0.9932(42)	0.19084(22)	0.78	0.7639(42)	0.8711(34)

Table A.14 *Reference mostly non-perturbative renormalisation results for all ensembles. This is a repeat of table 2.12 (and is described there) for comparison with table A.13.*

The alternative fits used to extract $Z_{V,\mathrm{hh}}$ on ensembles M1, M2 and M3 are shown in figures A.71, A.72 and A.73 respectively.

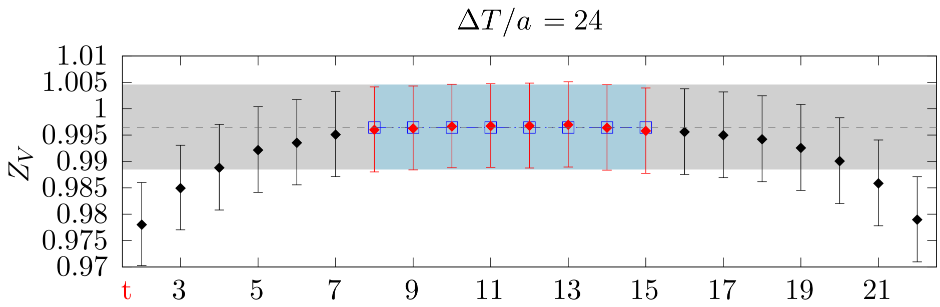

Figure A.71 *Ensemble M1, heavy action,* (2.95) $Z_{V,hh} = 0.9964(80)$ *from decay of heavy quark with strange spectator, wall separation* $\Delta T/a = 24$.

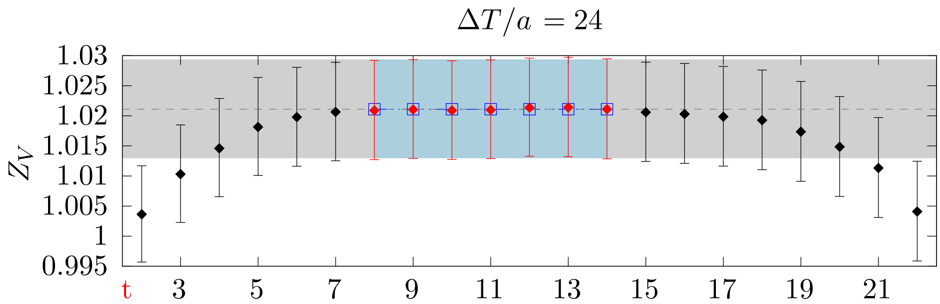

Figure A.72 *Ensemble M2, heavy action,* (2.95) $Z_{V,hh} = 1.0211(82)$ *from decay of heavy quark with strange spectator, wall separation* $\Delta T/a = 24$.

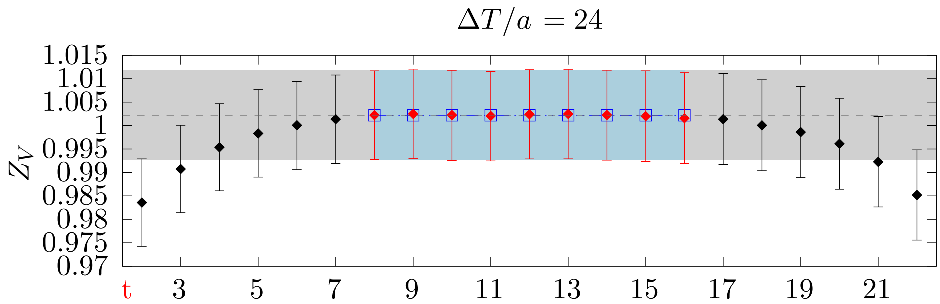

Figure A.73 *Ensemble M3, heavy action,* (2.95) $Z_{V,hh} = 1.0022(96)$ *from decay of heavy quark with strange spectator, wall separation* $\Delta T/a = 24$.

Bibliography

[1] Makoto Kobayashi. "CP Violation and Flavor Mixing (Nobel Lecture)". eng. In: *ChemPhysChem* 10.11 (2009), pp. 1706–1713. ISSN: 1439-4235. DOI: 10.1002/cphc.200900215 (cit. on p. i).

[2] Nicola Cabibbo. "Unitary Symmetry and Leptonic Decays". eng. In: *Physical Review Letters* 10.12 (June 1963), pp. 531–533. ISSN: 0031-9007. DOI: 10.1103/PhysRevLett.10.531 (cit. on pp. i, 1).

[3] Makoto Kobayashi and Toshihide Maskawa. "CP-Violation in the Renormalizable Theory of Weak Interaction". eng. In: *Progress of theoretical physics* 49.2 (2 Feb. 1973), pp. 652–657. ISSN: 0033-068X. DOI: 10.1143/PTP.49.652 (cit. on pp. i, 1).

[4] Peter A. Boyle et al. "SU(3)-breaking ratios for $D_{(s)}$ and $B_{(s)}$ mesons". In: (Dec. 2018). arXiv: 1812.08791 [hep-lat] (cit. on pp. ii, 55–58, 127, 128, 139).

[5] Colin Morningstar and Mike J. Peardon. "Analytic smearing of SU(3) link variables in lattice QCD". In: *Physical Review D* 69 (5 Mar. 2004), p. 054501. DOI: 10.1103/PhysRevD.69.054501. arXiv: hep-lat/0311018 [hep-lat] (cit. on pp. ii, 40, 58).

[6] Richard C. Brower, Harmut Neff and Kostas Orginos. "The Möbius Domain Wall Fermion Algorithm". In: *Comput. Phys. Commun.* 220 (2017), pp. 1–19. DOI: 10.1016/j.cpc.2017.01.024. arXiv: 1206.5214 [hep-lat] (cit. on pp. ii, 18, 57).

[7] David B. Kaplan. "A method for simulating chiral fermions on the lattice". In: *Physics Letters B* 288.3-4 (Aug. 1992), pp. 342–347. DOI: 10.1016/0370-2693(92)91112-M. arXiv: hep-lat/9206013 [hep-lat] (cit. on pp. ii, 18, 55, 57).

[8] Yigal Shamir. "Chiral fermions from lattice boundaries". eng. In: *Nuclear Physics B* 406.1-2 (1993), pp. 90–106. ISSN: 0550-3213. DOI: 10.1016/0550-3213(93)90162-I. arXiv: hep-lat/9303005 (cit. on pp. ii, 18, 57).

[9] Vadim Furman and Yigal Shamir. "Axial symmetries in lattice QCD with Kaplan fermions". In: *Nuclear Physics B* 439.1-2 (Apr. 1995), pp. 54–78. DOI: 10.1016/0550-3213(95)00031-m. arXiv: hep-lat/9405004 [hep-lat] (cit. on pp. ii, 18, 57).

[10] T. Blum and A. Soni. “QCD with domain wall quarks”. In: *Physical Review D* 56.1 (July 1997), pp. 174–178. DOI: 10.1103/physrevd.56.174. arXiv: hep-lat/9611030 [hep-lat] (cit. on pp. ii, 18, 55, 57).

[11] T. Blum and A. Soni. “Domain wall quarks and kaon weak matrix elements”. In: *Physical Review Letters* 79 (1997), pp. 3595–3598. DOI: 10.1103/PhysRevLett.79.3595. arXiv: hep-lat/9706023 (cit. on pp. ii, 18, 55, 57).

[12] Peter Boyle et al. “Semileptonic $D \to \pi\ell\nu$, $D \to K\ell\nu$ and $D_s \to K\ell\nu$ decays with 2+1f domain wall fermions”. In: 38th International Symposium on Lattice Field Theory (Lattice 2021) (Zoom/Gather@Massachusetts Institute of Technology, 26th–30th July 2021). Vol. Lattice2021. July 2022, p. 416. DOI: 10.22323/1.396.0416. arXiv: 2201.02680 [hep-lat]. URL: https://arxiv.org/pdf/2201.02680 (cit. on pp. iii, 26).

[13] Peter A. Boyle. “Electroweak Sector of Standard Model 2017”. Lecture notes. Jan. 2017 (cit. on p. 2).

[14] Cliff Peter Burgess and Guy David Moore. *The standard model. A primer*. Cambridge University Press, 2007. ISBN: 978-0-521-86036-9 (cit. on p. 2).

[15] W. Noel Cottingham and Derek A. Greenwood. *An introduction to the standard model of particle physics*. 2nd ed. Cambridge University Press, 2007. ISBN: 978-0-521-85249-4 (cit. on p. 2).

[16] Matthew D. Schwartz. *Quantum field theory and the standard model*. Cambridge University Press, 2014. ISBN: 978-1-107-03473-0 (cit. on p. 2).

[17] Michael Edward Peskin and Daniel V. Schroeder. *An introduction to quantum field theory*. Westview Press, 1995. ISBN: 9780201503975 (cit. on p. 2).

[18] Lev Borisovich Okun. *Leptons and quarks*. Special edition commemorating the discovery of the Higgs boson. Trans. by V. I. Kisin. World Scientific, 2014. ISBN: 978-981-4603-00-3 (cit. on p. 2).

[19] Emmanuel A. Paschos. *Electroweak theory*. Cambridge University Press, 2007. ISBN: 978-0-521-86098-7 (cit. on p. 2).

[20] T. Aoyama et al. “The anomalous magnetic moment of the muon in the Standard Model”. In: *FERMILAB-PUB-20-207-T, INT-PUB-20-021, KEK Preprint 2020-5, MITP/20-028, CERN-TH-2020-075, IFT-UAM/CSIC-20-74, LMU-ASC 18/20, LTH 1234, LU TP 20-20, MAN/HEP/2020/003, PSI-PR-20-06, UWThPh 2020-14, ZU-TH 18/20* (June 2020). DOI: https://doi.org/10.1016/j.physrep.2020.07.006. eprint: 2006.04822. URL: https://arxiv.org/pdf/2006.04822.pdf (cit. on p. 2).

[21] Howard Georgi and S.L. Glashow. “Unity of all elementary-particle forces”. eng. In: *Physical review letters* 32.8 (1974), pp. 438–441. ISSN: 0031-9007 (cit. on p. 2).

[22] N. Furey. “An Algebraic Roadmap of Particle Theories, Part I: General construction”. In: *HU-EP-23/64* (Dec. 2023). eprint: 2312.12377. URL: https://arxiv.org/pdf/2312.12377.pdf (cit. on p. 2).

[23] Philip Bechtle et al. “Bottoms Up: Standard Model Effective Field Theory from a Model Perspective”. In: (Jan. 2022). eprint: 2201.08819. URL: https://arxiv.org/pdf/2201.08819.pdf (cit. on p. 2).

[24] Marzia Bordone, Oscar Catà and Thorsten Feldmann. “Effective Theory Approach to New Physics with Flavour: General Framework and a Leptoquark Example”. In: (Oct. 2019). DOI: 10.1007/JHEP01(2020)067. eprint: 1910.02641. URL: https://arxiv.org/pdf/1910.02641.pdf (cit. on p. 2).

[25] R. L. Workman et al. “Review of Particle Physics”. In: *PTEP* 2022 (2022), p. 083C01. DOI: 10.1093/ptep/ptac097. URL: https://pdg.lbl.gov (cit. on pp. 2, 3, 8, 52, 58, 127).

[26] Steven White Jr. *Standard model of elementary particles: the 12 fundamental fermions and 5 fundamental bosons.* released into the public domain by the copyright holder. Sept. 2019. URL: https://commons.wikimedia.org/wiki/File:Standard_Model_of_Elementary_Particles.svg (visited on 13/09/2023) (cit. on p. 2).

[27] Y. Ne’eman. “Derivation of strong interactions from a gauge invariance”. eng. In: *Nuclear physics* 26.2 (1961), pp. 222–229. ISSN: 0029-5582 (cit. on p. 4).

[28] Murray Gell-Mann. “Symmetries of baryons and mesons”. eng. In: *Physical review* 125.3 (1962), pp. 1067–1084. ISSN: 0031-899X (cit. on p. 4).

[29] M. Gell-Mann. “A schematic model of baryons and mesons”. eng. In: *Physics letters* 8.3 (Jan. 1964), pp. 214–215. ISSN: 0031-9163 (cit. on p. 4).

[30] G. Zweig. *An SU_3 Model for Strong Interaction Symmetry and its Breaking: II.* Report 8419/TH.412. Geneva: CERN, Feb. 1964. URL: https://cds.cern.ch/record/352337/files/CERN-TH-401.pdf (visited on 06/12/2023) (cit. on p. 4).

[31] G. Zweig. *An SU_3 Model for Strong Interaction Symmetry and its Breaking. Preprint.* Report 8182/TH.401. Geneva: CERN, Jan. 1964. URL: https://cds.cern.ch/record/352337/files/CERN-TH-401.pdf (visited on 06/12/2023) (cit. on p. 4).

[32] H. Fritzsch, M. Gell-Mann and H. Leutwyler. “Advantages of the color octet gluon picture”. eng. In: *Physics letters. B* 47.4 (1973), pp. 365–368. ISSN: 0370-2693 (cit. on p. 4).

[33] Sheldon L. Glashow. “Partial-symmetries of weak interactions”. eng. In: *Nuclear physics* 22.4 (1961), pp. 579–588. ISSN: 0029-5582 (cit. on p. 6).

[34] Jeffrey Goldstone, Abdus Salam and Steven Weinberg. “Broken symmetries”. eng. In: *Physical review* 127.3 (1962), pp. 965–970. ISSN: 0031-899X (cit. on p. 6).

[35] HFLAV Collaboration et al. “Averages of b-hadron, c-hadron, and τ-lepton properties as of 2021”. In: *Phys. Rev. D* 107 (Jan. 2023), p. 052008. DOI: https://doi.org/10.1103/PhysRevD.107.052008. arXiv: 2206.07501 [hep-ex] (cit. on p. 11).

[36] Richard J. Hill. “The modern description of semileptonic meson form factors”. In: *FERMILAB-CONF-06-155-T* (2006). arXiv: hep-ph/0606023 [hep-ph] (cit. on p. 11).

[37] Rajan Gupta. “Calculations of hadronic matrix elements using lattice qcd”. In: (Aug. 1993). arXiv: hep-lat/9308002 [hep-lat] (cit. on p. 11).

[38] M. Crisafulli et al. “A lattice study of semileptonic decays of d-mesons”. eng. In: *Physics letters. B* 223.1 (1989), pp. 90–96. ISSN: 0370-2693 (cit. on pp. 11, 46).

[39] Christof Gattringer and Christian B. Lang. *Quantum Chromodynamics on the Lattice. An Introductory Presentation.* 1st ed. Lecture Notes in Physics. Springer-Verlag Berlin Heidelberg, 2010. ISBN: 978-3-642-01849-7 (cit. on p. 12).

[40] Heinz J. Rothe. *Lattice gauge theories. An Introduction.* 4th ed. Vol. 82. World Scientific lecture notes in physics. World Scientific Publishing Co. Pte. Ltd., 2012. ISBN: 978-981-4365-85-7 (cit. on p. 12).

[41] Laurent Lellouch et al., eds. *Modern perspectives in lattice QCD. quantum field theory and high performance computing.* Ecole d’été de physique théorique (Les Houches, Haute-Savoie, France), session XCIII, 3–28 August 2009. Vol. 93. Lecture notes of the Les Houches Summer School. Oxford University Press, 2011. ISBN: 978-0-19-969160-9 (cit. on p. 12).

[42] P.T. Matthews and A. Salam. “Propagators of quantized field”. In: *Il Nuovo Cimento* 2.1 (May 1955) (cit. on p. 13).

[43] A.D. Kennedy and B.J. Pendleton. “Improved heatbath method for Monte Carlo calculations in lattice gauge theories”. eng. In: *Physics letters. B* 156.5 (1985), pp. 393–399. ISSN: 0370-2693 (cit. on p. 14).

[44] Kenneth G. Wilson. “Confinement of quarks”. In: *Physical Review D* 10.8 (1974), pp. 2445–2459. ISSN: 05562821 (cit. on pp. 15, 16).

[45] Y. Iwasaki. “Renormalization Group Analysis of Lattice Theories and Improved Lattice Action. II – four-dimensional non-abelian SU(N) gauge model”. In: *UTHEP-118* (Dec. 1983). arXiv: 1111.7054 [hep-lat] (cit. on pp. 15, 55).

[46] Y Aoki et al. “Domain wall fermions with improved gauge actions”. eng. In: *Physical review. D, Particles, fields, gravitation, and cosmology* 69.7 (2004). ISSN: 1550-7998. arXiv: hep-lat/0211023 [hep-lat] (cit. on pp. 15, 19, 57).

[47] Leonard Susskind. “Lattice fermions”. eng. In: *Physical review. D, Particles and fields* 16.10 (1977), pp. 3031–3039. ISSN: 0556-2821 (cit. on p. 16).

[48] Paul H. Ginsparg and Kenneth G. Wilson. “A remnant of chiral symmetry on the lattice”. eng. In: *Physical review. D, Particles and fields* 25.10 (1982), pp. 2649–2657. ISSN: 0556-2821 (cit. on p. 16).

[49] H.B. Nielsen and M. Ninomiya. “Absence of neutrinos on a lattice. (I). Proof by homotopy theory”. eng. In: *Nuclear physics. B* 185.1 (1981), pp. 20–40. ISSN: 0550-3213 (cit. on p. 17).

[50] H.B. Nielsen and M. Ninomiya. “Absence of neutrinos on a lattice. (II). Intuitive topological proof”. eng. In: *Nuclear physics. B* 193.1 (1981), pp. 173–194. ISSN: 0550-3213 (cit. on p. 17).

[51] H.B. Nielsen and M. Ninomiya. “A no-go theorem for regularizing chiral fermions”. eng. In: *Physics letters. B* 105.2 (1981), pp. 219–223. ISSN: 0370-2693 (cit. on p. 17).

[52] Antonin Portelli. “Lattice Field Theory”. Lecture notes. Mar. 2018 (cit. on p. 17).

[53] Herbert Neuberger. “Exactly massless quarks on the lattice”. eng. In: *Physics letters. B* 417.1 (1998), pp. 141–144. ISSN: 0370-2693. arXiv: hep-lat/9707022 [hep-lat] (cit. on p. 17).

[54] Herbert Neuberger. “More about exactly massless quarks on the lattice”. eng. In: *Physics letters. B* 427.3 (1998), pp. 353–355. ISSN: 0370-2693. arXiv: hep-lat/9801031 [hep-lat] (cit. on p. 17).

[55] A.D. Kennedy. “Algorithms for dynamical fermions”. In: Perspectives in Lattice QCD (Nara International Seminar House, Nara, Japan, 31st Oct.–11th Nov. 2005). Ed. by Yoshinobu Kuramashi. University of Tsukuba, Japan. Feb. 2012. Chap. 2, pp. 15–81. DOI: 10.1142/6216. arXiv: hep-lat/0607038. (Visited on 12/11/2020) (cit. on p. 18).

[56] Richard C. Brower, Hartmut Neff and Kostas Orginos. “Möbius Fermions: Improved Domain Wall Chiral Fermions”. In: *Nuclear Physics B - Proceedings Supplements* 140 (Mar. 2005), pp. 686–688. DOI: 10.1016/j.nuclphysbps.2004.11.180. arXiv: hep-lat/0409118 (cit. on p. 18).

[57] Peter A. Boyle. “Bagel 5d chiral fermion support”. Oct. 2018. URL: https://rbc.phys.columbia.edu/rbc_ukqcd/individual_postings/pab/DWF4d.pdf (visited on 25/11/2020) (cit. on p. 18).

[58] Peter Boyle et al. “Domain Wall Charm Physics with Physical Pion Masses: Decay constants, bag and ξ parameters”. In: (Nov. 2015). eprint: 1511.09328. URL: https://arxiv.org/pdf/1511.09328.pdf (cit. on pp. 19, 57, 58).

[59] Yong-Gwi Cho et al. “Improved lattice fermion action for heavy quarks”. In: *Journal of High Energy Physics* 2015.5 (May 2015). ISSN: 1029-8479. DOI: 10.1007/jhep05(2015)072. arXiv: 1504.01630 [hep-lat]. URL: http://dx.doi.org/10.1007/JHEP05(2015)072 (cit. on pp. 19, 57, 58).

[60] T. Blum et al. “Quenched lattice QCD with domain wall fermions and the chiral limit”. In: *Physical Review D* 69.7 (Apr. 2004). DOI: 10.1103/physrevd.69.074502. arXiv: hep-lat/0007038 [hep-lat] (cit. on pp. 19, 57).

[61] Michael Marshall. “Operator diagonalisation”. RBC/UKQCD collaboration individual posting (proof correlators real or imaginary in § 2.c.ii and § 2.d). Dec. 2019. URL: http://lqcd.me/PhD/CorrRealImag.pdf (cit. on p. 21).

[62] Shao-Jing Dong and Keh-Fei Liu. “Stochastic estimation with Z2 noise”. eng. In: *Physics letters. B* 328.1-2 (1994), pp. 130–136. ISSN: 0370-2693 (cit. on p. 26).

[63] E. Endress, A. Jüttner Andreas and H. Wittig. “On the efficiency of stochastic volume sources for the determination of light meson masses”. In: (2011). arXiv: 1111.5988 [hep-lat] (cit. on p. 26).

[64] Peter Boyle et al. “An exploratory study of heavy-light semileptonic form factors using distillation”. In: *PoS* 363 (Aug. 2020), p. 169. DOI: 10.22323/1.363.0169. arXiv: 1912.07563 [hep-lat] (cit. on p. 26).

[65] Peter Boyle et al. *BSM $B - \bar{B}$ mixing on JLQCD and RBC/UKQCD $N_f = 2 + 1$ DWF ensembles*. Nov. 2021. arXiv: 2111.11287 [hep-lat]. URL: https://arxiv.org/pdf/2111.11287 (cit. on p. 26).

[66] Antonin Portelli et al. *aportelli/Hadrons: Hadrons*. Version v1.2. Oct. 2020. DOI: 10.5281/zenodo.4063666. URL: https://doi.org/10.5281/zenodo.4063666 (cit. on pp. 29, 30, 53).

[67] Peter Boyle et al. “Grid: A next generation data parallel C++ QCD library”. In: (July 2016). DOI: https://doi.org/10.22323/1.251.0023. arXiv: 1512.03487 [hep-lat] (cit. on pp. 30, 53, 57).

[68] D Brömmel et al. “The pion form factor from lattice QCD with two dynamical flavours”. eng. In: *The European physical journal. C, Particles and fields* 51.2 (2007), pp. 335–345. ISSN: 1434-6052 (cit. on p. 34).

[69] P. A. Boyle et al. “The kaon semileptonic form factor with near physical domain wall quarks”. In: *Journal of High Energy Physics* 2013.8 (Aug. 2013). DOI: 10.1007/jhep08(2013)132. arXiv: 1305.7217 [hep-lat] (cit. on p. 34).

[70] G Martinelli and C.T Sachrajda. “A lattice study of nucleon structure”. eng. In: *Nuclear Physics, Section B* 316.2 (1989), pp. 355–372. ISSN: 0550-3213 (cit. on p. 35).

[71] L. Giusti et al. “Lattice gauge fixing for parameter dependent covariant gauges”. eng. In: *Physical review. D* 63.1 (2001), pp. 145011–145016. ISSN: 0556-2821 (cit. on p. 38).

[72] M.R. Hestenes. “Iterative methods for solving linear equations”. eng. In: *Journal of optimization theory and applications* 11.4 (1973), pp. 323–334. ISSN: 0022-3239 (cit. on p. 39).

[73] Martin Lüscher. “Local coherence and deflation of the low quark modes in lattice QCD”. In: 2007.07 (July 2007), pp. 081–081. DOI: 10.1088/1126-6708/2007/07/081. arXiv: 0706.2298 [hep-lat] (cit. on p. 39).

[74] Gene H. Golub and Qiang Ye. “Inexact preconditioned conjugate gradient method with inner-outer iteration”. eng. In: *SIAM journal on scientific computing* 21.4 (1999), pp. 1305–1320. ISSN: 1064-8275 (cit. on p. 39).

[75] Peter A. Boyle. “Hierarchically deflated conjugate gradient”. In: *Edinburgh 2014/03* (Feb. 2014). arXiv: 1402.2585 [hep-lat]. URL: https://arxiv.org/pdf/1402.2585.pdf (cit. on p. 39).

[76] M. Antonelli et al. “Flavor physics in the quark sector”. In: *Physics Reports* 494.3-4 (Sept. 2010), pp. 197–414. ISSN: 0370-1573. DOI: 10.1016/j.physrep.2010.05.003. arXiv: 0907.5386 [hep-lat] (cit. on p. 40).

[77] Enrico Franco and Vittorio Lubicz. “Quark mass renormalization in the MS and RI schemes up to the NNLO order”. eng. In: *Nuclear physics. B* 531.1-3 (1998), pp. 641–651. ISSN: 0550-3213 (cit. on p. 43).

[78] G Martinelli et al. “A general method for non-perturbative renormalization of lattice operators”. eng. In: *Nuclear physics. B* 445.1 (1995), pp. 81–105. ISSN: 0550-3213 (cit. on p. 43).

[79] C Sturm et al. “Renormalization of quark bilinear operators in a momentum-subtraction scheme with a nonexceptional subtraction point”. eng. In: *Physical review. D, Particles, fields, gravitation, and cosmology* 80.1 (2009). ISSN: 1550-7998. DOI: 10.1103/PhysRevD.80.014501 (cit. on p. 44).

[80] Peter Boyle, Luigi Del Debbio and Ava Khamseh. “A massive momentum-subtraction scheme”. In: *Phys. Rev. D* 95 (2017), p. 054505. DOI: 10.1103/PhysRevD.95.054505. arXiv: 1611.06908 [hep-lat] (cit. on p. 44).

[81] Peter Boyle et al. “The decay constants f_D and f_{Ds} in the continuum limit of Nf = 2 + 1 domain wall lattice QCD”. eng. In: *Journal of High Energy Physics* 2017.12 (Dec. 2017), pp. 1–38. ISSN: 1029-8479. DOI: 10.1007/jhep12(2017)008. arXiv: 1701.02644 [hep-lat]. URL: http://dx.doi.org/10.1007/JHEP12(2017)008 (cit. on pp. 44, 55, 56).

[82] M. Gockeler et al. “Nonperturbative Renormalisation of Composite Operators in Lattice QCD”. In: *DESY 98-097, TPR-98-19, HUB-EP-98/45* (1999). DOI: https://doi.org/10.1016/S0550-3213%2899%2900036-X. arXiv: hep-lat/9807044 [hep-lat] (cit. on p. 44).

[83] Giulia Maria de Divitiis, Roberto Petronzio and Nazario Tantalo. “Quenched lattice calculation of semileptonic heavy-light meson form factors”. In: *Journal of High Energy Physics* 2007.10 (Oct. 2007), pp. 062–062. ISSN: 1029-8479. DOI: 10.1088/1126-6708/2007/10/062. arXiv: 0707.0587 [hep-lat] (cit. on p. 46).

[84] J. M. Flynn and C. T. Sachrajda. “SU(2) chiral perturbation theory for $K\ell 3$ decay amplitudes”. In: *SHEP-08-26* (Sept. 2008). DOI: https://doi.org/10.1016/j.nuclphysb.2008.12.001. arXiv: 0809.1229 [hep-ph] (cit. on p. 50).

[85] Johan Bijnens and Ilaria Jemos. “Hard Pion Chiral Perturbation Theory for $B \to \pi$ and $D \to \pi$ Formfactors”. In: *LU TP 10-16* (June 2010). DOI: https://doi.org/10.1016/j.nuclphysb.2010.06.021. arXiv: 1006.1197 [hep-ph]. URL: https://arxiv.org/pdf/1006.1197.pdf (cit. on p. 50).

[86] Jonathan M. Flynn et al. “Exclusive semileptonic $B_s \to K\ell\nu$ decays on the lattice”. In: (2023). arXiv: 2303.11280 [hep-lat] (cit. on pp. 50, 142).

[87] Alexei Bazavov et al. "D-meson semileptonic decays to pseudoscalars from four-flavor lattice QCD". eng. In: *Physical review. D* 107.9 (May 2023). ISSN: 2470-0010. arXiv: 2212.12648 [hep-lat] (cit. on pp. 51, 52, 150–153, 155, 156).

[88] George B. Arfken, Hans J. Weber and Frank E. Harris. *Mathematical methods for physicists. A comprehensive guide*. 7th ed. Elsevier, 2013. ISBN: 9780123846549 (cit. on p. 52).

[89] NIST/SEMATECH. *e-Handbook of Statistical Methods*. en. National Institute of Standards and Technology, U.S. Department of Commerce, Apr. 2012. DOI: https://doi.org/10.18434/M32189. URL: https://www.itl.nist.gov/div898/handbook (cit. on pp. 52, 66).

[90] M. et al Galassi. *GNU Scientific Library Reference Manual*. 2018. URL: https://www.gnu.org/software/gsl (cit. on pp. 52, 53, 69, 72, 76, 79).

[91] Michael Marshall. *Meson Lattice Utilities (MLU). aka Mike's Lattice Utilities (Mike's PhD)*. 2023. URL: http://lqcd.me/PhD (cit. on pp. 53, 69, 71).

[92] *DiRAC*. URL: https://dirac.ac.uk (visited on 27/11/2023) (cit. on p. 53).

[93] *Science and Technology Facilities Council*. URL: https://www.ukri.org/councils/stfc/ (visited on 27/11/2023) (cit. on p. 53).

[94] *DiRAC Extreme Scaling CPU*. URL: https://www.epcc.ed.ac.uk/dirac-tesseract-cpu (visited on 27/11/2023) (cit. on p. 54).

[95] *DiRAC Extreme Scaling CPU*. URL: https://www.epcc.ed.ac.uk/hpc-services/dirac-tursa-gpu (visited on 27/11/2023) (cit. on p. 54).

[96] C. Allton et al. "Physical Results from 2+1 Flavor Domain Wall QCD and SU(2) Chiral Perturbation Theory". In: *Physics Review D* 78 (2008), p. 114509. DOI: 10.1103/PhysRevD.78.114509. arXiv: 0804.0473 [hep-lat] (cit. on pp. 55, 56).

[97] Y. Aoki et al. "Continuum Limit Physics from 2+1 Flavor Domain Wall QCD". In: *Physics Review D* 83 (2011), p. 074508. DOI: 10.1103/PhysRevD.83.074508. arXiv: 1011.0892 [hep-lat]. (Visited on 28/03/2019) (cit. on pp. 55, 56).

[98] Y. Aoki et al. "Continuum Limit of B_K from 2+1 Flavor Domain Wall QCD". In: *Phys. Rev. D* 84 (2011), p. 014503. DOI: 10.1103/PhysRevD.84.014503. arXiv: 1012.4178 [hep-lat] (cit. on pp. 55, 56).

[99] T. Blum et al. "Domain wall QCD with physical quark masses". In: *Physical Review D* 93.7 (Apr. 2016). ISSN: 2470-0029. DOI: 10.1103/physrevd.93.074505. arXiv: 1411.7017 [hep-lat] (cit. on pp. 56, 139).

[100] David J. Olive. *Robust Multivariate Analysis*. eng. 1st ed. Cham: Springer International Publishing, 2017. ISBN: 3-319-68253-9 (cit. on pp. 67, 68).

[101] Harold Hotelling. “The Generalization of Student’s Ratio”. In: *The Annals of Mathematical Statistics* 2.3 (Apr. 1931), pp. 360–378. DOI: 10.1214/aoms/1177732979. URL: https://projecteuclid.org/journals/annals-of-mathematical-statistics/volume-2/issue-3/The-Generalization-of-Students-Ratio/10.1214/aoms/1177732979.full (cit. on p. 68).

[102] Wolfram Research. *HotellingTSquareDistribution*. https://reference.wolfram.com/language/ref/HotellingTSquareDistribution.html. 2016. (Visited on 22/06/2022) (cit. on p. 68).

[103] Harold Hotelling. “Multivariate quality control. Illustrated by the air testing of sample bombsights”. In: *Selected techniques of statistical analysis*. Ed. by Churchill Eisenhart, Millard W. Hastay and W. Allen Wallis. 1st ed. McGraw-Hill book company, Inc., 1947. Chap. 3, pp. 111–186 (cit. on p. 69).

[104] Christopher Kelly. “Probability of fit result when using sample covariance matrix”. RBC/UKQCD collaboration personal postings. June 2019. URL: https://rbc.phys.columbia.edu/rbc_ukqcd/individual_postings/ckelly/Gparity/hotelling_v10.pdf (visited on 22/06/2022) (cit. on p. 69).

[105] F. James, M. Winkler et al. *Minuit2*. 2002. URL: https://root.cern.ch/doc/master/Minuit2Page.html (visited on 25/06/2020) (cit. on pp. 72, 79).

[106] Donald W. Marquardt. “An Algorithm for Least-Squares Estimation of Nonlinear Parameters”. eng. In: *Journal of the Society for Industrial and Applied Mathematics* 11.2 (1963), pp. 431–441. ISSN: 0368-4245. URL: https://www.jstor.org/stable/2098941 (cit. on pp. 73, 74).

[107] Kenneth Levenberg. “A method for the solution of certain non-linear problems in least squares”. eng. In: *Quarterly of applied mathematics* 2.2 (1944), pp. 164–168. ISSN: 0033-569X (cit. on p. 73).

[108] Haskell B. Curry. “The method of steepest descent for non-linear minimization problems”. eng. In: *Quarterly of applied mathematics* 2.3 (Jan. 1944), pp. 258–261. ISSN: 0033-569X (cit. on p. 75).

[109] Felix Erben et al. “$B(s)$-mixing parameters from all-domain-wall-fermion simulations. In preparation”. In: 40th International Symposium on Lattice Field Theory (Lattice 2023) (Fermilab, Batavia, Illinois, USA, 31st July–4th Aug. 2023). Vol. Lattice2021. Aug. 2023, p. 416. URL: https://indico.fnal.gov/event/57249/contributions/271292/ (cit. on pp. 121, 122).

[110] J. M. Flynn et al. “$B \to \pi\ell\nu$ and $B_s \to K\ell\nu$ form factors and $|V_{ub}|$ from 2+1-flavor lattice QCD with domain-wall light quarks and relativistic heavy quarks”. In: *Physical Review D* 91.7 (Apr. 2015). ISSN: 1550-2368. DOI: 10.1103/physrevd.91.074510. arXiv: 1501.05373 [hep-lat] (cit. on p. 142).

[111] Olivier Ledoit and Michael Wolf. "A well-conditioned estimator for large-dimensional covariance matrices". eng. In: *Journal of multivariate analysis* 88.2 (2004), pp. 365–411. ISSN: 0047-259X (cit. on pp. 148, 151).

[112] Olivier Ledoit and Michael Wolf. "Nonlinear shrinkage estimation of large-dimensional covariance matrices". In: *IMS-AOS-AOS989* (July 2012). DOI: https://doi.org/10.1214/12-AOS989. eprint: 1207.5322. URL: https://arxiv.org/pdf/1207.5322.pdf (cit. on pp. 148, 151).

[113] BESIII Collaboration et al. "First measurement of the form factors in $D_s^+ \to K^0 e^+ \nu_e$ and $D_s^+ \to K^{*0} e^+ \nu_e$ decays". In: *Phys. Rev. Lett.* 122 (2019), p. 061801. DOI: https://doi.org/10.1103/PhysRevLett.122.061801. arXiv: 1811.02911 [hep-ex]. URL: https://arxiv.org/pdf/1811.02911.pdf (cit. on pp. 150, 152–155).

[114] Y. Aoki et al. "FLAG Review 2021". In: *CERN-TH-2021-191, JLAB-THY-21-3528* (Nov. 2021). arXiv: 2111.09849 [hep-lat]. URL: https://arxiv.org/pdf/2111.09849.pdf (cit. on pp. 155–157).

[115] S. Di Vita et al. "Form factors of the $D \to \pi$ and $D \to K$ semileptonic decays with $N_f = 2$ twisted mass lattice QCD". In: *PoS LAT2010:301* (Apr. 2011). eprint: 1104.0869. URL: https://arxiv.org/pdf/1104.0869.pdf (cit. on p. 155).

[116] C. Aubin et al. "Semileptonic decays of D mesons in three-flavor lattice QCD". eng. In: *Physical review letters* 94.1 (2005), pp. 011601.1–011601.5. ISSN: 0031-9007. arXiv: hep-ph/0408306 [hep-ph] (cit. on p. 156).

[117] Jon A. Bailey et al. "Charm semileptonic decays and $|V_{cs(d)}|$ from heavy clover quarks and 2+1 flavor asqtad staggered ensembles". In: *FERMILAB-CONF-12-610-T* (Nov. 2012). arXiv: 1211.4964 [hep-lat]. URL: https://arxiv.org/pdf/1211.4964.pdf (cit. on p. 156).

[118] Heechang Na et al. "$D \to K \ell \nu$ semileptonic decay scalar form factor and $|V_{cs}|$ from lattice QCD". eng. In: *Physical review. D, Particles, fields, gravitation, and cosmology* 82.11 (Dec. 2010). ISSN: 1550-7998. DOI: 10.1103/physrevd.82.114506. arXiv: 1008.4562 [hep-ph] (cit. on p. 156).

[119] Heechang Na et al. "$D \to \pi \ell \nu$ semileptonic decays,$|V_{cd}|$ and second row unitarity from lattice QCD". In: *Physical Review D* 84.11 (Dec. 2011). DOI: 10.1103/physrevd.84.114505. arXiv: 1109.1501 [hep-lat] (cit. on p. 156).

[120] HPQCD Collaboration et al. "The $D \to K$ and $D \to \pi$ semileptonic decay form factors from Lattice QCD". In: (Nov. 2011). arXiv: 1111.0225 [hep-lat]. URL: https://arxiv.org/pdf/1111.0225.pdf (cit. on p. 156).

[121] J. Koponen, C. T. H. Davies and G. Donald. "$D \to K$ and $D \to \pi$ semileptonic form factors from Lattice QCD". In: (Aug. 2012). arXiv: 1208.6242 [hep-lat]. URL: https://arxiv.org/pdf/1208.6242.pdf (cit. on p. 156).

[122] Takashi Kaneko et al. "D meson semileptonic form factors in Nf = 3 QCD with Möbius domain-wall quarks". In: *EPJ Web of Conferences* 175 (2018). Ed. by M. Della Morte et al., p. 13007. DOI: 10.1051/epjconf/201817513007. arXiv: 1711.11235 [hep-lat]. URL: https://doi.org/10.1051%2Fepjconf%2F201817513007 (cit. on p. 156).

[123] V Lubicz et al. "Scalar and vector form factors of $D \to \pi\,(K)\,\ell\nu$ decays with $N_f = 2+1+1$ twisted fermions". eng. In: *Physical review. D* 96.5 (2017). ISSN: 2470-0010. arXiv: 1706.03017 [hep-lat] (cit. on p. 156).

[124] V. Lubicz et al. "Tensor form factor of $D \to \pi(K)\ell\nu$ and $D \to \pi(K)\ell\ell$ decays with Nf=2+1+1 twisted-mass fermions". eng. In: *Physical review. D* 98.1 (2018). ISSN: 2470-0010. arXiv: 1803.04807 [hep-lat] (cit. on p. 156).

[125] Bipasha Chakraborty et al. "Improved V_{cs} determination using precise lattice QCD form factors for $D \to K\ell\nu$". eng. In: *Physical review. D* 104.3 (Apr. 2021), pp. 1–. ISSN: 2470-0010. arXiv: 2104.09883 [hep-lat]. URL: https://arxiv.org/pdf/2104.09883 (cit. on p. 156).

[126] Paolo Gambino et al. "Lattice QCD study of inclusive semileptonic decays of heavy mesons". eng. In: *The journal of high energy physics* 2022.7 (2022), pp. 83–51. ISSN: 1029-8479 (cit. on p. 157).

[127] Paolo Gambino et al. "On the study of inclusive semileptonic decays of B_s-meson from lattice QCD". In: (Nov. 2023). arXiv: 2311.09892 [hep-lat]. URL: https://arxiv.org/pdf/2311.09892.pdf (cit. on p. 157).